MONASH University

Dynamic Mineral Recrystallization of Manganese Oxides
–
Effects on Metal Mobility and Enrichment in
Deep-sea Ferromanganese Nodules and Crusts

Tobias Hens

MSc Earth Sciences

A thesis submitted for the degree of

Doctor of Philosophy

at Monash University in 2019

School of Earth, Atmosphere and Environment

Copyright Notice

Abstract

Global challenges, such as population growth and climate change, necessitate the rapid advancement of *green* technologies. However, innovative zero-emission transport solutions (e.g., electric vehicles) and growing shares of renewable energy production require large amounts of critical metals. The rising demand for these raw materials increases pressures on land-based mineral deposits, some of which already face declining ore grades and socioeconomic problems. Hence, marine mineral deposits – in particular deep-sea ferromanganese nodules and crusts – are considered future resources by an emerging marine mining industry due to their enrichment in traditional and non-traditional metals. Formed on abyssal plains (nodules) or localized seamounts (crusts), deep-sea ferromanganese concretions with economic ore grades are abundantly available in comparatively small areas of the global oceans. Utilizing these deposits may help drive the *green*-tech revolution.

Deep-sea ferromanganese nodules and crusts are composed of iron and manganese (oxyhydr)oxide mineral phases, which form during biogeochemical redox cycling of these two metals in the ocean. Considering only the redox cycling of manganese (Mn), oxidation of aqueous Mn(II) (Mn(II)$_{aq}$) to Mn(III,IV) oxides occurs simultaneously with (a)biotic reduction of these oxides to Mn(II)$_{aq}$. Since dissolved manganese is in direct contact with Mn oxides, back-reactions via abiotic pathways, such as continuous recrystallization of the Mn oxides through coupled dissolution-reprecipitation processes, may ensue. Consequently, these processes may influence release, sorption, and subsequent incorporation of trace metals (e.g., nickel) into the crystal structure of manganese oxides. Interactions between minerals and fluids and their effects on the enrichment and partitioning of metals in deep-sea ferromanganese concretions remain, however, poorly constrained.

Experimental work in this thesis, hence, focuses on the exchangeability of nickel (Ni) between solids and solutions during Mn oxide mineral recrystallization. To infer the effects of dissolved Mn(II) on Ni exchange in synthetic and natural Mn oxides, state-of-the-art synchrotron-based research was combined with well-established stable isotope tracer geochemistry techniques in an integrated approach. Reactions between synthetic Ni-substituted manganite (γ-Mn(III)OOH) and solutions show that, in comparison to Mn(II)$_{aq}$-free reactions, increased concentrations of dissolved Mn(II) catalyze Ni exchange through continuous recrystallization. Coupled dissolution-reprecipitation reactions enable fluid penetration of the bulk mineral, allowing for structural Ni incorporation without causing significant mineral phase transformations.

Experiments utilizing synthetic layer-type Mn(IV) oxides (phyllomanganates) indicate that, although Ni exchange is largely independent of $Mn(II)_{aq}$ concentrations, variable phyllomanganate properties influence the extent of Ni exchange. The fact that Ni exchanges between deep-sea ferromanganese concretions (Mn(IV) oxides) and solutions demonstrates the susceptibility of structurally incorporated Ni to mineral-fluid repartitioning in deep-sea ferromanganese nodules and crusts.

The work of this thesis aims to advance our understanding of how dissolved Mn(II) influences Mn oxides, as these minerals exert strong control on metal enrichment and contaminant mobility in natural settings. For instance, a thorough understanding of ferromanganese nodules and crust mineral-fluid repartitioning is vital for future development of tailored hydro-metallurgical applications. Targeting, and selectively removing, specific metals of interest in an energy-efficient, environmentally responsible manner constitutes a critical component that will positively affect good governance and overall economics of the marine mining value chain.

Declaration – Publications During Enrolment

Hens, T., Brugger, J., Etschmann, B., Paterson, D., Brand, H.E.A., Whitworth, A., Frierdich, A.J., 2019. *Nickel Exchange Between Aqueous Ni(II) and Deep-sea Ferromanganese Nodules and Crusts*. Chemical Geology, In Press, doi: 10.1016/j.chemgeo.2019.119276

Hens, T., Brugger, J., Cumberland, S.A., Etschmann, B., Frierdich, A.J., 2018. *Recrystallization of Manganite (γ-MnOOH) and Implications for Trace Element Cycling*. Environmental Science & Technology, 52(3): 1311-1319, doi: 10.1021/acs.est.7b05710

Declaration – Thesis Including Published Works

I hereby declare that this thesis contains no material which has been accepted for the award of any other degree or diploma at any university or equivalent institution and that, to the best of my knowledge and belief, this thesis contains no material previously published or written by another person, except where due reference is made in the text of the thesis.

This thesis includes (1) original paper published in peer reviewed journals and (1) submitted publication. The core theme of the thesis is *Mn(II)$_{aq}$-catalyzed mineral recrystallization of Mn oxides and its effects on deep-sea ferromanganese nodules and crusts*. The ideas, development and writing up of all the papers in the thesis were the principal responsibility of myself, the candidate, working within the *School of Earth, Atmosphere and Environment* under the supervision of *Dr. Andrew Frierdich and Prof. Joël Brugger.*

The inclusion of co-authors reflects the fact that the work came from active collaboration between researchers and acknowledges input into team-based research.

In the case of Chapters 2, 3, and 4 my contribution to the work involved the following:

Thesis Chapter	Publication Title	Status[1]	Nature and extent (%) of student contribution	Co-author name(s) and extent of Co-author's contribution[2]	
2	Recrystallization of Manganite (γ-MnOOH) and Implications for Trace Element Cycling	Published	**70%**; - experiments - data collection - manuscript draft	Joël Brugger Susan A. Cumberland Barbara Etschmann Andrew J. Frierdich	5% 1.25% 3.75% 20%
3	Nickel Exchange Between Aqueous Ni(II) and Synthetic Phyllomanganates	Not Submitted	**95%**; - experiments - data collection - manuscript draft	Andrew J. Frierdich	5%
4	Nickel Exchange Between Aqueous Ni(II) and Deep-sea Ferromanganese Nodules and Crusts	In Press	**85%**; - experiments - data collection - manuscript draft	Joël Brugger Barbara Etschmann David Paterson Helen E. A. Brand Anne Whitworth* Andrew J. Frierdich	2.5% 2.5% 1.25% 1.25% 1.25% 6.25%

[1]e.g. (Not) Submitted/In Review/Returned for Revision/Accepted/In Press/Published
[2]Co-authors are not Monash students unless indicated by *

I have renumbered sections of submitted or published papers in order to generate a consistent presentation within the thesis.

Student signature: Not required in final version   **Date:** 19.08.2019

The undersigned hereby certify that the above declaration correctly reflects the nature and extent of the student's and co-authors' contributions to this work. In instances where I am not the responsible author I have consulted with the responsible author to agree on the respective contributions of the authors.

Main Supervisor signature: Not required in final version   **Date:** 19.08.2019

Acknowledgments

I would like to acknowledge the many people who contributed to make this thesis a truly life-changing experience. Firstly, to my main supervisor Andrew J. Frierdich who provided valuable advice and guidance along the way. I am profoundly grateful to Joël Brugger, my co-supervisor, and Barbara Etschmann for their roles during Synchrotron data acquisition and analysis. My sincere thanks to beamline scientists Peter Kappen, Susan Cumberland, and David Paterson for their help at the Synchrotron. I am thankful to Massimo Raveggi, and Yona Nebel-Jacobsen for assistance with in-house sample preparation and the team members of the School of Earth, Atmosphere, and Environment who helped me battle the administrative tasks.

I am especially indebted to Barrie Bolton who provided deep-sea ferromanganese nodules and crusts from his personal collection. This project would not have been successful without them. I am grateful to have met and engaged in fruitful discussions with Jim Hein, Thomas Kuhn, Andrea Koschinsky, Peter Halbach, Georgy Cherkashov, Robert Goodden, as well as Charles and Karynne Morgan about diverse aspects related to Deep-Sea Mining.

Thank you to my family. Mama and Papa, you have been generous, always encouraged me, and taught me strong values. Sílvia, thank you for 'being in the present' when I focus too much on the future. Your unwavering optimism during our daily struggles is refreshing.

Finally, I would like to thank a very special group of people, sheepdogs and students of a meaningful and purpose-driven life, who continue to inspire me to face adversity head-on and push myself harder, physically and mentally. David, Mark, Jason, Jocko, Thom, Les, Earl, and Jordan, the way you overcame adversity in your lives (and still do to this day) opened my eyes in ways I could have never imagined.

We do today what others won't so we can do tomorrow what others can't

x

Contents

Chapter 1 –

Introduction & Thesis Background

Chapter 2 –

Recrystallization of Manganite (γ-MnOOH) and Implications for Trace Element Cycling

Chapter 3 –

Nickel Exchange Between Aqueous Ni(II) and Synthetic Phyllomanganates

Chapter 4 –

Nickel Exchange Between Aqueous Ni(II) and Deep-Sea Ferromanganese Nodules and Crusts

Chapter 5 –

Conclusions

List of Figures

Chapter 1

Chapter 2

Chapter 3

Chapter 4

List of Tables

Chapter 2

Chapter 3

Chapter 4

Nomenclature

Symbol/ Abbreviation	Description
Å	Ångstrom
AOS	Average Oxidation State
aq	Aqueous
CCZ	Clarion-Clipperton Zone
CFA	Carbonate Fluorapatite
CI	Cook Islands
CIOB	Central Indian Ocean Basin
CP-DP	Comproportionation-Disproportionation
cps	Counts per second
DMR	Dynamic Mineral Recrystallization
EEZ	Exclusive Economic Zone
eq	equation
ET-AE	Electron Transfer-Atom Exchange
eV/ keV	Electron Volts/ Kilo Electron Volts
EXAFS	Extended X-ray Absorption Fine Structure
f	(isotopic) fraction
Fe_2O_3	Hematite
FeOOH/ δ-FeOOH	Goethite/ Feroxyhite
HEPES	4-(2-hydroxyethyl)-1-piperazineethanesulfonic acid buffer
ICP-OES	Inductively Coupled Plasma-Optical Emission Spectrometry
ICP-MS	Inductively Coupled Plasma-Mass Spectrometry
ISA	International Seabed Authority
Ma/ ka	Million years/ Thousand years
MBL	Mass Balance Line
MES	2-(4-morpholino)ethanesulfonic acid buffer
M/ mM/ µM/ nM	Molar/ Millimolar/ Micromolar/ Nanomolar
δ-MnO_2/ δ-$Mn(IV)O_2$	Vernadite

Symbol/ Abbreviation	Description
α-MnOOH/ α-Mn(III)OOH	Groutite
β-MnOOH/ β-Mn(III)OOH	Feitknechtite
γ-MnOOH/ Mn(III)OOH/ MnOOH	Manganite
MOPS	3-(1-morpholino)propanesulfonic acid buffer
NA	Natural Abundance
OMZ	Oxygen Minimum Zone
PB	Peru Basin
PCZ	Prime Crust Zone
PD	Powder Diffraction
REE	Rare Earth Element
REY	Rare Earth Elements + Yttrium
s	Solid
SN	Shale-Normalized
SXFM/ μ-SXRF	Synchrotron-based X-ray Fluorescence Microscopy/ Micro-Scanning X-ray Fluorescence
UCC	Upper Continental Crust
UN	United Nations
wt%	Weight percent
XANES	X-ray Absorption Near Edge Structure
XAS	X-ray Absorption Spectroscopy
XFM	X-ray Fluorescence Microscopy
XRD/ SXRD	X-ray Diffraction/ Synchrotron-based X-ray Diffraction
δ	Delta
θ	Theta
μ	Mu, Micro
χ	Chi
Ω	Ohm
≤ / ≥	Less than or equal to / greater than or equal to
°	Degree

Chapter 1

Introduction & Thesis Background
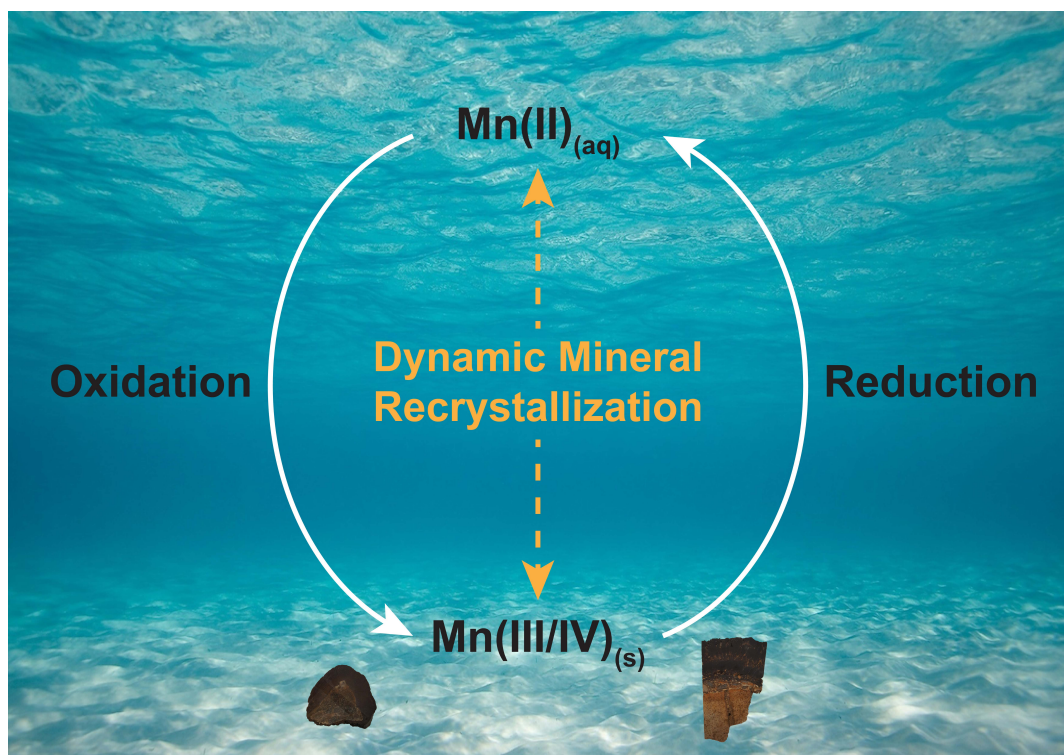
1. Introduction

Mankind has seen an unprecedented rise of technological advances driven by ever-evolving scientific research and innovation in the past two centuries. Land-based mineral deposits, which provide a wide array of metals, have been one of the cornerstones enabling our modern-day, high-tech lifestyle. However, despite our increasing prosperity, we face global challenges, such as continuing population growth (UN, 2017), the consequent pressures on resources (Hein, 2016b), and anthropogenic climate change (Rosenzweig et al., 2008). Hence, we move towards *green*-technology solutions (e.g., Mulvaney, 2011) and shift our focus to the marine realm to satisfy our increasing demand for raw materials.

The deepest parts of the global oceans hold vast amounts of mineral resources. Deep-sea ferromanganese (Fe-Mn) nodules and cobalt-rich crusts[1] are merely two types of deposits coming within our reach due to advancing technology and rapidly growing knowledge about the deep-marine environment. Ferromanganese nodules and crusts are considered prime targets for future raw material supply as they can exhibit significant enrichment of metals in comparison to land-based deposits (Hein et al., 2013). Geoscientific research on these metallic concretions has been conducted since the 1950s (Mero, 1965) and picked up pace in recent years since the global demand for high-tech and green-tech metals is on the rise (Haxel et al., 2002; Hein, 2016a; Hein et al., 2013). Metals, such as Te (photovoltaic solar cells), Bi and Nb (high-temperature superalloys), Pt (hydrogen fuel cells), Y (flat-screen displays), and Nd (high-strength permanent magnets), among other elements (e.g., REE) are coming increasingly into focus aside from Mn, Cu, Ni, and Co, respectively (Hein et al., 2013). Consequently, other disciplines have been attracted by the possibility of deep-sea mining of Fe-Mn deposits taking place in the future.

Design and operation of suitable technical equipment to harvest Fe-Mn deposits in water depths and pressures of several thousand meters are subject to diverse fields of engineering. Jurisdictional challenges, arising from the fact that many Fe-Mn deposits are located in international waters ('the Area') beyond the Exclusive Economic Zones of nation states (e.g., ISA, 2000; ISA, 2001), have to be dealt with by appropriate governing bodies such as the International Seabed Authority (ISA). Drafting and implementation of sustainable policies are

---

[1] Ferromanganese nodules and crusts are also often referred to as Fe-Mn nodules/crusts, iron-manganese nodules/crusts, polymetallic nodules/crusts, cobalt crusts, cobalt-rich ferromanganese crusts in the scientific literature. These terms are used synonymous throughout this thesis.

essential requirements for Fe-Mn resources which are considered *common heritage of mankind* by the United Nations (Nicholson, 2002; Sharma, 2017b). Furthermore, environmental impacts on the largely unknown deep-ocean ecosystem are one of the most pressing concerns for scientists and the informed public alike, as deep-sea mining-induced disturbances (e.g., sediment plume formation and dispersion) may create potential threats to marine biodiversity and long-term habitat loss (e.g., Gollner et al., 2017; Kim, 2017; Miljutin et al., 2011; Miller et al., 2018; Sharma et al., 2001).

The technological, legislative, and environmental challenges briefly listed here, amongst many others, and their possible solutions will have to be addressed sufficiently by engineers, policy makers, and scientists across multiple disciplines. An in-depth discussion of these issues is, however, well beyond the scope of this thesis which focuses on geochemical processes relating to Fe-Mn nodules and crusts. Hence, the interested reader is referred to the steadily growing body of literature providing summaries, reviews, and detailed information about the current status of deep-sea mining-related research (e.g., Hein and Koschinsky, 2014; Lusty and Murton, 2018; Sharma, 2017a and references therein).

1.1. Research Rationale and Hypothesis

In addition to the aforementioned challenges, it is of critical importance to advance our fundamental understanding of Fe-Mn nodule and crust geochemistry and, more specifically, their manganese (oxyhydr)oxide minerals (hereon Mn oxides), which are host phases to critical metals. We currently have limited comprehension of how (bio)geochemical processes influence metal sorption and subsequent incorporation into the crystal structure of Mn oxides during the formation and alteration of Fe-Mn concretions. The effects of interactions between mineral- and fluid phases on the enrichment and partitioning of (trace) metals remain poorly constrained.

A fundamental understanding of these effects is, for instance, required by researchers investigating metal fluxes in the environment. Interactions between Mn oxides and fluids may play an important role for metal mobility in aquatic environments (Bargar et al., 2009; Frierdich et al., 2011a) as well as for element uptake and release in Fe-Mn nodules and crusts, due to the potential cycling of major, minor, and trace elements (Hein and Koschinsky, 2014; Peacock and Sherman, 2007b). Likewise, metallurgists who consider the innovation of (hydro)metallurgical extraction processes may focus on mineral-fluid interactions, since

established metallurgical treatment and conventional beneficiation methods are perceived as insufficient solutions for Fe-Mn concretions (Burns and Burns, 1977; Haynes et al., 1985; Von Heimendahl et al., 1976; Wegorzewski et al., 2018).

One such mineral-fluid interaction affecting Mn oxides is referred to as Dynamic Mineral Recrystallization (DMR)[2]. This process can occur during (bio)geochemical redox cycling of Mn, a cornerstone mechanism for Mn oxide formation in nature (2.1). Redox cycling of Mn is characterized by microbial oxidation of aqueous Mn(II) (Mn(II)$_{aq}$) to Mn(III,IV) oxides and (a)biotic reduction of these oxides to Mn(II)$_{aq}$. During this cycling Mn(II)$_{aq}$ can be in direct contact with Mn(III,IV) oxides and back-react via abiotic pathways under both Mn-oxidizing and Mn-reducing conditions (e.g., Elzinga, 2016).

Recent work by Hinkle et al. (2016), for instance, has shown that Mn oxides commonly found in Fe-Mn nodules and crusts (phyllomanganates) are able to both adsorb and incorporate Mn(II). Phyllomanganates consist of negatively charged octahedral sheets separated by hydrated interlayers (2.2.3). To compensate for the negative charge, which develops as a result of Mn(IV) vacancies and Mn(III) substitutions in the octahedral sheets, exchangeable cations (e.g., Mn(II)) can sorb above/below vacant sites and be incorporated into the mineral structure over time (Zhao et al., 2016; Zhu et al., 2010). Mn(II) adsorption can also involve electron transfer via Mn(II)-Mn(IV) comproportionation reactions resulting in increased structural Mn(III) content (Hinkle et al., 2016; Webb et al., 2005a). Most notably, however, these reactions may impact adsorption and redox transformation of trace elements already structurally incorporated in Mn oxides through simultaneously occurring dissolution (trace metal release) – reprecipitation (trace metal incorporation) processes of the Mn oxide substrate (Elzinga, 2011; Elzinga, 2016; Johnson et al., 2016; Learman et al., 2011; Lefkowitz and Elzinga, 2015; Lefkowitz et al., 2013; Perez-Benito, 2002; Tu et al., 1994).

Furthermore, experiments reacting manganite (γ-Mn(III)OOH) with Mn(II)$_{aq}$ in the presence of oxygen isotope tracer solutions have shown that Mn(II)$_{aq}$ enhances exchange between structural oxygen in manganite with water (Frierdich et al., 2016). This suggests the occurrence of electron transfer and atom exchange (ET-AE) processes between Mn(II)$_{aq}$ and structural Mn(III) in stable Mn(III) oxides. Chapter 2 provides a detailed description and in-depth

---

[2] Dynamic Mineral Recrystallization (DMR) is also often referred to as Mn(II)$_{aq}$-catalyzed mineral recrystallization, Mn(II)$_{aq}$-accelerated recrystallization, redox-driven recrystallization, stable mineral recrystallization. These terms are used synonymously throughout this thesis.

discussion of related experiments reacting manganite with $Mn(II)_{aq}$ and a $Ni(II)_{aq}$ isotope tracer solution to investigate Ni cycling between solid and solution through redox-driven mineral recrystallization (Fig. 1).
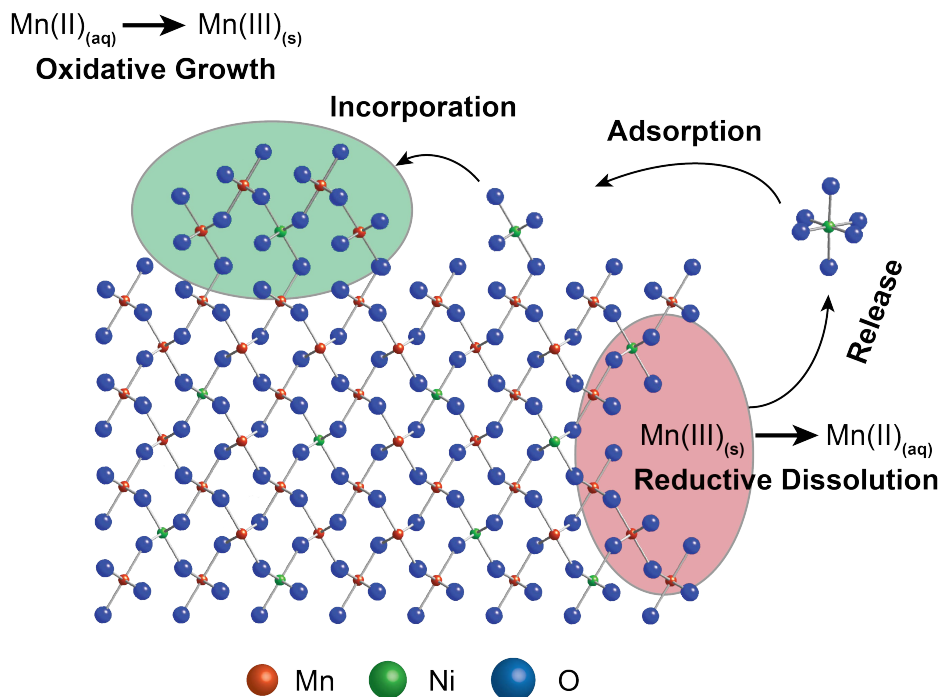
Fig. 1. Conceptual model of $Mn(II)_{aq}$-catalyzed mineral recrystallization. Abiotic dissolution-reprecipitation reactions cycle Ni between the Mn oxide manganite and solution, following $Mn(II)_{aq}$ sorption onto the manganite surface (not depicted). Schematic modified after Frierdich et al. (2011b).

Studies on iron oxides, similarly, showed Ni cycling between aqueous Fe(II)-bearing solutions and goethite (FeOOH) as well as hematite (Fe_2O_3) during redox-driven mineral recrystallization processes (Frierdich et al., 2011b). X-ray absorption spectroscopy demonstrated that during recrystallization surface-adsorbed Ni becomes progressively incorporated into the crystal structure of the iron minerals. It was suggested that the net directionality of trace element repartitioning will vary among environments, but should be thermodynamically controlled and dependent on the relative activities of trace elements in solution, adsorbed on the surface, and incorporated within the mineral structure (Frierdich and Catalano, 2012). This proposed mechanism of metal incorporation and release is catalyzed by aqueous Fe(II), which initiates the recrystallization of Fe(III) oxides. Over time, surface-adsorbed Ni is then overgrown in regions of Fe(II) oxidative adsorption whereas pre-incorporated Ni is released in regions of reductive dissolution of structural Fe(III) (Frierdich et al., 2011b).

On the basis of the research outlined above, and considering that the effects of interactions between mineral- and fluid phases on the enrichment and partitioning of (trace) metals in Mn oxides remain poorly constrained, the following hypothesis is proposed:

- Trace metal (e.g., Ni) surface-sorption and subsequent incorporation into the mineral structure of Mn oxides will occur, and is catalyzed, in the presence of $Mn(II)_{aq}$.

- Mechanistically, Mn(II) undergoes electron transfer-atom exchange (ET-AE) and disproportionation-comproportionation (DC-CP) reactions, which are ultimately driving $Mn(II)_{aq}$-accelerated mineral recrystallization of Mn oxides.

- Trace metals, specifically Ni, are susceptible to mineral-fluid repartitioning after structural incorporation into the Mn oxide phases of Fe-Mn nodules and crusts, as $Mn(II)_{aq}$ makes the bulk mineral structure accessible to fluids.

1.2. Research Aims

The overarching research aim of this thesis is to investigate the effects of Dynamic Mineral Recrystallization on Mn oxides to infer influences on deep-sea ferromanganese nodule and crust genesis, alteration, and trace element mobility. Consequently, three project objectives were devised and consolidated into the following three research chapters:

- Chapter 2 is aimed at understanding the role that $Mn(II)_{aq}$-catalyzed recrystallization plays during Ni(II) sorption and incorporation into the synthetic Mn oxide manganite.

- Chapter 3 focuses on the exchangeability of Ni between solutions and synthetic phyllomanganates, which represent reliable analogues to Mn oxides occurring in deep-sea ferromanganese nodules and crusts.

- Chapter 4 examines the exchangeability of Ni between solutions and deep-sea ferromanganese nodule and crust samples.

These project objectives helped elucidate the fate of trace elements during the recrystallization of Mn oxides. By transitioning from synthetic manganite to synthetic phyllomanganates and then to deep-sea ferromanganese concretions, the effects of DMR on Mn oxides could be investigated in systems of increasing mineralogical complexity.

1.3. Thesis Structure

The work composing this thesis is presented in five chapters. This introduction chapter is followed by three research chapters, and a final conclusion chapter. Monash University allows PhD theses to be structured as a collection of research papers that are either submitted for publication, accepted, published, or formatted as articles but not submitted. Accordingly, the research chapters of this thesis are presented in the form of stand-alone and peer-reviewed journal articles. This has invariably resulted in the repetition of some material, notably in the introduction and methods sections of several chapters. Chapter 2 has been published in *Environmental Science & Technology* (Hens et al., 2018). Chapter 3 has not been published, whereas Chapter 4 has been published in *Chemical Geology*. The fifth chapter draws conclusions from the discussion sections of the respective research chapters.

Chapter 1: *Introduction and Thesis Background.* Chapter 1 introduces the rationale behind the research into the recrystallization of synthetic Mn oxides and deep-sea Fe-Mn concretions addressed in the following chapters. This is followed by an overview of analytical techniques used and general background of the topics covered in this thesis.

Chapter 2: *Recrystallization of Manganite (γ-MnOOH) and Implications for Trace Element Cycling*; published in *Environmental Science & Technology* explores how Ni is cycled during $Mn(II)_{aq}$-catalyzed mineral recrystallization of manganite. Ni sorption and progressive incorporation into the manganite structure are investigated with synchrotron-based X-ray Absorption Spectroscopy. The extent of Ni exchange between solid and solution is evaluated by employing Ni stable-isotope tracer experiments.

Chapter 3: *Nickel Exchange Between Aqueous Ni(II) and Synthetic Phyllomanganates*; examines Ni exchangeability between fluids and synthetic variations of vernadite, hexagonal birnessite, and triclinic birnessite. These phyllomanganates, which resemble naturally occurring minerals, were synthesized and subjected to $Mn(II)_{aq}$- and Ni(II)-bearing solutions to measure the extent of Ni exchange.

Chapter 4: *Nickel Exchange Between Aqueous Ni(II) and Deep-sea Ferromanganese Nodules and Crusts*; accepted for publication in *Chemical Geology* investigates Ni exchangeability between fluids and Fe-Mn nodule and crust samples. Ni exchange is evaluated by employing Ni stable isotope tracer experiments and synchrotron-based X-ray fluorescence microscopy and powder diffraction.

Chapter 5: *Conclusions*; synthesizes the findings of the research chapters and draws conclusions about the implications of Dynamic Mineral Recrystallization on Mn oxides and Fe-Mn nodules and crusts. Future research directions are presented and discussed briefly.

1.4. Analytical Techniques

The experimental work conducted in this thesis follows an integrated approach that combines well-established stable isotope tracer geochemistry techniques with state-of-the-art synchrotron-based research. The combination of different techniques allows for data validation and a better understanding of geochemical process interactions. A brief outline of the applied methods is provided below, whereas a detailed methodology can be found in the relevant research chapters.

1.4.1. X-ray Diffraction

Benchtop X-ray diffraction (XRD) analyses were used to quickly and reliably determine the phase identity and structure of crystalline samples. The interaction of X-rays with the crystal array of the sample results in a scattering pattern that is unique for the atomic arrangements of a sample. X-ray diffraction of mineral powders was utilized in this thesis to verify the products of Mn oxide syntheses and identify phase transformations of Mn oxides during and after recrystallization experiments.

1.4.2. Inductively Coupled Plasma Spectrometry

Both Inductively Coupled Plasma – Optical Emission Spectrometry (ICP-OES) and Inductively Coupled Plasma – Mass Spectrometry (ICP-MS) were used to analyze major, minor, and trace element concentrations of synthetic, natural, and batch reaction experiment samples. These analyses allowed to examine the initial bulk geochemical composition of synthetic and ferromanganese materials, and track metal fluxes between solid and solution during recrystallization reactions.

1.4.3. Iodometric Titrations for Mn Average Oxidation State Determination

Iodometric titrations are a proven and effective tool to determine the Mn oxidation state of Mn oxides. Iodine, which was produced through a reaction of excess iodide with Mn ions, was titrated with thiosulfate solution to directly provide a number of moles of manganese that are reduced during the process of iodide oxidation by manganese species having a greater than +II oxidation state (Birkner et al., 2013).

1.4.4. Synchrotron-based X-ray Absorption Spectroscopy

Synchrotron X-ray Absorption Spectroscopy (XAS) is a powerful tool to obtain quantitative and qualitative information about crystal structures and coordination environments around single atoms that cannot be acquired with other techniques in the same manner. In this thesis, X-ray Absorption Near Edge Structure (XANES) spectroscopy and Extended X-ray Absorption Fine Structure (EXAFS) spectroscopy were used to explore changes in the oxidation state of atoms and local coordination geometry of synthetic manganite phases.

1.4.5. Synchrotron-based Powder Diffraction

Synchrotron-based Powder Diffraction (PD), also referred to as Synchrotron-based XRD (SXRD) in Chapter 4, is characterized by a higher resolution and better signal-to-noise ratio compared to laboratory-based XRD, due to the use of synchrotron radiation delivering high-intensity X-rays over a continuous and broad energy range. Successful analysis of poorly-crystalline samples such as ferromanganese nodules and crusts was achieved by measuring the samples as powders to expose random crystal orientation to the X-ray beam.

1.4.6. Synchrotron-based X-ray Fluorescence Microscopy

Synchrotron-based X-ray Fluorescence Microscopy (SXFM), has been utilized to determine the abundance and distribution of trace elements in Fe-Mn nodules and crusts by means of fully quantitative maps. This technique, moreover, enabled the measurement of Mn oxidation states via XANES imaging and the resolution of μm-scale growth features (2-4 μm horizontal spatial resolution) with high throughput of samples.

2. Thesis Background

2.1. Manganese Geochemistry and the Biogeochemical Mn Cycle

Manganese is the tenth most abundant element in the Earth's crust with known oxidation states ranging from -III to +VII (Crerar et al., 1980; Post, 1999). The predominant oxidation states in nature are +II, +III, and +IV which, in turn, are determined by ambient environmental conditions (Crerar et al., 1980; Post, 1999). Mn(II) constitutes the most stable Mn oxidation state in solution that readily interacts with ligands (Lindsay, 1979). Soils, sediments, and rocks are hosts to over 30 (oxyhydr)oxide minerals of manganese that exist as fine-grained aggregates, marine and fresh-water concretions (e.g., ferromanganese nodules and crusts), veins, dendrites, and coatings on other mineral particles and rock surfaces (Post, 1999). With oxidation states ranging from +II to +IV and a remarkable diversity of atomic

architectures that can accommodate other metal cations, these ubiquitous minerals are powerful oxidants and among the strongest metal scavengers in the environment (Goldberg, 1954; Miyata et al., 2007; Post, 1999; Tebo et al., 2004).

The cornerstone process of Mn oxide formation is (bio)geochemical redox cycling of Mn (Fig. 2). Oxidation of aqueous Mn(II) can occur through autocatalytic (abiotic) reactions, but is commonly mediated by microbial processes (biogenic) (Lovely, 2000; Myers and Nealson, 1988; Skinner and Fitzpatrick, 1992; Villalobos et al., 2006; Webb et al., 2005b). This may result in the formation of δ-MnO$_2$-like phyllomanganates, which subsequently act as potent metal scavengers, affecting mobility and distribution of dissolved metals and metallic complexes (i.e. enrichment of metals, such as Cd or Co, in the Mn fraction of deep-sea Fe-Mn concretions in contrast to the Fe fraction as some metals and complexes have stronger affinity for Mn oxides) (Koschinsky and Halbach, 1995; Koschinsky and Hein, 2003; Varentsov and Grassely, 1980).

Conversely, reduction of Mn oxides occurs when Mn oxides serve as electron acceptors during microbial respiration or when the redox conditions change (Lovely, 2000; Myers and Nealson, 1988). This leads to (a)biotic reductive dissolution of solid-phase Mn(III,IV) and release of dissolved Mn(II) into groundwater and sediment pore water. During this cycling dissolved Mn(II) is evidently in direct contact with solid-phase Mn(III,IV) oxides and can back-react via abiotic pathways such as Dynamic Mineral Recrystallization (Fig. 2).
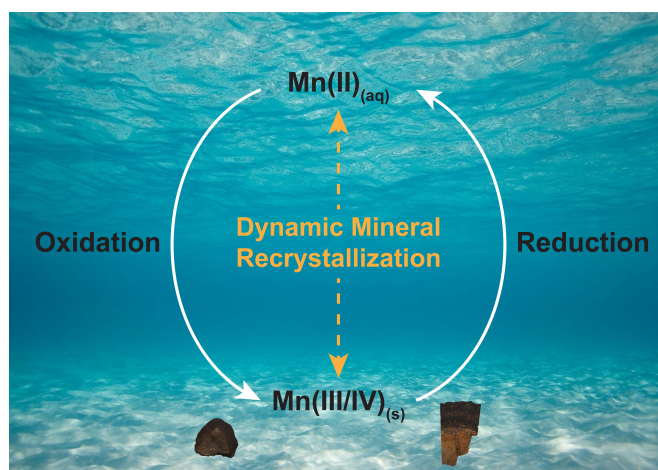
Fig. 2. Simplified illustration of the (bio)geochemical Mn cycle. Mn(II)$_{aq}$ oxidation through abiotic and microbial mediation forms Mn(III/IV) oxides which act as potent metal scavengers. Reductive dissolution of Mn oxides via (a)biotic pathways leads to release of Mn(II)$_{aq}$ into the environment. Abiotic back-reactions between Mn(II)$_{aq}$ and Mn(III/IV) oxides can lead to Dynamic Mineral Recrystallization which, in turn, may directly impact trace metal enrichment and mobility in marine ferromanganese deposits. Background modified from www.tidalvisionusa.com (2017).

2.2. Ni Isotope Tracers and Synthetic Manganese Oxides

2.2.1. Ni Isotope Tracers

To investigate the effects of dissolved Mn(II) on the recrystallization of Mn oxides experimental work in this thesis focuses on Ni exchange reactions between minerals and fluids. Ni isotope tracer solutions, which are highly enriched in ^{62}Ni (~98%, see *Materials and Methods* sections of Chapters 2, 3, and 4), were reacted with Mn oxides that contained Ni of natural abundance composition. Nickel has five stable isotopes with the following natural abundances: ^{58}Ni – 68.077%, ^{60}Ni – 26.223%, ^{61}Ni – 1.140%, ^{62}Ni – 3.635%, and ^{64}Ni – 0.926%, respectively (Wieser, 2006). The presence of two pools of Ni isotopes with distinctly different isotope compositions allowed to track Ni exchange between solid and solution. Consequently, by characterizing the extent of Ni exchange it is possible to draw conclusions about the influence of dissolved Mn(II) on the recrystallization process and infer possible reaction mechanisms.

2.2.2. Manganite

Synthetic variations of manganite (e.g., Ni-free manganite, Ni-substituted manganite; Fig. 3) were utilized as part of the experimental work conducted in Chapter 2. Manganite was chosen as it is the most stable Mn(III) (oxyhydr)oxide occurring in natural environments (Varentsov and Grassely, 1980). Moreover, it is an important precursor for forming MnO_2 by disproportionation (Ramstedt and Sjöberg, 2005). Lastly, its use aligned with a previous study conducted by (Frierdich et al., 2016), which investigated oxygen exchange between manganite and water, and resultantly allowed for a direct comparison of oxygen and Ni exchange.
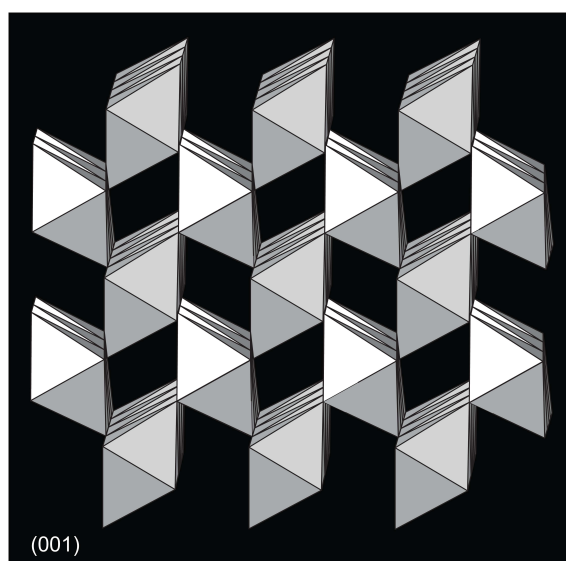
Fig. 3. View along the (001) plane of the manganite crystal structure. Modified after Ramstedt et al. (2004).

The crystal structure of manganite is defined by a framework of MnO_6 octahedra sharing corners or edges (Varentsov and Grassely, 1980) that is similar to a rutile (TiO_2) structure with rows of $Mn(IV)O_6$ octahedra (Fig. 3). The characteristic d^4 valence electron configuration of Mn(III) (Crerar et al., 1980), however, leads to Jahn-Teller distortion of the octahedra with two long apical distances and four short axial distances and replacement of half of the oxygen atoms by OH-groups (Kohler et al., 1997).

2.2.3. Phyllomanganates

Three synthetic phyllomanganates – vernadite (δ-MnO_2), c-disordered (hexagonal) H^+-birnessite, and triclinic birnessite (hereon vernadite, HexB, TriB) – with a portion of Mn substituted by approximately 1-2 mol% Ni were utilized during experiments for the following reasons: (i) these minerals are reliable analogues to naturally occurring Mn oxides in deep-sea Fe-Mn concretions, and (ii) their crystal structure (i.e. synthesized with Ni-substitution, yet without potentially interfering impurities) represents a step of intermediate complexity between synthetic manganite (simple mineralogy) and natural Fe-Mn samples (highly complex mineralogical composition). Detailed information about phyllomanganate syntheses is provided in Chapter 3.

Phyllomanganates are typically made up of MnO_6 octahedra forming layers (sheets) which are separated by hydrated interlayer(s) (Fig. 4). If one plane of water is present in the interlayer, the layer-to-layer distance is ~7 Å. Two planes of water increase the sheet distance to ~10 Å. Thus, phyllomanganates are also often referred to as 7 Å or 10 Å manganates in the literature (e.g., Kuhn et al., 2017). A further subdivision based on crystallography into ordered and disordered (turbostratic) phyllomanganates can be also made. Fe-bearing (ferruginous) vernadite for instance, which makes up to 90% of the poorly crystalline phases in Fe-Mn nodules, is a 7 Å phyllomanganate with the crystallographic structure of turbostratic hexagonal birnessite. Buserite is an example for an ordered 10 Å phyllomanganate (Hein and Koschinsky, 2014; Kuhn et al., 2017).

Due to their layered structure phyllomanganates are characterized by high internal surface areas (up to >300 m^2/g) and layers charge deficits (Hein et al., 2013; Post, 1999). This, consequently, leads to a high sorptive capacity for different metal cations which are incorporated into the sheet structures over time to stabilize them following initial oxidative sorption processes. (Hein, 2016b; Kuhn et al., 2017). Layer charge deficits are a direct result of

isomorphic substitution of Mn(IV) by compatible elements with lesser oxidation state in some of the MnO_6 octahedra and layer vacancies in the octahedron structure. Mn(IV) can be substituted by Mn(III), Ni(II), Cu(II), or Co(III), and vacancies can be balanced by incorporation of suitable cations above/below the layer vacancy sites (Manceau et al., 1997; Manceau et al., 2014; Peacock and Sherman, 2007a; Peacock and Sherman, 2007b; Post and Bish, 1988).
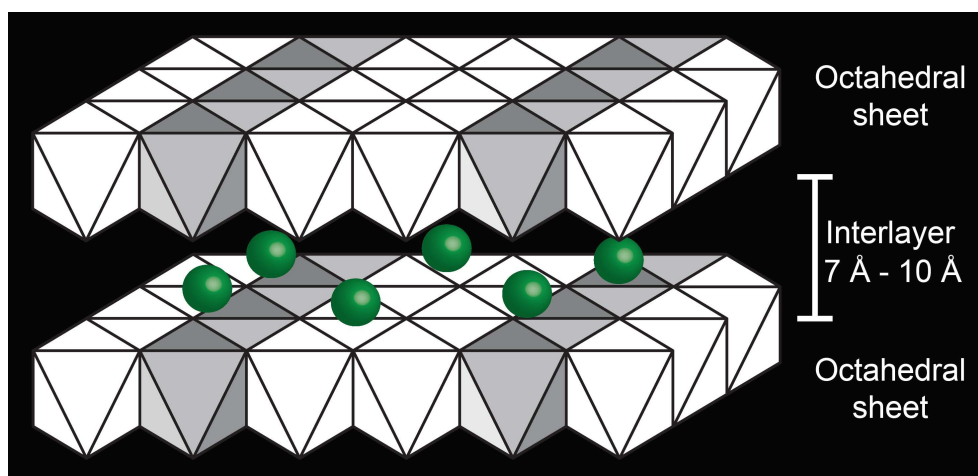
Fig. 4. Schematic illustration of a phyllomanganate crystal structure. Phyllomanganates form octahedral (MnO_6) layers with hydrated interlayers (one plane of water results in a 7 Å layer distance; two planes of water increase the sheet distance to 10 Å) which take up cations (green spheres) for layer charge balance. Modified after Manceau et al. (2012).

2.3. Deep-sea Ferromanganese Nodules and Crusts

The Encyclopedia of Marine Geosciences defines deep-sea ferromanganese nodules (Fig. 5B,D) as: *"Manganese and iron oxide mineral deposits formed on or just below the sediment-covered surface of the deep-ocean seabed by accretion (precipitation) of oxide layers around a nucleus, thereby forming nodules of various shapes and sizes and which contain minor but significant amounts of nickel, copper, cobalt, lithium, molybdenum, zirconium, and rare earth elements"* (Hein, 2016b), whereas deep-sea ferromanganese crusts (Fig. 5A,C,E) are: *"Layered manganese oxide and iron oxyhydroxide deposits formed from direct and very slow precipitation of minerals from seawater onto hard substrates; crusts contain minor but significant concentrations of cobalt, titanium, nickel, platinum, molybdenum, tellurium, zirconium, and other metallic and rare-earth elements sorbed from seawater by the particulate manganese and iron minerals"* (Hein, 2016a). The following sections provide appropriate detail to these concise definitions.
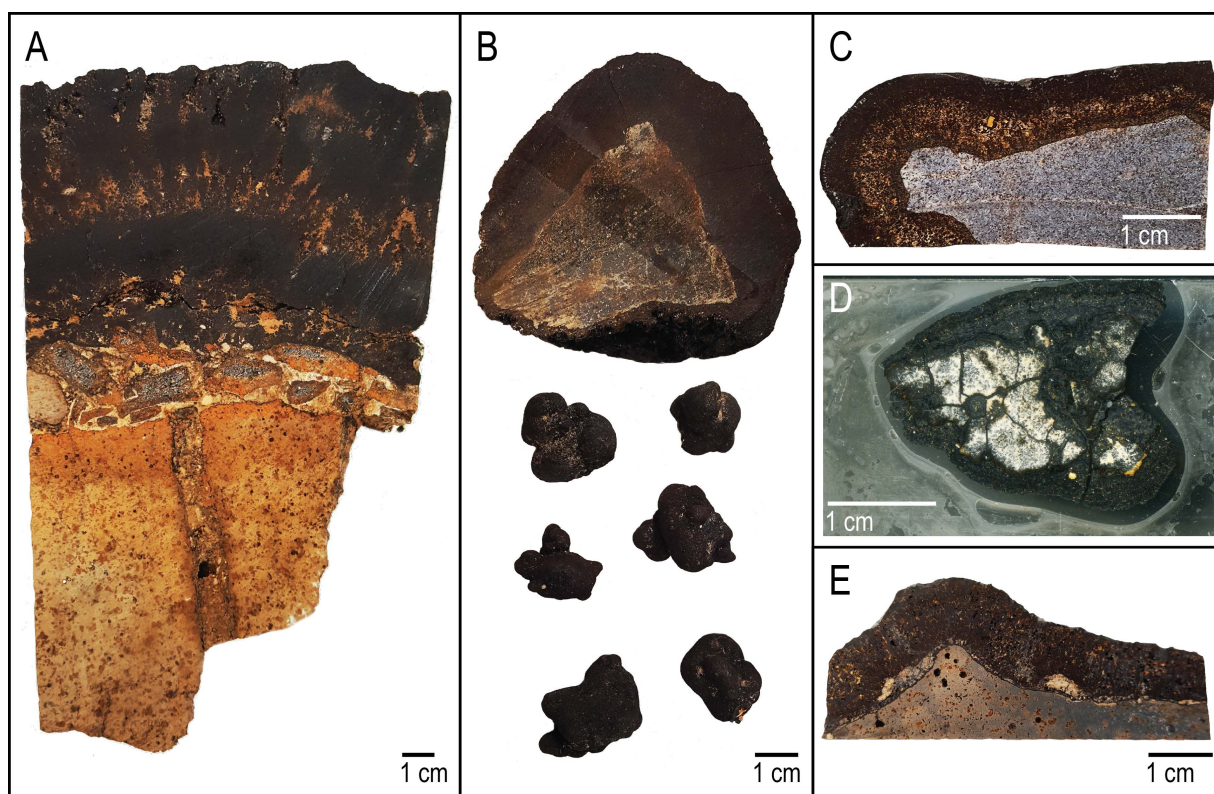
Fig. 5. Photographs of deep-sea ferromanganese nodules and crusts. (A) Thick Fe-Mn crust (black) on volcanic substrate (brown) collected from the Coral Sea east of Australia. (B) Fe-Mn nodules of various sizes and morphologies from the Coral Sea (top) and the Southern part of the Central Pacific Basin (bottom). (C) Fe-Mn crust on basalt fragment collected from the South Tasman Rise depicting distinct growth layers. (D) Petrographic thin section of a Fe-Mn nodule from the Southern part of the Central Pacific Basin (see Chapter 4 for high-resolution three-color XFM image of this sample). (E) Fe-Mn crust on altered basalt substrate from the Coral Sea.

2.3.1. Formation Processes

The formation of deep-sea Fe-Mn nodules and crusts is controlled by three processes – hydrogenetic, diagenetic, and hydrothermal precipitation – which exert influence on mineralogical composition, element enrichment, and texture. Hydrogenetic formation occurs when dissolved metals precipitate directly from oxic ambient seawater around a nucleus (i.e., mineral or rock fragments, pumice shards, coral fragments, shark teeth (Mero, 1977)) on the surface of soft sediment (nodule) or onto sediment-free hard-rock substrate (crust). Remobilization of metals by pore water fluids leads to diagenetic precipitation under oxic or suboxic conditions within the sediment or on the sediment surface. During hydrothermal formation metals precipitate within and at the seafloor as stratabound layers or irregular shapes as a result of mixing of hydrothermal fluids with cold oxic seawater. (Hein and Koschinsky, 2014; Hein et al., 2003; Hein et al., 2013; Koschinsky and Halbach, 1995; Koschinsky and Hein, 2003; Kuhn et al., 2017).

Most Fe-Mn nodules are formed through mixed-type hydrogenetic-diagenetic processes. Purely hydrogenetic and diagenetic end-member types are, however, known from regions of economic interest around the world (2.3.6). Fe-Mn crusts almost exclusively form through hydrogenetic precipitation due to their comparably restricted deposit locations, whereas hydrothermal deposits experience rapid hydrogenetic alteration once in contact with seawater (Hein and Koschinsky, 2014).

It is, furthermore, noteworthy that microbial activity may play a role during Fe-Mn nodule and crust formation and alteration (Crerar and Barnes, 1974). Mixed populations of bacterial communities, such as Mn(II)-oxidizing, Mn(IV)-reducing bacteria, as well as bacteria unrelated to Mn cycling, are found in association with Fe-Mn nodules (Blöthe et al., 2015; Ehrlich, 1963; Ehrlich, 2000; Ehrlich et al., 1972). Laboratory experiments have shown that the oxidation rate of Mn(II) is accelerated by several orders of magnitude over abiotic oxidation by microbial activity (Tebo et al., 2007; Villalobos et al., 2003), which may imply biomineralization as a component of Mn oxide formation. However, it is still unknown if biomineralization of Mn oxides, which is an efficient process in freshwater, seawater, and soil settings, is applicable during Fe-Mn nodule and crust formation in deep-marine environments (Hein and Koschinsky, 2014).

2.3.2. Mineral Phases

The mineralogical composition of Fe-Mn concretions is strongly influenced by the respective formation process and environmental factors, such as geographic location, water depth, or oxygen content of bottom waters (Halbach et al., 1982; Hein and Koschinsky, 2014; Hein et al., 2000; Kuhn et al., 2017). Typical phyllomanganates are vernadite, birnessite, buserite, and asbolane (Hein, 2016a; Hein, 2016b; Hein and Koschinsky, 2014). Well-crystallized todorokite, a tectomanganate, which is structurally defined by 3D tunnel structures that are formed by edge-sharing MnO_6 octahedral chains instead of octahedral sheets (Bodeï et al., 2007; Chukhrov et al., 1979; Kuhn et al., 2017; Post et al., 2003), is commonly found in hydrothermal Mn oxides (Hein and Koschinsky, 2014; Kuhn et al., 2017). It has been shown that post-depositional alteration processes (i.e., oxic diagenesis, mild hydrothermal conditions) can lead to todorokite formation from a phyllomanganate (i.e., birnessite) precursor (Bodeï et al., 2007).

Other mineral phases in Fe-Mn nodules and crusts encompass X-ray amorphous Fe oxyhydroxides with the structure of feroxyhite (δ-FeO(OH)) which is typically epitaxially intergrown with vernadite, ferrihydrite and goethite (Baturin, 1988; Halbach et al., 2017). Accessory mineral phases consist of fine-grained detrital materials such as quartz, plagioclase, K-feldspar, pyroxene, and authigenic minerals (e.g., phillipsite, and carbonate fluorapatite (CFA)). Quartz and most alumosilicate grains originate from the input of aeolian dust into the ocean or weathering of seabed outcrops, whereas calcite can occur as fragments of foraminiferal skeletons. (Halbach et al., 2017; Hein, 2016a). Secondary mineralization, i.e., during diagenetic alteration of the older parts of hydrogenetic precipitates, can lead to the formation of CFA (Halbach et al., 2017; Hein and Koschinsky, 2014), which may constitute up to 30% in thick ferromanganese crusts with an average of 9-10% (Halbach et al., 2017).

2.3.3. Element Enrichment

Enrichment of elements in Fe-Mn concretions up to a factor 10^9 over ambient seawater (Hein et al., 2010) is controlled by the prevalent formation process and environmental factors, such as current patterns and surface bioproductivity (Halbach et al., 2017). Furthermore, the overall availability of metals in seawater and pore water, the ratio of Mn to Fe oxides (Wegorzewski et al., 2015), and the internal surface area of Mn and Fe oxides play a key role. Element concentrations are, moreover, directly proportional to growth rates, as slower growth rates imply longer periods of metal accumulation.

Mechanistically, element enrichment is achieved through formation of surface-sorbed metal complexes, surface oxidation, substitution, and potential precipitation of discrete phases (Hein et al., 2013; Koschinsky and Halbach, 1995; Koschinsky and Hein, 2003). Oxidative processes are followed by the formation of covalent bonds and progressive incorporation of metals into the crystal lattice of the Mn and Fe oxides (Hein, 2016a; Hein, 2016b). Furthermore, changes of metal oxidation state from mobile to immobile forms (e.g., $Co^{2+} \rightarrow Co^{3+}$, $Ce^{3+} \rightarrow Ce^{4+}$, $Tl^+ \rightarrow Tl^{3+}$) (Hein et al., 2003) allow suitable cations to fill layer vacancies in the oxide phases. In contrast to strong oxidative sorption of Mn oxides, the sorption and enrichment of metals on Fe oxyhydroxide surfaces is predominantly controlled by covalent and coordinative bonding (Kuhn et al., 2017). Preferential sorption of anionic complexes, such as carbonate ($REE(CO_3)_2^-$), hydroxide ($Hf(OH)_5^-$), or oxyanion complexes (MoO_4^{2-}), occurs due to the slightly positive charge of Fe oxyhydroxide particles (Hein et al., 2013; Koschinsky and Halbach, 1995; Koschinsky and Hein, 2003).

Differences in the enrichment behavior of elements occur between Fe-Mn nodules and crusts. The traditional metals of economic interest are Ni-Cu-Mn for nodules and Co-Ni-Mn for crusts (Hein et al., 2010). However, research in past decades has also found significant enrichment of other metals, such as Ti, REY, Zr, Nb, Ta, Hf, Co, Ce, and Te in hydrogenetic nodules and Ni, Cu, Ba, Zn, Mo, Li, and Ga in diagenetic nodules (Hein et al., 2013; Koschinsky and Hein, 2003). Halbach et al. (2017) note high concentrations of Bi, Mo, Nb, Pt, REE, Te, Th, Ti, W, Y, and Zr in Fe-Mn crusts. The degree of enrichment of elements in Fe-Mn nodules and crusts can be visualized in comparison to average element concentrations in the Upper Continental Crust (UCC) as shown in Fig. 6.
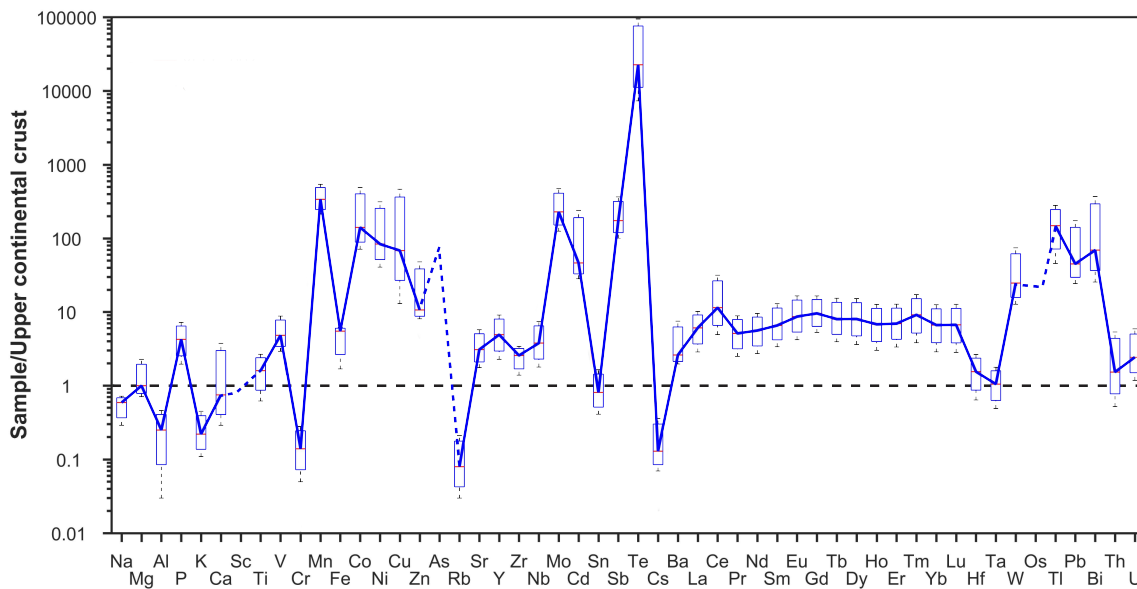
Fig. 6. Example of element enrichment patterns of Fe-Mn nodules and crusts (n = 13) collected from locations (south)east of Australia, relative to their mean abundances in the upper continental crust (UCC) (Hein et al., 2003; Rudnick and Gao, 2003). Boxes represents UCC-normalized minimum and maximum element enrichment values, whereas the blue line connects median values. Dashed lines represent elements that have not been analyzed or were below detection limit. Figure modified after Goto et al. (2017).

2.3.4. Genetic Classification

By graphically plotting measured element concentrations into genetic discrimination diagrams, Fe-Mn nodules and crusts can be classified based on their formation process. Bonatti et al. (1972) first proposed a ternary diagram that utilizes bulk Fe – Mn – 10x (Cu + Ni + Co) concentrations (Fig. 7). For instance, hydrogenetic deposits generally have high Fe and Mn concentrations (>10%) and Mn/Fe ratios ≤5 (Halbach et al., 1988). Diagenetic and hydrothermal deposits are, however, characterized by a strong fractionation of Fe and Mn (e.g., Mn/Fe ratio of diagenetic nodules >5 (Halbach et al., 1988)). Consequently these genetic types plot in different regions of the ternary diagram (Bonatti et al., 1972; Glasby, 2006).

18
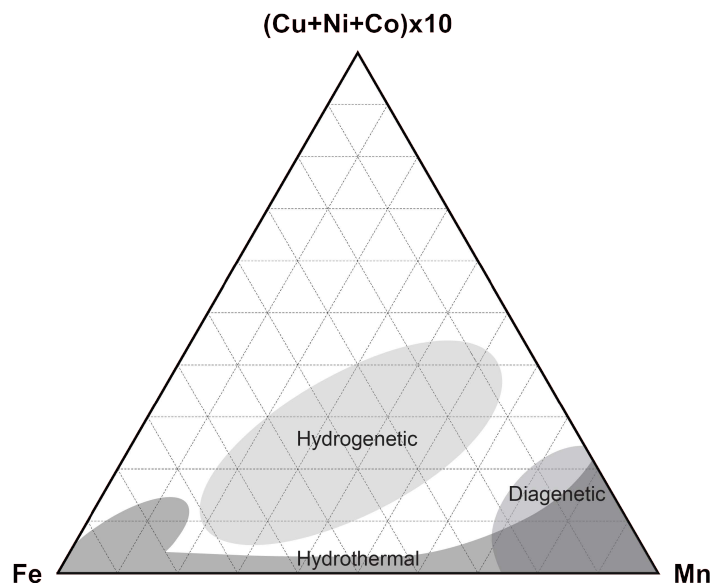
Fig. 7. Ternary discrimination diagram for deep-sea Fe-Mn deposits. Depicted are distinct regions wherein the deposits plot depending on their formation process. Modified after Bonatti et al. (1972).
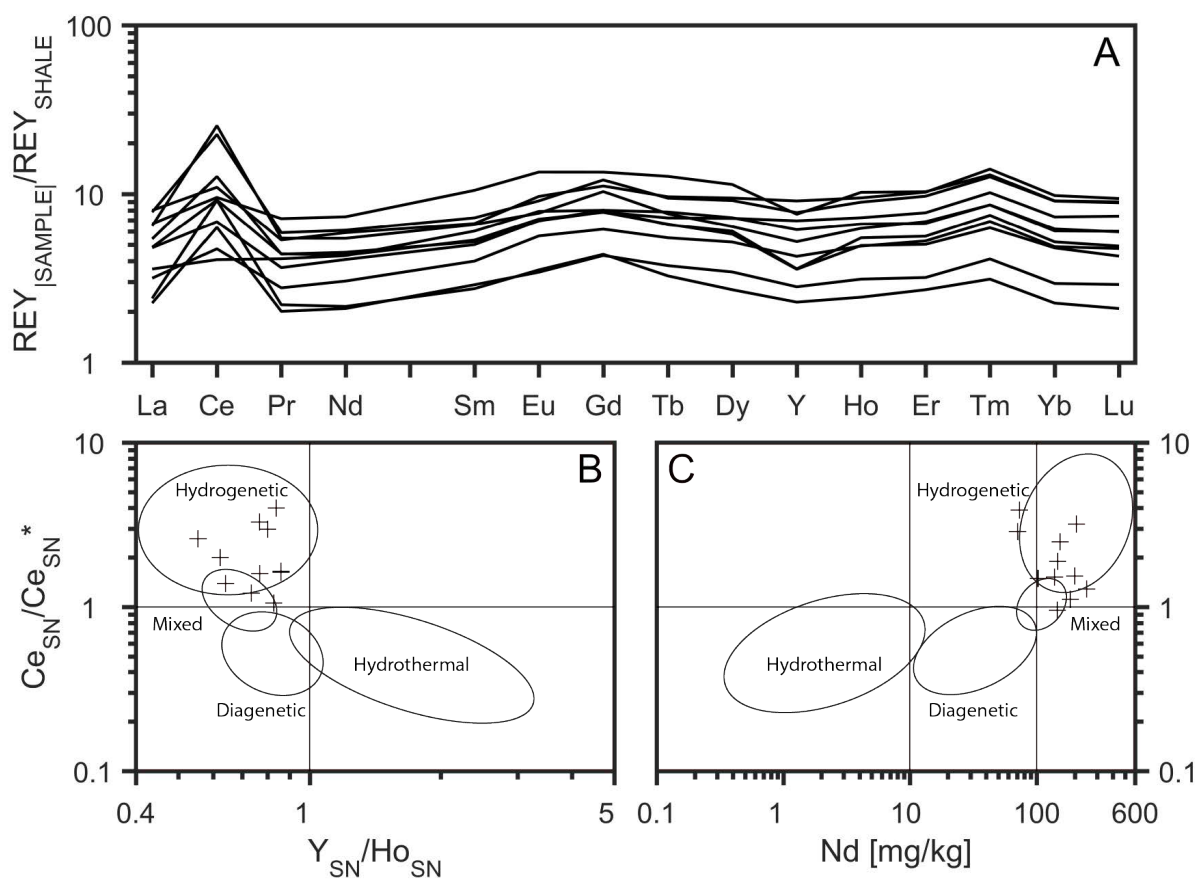
Fig. 8. (A) Post-Archean Australian Shale-normalized (McLennan, 2001; Taylor and McLennan, 1985) REY_{SN} patterns of deep-sea ferromanganese samples (n = 13) collected from locations (south)east of Australia. Samples show patterns characteristic of hydrogenetic to mixed-type hydrogenetic-diagenetic Fe-Mn deposits (i.e. positive Ce anomaly/negative Y anomaly). (B) Genetic classification of samples and reference materials using the $Ce_{SN}/Ce_{SN}*$ ratio vs Y_{SN}/Ho_{SN} ratio and (C) $Ce_{SN}/Ce_{SN}*$ ratio vs Nd concentration. Discrimination diagrams and fields modified after Bau et al. (2014).

More recently it has been noted that the bulk concentrations may, however, not be a sufficient tool to clearly infer genesis, as individual growth layers of Fe-Mn nodules and crusts may have distinctly different element concentrations from bulk composition as a result of changing environmental conditions (Josso et al., 2016; Kuhn et al., 2017). Hence, Bau et al. (2014) proposed to utilize Post-Archean Australian Shale-normalized rare earth element + Yttrium (REY_{SN}) concentrations to discriminate the genetic type of non-phosphatized Fe-Mn deposits due to the coherent behavior of REY during fractionation in natural environments (Fig. 8A). REY_{SN} values are plotted in bivariate diagrams (Fig. 8B,C) of $Ce_{SN}/Ce_{SN}*$ vs. Nd and $Ce_{SN}/Ce_{SN}*$ vs. Y_{SN}/Ho_{SN}, where $CE_{SN}*$ is calculated as $CE_{SN}* = 0.5La_{SN} + 0.5Pr_{SN}$ or alternatively as $CE_{SN}* = 0.67La_{SN} + 0.33Nd_{SN}$. Further discrimination schemes for Fe-Mn deposits, which are based on high field strength and rare earth element concentrations (Josso et al., 2016), were not used in this thesis and have thus been omitted from description.

2.3.5. Growth Rates and Morphologies

Growth rates, which are influenced by formation processes and environmental factors, exert control on the size, shape, surface texture, and internal growth structures of deep-sea Fe-Mn concretions. Hydrogenetic Fe-Mn precipitates exhibit growth rates between 1-5 mm/million years (Halbach et al., 1988), whereas growth rates up to 250 mm/million years are known from diagenetic precipitates (Von Stackelberg, 2000). Shallow-water Fe-Mn nodules from the Black Sea and Baltic can have even higher rates of growth (0.013 – 1mm/year) as a result of increased metal and nutrient influx from continents in close proximity to the deposit locations (Hlawatsch et al., 2002).

Typical dimensions of deep-sea Fe-Mn nodules range from a few millimeters (micronodules) up to 15 cm (Kuhn et al., 2017). Von Stackelberg (1997) reported extremely large nodules of up to 21 cm from the Peru Basin where formation is dominated by diagenetic precipitation. However, the average size of Fe-Mn nodules of economic interest can best be described as golf ball- and potato-sized. Similarly, Fe-Mn crusts can form coatings of only a few millimeters up to >10 centimeters of thickness on substrate (Halbach et al., 2017).

Diverse shapes of Fe-Mn nodules, such as spheroidal, ellipsoidal, elongated, discoidal, platy, cauliflower-like, irregular, and poly-nodular shape have been described (Kuhn et al., 2017). Figure 5B (bottom) depicts Fe-Mn nodules with poly-nodular shape. Internal growth features, as depicted and described in Chapter 4 for samples used in this thesis, can be characterized as

laminated, columnar, pillar-like, dendritic, and massive morphologies (Kuhn et al., 2017; Von Stackelberg, 1987). Hydrogenetic layers of Fe-Mn crusts are typically composed of finely laminated to columnar structures, whereas diagenetic precipitation of Fe-Mn nodules mainly leads to the development of dendritic layers, and less frequently, to massive layers (Kuhn et al., 2017). Depending on the specimen age distinct growth generations may also be differentiated (Halbach et al., 2017).

2.3.6. Deposit Locations and Regions of Economic Interest

Deep-sea Fe-Mn nodules occur in vast patches (several thousand km^2) of monodisperse layers on or shortly below ($\leq$10 cm) the soft-sediment surface of abyssal plains in depths of 4000 to 6000 m in all major oceans (Kuhn et al., 2017). In contrast, Fe-Mn crusts usually form extensive pavements on rock surfaces that have been swept free of sediment by currents. Occurrences of Fe-Mn crusts throughout the global oceans in depths of 400-7000 m, for instance, on the flanks of extinct volcanoes (seamounts, guyots), ridges, and plateaus have been recorded, although Fe-Mn crusts of economic significance are generally formed between 800-2500 m water depths (Hein, 2016a).

Since the 1950s several regions of economic interest have been identified in the global oceans, which hold Fe-Mn deposits both in terms of sufficient tonnage and metal content for future exploitation (Fig. 9). The *Clarion-Clipperton Zone* (CCZ), the *Cook Islands EEZ* (CI), the *Peru Basin* (PB), and the *Central Indian Ocean Basin* (CIOB) are regions of economic interest for Fe-Mn nodules. The *Prime Crust Zone* (PCZ) in the Western Pacific, as depicted in Fig. 9, is known for significant crust deposits (Hein and Koschinsky, 2014; Kuhn et al., 2017).

The Clarion-Clipperton Zone is located in the Central Pacific just north of the equator between Hawaii and Mexico. Covering an area of about four million km^2, it is the region with the largest contiguous occurrence of mixed-type hydrogenetic-diagenetic origin Fe-Mn nodule fields (Kuhn et al., 2017). The Cook Island EEZ is located in the SW Pacific and includes the Penrhyn Basin and Manihiki Plateau. Here, long-term stable environmental conditions enable the growth of hydrogenetic end-member Fe-Mn nodules (Kuhn et al., 2017). Diagenetic end-member Fe-Mn nodules found in the Peru Basin cover and area roughly half the size of the CCZ about 3000 km off the Peruvian coast (Von Stackelberg, 1997). The Central Indian Ocean Basin hosts Fe-Mn nodules in an area between 10°S and 16°30′S and 72°E and 80°E covering about 700,000 km^2 (Kuhn et al., 2017).

Analogous to CCZ deposits, CIOB Fe-Mn nodules represent mixed-type hydrogenetic-diagenetic precipitates. Their overall metal content is, however, lower compared to CCZ nodules (Hein et al., 2013). The most significant Fe-Mn crusts resources are located in water depths of 800 – 3000 m within the Prime Crust Zone in the Northwest and Central Pacific (Fig. 9) due to the high abundance of old (Cretaceous age) seamounts in that region (compared to the Atlantic and Indian Ocean) (Halbach et al., 2017).

Fe-Mn nodule and crust samples used for experimental work in this thesis were collected by Dr. Barrie R. Bolton from locations (south)east of Australia and the Southern Central Pacific Basin in the late 1980s and early 1990s. Further information and a comprehensive discussion of geologic settings and macroscopic nodule and crust features, such as surface textures and internal structures, can be found in Chapter 4 and Bolton et al. (1986), Bolton et al. (1988), and Bolton et al. (1992).
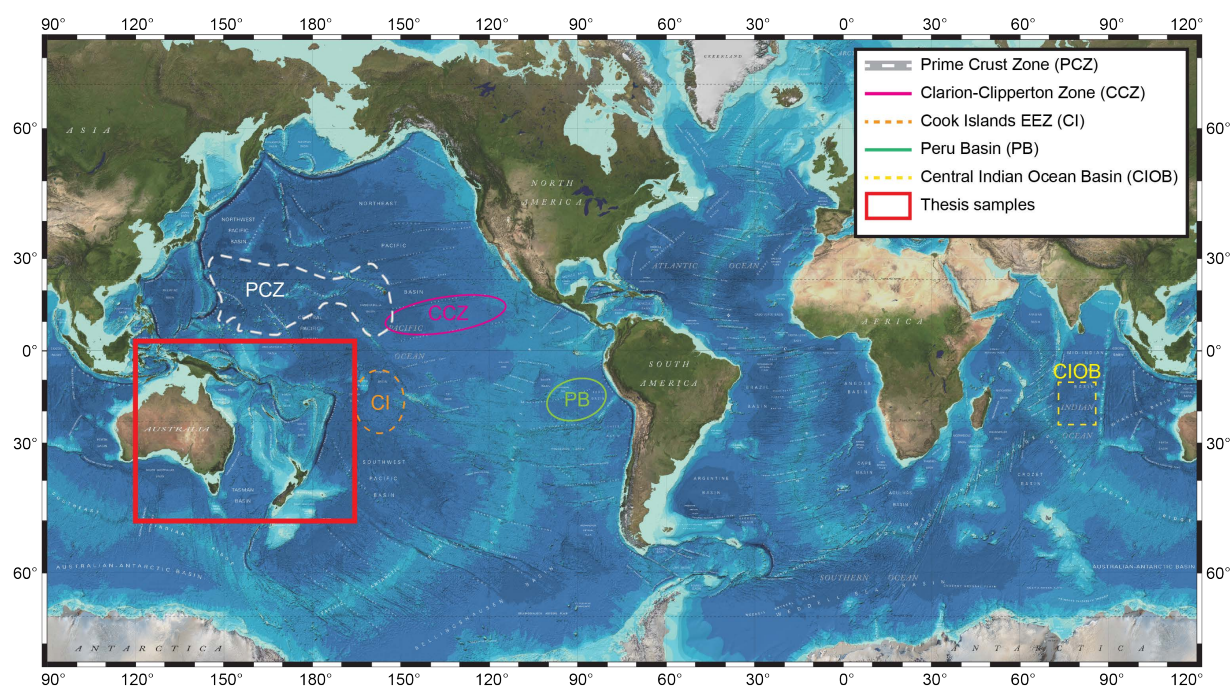
Fig. 9. Global distribution of Fe-Mn nodules and crust regions of economic interest. Samples used for experimental work as part of this thesis were collected from locations inside the red rectangle (see Fig. 10). Figure adapted from Hein et al. (2013). Map image reproduced from the GEBCO world map 2014 (www.gebco.net, 2017).
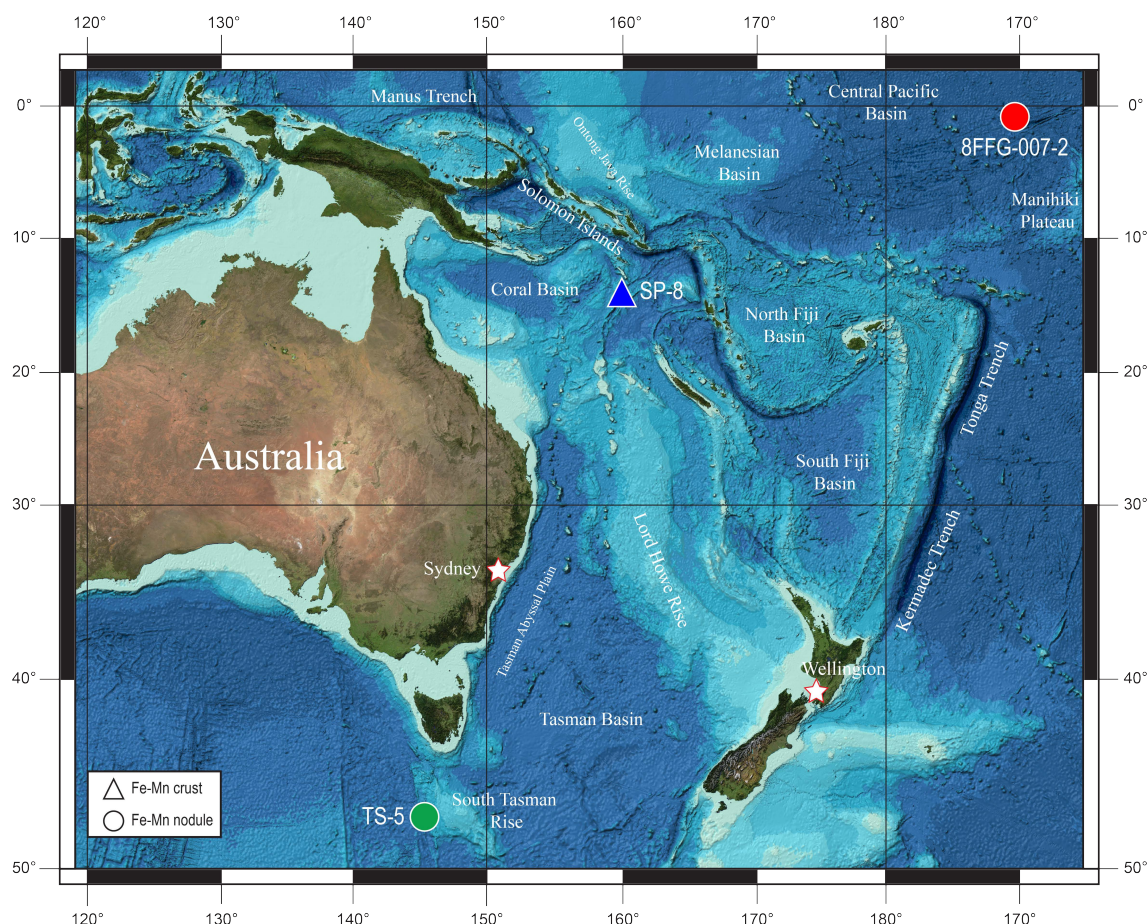
Fig. 10. Ferromanganese nodules and crusts (TS-5, SP-8, 8FFG-007-2) used for experimental work in Chapter 4 were collected from locations (south)east of Australia and the Southern part of the Central Pacific Basin. Map image reproduced from the GEBCO world map 2014 (www.gebco.net, 2017).

2.3.7. Relevance of Deep-sea Ferromanganese Deposits as Archives

In addition to their resource potential, Fe-Mn concretions are also considered valuable archives for geochemical and paleoceanographic studies. The layer-by-layer growth of hydrogenetic crusts in particular leads to condensed stratigraphic sections that might span thousands to tens of millions of years (Koschinsky and Hein, 2017; Lusty and Murton, 2018). Isotope analyses by means of U-series, Be, Os, Pb, Nd, and Hf isotope systems among others (e.g., Tl, Mo, Fe, Cd) are efficient tools to gain geochemical and paleoceanographic information. While U-series, Be, and Os isotope ratios have been used to determine the growth rate and ages of crusts, Hein (2016a) notes that temporal changes in trace metal isotope distributions (e.g., Pb, Nd, Hf isotopes) have been employed for the reconstruction of past circulation patterns and erosion rates of continents. Moreover, ocean mixing, the extend and intensity of the oxygen minimum zones (OMZ), primary productivity, the plate tectonic migration of seamounts and their subsidence, have been related to textural and geochemical changes in crusts (Hein, 2016a).

3. References

Bargar, J.R., Fuller, C.C., Marcus, M.A., Brearley, A.J., De la Rosa, M.P., Webb, S.M., Caldwell, W.A., 2009. Structural characterization of terrestrial microbial Mn oxides from Pinal Creek, AZ. Geochimica et Cosmochimica Acta, 73: 889-910.

Baturin, G.N., 1988. The Geochemistry of Manganese and Manganese Nodules in the Ocean. Sedimentology and Petroleum Geology. Springer Netherlands, Dordrecht, 356 pp.

Bau, M., Schmidt, K., Koschinsky, A., Hein, J., Kuhn, T., Usui, A., 2014. Discriminating between different genetic types of marine ferro-manganese crusts and nodules based on rare earth elements and yttrium. Chemical Geology, 381: 1-9.

Birkner, N., Nayeri, S., Pashaei, B., Najafpour, M.M., Casey, W.H., Navrotsky, A., 2013. Energetic basis of catalytic activity of layered nanophase calcium manganese oxides for water oxidation. Proceedings of the National Academy of Sciences, 110(22): 8801-8806.

Blöthe, M., Wegorzewski, A.V., Müller, C., Simon, F., Kuhn, T., Schippers, A., 2015. Manganese-Cycling Microbial Communities Inside Deep-Sea Manganese Nodules. Environmental Science & Technology, 49(13): 7692-7700.

Bodeï, S., Manceau, A., Geoffroy, N., Baronnet, A., Buatier, M., 2007. Formation of todorokite from vernadite in Ni-rich hemipelagic sediment. Geochimica et Cosmochimica Acta, 71(23): 5698-5716.

Bolton, B.R., Bogi, J., Cronan, D.S., 1992. Geochemistry and mineralogy of ferromanganese nodules from the Kiribati region of the eastern Central Pacific Basin. In: Keating, B.H., Bolton, B.R. (Eds.), Geology and offshore mineral resources of the central Pacific basin, Circum-Pacific Council for Energy and Mineral Resources Earth Science Series Springer, New-York, pp. 247-260.

Bolton, B.R., Exon, N.F., Ostwald, J., Kudrass, H.R., 1988. Geochemistry of ferromanganese crusts and nodules from the South Tasman Rise, southeast of Australia. Marine Geology, 84: 53-80.

Bolton, B.R., Ostwald, J., Monzier, M., 1986. Precious metals in ferromanganese crusts from the south-west Pacific. Nature, 320: 318-320.

Bonatti, E., Kraemer, T., Rydell, H., 1972. Classification and genesis of submarine iron-manganese deposits. In: Horn, D.R. (Editor), Papers from a Conference on Ferromanganese Deposits on the Ocean Floor. National Science Foundation, pp. 149-166.

Burns, R.G., Burns, V.M., 1977. The mineralogy and crystal chemistry of deep-sea manganese nodules, a polymetallic resource of the twenty-first century. Philosophical Transactions of the Royal Society London, A286: 283-301.

Chukhrov, F.V., Gorshkov, A.I., Beresovskaya, V.V., Sivtsov, A.V., 1979. Contributions to the mineralogy of authigenic manganese phases from marine manganese deposits. Mineralium Deposita, 14(3): 249-261.

Crerar, D.A., Barnes, H.L., 1974. Deposition of deep-sea manganese nodules. Geochimica et Cosmochimica Acta, 38(2): 279-300.

Crerar, D.A., Cormick, R.K., Barnes, H.L., 1980. Geochemistry of manganese: An overview. In: Varentsov, I.M., Grassely, G.Y. (Eds.), Geology and Geochemistry of Manganese. E. Schweizerbart'sche Verlagsbuchhandlung, Stuttgart, pp. 293-334.

Ehrlich, H.L., 1963. Bacteriology of manganese nodules: I. Bacterial action on manganese in nodules enrichments. Applied Microbiology, 11: 15-19.

Ehrlich, H.L., 2000. Ocean manganese nodules: biogenesis and bioleaching possibilities. Minerals and Metallurgical Processing, 17: 121-128.

Ehrlich, H.L., Yang, S.H., Mainwaring Jr., J.D., 1972. Bacteriology of manganese nodules. Zeitschrift für Allgemeine Mikrobiologie, 13(1): 39-48.

Elzinga, E.J., 2011. Reductive Transformation of Birnessite by Aqueous Mn(II). Environmental Science & Technology, 45(15): 6366-6372.

Elzinga, E.J., 2016. ^{54}Mn Radiotracers Demonstrate Continuous Dissolution and Reprecipitation of Vernadite (δ-MnO$_2$) during Interaction with Aqueous Mn(II). Environmental Science & Technology, 50(16): 8670-8677.

Frierdich, A.J., Catalano, J.G., 2012. Controls on Fe(II)-Activated Trace Element Release from Goethite and Hematite. Environmental Science & Technology, 46(3): 1519-1526.

Frierdich, A.J., Hasenmueller, E.A., Catalano, J.G., 2011a. Composition and structure of nanocrystalline Fe and Mn oxide cave deposits: Implications for trace element mobility in karst systems. Chemical Geology, 284(1-2): 82-96.

Frierdich, A.J., Luo, Y., Catalano, J.G., 2011b. Trace element cycling through iron oxide minerals during redox-driven dynamic recrystallization. Geology, 39(11): 1083-1086.

Frierdich, A.J., Spicuzza, M.J., Scherer, M.M., 2016. Oxygen Isotope Evidence for Mn(II)-Catalyzed Recrystallization of Manganite (γ-MnOOH). Environmental Science & Technology, 50(12): 6374-6380.

Glasby, G.P., 2006. Manganese: predominant role of nodules and crusts. In: Schulz, H.D., Zabel, M. (Eds.), Marine Geochemistry. Springer-Verlag, Berlin, Heidelberg, pp. 371–427.

Goldberg, E.D., 1954. Marine Geochemistry 1. Chemical scavengers of the sea. The Journal of Geology, 62: 249-265.

Gollner, S., Kaiser, S., Menzel, L., Jones, D.O.B., Brown, A., Mestre, N.C. et al., 2017. Resilience of benthic deep-sea fauna to mining activities. Marine Environmental Research, 129: 76-101.

Goto, K.T., Nozaki, T., Toyofuku, T., Augustin, A.H., Shimoda, G., Chang, Q. et al., 2017. Paleoceanographic conditions on the São Paulo Ridge, SW Atlantic Ocean, for the past 30 million years inferred from Os and Pb isotopes of a hydrogenous ferromanganese crust. Deep Sea Research Part II: Topical Studies in Oceanography, 146: 82-92.

Halbach, P., Friedrich, G., Von Stackelberg, U., 1988. The manganese nodule belt of the Pacific Ocean. Enke, Stuttgart, 254 pp.

Halbach, P., Giovanoli, R., von Borstel, D., 1982. Geochemical processes controlling the relationship between Co, Mn, and Fe in early diagenetic deep-sea nodules. Earth and Planetary Science Letters, 60(2): 226–236.

Halbach, P., Jahn, A., Cherkashov, G., 2017. Marine Co-Rich Ferromanganese Crust Deposits: Description and Formation, Occurrences and Distribution, Estimated World-wide Resources. In: Sharma, R. (Ed.), Deep-Sea Mining: Resource Potential, Technical and Environmental Considerations. Springer International Publishing AG, pp. 65-141.

Haxel, G.B., Hedrick, J.B., Orris, G.J., Stauffer, P.H., Hendley II, J.W., 2002. Rare earth elements: critical resources for high technology, USGS Fact Sheet 087-02, pp. 4.

Haynes, B.W., Law, S.L., Barron, D.C., Kramer, G.W., Maeda, R., 1985. Pacific Manganese Nodules: Characterization and Processing Bulletin (United States Bureau of Mines), pp. 43.

Hein, J.R., 2016a. Cobalt-rich Manganese Crusts. In: Harff, J., Meschede, M., Petersen, S., Thiede, J. (Eds.), Encyclopedia of Marine Geosciences. Encyclopedia of Earth Sciences Series. Springer, Dordrecht, pp. 113-117.

Hein, J.R., 2016b. Manganese Nodules. In: Harff, J., Meschede, M., Petersen, S., Thiede, J. (Eds.), Encyclopedia of Marine Geosciences. Encyclopedia of Earth Sciences Series. Springer, Dordrecht, pp. 408-412.

Hein, J.R., Conrad, T.A., Staudigel, H., 2010. Seamount mineral deposits. A source of rare metals for high-technology industries. Oceanography, 23(1): 184-189.

Hein, J.R., Koschinsky, A., 2014. 13.11 - Deep-Ocean Ferromanganese Crusts and Nodules. In: Holland, H.D., Turekian, K.K. (Eds.), Treatise on Geochemistry (Second Edition). Elsevier, Oxford, pp. 273-291.

Hein, J.R., Koschinsky, A., Bau, M., Manheim, F.T., Kang, J.-K., Roberts, L., 2000. Cobalt-rich ferromanganese crusts in the Pacific. In: Cronan, D.S. (Ed.), Handbook of marine mineral deposits. CRC Press, London, pp. 239–279.

Hein, J.R., Koschinsky, A., Halliday, A.N., 2003. Global occurrence of tellurium-rich ferromanganese crusts and a model for the enrichment of tellurium. Geochimica et Cosmochimica Acta, 67(6): 1117-1127.

Hein, J.R., Mizell, K., Koschinsky, A., Conrad, T.A., 2013. Deep-ocean mineral deposits as a source of critical metals for high- and green-technology applications: Comparison with land-based resources. Ore Geology Reviews, 51: 1-14.

Hens, T., Brugger, J., Cumberland, S.A., Etschmann, B., Frierdich, A.J., 2018. Recrystallization of Manganite (γ-MnOOH) and Implications for Trace Element Cycling. Environmental Science & Technology, 52(3): 1311-1319.

Hinkle, M.A.G., Flynn, E.D., Catalano, J.G., 2016. Structural response of phyllomanganates to wet aging and aqueous Mn(II). Geochimica et Cosmochimica Acta, 192: 220-234.

Hlawatsch, S., Garbe-Schönberg, C.D., Lechtenberg, F., Manceau, A., Tamura, N., Kulik, D.A., Kersten, M., 2002. Trace metal fluxes to ferromanganese nodules from the western Baltic Sea as a record for long-term environmental changes. Chemical Geology, 182(2-4): 697-709.

ISA, 2000. Decision of the assembly relating to the regulations on prospecting and exploration for polymetallic nodules in the Area. International Seabed Authority, Jamaica, pp. 48.

ISA, 2001. Recommendations for guidance of contractors for the assessment of the possible environmental impacts arising from exploration for polymetallic nodules in the Area. International Seabed Authority, Jamaica, pp. 11.

Johnson, J.E., Savalia, P., Davis, R., Kocar, B.D., Webb, S.M., Nealson, K.H., Fischer, W.W., 2016. Real-time manganese phase dynamics during biological and abiotic manganese oxide reduction. Environmental Science & Technology, 50: 4248-4258.

Josso, P., Pelleter, E., Pourret, O., Fouquet, Y., Etoubleau, J., Cheron, S., Bollinger, C., 2016. A new discrimination scheme for oceanic ferromanganese deposits using high field strength and rare earth elements. Ore Geology Reviews, 87: 3-15.

Kim, R.E., 2017. Should deep seabed mining be allowed? Marine Policy, 82: 134-137.

Kohler, T., Armbruster, T., Libowitzky, E., 1997. Hydrogen Bonding and Jahn-Teller Distortion in groutite, α-MnOOH, and manganite, γ-MnOOH, and Their Relation to the Manganese Dioxides Ramsdellite and Pyrolusite. Journal of Solid State Chemistry, 133: 486-500.

Koschinsky, A., Halbach, P., 1995. Sequential leaching of marine ferromanganese precipitates: Genetic implications. Geochimica et Cosmochimica Acta, 59(24): 5113-5132.

Koschinsky, A., Hein, J.R., 2003. Uptake of elements from seawater by ferromanganese crusts: solid-phase associations and seawater speciation. Marine Geology, 198(3-4): 331-351.

Koschinsky, A., Hein, J.R., 2017. Marine ferromanganese encrustations: archives of changing oceans. Elements, 13: 177-182.

Kuhn, T., Wegorzewski, A., Rühlemann, C., Vink, A., 2017. Composition, Formation, and Occurence of Polymetallic Nodules. In: Sharma, R. (Ed.), Deep-Sea Mining. Springer International Publishing AG, Cham, pp. 23-63.

Learman, D.R., Wankel, S.D., Webb, S.M., Martinez, N., Madden, A.S., Hansel, C.M., 2011. Coupled biotic-abiotic Mn(II) oxidation pathway mediates the formation and structural evolution of biogenic Mn oxides. Geochimica et Cosmochimica Acta, 75(20): 6048-6063.

Lefkowitz, J.P., Elzinga, E.J., 2015. Impacts of aqueous Mn(II) on the sorption of Zn(II) by hexagonal birnessite. Environmental Science & Technology, 49: 4886-4893.

Lefkowitz, J.P., Rouff, A.A., Elzinga, E.J., 2013. Influence of pH on the reductive transformation of birnessite by aqueous Mn(II). Environmental Science & Technology, 47(18): 10364−10371.

Lindsay, W.L., 1979. Chemical Equilibria in Soils. John Wiley and Sons, New York, pp. 450.

Lovely, D.R., 2000. Fe(III) and Mn(IV) reduction. In: Lovely, D.R. (Ed.), Environmental metal-microbe interactions. ASM Press, Washington, D.C., pp. 3-30.

Lusty, P.A.J., Murton, B.J., 2018. Deep-ocean mineral deposits: metal resources and windows into Earth processes. Elements, 14: 301-306.

Manceau, A., Drits, V.A., Silvester, E., Bartoli, C., Lanson, B., 1997. Structural mechanism of Co^{2+} oxidation by the phyllomanganate buserite. American Mineralogist, 88(11-12): 1150-1175.

Manceau, A., Lanson, M., Takahashi, Y., 2014. Mineralogy and crystal chemistry of Mn, Fe, Co, Ni, and Cu in a deep-sea Pacific polymetallic nodule. American Mineralogist, 99(10): 2068-2083.

Manceau, A., Marcus, M.A., Grangeon, S., 2012. Determination of Mn valence states in mixed-valent manganates by XANES spectroscopy. American Mineralogist, 97(5-6): 816-827.

McLennan, S.M., 2001. Relationships between the trace element composition of sedimentary rocks and upper continental crust. Geochemistry Geophysics Geosystems, 2(4): 2000GC000109.

Mero, J.L., 1965. The Mineral Resources of the Sea. In: Mero, J.L. (Ed.), The Mineral Resources of the Sea. Elsevier Oceanography Series. Elsevier, Amsterdam, pp. 312.

Mero, J.L., 1977. In: Glasby, G.P. (Ed.), Marine Manganese Nodules. Elsevier, Amsterdam, pp. 327-355.

Miljutin, D.M., Miljutina, M.A., Arbizu, P.M., Galéron, J., 2011. Deep-sea nematode assemblage has not recovered 26 years after experimental mining of polymetallic nodules (Clarion-Clipperton Fracture Zone, Tropical Eastern Pacific). Deep Sea Research Part I: Oceanographic Research Papers, 58(8): 885-897.

Miller, K.A., Thompson, K.F., Johnston, P., Santillo, D., 2018. An Overview of Seabed Mining Including the Current State of Development, Environmental Impacts, and Knowledge Gaps. Frontiers in Marine Science, 4(418): 1-24.

Miyata, N., Tani, Y., Sakata, M., Iwahori, K., 2007. Microbial manganese oxide formation and interaction with toxic metal ions. Journal of Bioscience and Bioengineering, 104(1): 1-8.

Mulvaney, D., 2011. Green technology: an A-to-Z guide. The Sage reference series on green society. Sage Publications, Thousand Oaks, CA, 524 pp.

Myers, C.R., Nealson, K.H., 1988. Bacterial manganese reduction and growth with manganese oxide as the sole electron acceptor. Science, 240: 1319-1321.

Nicholson, G., 2002. The Common Heritage of Mankind and Mining: An Analysis of the Law as to the High Seas, Outer Space, the Antarctic and World Heritage. New Zealand Journal of Environmental Law, 6: 177-198.

Peacock, C.L., Sherman, D.M., 2007a. Crystal-chemistry of Ni in marine ferromanganese crusts and nodules. American Mineralogist, 92(7): 1087-1092.

Peacock, C.L., Sherman, D.M., 2007b. Sorption of Ni by birnessite: Equilibrium controls on Ni in seawater. Chemical Geology, 238(1-2): 94-106.

Perez-Benito, J.F., 2002. Reduction of Colloidal Manganese Dioxide by Manganese(II). Journal of Colloid and Interface Science, 248(1): 130-135.

Post, J.E., 1999. Manganese oxide minerals: Crystal structures and economic and environmental significance. Proceedings of the National Academy of Sciences of the United States of America, 96(7): 3447-3454.

Post, J.E., Bish, D.L., 1988. Rietveld refinement of the todorokite structure. American Mineralogist, 73: 861-869.

Post, J.E., Heaney, P.J., Hanson, J., 2003. Synchrotron X-ray diffraction of the structure and dehydration behavior of todorokite. American Mineralogist, 88: 142-150.

Ramstedt, M., Andersson, B.M., Shchukarev, A., Sjöberg, S., 2004. Surface Properties of Hydrous Manganite (γ-MnOOH). A Potentiometric, Electroacoustic, and X-ray Photoelectron Spectroscopy Study. Langmuir, 20(19): 8224-8229.

Ramstedt, M., Sjöberg, S., 2005. Phase transformations and proton promoted dissolution of hydrous manganite (γ-MnOOH). Aquatic Geochemistry, 11: 413-431.

Rosenzweig, C., Karoly, D., Vicarelli, M., Neofotis, P., Wu, Q., Casassa, G. et al., 2008. Attributing physical and biological impacts to anthropogenic climate change. Nature, 453: 353.

Rudnick, R.L., Gao, S., 2003. Composition of the continental crust. In: Rudnick, R.L. (Ed.), Treatise on Geochemistry. Elsevier, Amsterdam, pp. 1-64.

Sharma, R., 2017a. Deep-Sea Mining - Resource Potential, Technical and Environmental Considerations. In: Sharma, R. (Ed.). Springer International Publishing, pp. 534.

Sharma, R., 2017b. Deep-Sea Mining: Current Status and Future Considerations. In: Sharma, R. (Ed.), Deep-Sea Mining: Resource Potential, Technical and Environmental Considerations. Springer International Publishing AG, pp. 3-22.

Sharma, R., Nagender Nath, B., Parthiban, G., Jai Sankar, S., 2001. Sediment redistribution during simulated benthic disturbance and its implications on deep seabed mining. Deep Sea Research Part II: Topical Studies in Oceanography, 48(16): 3363-3380.

Skinner, H.C.W., Fitzpatrick, R.W., 1992. Biomineralization Processes of Iron and Manganese: Modern and Ancient Environments. Catena-Verlag, Cremlingen-Destedt, pp. 432.

Taylor, S.R., McLennan, S.M., 1985. The Continental Crust: Its Composition and Evolution. Blackwell Scientific Publications, Oxford, pp. 312.

Tebo, B.M., Bargar, J.M., Clement, B.G., Dick, G.J., Murray, K.J., Parker, D., Verity, R., Webb, S.M., 2004. Biogenic manganese oxides: Properties and Mechanisms of Formation. Annual Review of Earth and Planetary Sciences, 32: 287-328.

Tebo, B.M., Clement, B.G., Dick, G.J., 2007. Biotransformation of manganese. In: Hurst, C.J. et al. (Eds.), Manual of Environmental Microbiology. ASM Press, Washington, DC, pp. 1223–1238.

Tu, S., Racz, G.J., Goh, T.B., 1994. Transformations of synthetic birnessite as affected by pH and manganese concentration. Clays and Clay Minerals, 42: 321-330.

UN, 2017. World Population Prospects: The 2017 Revision, Key Findings and Advance Tables, World Population Prospects. United Nations, pp. 53.

Varentsov, I.M., Grassely, G.Y., 1980. Geology and Geochemistry of Manganese. Schweizerbart'sche Verlagsbuchhandlung, Stuttgart, pp. 463.

Villalobos, M., Lanson, B., Manceau, A., Toner, B., Sposito, G., 2006. Structural model for the biogenic Mn oxide produced by *Pseudomonas putida*. American Mineralogist, 91(4): 489-502.

Villalobos, M., Toner, B., Bargar, J., Sposito, G., 2003. Characterization of the manganese oxide produced by *Pseudomonas putida* strain MnB1. Geochimica et Cosmochimica Acta, 67(14): 2649-2662.

Von Heimendahl, M., Hubred, G.L., Fuerstenau, D.W., Thomas, G., 1976. A transmission electron microscope study of deep-sea manganese nodules. Deep Sea Research Oceanography Abstracts 23: 69-79.

Von Stackelberg, U., 1987. Manganese nodule from the equatorial North Pacific Ocean. Geologisches Jahrbuch, D87: 123-227.

Von Stackelberg, U., 1997. Growth history of manganese nodules and crusts of the Peru Basin, Manganese mineralization: geochemistry and mineralogy of terrestrial and marine deposits. Geological Society Special Publications, pp. 153-176.

Von Stackelberg, U., 2000. Manganese nodules of the Peru Basin. In: Cronan, D.S. (Ed.), Handbook of marine mineral deposits. CRC Press, Boca Raton, pp. 197-238.

Webb, S.M., Dick, G.J., Bargar, J.R., Tebo, B.M., 2005a. Evidence for the presence of Mn(III) intermediates in the bacterial oxidation of Mn(II). Proceedings of the National Academy of Sciences USA, 102: 5558-5563.

Webb, S.M., Tebo, B.M., Bargar, J.R., 2005b. Structural characterization of biogenic Mn oxides produced in seawater by the marine *bacillus sp.* strain SG-1. American Mineralogist, 90(8-9): 1342-1357.

Wegorzewski, A., Köpcke, M., Kuhn, T., Sitnikova, M., Wotruba, H., 2018. Thermal Pre-Treatment of Polymetallic Nodules to Create Metal (Ni, Cu, Co)-Rich Individual Particles for Further Processing. Minerals, 8(11): 523.

Wegorzewski, A., Kuhn, T., Dohrmann, R., Wirth, R., Grangeon, S., 2015. Mineralogical characterization of individual growth structures of Mn-nodules with different Ni+Cu content from the central Pacific Ocean. American Mineralogist, 100: 2497-2508.

Wieser, M.E., 2006. Atomic weights of the elements 2005 (IUPAC Technical Report). Pure and Applied Chemistry, 78(11): 2051-2066.

Zhao, H., Zhu, M., Li, W., Elzinga, E.J., Villalobos, M., Liu, F., Zhang, J., Feng, X., Sparks, D.L., 2016. Redox Reactions between Mn(II) and Hexagonal Birnessite Change Its Layer Symmetry. Environmental Science & Technology, 50(4): 1750-1758.

Zhu, M., Ginder-Vogel, M., Parikh, S.J., Feng, X.H., Sparks, D.L., 2010. Cation effects on the layer structure of biogenic Mn-oxides. Environmental Science & Technology, 44: 4465-4471.

Websites:

www.gebco.net, 2017. GEBCO world map 2014. British-Oceanographic-Data-Centre (Ed.) https://www.gebco.net/data_and_products/printable_maps/gebco_world_map/. Accessed on 13.11.2017.

www.tidalvisionusa.com, 2017. *Ocean* http://www.tidalvisionusa.com/wpcontent/uploads/2015/05/ocean-floor-background.png. Accessed on 13.11.2017.

Chapter 2

Recrystallization of Manganite (γ-MnOOH) and Implications for Trace Element Cycling

Tobias Hens[1], Joël Brugger[1], Susan A. Cumberland[1,2], Barbara Etschmann[1], Andrew J. Frierdich[1]

[1]School of Earth, Atmosphere & Environment, Monash University, Clayton, VIC 3800, Australia
[2]Australian Synchrotron, Clayton, VIC 3168, Australia

Recrystallization of Manganite (γ-MnOOH) and Implications for Trace Element Cycling

Tobias Hens,[†] Joël Brugger,[†][®] Susan A. Cumberland,[†,‡] Barbara Etschmann,[†] and Andrew J. Frierdich*[,†][®]

[†]School of Earth, Atmosphere & Environment, Monash University, Clayton, Victoria 3800, Australia

[‡]Australian Synchrotron, Clayton, Victoria 3168, Australia

S *Supporting Information*

ABSTRACT: The recrystallization of Mn(III,IV) oxides is catalyzed by aqueous Mn(II) ($Mn(II)_{aq}$) during (bio)geochemical Mn redox cycling. It is poorly understood how trace metals associated with Mn oxides (e.g., Ni) are cycled during such recrystallization. Here, we use X-ray absorption spectroscopy (XAS) to examine the speciation of Ni associated with Manganite (γ-Mn(III)OOH) suspensions in the presence or absence of $Mn(II)_{aq}$ under variable pH conditions (pH 5.5 and 7.5). In a second set of experiments, we used a ^{62}Ni isotope tracer to quantify the amount of dissolved Ni that exchanges with Ni incorporated in the Manganite crystal structure during reactions in 1 mM $Mn(II)_{aq}$ and in Mn(II)-free solutions. XAS spectra show that Ni is initially sorbed on the Manganite mineral surface and is progressively incorporated into the mineral structure over time (13% after 51 days) even in the absence of dissolved Mn(II). The amount of Ni incorporation significantly increases to about 40% over a period of 51 days when $Mn(II)_{aq}$ is present in solution. Similarly, $Mn(II)_{aq}$ promotes Ni exchange between Ni-substituted Manganite and dissolved Ni(II), with around 30% of Ni exchanged at pH 7.5 over the duration of the experiment. No new mineral phases are detected following recrystallization as determined by X-ray diffraction and XAS. Our results reveal that Mn(II)-catalyzed mineral recrystallization partitions Ni between Mn oxides and aqueous fluids and can therefore affect Ni speciation and mobility in the environment.
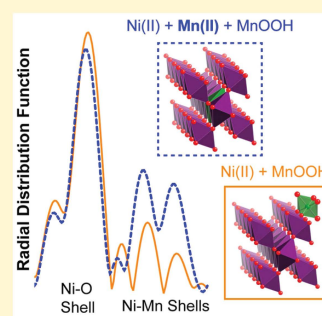
■ INTRODUCTION

Over 30 (oxyhydr)oxide minerals of manganese (hereon Mn oxides) occur in soils, sediments, and rocks.[1] These ubiquitous minerals are powerful oxidants and among the strongest metal scavengers in the environment.[2−4] This leads to Mn oxides being host phases of economic quantities of critical metals, for instance, in marine ferromanganese nodules and polymetallic crusts.[5] They also often serve as electron acceptors during microbial respiration,[6,7] which leads to the reductive dissolution of solid-phase Mn(III,IV) and release of dissolved Mn(II) into groundwater and sediment pore water. Biogenic processes can oxidize aqueous Mn(II) ($Mn(II)_{aq}$)[8,9] to form δ-MnO$_2$-like phyllomanganates.[6,7,10−12] Consequently, $Mn(II)_{aq}$ may coexist and abiotically back-react with Mn oxides at redox interfaces during biogeochemical manganese cycling.

When the oxidation rate of $Mn(II)_{aq}$ is slow, or when newly formed phyllomanganates are in contact with low concentrations of $Mn(II)_{aq}$ (e.g., $Mn(II)_{aq}$ to solid-phase Mn(IV) ratios <1), the mineral phase products have increasing crystallinity and decreasing Mn average oxidation states.[13−20] This likely results from abiotic comproportionation reactions between Mn(II) and Mn(IV) to generate Mn(III) within and above/below octahedral sheet vacancies of phyllomanganates.[21,22] The filling or blocking of phyllomanganate sheet vacancies by Mn(III) limits trace element uptake by these phases.[23−25]

In cases where phyllomanganates are subjected to high concentrations of $Mn(II)_{aq}$, net Mn(II) oxidation and Mn(IV) reduction causes a reductive phase transformation to Mn(III)-bearing minerals (e.g., Manganite [γ-MnOOH]).[26−29] These chemical and mineralogical changes result in nearly complete exchange between dissolved and solid-phase Mn.[27] Elzinga[30] later demonstrated that even in the absence of a phase transformation, $Mn(II)_{aq}$ actively catalyzes phyllomanganate recrystallization through coupled comproportionation (Mn(II) + Mn(IV) → 2Mn(III)) and disproportionation (2Mn(III) → Mn(II) + Mn(IV)) of Mn species. We have recently shown that $Mn(II)_{aq}$ enhances exchange between structural oxygen in Manganite with water,[31] suggesting that $Mn(II)_{aq}$ undergoes electron transfer and atom exchange with structural Mn(III) in stable Mn(III) oxides similar to what has been reported for aqueous Fe(II) and some Fe(III) minerals.[32,33] On the basis of these findings, we hypothesize that structurally compatible trace elements and contaminants associated with Mn oxides may undergo mineral-fluid repartitioning during reactions with Mn(II)-bearing fluids, as described for Fe oxides in the presence of aqueous Fe(II).[34]

Here, we evaluate Ni(II) cycling during Mn(II)-catalyzed recrystallization of Manganite in two sets of complementing experiments. First, the speciation of Ni in Manganite suspensions over time was examined in the presence or absence of dissolved Mn(II) using wet-chemistry measurements and synchrotron-based X-ray absorption spectroscopy (XAS). Second, Manganite with Ni preincorporated in the structure was reacted with a ^{62}Ni isotope tracer in solution to quantify the labile solid-phase Ni pool with and without Mn(II)$_{aq}$. In both cases we explored the effects of the concentration of Mn(II)$_{aq}$, pH, and reaction time.

■ METHODS

Synthesis and Characterization of Manganite. Manganite was synthesized following a procedure similar to our prior work.[31] Briefly, 210 mL of 0.2 M NH$_4$OH was added to 700 mL of 0.06 M MnSO$_4$ over 1 min during vigorous stirring to yield a suspension of Mn(OH)$_2$. This precipitate was oxidized by dropwise addition of 21 mL of 30% H$_2$O$_2$ over 3 min. The resulting solid was then triply washed by centrifugation of the suspension (~10 000 g), decantation of the supernatant, and resuspension of the solid in ≥18.2 MΩ·cm water (hereon water). The washed solid was then dried overnight at 70 °C, ground to a fine powder using a mortar and pestle, and passed through a 90 μm sieve. Ni-substituted Manganite was synthesized identically to Manganite, except 0.084 mL of 1 M NiSO$_4$·xH$_2$O was added to the MnSO$_4$ solution (Ni/Mn = 0.002) to coprecipitate Mn(II) and Ni(II) during the addition of NH$_4$OH. This mixed metal hydroxide was then oxidized by 30% H$_2$O$_2$ as noted above.

Mineral phase identity of solid samples was determined by X-ray diffraction (XRD) on a Bruker D8 Advance diffractometer at the Monash X-ray Platform using Cu K$_\alpha$ radiation (see Supporting Information (SI) for further details). Iodometric titration was performed to determine the Mn average oxidation state (Mn AOS) of the synthetic Manganite starting materials (SI Section S2). The mole percent of Ni (Ni mol % = [moles Ni/(moles Ni + moles Mn)] × 100) in Ni-substituted MnOOH was determined by inductively coupled plasma mass spectrometry (ICP-MS) using a Thermo Scientific iCAP-Q following dissolution of the solid in 5 mL of 5 M HCl. Analysis of the final Ni-substituted MnOOH product revealed a nickel content of 0.18 mol %.

Reaction of Manganite with Ni(II)- and Mn(II)-Bearing Solutions. All experiments were conducted in an anaerobic chamber (Coy Laboratory Products, Inc., 1.5−3.0% H$_2$ atmosphere with N$_2$ balance) with oxygen levels maintained at less than 1 ppm by continual circulation of the atmosphere over Pd catalysts. All labware and reagents were equilibrated with the chamber atmosphere for ≥48 h prior to use. Water was presparged with N$_2$ for 30 min outside the chamber in a closed vessel and further deoxygenated for 30 min by bubbling with the chamber atmosphere, which was first passed through an aqueous solution containing 15% pyrogallol and 50% KOH to remove trace O$_2$ and CO$_2$.

Duplicate reactors were set up by adding 8.8 mL water to 15 mL tubes containing 20 ± 0.2 mg of Manganite. Solution pH of 7.5 ± 0.05 or 5.5 ± 0.05 was buffered by adding 1 mL of a 0.1 M MOPS (3-(1-morpholino)propanesulfonic acid)/NaCl solution or 1 mL of a 0.1 M MES (2-(4-morpholino)-ethanesulfonic acid)/NaCl solution, respectively. Reactions were then initiated by addition of a constant volume of 0.2 mL of 10 mM NiCl$_2$ solution ([Ni(II)]$_{aq}$ = 0.2 mM) and either

0.02 or 0.1 mL of 100 mM MnCl$_2$ solution to yield a final Mn(II) concentration of either 0.2 or 1 mM in the reactors. Small volumes (<0.05 mL) of 1 M NaOH were added to the reactors for pH adjustment when necessary. Subsequently, all tubes were wrapped in Al foil and mixed by gyration until sampling. Solution pH was measured at the time of reactor preparation and prior to sampling and was found to vary by less than 0.1 pH unit.

Samples were sacrificed after aging for a duration of 1, 7, and 51 days and filtered with a reusable syringe filter assembly (Merck Millipore Swinnex with a 0.22 μm Durapore membrane) to retain the solid fraction for XAS analyses. The filtrate was acidified to 0.1 M HCl and saved for chemical analysis by ICP-MS, whereas the solid samples were fixated individually as wet pastes between two layers of 25 μm Kapton tape inside the anaerobic chamber. Each sample was heat-sealed in polyethylene bags to preserve anaerobic conditions until analysis by XAS.

Nickel isotope exchange experiments were conducted in a similar fashion except 0.05 mL of a 10 mM ^{62}Ni-enriched Ni(II) solution, which was prepared by the dissolution of Ni^0 in 1 M HCl (98% isotopic purity, Isoflex, U.S.A.), was added to the Ni-substituted Manganite suspension just prior to the introduction of Mn(II)$_{aq}$. Filtrates were treated as noted above. Solid samples collected after reactions were dried on filter membranes inside the anaerobic chamber for ≥72 h and then characterized by XRD.

XAS Data Collection and Spectral Analysis. X-ray absorption near-edge structure (XANES) and extended X-ray fine-structure (EXAFS) spectra of Mn and Ni were collected for selected samples on the XAS Beamline at the Australian Synchrotron in fluorescent yield mode with a Canberra 100 element Ge fluorescence detector. The X-ray beam energy, selected with a Si(111) crystal monochromator with harmonic content reduced to <10^{-5} over the entire energy range by a harmonic rejection mirror, was calibrated by setting the maximum in the first derivative of the XANES scan of Ni and Mn metal foils to 8333 and 6539 eV for the Ni and Mn K-edges, respectively. X-ray flux was increased by focusing the beam size to 0.7 mm by 1.5 mm. Beam damage to the sample was assessed by collecting rapid XANES scans across the Mn K-edge in succession; no spectral changes were observed and thus beam damage was deemed negligible. XAS spectra were averaged, normalized, and background subtracted using IFEFFIT[35] with the Athena interface[36] whereas the k^3-weighted EXAFS spectra of Ni were quantitatively analyzed using Artemis.[36] Phase and amplitude functions were generated from the structures of Manganite [γ-MnOOH][37] using FEFF.[38] Coordination number (N), interatomic distance (R), and σ^2 (a Debye−Waller-type factor based on a Gaussian distribution of interatomic distances), were refined using a nonlinear least-squares fitting routine with the amplitude reduction factor, S_0^2, fixed to 1.07.

Ni Isotope Exchange in Ni-substituted Manganite. Metal isotopes in the aqueous phase were measured by ICP-MS operated in collision cell mode using helium to remove polyatomic interferences. Blanks and calibration standards were run with each sample set. Quantification of manganese was done by analysis of counts on the mass-55 channel. For samples containing Ni with a natural abundance isotope composition (hereon natural abundance Ni), counts on the mass-60 channel were used for Ni concentration calibrations. However, for experiments that utilized the ^{62}Ni tracer, which had a changing

Table 1. Ni K-Edge EXAFS Spectra Structural Fitting Results

						crystallographic values[a]	
shell	N	R (Å)	σ^2 (Å^2)	ΔE_0 (eV)	R-factor	N	R (Å)
	Ni-substituted Manganite						
O	4[b,c]	2.02(1)[d]	0.003(1)	−3(1)	0.01	2	1.89
						2	1.98
O	2[c]	2.19(3)	0.003(1)	−3(1)		1	2.21
						1	2.34
Mn	2[c]	2.93(2)	0.008(2)	−3(1)		1	2.78
						1	2.98
Mn	4	3.67(3)	0.008(3)	−3(1)		4	3.66
Mn	4	3.86(1)	0.014(8)	−3(1)		4	3.82
	Ni-sorbed on Manganite						
O	6	2.04(2)	0.007(1)	−6(3)	0.01	NA	NA
Mn	0.9(6)	2.99(5)	0.008	−6(3)		NA	NA
Mn	1(1)	3.69(7)	0.008	−6(3)		NA	NA

[a]Interatomic distances and coordination numbers for the crystal structure of Manganite. [b]Parameters with no listed uncertainties were not varied during refinement. [c]Multiple unresolvable shells. See crystallographic values. [d]Statistical uncertainties in the last digit are reported in parentheses at the 95% confidence level.

isotope composition as a result of exchange with natural abundance Ni in Ni-substituted MnOOH, the sum of the Ni counts were used for concentration calibration. Nickel isotope mole fractions (f) were calculated by dividing the counts per second (cps) of isotope n by the sum of the total Ni isotope cps as given below:

$$\frac{n_{cps}}{^{58}cps + {}^{60}cps + {}^{61}cps + {}^{62}cps} = f^n Ni \quad (1)$$

An interference on the Ni counts at mass 64 was observed at low Ni concentration and thus ^{64}Ni counts were not included in the calculation of Ni isotope fractions. These amounted to less than 0.7% (average) of the total Ni counts for spiked samples and therefore have a minor effect on calculated Ni isotope fractions.

The percent of Ni in Manganite that exchanges with dissolved Ni and the Ni isotope mass balance were calculated as follows (see our prior work for equation derivation[32,39]):

$$\%Ni\ exchange = \frac{N_{aq} \times \left(f^n Ni^i_{aq} - f^n Ni^t_{aq}\right)}{N^{Tot}_{Man} \times \left(f^n Ni^t_{aq} - f^n Ni^i_{Man}\right)} \times 100 \quad (2)$$

$$mass\ balance = \frac{\left(f^n Ni^i_{aq} \times N_{aq}\right) + \left(f^n Ni^i_{Man} \times N^{Tot}_{Man}\right)}{\left(N_{aq} + N^{Tot}_{Man}\right)} \quad (3)$$

where N_{aq} represents the total moles of Ni(II) added to the aqueous phase, N^{Tot}_{Man} are the total moles of Ni(II) initially associated with Manganite, $f^n Ni^i_{aq}$ is the initial isotope composition of aqueous Ni(II), $f^n Ni^i_{Man}$ is the initial isotope composition of Ni in Manganite, and $f^n Ni^t_{aq}$ is the isotopic composition of Ni(II)$_{aq}$ at time $t > 0$. No correction for mass-dependent isotope fractionation is applied to $f^n Ni^t_{aq}$ since equilibrium and kinetic isotope fractionations are negligible relative to the large isotopic enrichment used here (e.g., a permil (‰) fractionation would change $f^n Ni$ by <0.0001).

■ RESULTS

Our study is based on two sets of complementary experiments. First, we reacted MnOOH with Ni(II)$_{aq}$ in the presence or absence of Mn(II)$_{aq}$ and used XAS to measure the speciation of Ni associated with the solid as a function of time, Mn(II)$_{aq}$ concentration, and solution pH. Second, we suspended Ni-substituted Manganite in Mn(II)$_{aq}$ solutions that also contained ^{62}Ni-enriched Ni(II)$_{aq}$ and measured the amount of Ni bound within the Manganite lattice that is exchanged with the fluid. This approach presumably approximates the degree by which Manganite undergoes dynamic recrystallization in Mn(II)-bearing solutions.

Mn and Ni K-Edge XAS. The role of dissolved Mn(II) and solution pH on Ni(II) sorption and incorporation into Manganite was investigated by Mn and Ni K-edge XAS. The addition of Ni(II)$_{aq}$ to MnOOH suspensions at pH 7.5 resulted in a rapid initial decrease in Ni(II)$_{aq}$ concentrations from 212 μM to 11 μM within 1 day, which is followed by a gradual decrease to 4 μM after 51 days (SI Table S1). A similar trend in Ni(II)$_{aq}$ concentrations is observed when Mn(II)$_{aq}$ is also present although slightly less Ni(II) is taken up by the solid, presumably due to competitive sorption between Ni(II) and Mn(II) for MnOOH surface sites. In all reactions at pH 7.5, however, Mn(II)$_{aq}$ had a relatively small effect on net Ni sorption as over 90% of the Ni initially added was taken up by MnOOH at all Mn(II)$_{aq}$ concentrations (SI Table S1). At pH 5.5, however, only about 10% of the Ni(II)$_{aq}$ initially added is taken up by MnOOH. Nickel sorption at pH 5.5 appears to be independent of added Mn(II)$_{aq}$ as similar amounts (same within error) of Ni are sorbed by MnOOH even when 1 mM Mn(II)$_{aq}$ is added to MnOOH suspensions. The sorption behavior of Mn(II) at pH 7.5 is similar to that of Ni(II), i.e., a rapid decrease in the Mn(II)$_{aq}$ concentration occurs within the first day and is followed by a slower decline over the remainder of the 51 day reaction period (SI Table S1). At pH 5.5, however, there is a net increase in the Mn(II)$_{aq}$ concentration, presumably due to the proton-promoted disproportionation of Mn(III).[40−42]

Although the presence of Mn(II)$_{aq}$ appears to have little effect on total Ni uptake by MnOOH, apart from minor competitive sorption, information about the solid-phase Ni speciation requires further spectroscopic analysis. To quantify the effect of dissolved Mn(II)$_{aq}$, solution pH, and reaction time on Ni speciation, we first established end-member spectra that represent Ni sorbed on the Manganite mineral surface and Ni
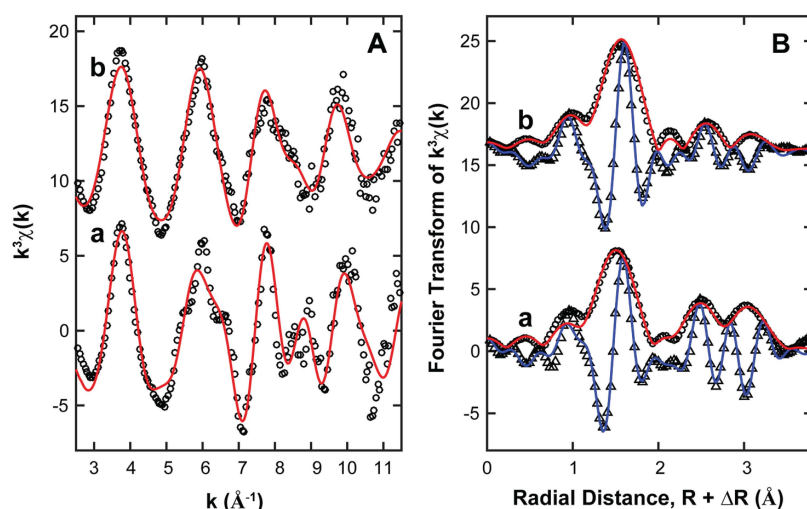
Figure 1. Nickel K-edge (A) k^3-weighted $\chi(k)$ EXAFS spectra of (a) Ni-substituted Manganite and (b) Ni sorbed on Manganite at pH 7.5 after 1 day of reaction time. (B) Radial distribution functions of the magnitude (circles) and real (triangles) components of the Fourier transform of $\chi(k)$. Refined parameters for the local structural model fits (lines) to the spectral data are in Table 1.

incorporated into the crystal structure. The Ni K-edge EXAFS spectral analysis results (Table 1, Figure 1) for Ni-substituted MnOOH are consistent with Ni substitution in a manganese octahedral site in the Manganite structure, albeit with a significant distortion of the first oxygen shell around Ni in Manganite due to the differences in the ionic radii of Mn^{3+} and Ni^{2+} (0.58 Å versus 0.69 Å[42]) and in their coordination chemistry (Jahn–Teller distortion of Mn(III)).

Best fits were obtained using two oxygen shells (Table 1) with coordination numbers of 4 and 2 at interatomic distances of 2.02 ± 0.01 Å and 2.19 ± 0.03 Å, respectively. The apparent Jahn–Teller distortion is consistent with the Mn(III) sites in Manganite.[37] However, the degree of distortion is significantly less than that of the crystallographic values for a Mn(III) site in Manganite (Table 1). Attempts to model the EXAFS spectra using a single O shell with a coordination number of 6 resulted in a less accurate fit (R-factor 0.03 and larger errors on interatomic distances). Similarly, modeling the spectrum with two O shells having coordination numbers of 3 had a negative impact on the fitting statistics. The presence of two substantial second shells in the Fourier transform is clear evidence of structurally incorporated Ni. The first Mn shell used in the fit yields an interatomic distance of 2.93 ± 0.02 Å, which is an excellent match for Ni substitution within the edge-sharing Mn(III) octahedral chains in MnOOH (Table 1). The overall fit was substantially improved by inclusion of two additional Mn shells representing corner-sharing octahedra in neighboring chains at distances of 3.67 ± 0.03 Å and 3.86 ± 0.01 Å.

Conversely, Ni K-edge EXAFS spectral fitting results for pure Manganite reacted with $Ni(II)_{aq}$ for 1 day at pH 7.5 is best fit using a structural model of Ni sorbed on the Manganite surface. Similar to Ni-substituted Manganite, there is a large amplitude in the Fourier transform from the Ni–O shell and the appearance of additional shells at higher interatomic distances (Figure 1). The best overall fit was obtained by fixing the coordination number of the O shell to 6. Two Mn shells were required to fully fit the spectrum and revealed Mn neighbors at 2.99 ± 0.05 Å and 3.69 ± 0.07 Å, consistent with edge- and

corner-sharing Ni–Mn octahedra. Small Mn coordination numbers (~1) for each Mn shell are typical for the smaller amplitudes, relative to Ni-substituted Manganite, seen in the Fourier transform (Figure 1). These fitting results are thus consistent with a surface complex rather than Ni incorporated in the structure. An attempt to fit the data using two oxygen shells, each with a fixed coordination number of 3, did not result in a significantly improved fit and parameters converged to Ni–Mn coordination numbers and interatomic distances that were identical within error.

The XANES spectra of these two solid phase samples can thus be used as end-members to quantify the relative proportions of "sorbed" and "incorporated" Ni present in samples that have reacted with $Ni(II)_{aq}$ in Mn(II)-bearing fluids. Indeed, for MnOOH samples reacted with $Ni(II)_{aq}$ in solutions also containing dissolved Mn(II), the XANES spectra appear as a mixture of the two, as indicated by spectral intersections at isosbestic points (Figure 2A,D). Linear-combination fits of Ni K-edge XANES spectra show that the fraction of solid-bound Ni that is incorporated in the MnOOH crystal lattice ranges from 13 ± 2% to 41 ± 1% with time and $Mn(II)_{aq}$ concentration at pH 7.5 (Table 2). Reactions at pH 5.5 show 29 ± 2% to 42 ± 2% of the solid-phase Ni (sorbed + incorporated) is incorporated after 51 days with increasing $Mn(II)_{aq}$ concentrations (0 mM − 1 mM), despite that Ni uptake by the solid was substantially lower compared to reactions at pH 7.5 (SI Table S1). Incorporation of Ni was similar at pH 5.5 and pH 7.5 after 51 days of reaction in the presence of 1 mM $Mn(II)_{aq}$ but Ni incorporation showed less time dependence during reactions at pH 5.5 (33 ± 2%, 37 ± 2%, and 42 ± 2% incorporation at pH 5.5 at times 1 day, 7 days, and 51 days in comparison to 17 ± 4%, 28 ± 3%, and 41 ± 1% at pH 7.5 over the same duration). Even at pH 7.5 when no exogenous Mn(II) was added, the extent of Ni incorporation was significant (13%) after 51 days, suggesting that background recrystallization may be occurring. Prior work has shown that even in the absence of added $Mn(II)_{aq}$, Manganite can recrystallize in aqueous fluids, as evidenced by
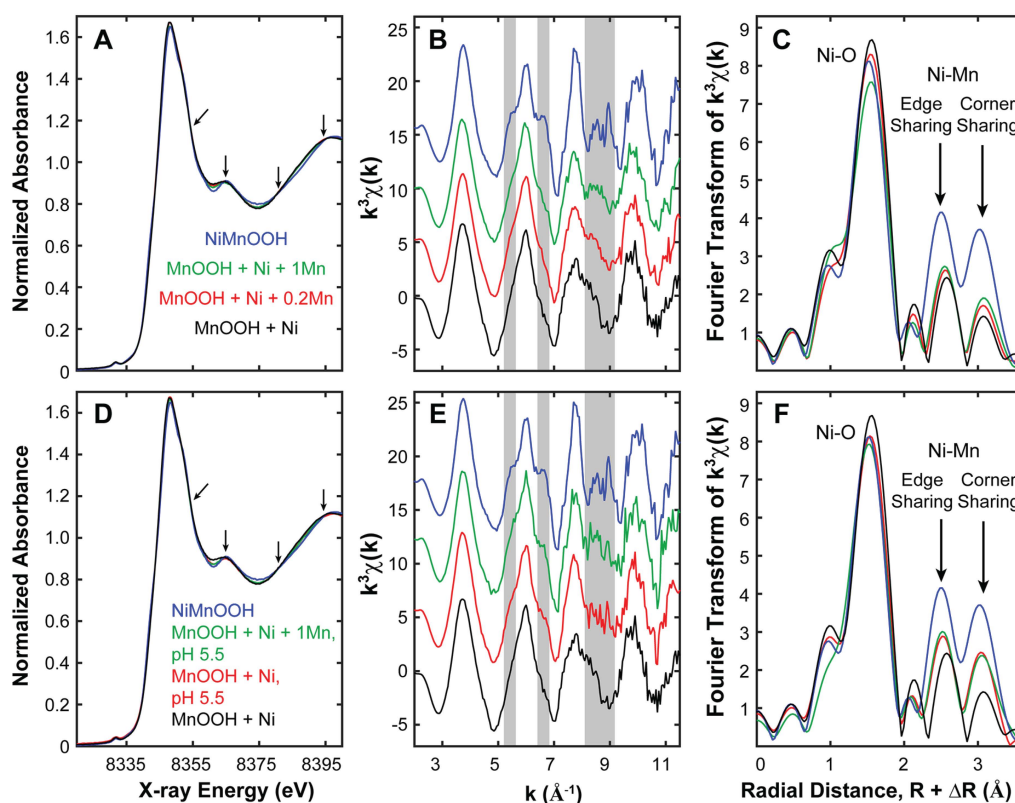
Figure 2. (A) Nickel K-edge XANES spectra for Manganite reacted in a 0.2 mM $Ni(II)_{aq}$ solution for 1 day in the absence of added $Mn(II)_{aq}$ (MnOOH + Ni) and after reaction for 51 days in the presence of 0.2 mM $Mn(II)_{aq}$ (MnOOH + Ni + 0.2Mn) and 1 mM $Mn(II)_{aq}$ (MnOOH + Ni + 1Mn). Spectrum for Ni-substituted MnOOH with Ni incorporated in the structure (NiMnOOH) is shown for comparison. (B) k^3-weighted $\chi(k)$ EXAFS spectra and (C) radial distribution functions of the four preceding samples. Distinctive features appearing at a $k \approx 5.5$ Å^{-1}, 6.8 Å^{-1} and 8.4 Å^{-1} are highlighted and correspond to increasing amplitudes for Ni−Mn shells (edge sharing octahedral and corner sharing octahedra). Comparison of (D) Nickel K-edge XANES spectra, (E) k^3-weighted $\chi(k)$ EXAFS spectra, and (F) radial distribution functions for 51 day Manganite reaction in a 0.2 mM $Ni(II)_{aq}$ solution in the absence (MnOOH + Ni, pH 5.5) and presence (MnOOH + Ni + 1Mn, pH 5.5) of 1 mM $Mn(II)_{aq}$ at pH 5.5.

structural oxygen in Manganite exchanging with water.[31] SI Figure S2 shows linear-combination fits for all samples in this study.

The results of XANES linear-combination fitting are supported by the Ni K-edge EXAFS spectra which exhibit characteristic features of incorporated Ni at wavenumbers (i.e., k values) of ~5.5 Å^{-1}, ~6.8 Å^{-1}, and ~8.4 Å^{-1}. These features are mostly absent for Ni sorbed on Manganite but become more prominent as a larger proportion of Ni becomes incorporated into the structure (Figure 2B,E). These features arise from scattering from neighboring Mn shells, resulting in radial distribution functions with progressively larger amplitudes at higher $R + \Delta R$ distances (Figure 2C,F). Structural fitting results of EXAFS spectra (Table 1) indicate that the peaks at ~2.5 Å ($R + \Delta R$) correspond to a Mn shell from adjacent Mn atoms in edge-sharing Mn(III) octahedral chains in MnOOH whereas the peak at ~3.2 Å ($R + \Delta R$) is a combination of two additional Mn shells representing corner-sharing octahedra in neighboring chains. Higher amplitudes in these shells indicate a greater number of Mn atoms surrounding the Ni absorber atoms and thus a greater degree of Ni incorporation into the Manganite structure. This trend increases with Mn(II) concentration and reaction time at pH

5.5 and 7.5, consistent with the results obtained by linear-combination fitting.

From the combined results of XAS and ICP-MS solution analyses, we show that dissolved Ni(II) is taken up by Manganite and up to ~40% of this solid-associated Ni is incorporated into the Manganite mineral structure. Such incorporation is promoted by Mn(II) in solution which presumably catalyzes mineral dissolution and reprecipitation processes, although at lower pH disproportionation-comproportionation reactions may be a significant mechanism for recrystallization (see Discussion Section). XRD analyses of solid samples collected after 51 days reactions in the absence and presence of 1 mM Mn(II) at pH 7.5 and 5.5 show that no mineral phase transformation occurs (SI Figure S1). Furthermore, Mn K-edge XANES spectra also show no significant change among these samples, indicating that neither the buffer solutions nor $Mn(II)_{aq}$ resulted in net reduction of the solid-phase Mn (SI Figure S3).

Ni Isotope Exchange between $Ni(II)_{aq}$ and Ni-Substituted Manganite. To determine whether $Ni(II)_{aq}$ exchanges with structural Ni in Manganite, and if $Mn(II)_{aq}$ promotes this process, we measured the Ni isotope fractions (f^mNi, eq 1) of $Ni(II)_{aq}$ during reactions between ^{62}Ni-enriched

Table 2. Results of linear-combination fitting (LCF) of the Ni K-edge XANES spectra using Ni-substituted Manganite and Ni-sorbed Manganite as end-member standards

experiment no.	pH	[Mn(II)] (mM)	reaction time (d)	% incorporated
1	7.5	0	1	0^a
2	7.5	0	7	NM^b
3	7.5	0	51	$13(2)^c$
4	7.5	0.2	1	9(3)
5	7.5	0.2	7	12(1)
6	7.5	0.2	51	16(1)
7	7.5	1	1	17(4)
8	7.5	1	7	28(3)
9	7.5	1	51	41(1)
10	5.5	0	1	21(3)
11	5.5	0	7	7(2)
12	5.5	0	51	29(2)
13	5.5	1	1	33(2)
14	5.5	1	7	37(2)
15	5.5	1	51	42(2)

^{a}Sorbed Ni end-member. ^{b}Not measured by XAS. ^{c}Statistical uncertainties in the last digit are reported in parentheses at the 95% confidence level. LCF from −20 eV below to 35 eV above the Ni K-edge.

Ni(II)$_{aq}$ with natural abundance Ni-substituted MnOOH in suspensions with variable pH and Mn(II)$_{aq}$ concentrations. At pH 7.5, Mn(II)$_{aq}$ concentrations decreased from their initial levels of ∼200 μM and ∼1000 μM to around 10 μM and 400 μM, respectively over the course of 51 days (SI Table S2). Dissolved Mn concentrations are small (∼1 μM) when no exogenous Mn(II) is added to the pH 7.5 reactors. Ni(II)$_{aq}$ concentrations, again, exhibited a rapid and extensive decrease (from ∼70 μM to 1 μM) for all reactions at pH 7.5 (SI Table S2). At pH 5.5, the Mn(II)$_{aq}$ concentrations experience similar behavior as previously described for the XAS experiments, i.e. Mn(II)$_{aq}$ concentrations increase by ∼100−300 μM from their initial values presumably due to disproportionation of Mn(III). Ni(II)$_{aq}$ concentrations decrease slightly at pH 5.5, but total amounts of Ni uptake by Ni-substituted MnOOH is substantially less than at pH 7.5 (SI Table S2). In summary, the concentrations of Ni(II)$_{aq}$ and Mn(II)$_{aq}$ exhibit temporal and pH dependent trends similar to experiments with MnOOH.

In the presence of Mn(II)$_{aq}$, the $f^{62}Ni^t_{aq}$ values decrease from the initial value of ∼0.98 to about 0.84. This decrease is significantly larger compared to changes in the Ni isotope composition of Ni(II)$_{aq}$ in the absence of added Mn(II)$_{aq}$ (Figure 3), indicating that Mn(II)$_{aq}$ enhances the amount of Ni isotope exchange between Ni(II)$_{aq}$ and Ni-substituted MnOOH. As expected, the $f^{62}Ni^t_{aq}$ remains constant over the course of the reaction when no Ni-substituted MnOOH is present (Figure 3) as the isotope composition can only change via exchange with a pool of Ni having a different isotopic composition.

The observed decrease in $f^{62}Ni^t_{aq}$ values indicate that dissolved Ni is being diluted and replaced by Ni atoms of a different isotope. Similar, but opposite, trends are seen for the $f^{58}Ni$ and $f^{60}Ni$ values (Figure 4) of Ni(II)$_{aq}$, indicating Ni atom movement from the Manganite structure into the aqueous phase. The isotopic fractions for all Ni isotopes either decrease ($f^{62}Ni$) or increase ($f^{58}Ni$ and $f^{60}Ni$) from their initial values
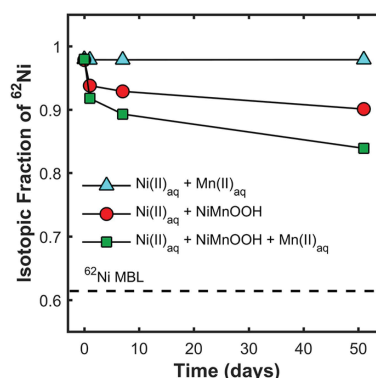
Figure 3. Evolution of the ^{62}Ni isotope fractions of Ni(II)$_{aq}$ in a 1 mM Mn(II)$_{aq}$ solution (without Ni-substituted MnOOH) and in suspensions of Ni-substituted MnOOH in the absence and presence of 1 mM Mn(II)$_{aq}$ at pH 7.5. Aqueous Ni(II) was initially enriched in ^{62}Ni ($f^{62}Ni = 0.978$), and hence depleted in the remaining Ni isotopes, whereas Ni-substituted Manganite has a natural abundance Ni isotope composition and a measured $f^{62}Ni$ value of 0.045. Values for data points represent the mean of duplicate reactions; error bars are smaller than symbols. MBL = mass balance line.
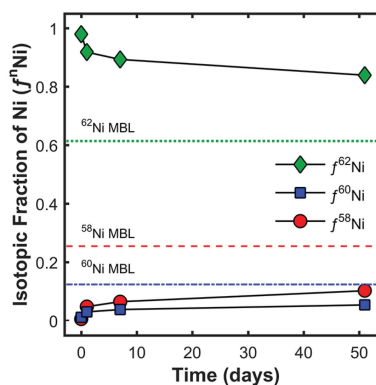
Figure 4. Evolution of the Ni isotope fractions of Ni(II)$_{aq}$ during its reaction with Ni-substituted Manganite and 1 mM Mn(II)$_{aq}$ over 51 days at pH 7.5. Aqueous Ni(II) was initially enriched in ^{62}Ni ($f^{62}Ni = 0.978$), and hence depleted in the remaining Ni isotopes ($f^{58}Ni = 0.006$, $f^{60}Ni = 0.011$, and $f^{61}Ni = 0.003$). Ni-substituted Manganite has a natural abundance Ni isotope composition and measured f^nNi values of 0.644, 0.298, 0.013, and 0.045 for ^{58}Ni, ^{60}Ni, ^{61}Ni, and ^{62}Ni, respectively. Values for data points represent the mean of duplicate reactions; error bars are smaller than symbols. MBL = mass balance line.

and move toward the respective Ni isotope mass balance values but in no instance attain an isotopic composition equal to the system mass balance. This thus indicates significant, yet incomplete, exchange of solid and aqueous Ni.

Insertion of $f^{62}Ni^t_{aq}$ values into eq 2 reveals that approximately 30% of Ni in Ni-substituted MnOOH exchanges with Ni(II)$_{aq}$ after 51 days at pH 7.5 in the presence of 1 mM Mn(II)$_{aq}$ (Figure 5A). The amount of exchange decreases at lower concentrations of added Mn(II)$_{aq}$, with ∼20% and ∼15% exchange observed for initial Mn(II)$_{aq}$ concentrations of 0.2 mM and 0 mM, respectively. The ∼15% of solid-phase Ni in Ni-substituted MnOOH that exchanges with dissolved Ni in
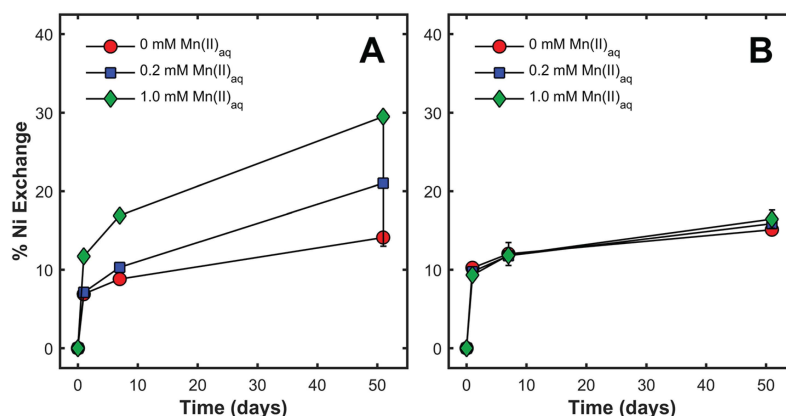
Figure 5. Percent exchange of Ni in Ni-substituted Manganite over time at (A) pH 7.5 and (B) pH 5.5 for variable concentrations of added $Mn(II)_{aq}$. Percent exchange was calculated by inserting $f^{62}Ni$ values of $Ni(II)_{aq}$ into eq 2. Values for data points represent the mean of duplicate reactions; error bars not visible are smaller than symbols.

the absence of added $Mn(II)_{aq}$ is similar to the estimated number of surface atoms in Ni-substituted MnOOH (see prior work for details[31]). Hence, $Mn(II)_{aq}$ enhances Manganite recrystallization such that Ni atoms in the bulk structure are likely exchangeable with the fluid.

Ni exchange at pH 5.5, however, appears to be independent of $Mn(II)_{aq}$ concentrations as roughly equal amounts of solid-phase Ni are exchangeable with $Ni(II)_{aq}$ at all $Mn(II)_{aq}$ concentrations (Figure 5B). Furthermore, only about 15% exchange is observed thus indicating that at pH 5.5 only surface atoms of Ni-substituted MnOOH interact with the fluid regardless of the concentration of $Mn(II)_{aq}$. Calculated amounts of exchangeable Ni in the solid-phase for pH 5.5 reactions are identical, within error, to the percent Ni exchange at pH 7.5 when no $Mn(II)_{aq}$ is added to solution.

■ DISCUSSION

Mechanistic Consideration. Our combined XAS and ^{62}Ni tracer results show that $Mn(II)_{aq}$ promotes the incorporation of sorbed Ni into MnOOH and the release of preincorporated Ni into solution. Thus, Ni is cycled between solid and solution during the recrystallization of Manganite through coupled dissolution-reprecipitation. Two possible mechanisms are proposed: disproportionation-comproportionation (DP-CP) and $Mn(II)-Mn(III)$ electron transfer-atom exchange (ET-AE).

The DP-CP of MnOOH occurs according to the following reaction:[43−46]

$$2MnOOH + 2H^+ \leftrightarrow MnO_2 + Mn^{2+} + 2H_2O \tag{4}$$
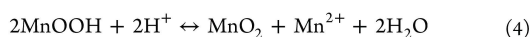
It is clear from eq 4 that disproportionation (left to right) is favored at low pH. This is consistent with the observed net leaching of $Mn(II)_{aq}$ during our pH 5.5 experiments and from previous studies.[40,41] The onset of disproportionation may occur at pH 7.5,[41] which when coupled to comproportionation (right to left in eq 4) can result in measurable amounts of dissolution-reprecipitation as evidenced from oxygen isotope exchange between water and MnOOH.[31] Frierdich et al. (2016) reported that recrystallization of MnOOH at pH 7.5 in the absence of added $Mn(II)_{aq}$ was roughly equivalent to the number of surface atoms of MnOOH. Interestingly, the amount of oxygen exchange between water and MnOOH[31] and Ni

exchange between $Ni(II)_{aq}$ and Ni-substituted MnOOH at pH 7.5 in Mn(II)-free solutions are nearly identical (cf. 18% vs 15%), suggesting that DP-CP is a significant process for mobilizing trace elements associated with Mn(III)-bearing minerals even if confined to surface exchange.

The second possible mechanism for Manganite recrystallization is interfacial $Mn(II)-Mn(III)$ ET-AE (eqs 5 and 6) where MnOOH oxidative growth (eq 5), via Mn(II) electron transfer to MnOOH and electron migration to a different structural Mn(III) site (i.e., *Mn(III)), is coupled to reductive dissolution (eq 6).[31]

$$Mn(II)_{aq} \rightarrow Mn(III)_s + e^- \tag{5}$$
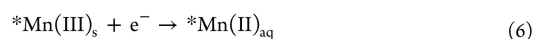
$$*Mn(III)_s + e^- \rightarrow *Mn(II)_{aq} \tag{6}$$

This mechanism is similar to that proposed for Fe(II)-catalyzed recrystallization of Fe(III) oxides.[32,33] As such, interfacial electron transfer between Mn(II) and solid-phase Mn(III) is only possible under conditions favorable for Mn(II) sorption to the mineral surface. At pH 5.5, no Mn(II) sorption is observed and therefore the Ni incorporation and exchange at these conditions is likely the result of DP-CP rather than $Mn(II)-Mn(III)$ ET-AE. At higher pH values (7.5), however, significant amounts of Mn(II) are taken up by MnOOH and this is accompanied by a significant increase in the amount of Ni exchange between $Ni(II)_{aq}$ and solid-phase Ni. Interestingly, Frierdich et al. (2016) observed approximately 30% oxygen exchange between water and MnOOH at pH 7.5 in the presence of 1 mM $Mn(II)_{aq}$, a value that is nearly identical to the amounts of Ni exchange between $Ni(II)_{aq}$ and Ni-substituted MnOOH observed in this study (Figure 5). Hence, $Mn(II)-Mn(III)$ ET-AE results in greater extents of Ni exchange between Ni-substituted Manganite and Ni in solution than that observed from DP-CP, with Ni atoms in the bulk mineral structure likely being accessible to the aqueous fluid.

Each of these mechanisms for Mn oxide recrystallization have been proposed during the Mn(II)-catalyzed recrystallization of vernadite.[30] Elzinga et al. (2016) observed complete Mn exchange between $Mn(II)_{aq}$ and vernadite (δ-MnO$_2$) at pH 5, and postulated that interfacial $Mn(II)-Mn(IV)$ comproportionation (right to left in eq 4) coupled to subsequent

disproportionation of transient Mn(III) species was responsible for the extensive amounts of recrystallization. Coupled ET-AE reactions between Mn(II) and solid-phase Mn(III) species may also contribute to the observed Mn exchange,[30] as well as drive the Mn(II)-catalyzed transformation of feitknechtite (β-MnOOH) to Manganite (γ-MnOOH).[26] Direct measurement of Mn exchange between Mn(II)$_{aq}$ and Manganite has not been reported but may be necessary to connect the Ni exchange observed here to the amount of recrystallization.

Environmental Implications. Mineral recrystallization in aqueous systems results in the exchange of elements between solids and solutions. Such mineral-fluid interactions are important for the cycling of major, minor, and trace elements as well as for the retention and release of contaminants. Net dissolution or net precipitation of a mineral phase in contact with a fluid can be determined from changes in the fluid composition. However, minerals may appear to be in chemical equilibrium with a surrounding fluid in many environments, yet continue to participate in mineral-fluid exchange. Here, our combined XAS measurements and [62]Ni isotope tracer experiments show that despite dissolved Mn(II) and Ni(II) concentrations reaching steady-state within short time periods (e.g., 1 day), Ni cycling occurs throughout the 51 day reaction. The findings provide direct evidence for Manganite-fluid Ni atom exchange promoted by Mn(II)$_{aq}$ without the occurrence of a mineral phase transformation. This has important implications for contaminant mobility in a wide variety of aquatic environments where Mn oxides are in contact with dissolved Mn(II), such as mine drainage and mineral seeps,[19,20] as well as for trace element uptake and release in deep-sea ferromanganese nodules and crusts.[5,47] Although Mn(IV)-bearing phyllomanganates predominate the initial Mn oxide mineralogy in near-surface aquatic systems, reductive processes during diagenesis of these phases can result in stable Mn(III) oxides.[48,49] Considering the rapid time-scale of Ni sorption, subsequent incorporation and exchangeability observed in our experiments, substantial changes in partitioning and speciation of Ni are to be expected due to Mn(II)$_{aq}$ interactions and Mn oxide recrystallization. Our work shows that Mn(II)-catalyzed recrystallization can initiate trace element cycling which potentially affects the partitioning of Ni in soils, sediments, and aquatic systems and the availability of these metals with respect to ligands and other solids.

■ ASSOCIATED CONTENT

Ⓢ Supporting Information

The Supporting Information is available free of charge on the ACS Publications website at DOI: 10.1021/acs.est.7b05710.

Details of the XRD measurements and sample characterization as well as data tables (PDF)

■ AUTHOR INFORMATION

Corresponding Author

*Tel.: (+61) 03 9905 4899; fax: (+61) 03 9905 4903; e-mail: andrew.frierdich@monash.edu (A.J.F.).

ORCID Ⓘ

Joël Brugger: 0000-0003-1510-5764
Andrew J. Frierdich: 0000-0002-2687-7252

Notes

The authors declare no competing financial interest.

■ REFERENCES

(1) Post, J. E. Manganese oxide minerals: Crystal structures and economic and environmental significance. *Proc. Natl. Acad. Sci. U. S. A.* **1999**, *96*, 3447−3454.

(2) Tebo, B. M.; Bargar, J. R.; Clement, B. G.; Dick, G. J.; Murray, K. J.; Parker, D.; Verity, R.; Webb, S. M. Biogenic manganese oxides: Properties and mechanisms of formation. *Annu. Rev. Earth Planet. Sci.* **2004**, *32*, 287−328.

(3) Goldberg, E. D. Marine Geochemistry 1. Chemical scavengers of the sea. *J. Geol.* **1954**, *62*, 249−265.

(4) Miyata, N.; Tani, Y.; Sakata, M.; Iwahori, K. Microbial manganese oxide formation and interaction with toxic metal ions. *J. Biosci. Bioeng.* **2007**, *104*, 1−8.

(5) Hein, J. R.; Koschinsky, A. Deep-Ocean Ferromanganese Crusts and Nodules. In *Treatise on Geochemistry*, 2nd ed.; Turekian, K. K., Ed.; Elsevier: Oxford, 2014; pp 273−291.

(6) Myers, C. R.; Nealson, K. H. Bacterial manganese reduction and growth with manganese oxide as the sole electron acceptor. *Science* **1988**, *240*, 1319−1321.

(7) Lovley, D. R. Fe(III) and Mn(IV) reduction. In *Environmental Metal−Microbe Interactions*; Lovley, D. R., Ed.; ASM Press: Washington, D.C., 2000; pp 3−30.

(8) Tebo, B. M.; Johnson, H. A.; McCarthy, J. K.; Templeton, A. S. Geomicrobiology of manganese(II) oxidation. *Trends Microbiol.* **2005**, *13* (9), 421−428.

(9) Emerson, D. Microbial oxidation of Fe(II) and Mn(II) at circumneutral pH. In *Environmental Metal−Microbe Interactions*; Lovley, D. R., Ed.; ASM Press: Washington, D.C., 2000; pp 31−52.

(10) Villalobos, M.; Lanson, B.; Manceau, A.; Toner, B.; Sposito, G. Structural model for the biogenic Mn oxide produced by *Pseudomonas putida. Am. Mineral.* **2006**, *91*, 489−502.

(11) Webb, S. M.; Tebo, B. M.; Bargar, J. R. Structural characterization of biogenic Mn oxides produced in seawater by the marine bacillus sp. strain SG-1. *Am. Mineral.* **2005**, *90*, 1342−1357.

(12) Skinner, H. C. W.; Fitzpatrick, R. W. *Biomineralization Processes of Iron and Manganese: Modern and Ancient Environments*; Catena-Verlag: Cremlingen-Destedt, 1992; Vol. Catena Supplement 21, p 432.

(13) Learman, D. R.; Wankel, S. D.; Webb, S. M.; Martinez, N.; Madden, A. S.; Hansel, C. M. Coupled biotic-abiotic Mn(II) oxidation pathway mediates the formation and structural evolution of biogenic Mn oxides. *Geochim. Cosmochim. Acta* **2011**, *75* (20), 6048−6063.

(14) Bargar, J. R.; Tebo, B. M.; Bergmann, U.; Webb, S. M.; Glatzel, P.; Chiu, V. Q.; Villalobos, M. Biotic and abiotic products of Mn(II) oxidation by spores of the marine Bacillus sp. strain SG-1. *Am. Mineral.* **2005**, *90*, 143−154.

(15) Mandernack, K. W.; Post, J.; Tebo, B. M. Manganese mineral formation by bacterial spores of the marine Bacillus, strain SG-1: Evidence for the direct oxidation of Mn(II) to Mn(IV). *Geochim. Cosmochim. Acta* **1995**, *59* (21), 4393−4408.

(16) Toner, B.; Fakra, S.; Villalobos, M.; Warwick, T.; Sposito, G. Spatially Resolved Characterization of Biogenic Manganese Oxide Production within a Bacterial Biofilm. *Appl. Environ. Microbiol.* **2005**, *71*, 1300−1310.

(17) Pecher, K.; McCubbery, D.; Kneedler, E.; Rothe, J.; Bargar, J.; Meigs, G.; Cox, L.; Nealson, K.; Tonner, B. Quantitative charge state analysis of manganese biominerals in aqueous suspension using scanning transmission X-ray microscopy (STXM). *Geochim. Cosmochim. Acta* **2003**, *67* (6), 1089−1098.

(18) Mann, S.; Sparks, N. H. C.; Scott, G. H. E.; Jong, E. W. d. V.-d. Oxidation of manganese and formation of Mn_3O_4 (hausmannite) by spore coats of a marine *Bacillus sp. Appl. Environ. Microbiol.* **1988**, *54*, 2140−2143.

(19) Bargar, J. R.; Fuller, C. C.; Marcus, M. A.; Brearley, A. J.; De la Rosa, M. P.; Webb, S. M.; Caldwell, W. A. Structural characterization of terrestrial microbial Mn oxides from Pinal Creek, AZ. *Geochim. Cosmochim. Acta* **2009**, *73*, 889−910.

(20) Frierdich, A. J.; Hasenmueller, E. A.; Catalano, J. G. Composition and structure of nanocrystalline Fe and Mn oxide cave deposits: Implications for trace element mobility in karst systems. *Chem. Geol.* **2011**, *284*, 82−96.

(21) Zhao, H.; Zhu, M.; Li, W.; Elzinga, E. J.; Villalobos, M.; Liu, F.; Zhang, J.; Feng, X.; Sparks, D. L. Redox Reactions between Mn(II) and Hexagonal Birnessite Change Its Layer Symmetry. *Environ. Sci. Technol.* **2016**, *50* (4), 1750−1758.

(22) Hinkle, M. A. G.; Flynn, E. D.; Catalano, J. G. Structural response of phyllomanganates to wet aging and aqueous Mn(II). *Geochim. Cosmochim. Acta* **2016**, *192*, 220−234.

(23) Hinkle, M. A. G.; Dye, K. G.; Catalano, J. G. Impact of Mn(II)-Manganese Oxide Reactions on Ni and Zn Speciation. *Environ. Sci. Technol.* **2017**, *51* (6), 3187−3196.

(24) Droz, B.; Dumas, N.; Duckworth, O. W.; Peña, J. A Comparison of the Sorption Reactivity of Bacteriogenic and Mycogenic Mn Oxide Nanoparticles. *Environ. Sci. Technol.* **2015**, *49* (7), 4200−4208.

(25) Lefkowitz, J. P.; Elzinga, E. J. Structural alteration of hexagonal birnessite by aqueous Mn(II): Impacts on Ni(II) sorption. *Chem. Geol.* **2017**, *466*, 524−532.

(26) Elzinga, E. J. Reductive Transformation of Birnessite by Aqueous Mn(II). *Environ. Sci. Technol.* **2011**, *45*, 6366−6372.

(27) Elzinga, E. J.; Kustka, A. B. A Mn-54 Radiotracer Study of Mn Isotope Solid-Liquid Exchange during Reductive Transformation of Vernadite (δ-MnO$_2$) by Aqueous Mn(II). *Environ. Sci. Technol.* **2015**, *49*, 4310−4316.

(28) Lefkowitz, J. P.; Rouff, A. A.; Elzinga, E. J. Influence of pH on the reductive transformation of birnessite by aqueous Mn(II). *Environ. Sci. Technol.* **2013**, *47* (18), 10364−10371.

(29) Perez-Benito, J. F. Reduction of Colloidal Manganese Dioxide by Manganese(II). *J. Colloid Interface Sci.* **2002**, *248* (1), 130−135.

(30) Elzinga, E. J. ^{54}Mn Radiotracers Demonstrate Continuous Dissolution and Reprecipitation of Vernadite (δ-MnO$_2$) during Interaction with Aqueous Mn(II). *Environ. Sci. Technol.* **2016**, *50* (16), 8670−8677.

(31) Frierdich, A. J.; Spicuzza, M. J.; Scherer, M. M. Oxygen Isotope Evidence for Mn(II)-Catalyzed Recrystallization of Manganite (γ-MnOOH). *Environ. Sci. Technol.* **2016**, *50* (12), 6374−6380.

(32) Handler, R. M.; Frierdich, A. J.; Johnson, C. M.; Rosso, K. M.; Beard, B. L.; Wang, C.; Latta, D. E.; Neumann, A.; Pasakarnis, T.; Premaratne, W. A. P. J.; Scherer, M. M. Fe(II)-catalyzed recrystallization of goethite revisited. *Environ. Sci. Technol.* **2014**, *48*, 11302−11311.

(33) Frierdich, A. J.; Helgeson, M.; Liu, C.; Wang, C.; Rosso, K. M.; Scherer, M. M. Iron atom exchange between hematite and aqueous Fe(II). *Environ. Sci. Technol.* **2015**, *49*, 8479−8486.

(34) Frierdich, A. J.; Luo, Y.; Catalano, J. G. Trace element cycling through iron oxide minerals during redox-driven dynamic recrystallization. *Geology* **2011**, *39*, 1083−1086.

(35) Newville, M. IFEFFIT: interactive EXAFS analysis and FEFF fitting. *J. Synchrotron Radiat.* **2001**, *8*, 322−324.

(36) Ravel, B.; Newville, M. ATHENA, ARTEMIS, HEPHAESTUS: data analysis for X-ray absorption spectroscopy using IFEFFIT. *J. Synchrotron Radiat.* **2005**, *12*, 537−541.

(37) Kohler, T.; Armbruster, T.; Libowitzky, E. Hydrogen Bonding and Jahn−Teller Distortion in Groutite,α-MnOOH, and Manganite,γ-MnOOH, and Their Relations to the Manganese Dioxides Ramsdellite and Pyrolusite. *J. Solid State Chem.* **1997**, *133* (2), 486−500.

(38) Ankudinov, A. L.; Ravel, B.; Rehr, J. J.; Conradson, S. D. Real-space multiple-scattering calculation and interpretation of x-ray absorption near-edge structure. *Phys. Rev. B: Condens. Matter Mater. Phys.* **1998**, *58*, 7565−7576.

(39) Frierdich, A. J.; Beard, B. L.; Rosso, K. M.; Scherer, M. M.; Spicuzza, M. J.; Valley, J. W.; Johnson, C. M. Low temperature, non-stoichiometric oxygen-isotope exchange coupled to Fe(II)-goethite interactions. *Geochim. Cosmochim. Acta* **2015**, *160*, 38−54.

(40) Bochatay, L.; Persson, P.; Sjöberg, S. Metal Ion Coordination at the Water−Manganite (γ-MnOOH) Interface. *J. Colloid Interface Sci.* **2000**, *229* (2), 584−592.

(41) Duckworth, O. W.; Sposito, G. Siderophore−manganese(III) interactions II. Manganite dissolution promoted by desferrioxamine B. *Environ. Sci. Technol.* **2005**, *39* (16), 6045−6051.

(42) Shannon, R. D. Revised effective ionic radii and systematic studies of interatomic distances in halides and chalcogenides. *Acta Crystallogr., Sect. A: Cryst. Phys., Diffr., Theor. Gen. Crystallogr.* **1976**, *32*, 751−767.

(43) Bricker, O. Some stability relations in the system Mn-O2-H2O at 25°C and one atmosphere total pressure. *Am. Mineral.* **1965**, *50*, 1296−1354.

(44) Hem, J. D. Redox processes at surfaces of manganese oxide and their effects on aqueous metal ions. *Chem. Geol.* **1978**, *21* (3−4), 199−218.

(45) Hem, J. D.; Lind, C. J. Nonequilibrium models for predicting forms of precipitated manganese oxides. *Geochim. Cosmochim. Acta* **1983**, *47* (11), 2037−2046.

(46) Murray, J. W.; Dillard, J. G.; Giovanoli, R.; Moers, H.; Stumm, W. Oxidation of Mn(II): Initial mineralogy, oxidation state and ageing. *Geochim. Cosmochim. Acta* **1985**, *49* (2), 463−470.

(47) Peacock, C. L.; Sherman, D. M. Sorption of Ni by birnessite: Equilibrium controls on Ni in seawater. *Chem. Geol.* **2007**, *238*, 94−106.

(48) Johnson, J. E.; Webb, S. M.; Ma, C.; Fischer, W. W. Manganese mineralogy and diagenesis in the sedimentary rock record. *Geochim. Cosmochim. Acta* **2016**, *173*, 210−231.

(49) Maynard, J. B. The Chemistry of Manganese Ores through Time: A Signal of Increasing Diversity of Earth-Surface Environments. *Econ. Geol. Bull. Soc. Econ. Geol.* **2010**, *105*, 535−552.

SUPPORTING INFORMATION FOR:

Recrystallization of Manganite (γ-MnOOH) and Implications for Trace Element Cycling

Tobias Hens[1], Joël Brugger[1], Susan A. Cumberland[1-2], Barbara Etschmann[1], Andrew J. Frierdich[1,*]

[1]School of Earth, Atmosphere & Environment, Monash University, Clayton, VIC 3800, Australia
[2]Australian Synchrotron, Clayton, VIC 3168, Australia

*Corresponding author: Tel.: (+61) 03 9905 4899; Fax: (+61) 03 9905 4903; E-mail:
andrew.frierdich@monash.edu

Number of Pages: 10
Number of Figures: 3
Number of Tables: 3

S1

42

SECTION S1: SAMPLE CHARACTERIZATION

XRD patterns were collected over a range of 15 to 45° 2θ with a 1 s dwell time, a step size of 0.03° 2θ, and sample stage rotation set to 15 rpm. Powder samples were deposited on a zero background sample holder (SiO_2) as an ethanol slurry with continuous mixing to minimize preferred orientation of particles. Measurements were conducted using Ni filtered Cu K_α radiation, a LynxEye XE strip detector, a 0.5° anti-scatter slit, and a 2.5° incident Soller slit. The X-ray generator tube voltage and current were set to 40 kV and 40mA. XRD analyses show that the synthesized starting materials used in all experiments are manganite and Ni-substituted manganite, respectively (Figure S1). Samples, which have been reacted with $Mn(II)_{aq}$- and $Ni(II)_{aq}$-bearing solutions for up to 51 days, do not show any significant phase transformation. Ni-substituted manganite shows minor peak broadening at ~26° 2θ due to increased structural Ni content. A minor peak at ~21° 2θ in all synthesized samples that has been detected prior to and after the time series experiment is consistent with a groutite (α-Mn(III)OOH) impurity. Although great care was taken during placement of the powder on the zero background holder, preferred orientation of the particles was not completely prevented as depicted at ~40° 2θ in all collected patterns.

SECTION S2: DETERMINATION OF MANGANESE OXIDATION STATE

Iodometric titration was performed to determine the Mn average oxidation state (Mn AOS) of the synthetic manganite starting material and Ni-substituted manganite.[1] Titrations were carried out in triplicate following a modified version of the previously published procedure by Birkner et al. (2013)[2] Briefly, to a 100 mL Erlenmeyer flask, 50 mL of water, 10 mL of NaI excess reagent solution, and 5 mL of 2 M H_2SO_4 were added. The solution was degassed with N_2 for 5 minutes followed by the addition of 30 mg of synthetic manganite powder. Following the complete dissolution of the sample, the solution was titrated with a $Na_2S_2O_3$ solution. Results were averaged and Mn AOS calculated as shown in equations 1 and 2 below:

$$Mn\ AOS = 4*(1-\alpha) + 3*\alpha \tag{1}$$

where α is the mole fraction of Mn(III) and is equal to:

$$\alpha = 2 - mol\ Na_2S_2O_3 / mol\ Mn \tag{2}$$

The results of the titrations of manganite and Ni-substituted manganite yield a Mn average oxidation state value of 2.98 (± 0.03) and 2.95 (± 0.03), respectively. These values support the results of the XRD analyses, indicating that the starting materials are indeed Mn(III) oxides.

FIGURES
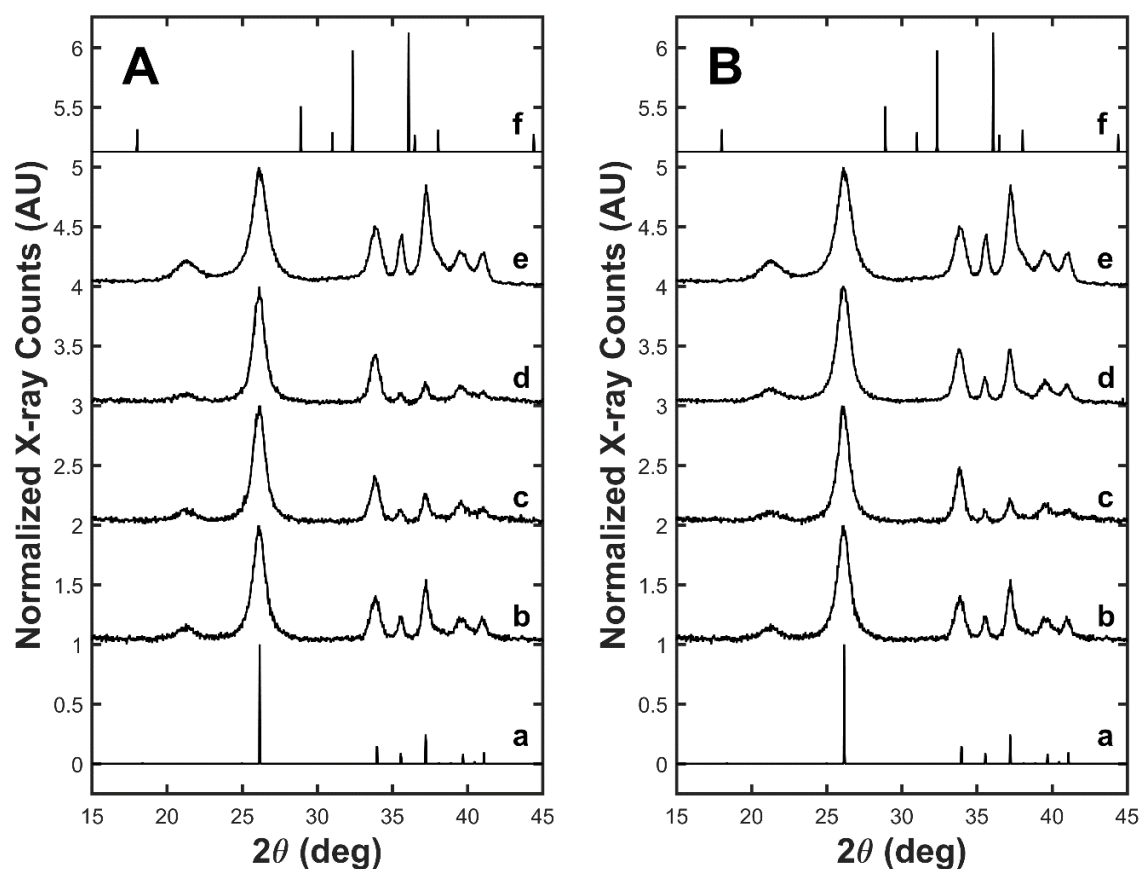
Figure S1. XRD patterns for solid samples at pH 5.5 (A) and pH 7.5 (B) compared with mineral standards. Peak positions and relative intensities for (a) manganite and (f) hausmannite. (b) Starting material (γ-Mn(III)OOH) (t=0). (c) Solid fraction after reaction in Mn(II)-free fluid for 51 days and (d) 1 mM aqueous Mn(II) fluid for 51 days. (e) Ni-substituted manganite (t=0). The peak located at ~21° 2Θ is consistent with a groutite (α-Mn(III)OOH) impurity.
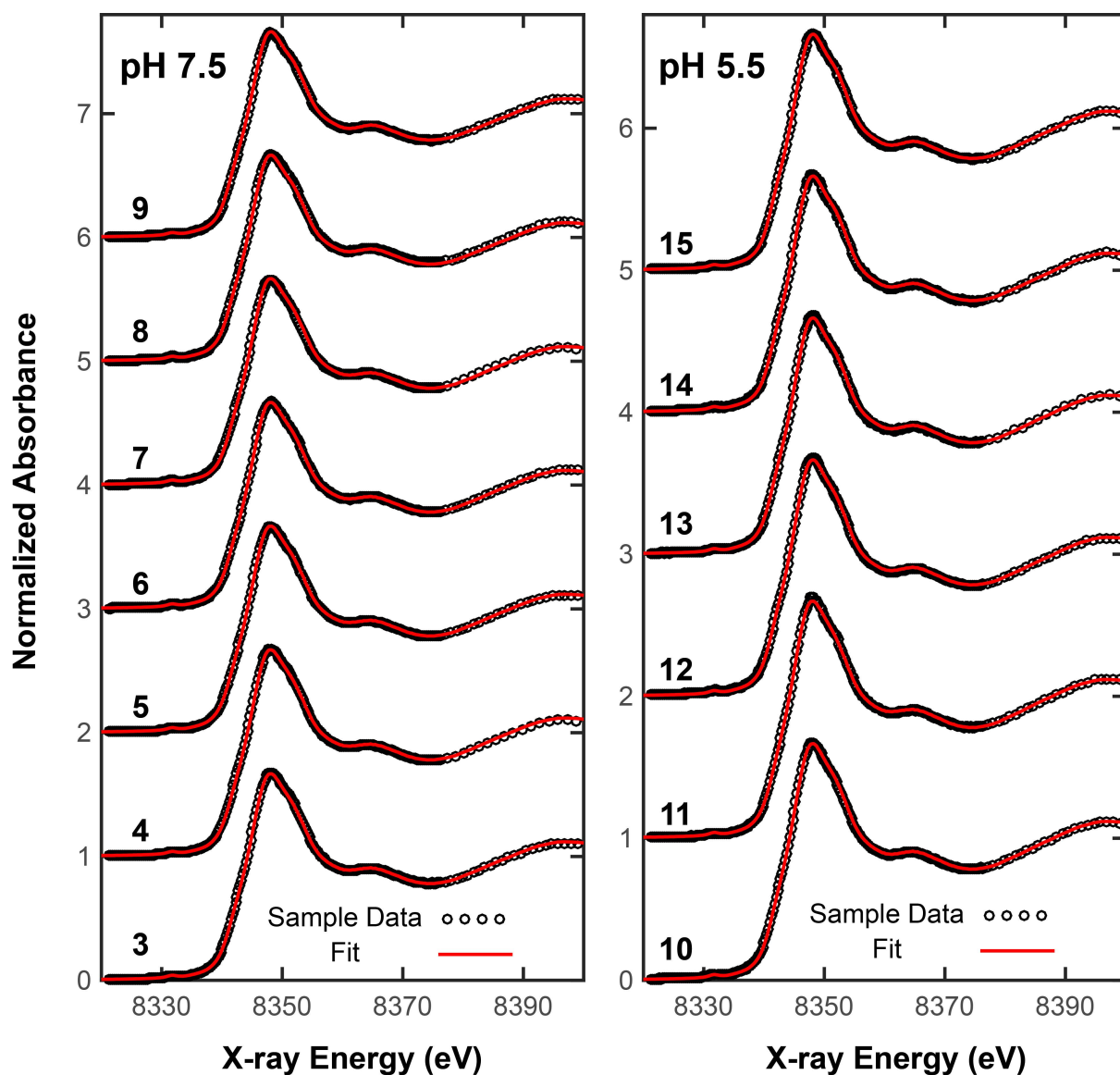
Figure S2. Graphical representation of the linear combination fits outlined in Table 2 of the main manuscript for XAS experiments conducted at pH 7.5 and pH 5.5.
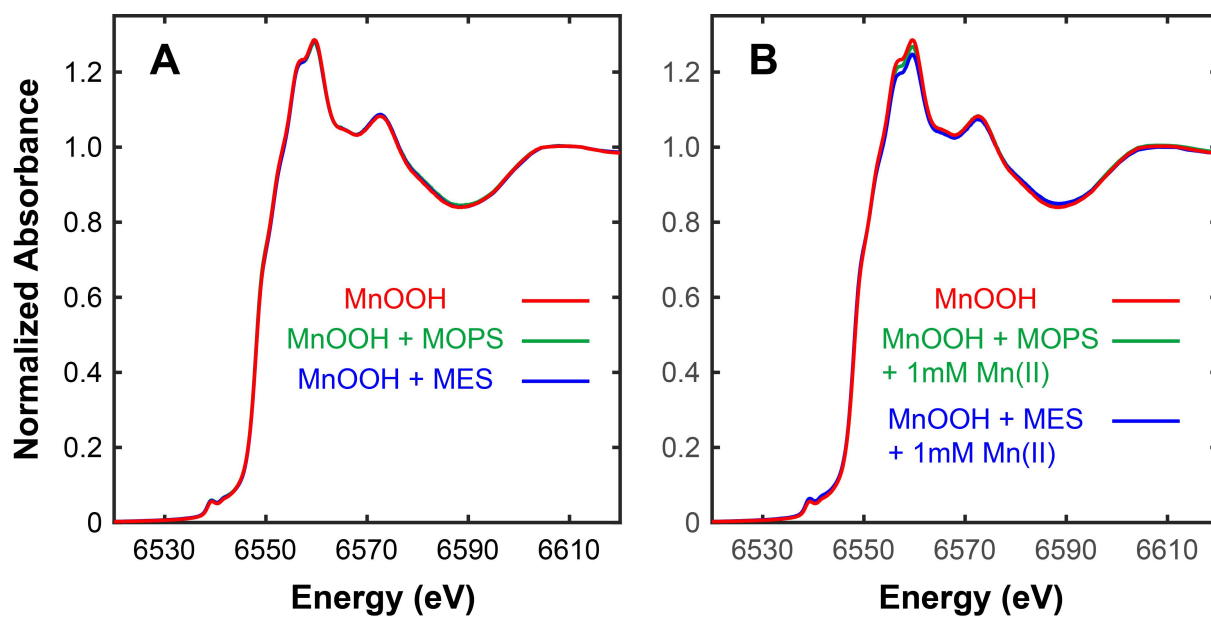
Figure S3. (A) Mn K-edge XANES scans for the MnOOH starting material, MnOOH reacted with 10 mM MOPS at pH 7.5 for 51 d, and MnOOH reacted with 10 mM MES at pH 5.5 for 51 d. **(B)** Same conditions as in (A) except reactions also contained 1 mM Mn(II)$_{aq}$.

Table S1. Dissolved Mn and Ni concentrations during XAS experiments (Table 2, main manuscript) for manganite reacted with Ni(II)$_{aq}$ in the presence and absence of Mn(II)$_{aq}$.

Experiment #	Time (d)	[Mn(II)] (μM)	[Ni(II)] (μM)
pH 7.5 – no Mn(II)$_{aq}$			
NA	0	0.24(3)[a]	211.4(7)
1	1	1.48(5)	10.7(2)
2[b]	7	0.6(3)	5(2)
3	51	0.51(8)	4.1(4)
pH 7.5 – 0.2 mM Mn(II)$_{aq}$			
NA	0	216(6)	205(3)
4	1	13.2(6)	16(1)
5	7	3.3(1)	6.2(2)
6	51	3.68(6)	8.8(3)
pH 7.5 – 1 mM Mn(II)$_{aq}$			
NA	0	1048(8)	212(1)
7	1	576(4)	14(1)
8	7	558(21)	12.05(5)
9	51	516(10)	20.6(1)
pH 5.5 – no Mn(II)$_{aq}$			
NA	0	0	212(1)
10	1	272(1)	187.1(6)
11	7	278.1(9)	182(1)
12	51	341(4)	175(2)
pH 5.5 – 1 mM Mn(II)$_{aq}$			
NA	0	998(6)	208(9)
13	1	1165(17)	191(1)
14	7	1140(6)	186(7)
15	51	1109(26)	180(5)

[a] Numbers in parentheses represent the uncertainty in the last digit at the 95% confidence level.
[b] Not measured by XAS.
NA = not applicable.

Table S2. Summary of Mn and Ni concentrations, and Ni isotope fractions, for experiments with ^{62}Ni-enriched aqueous Ni(II) reactions with nickel-substituted manganite in the presence and absence of Mn(II)$_{aq}$ in pH 5.5 and 7.5 fluid.

Time (d)	[Mn(II)]$_{aq}$ (μM)	[Ni(II)]$_{aq}$ (μM)	f ^{58}Ni	f ^{60}Ni	f ^{62}Ni	% Ni Exchange[a]
pH 5.5 – 0 mM Mn(II)$_{aq}$						
0	2(3)[b]	65(2)	0.008(1)	0.0132(5)	0.9756(5)	0
1	242(3)	47.9(7)	0.048(1)	0.030(1)	0.917(2)	10.2(3)
7	253(18)	46(7)	0.055(6)	0.033(2)	0.908(8)	12(1)
51	318(20)	44(2)	0.066(2)	0.037(1)	0.892(3)	15.1(5)
pH 5.5 – 0.2 mM Mn(II)$_{aq}$						
0	228(2)	65(1)	0.008(1)	0.0123(2)	0.9766(2)	0
1	429(11)	58.3(4)	0.047(2)	0.029(1)	0.920(2)	9.7(4)
7	452(22)	56(3)	0.055(2)	0.0316(4)	0.909(3)	11.7(5)
51	498(10)	53.0(2)	0.068(3)	0.03951(5)	0.888(3)	15.8(6)
pH 5.5 – 1 mM Mn(II)$_{aq}$						
0	996(132)	59(7)	0.0074(2)	0.0124(2)	0.9768(2)	0
1	1166(61)	60(5)	0.049(3)	0.0297(2)	0.918(2)	9.3(4)
7	1150(15)	59.0(1)	0.058(2)	0.0345(5)	0.903(2)	11.8(5)
51	1155(22)	56.7(9)	0.077(6)	0.041(1)	0.878(6)	16(1)
pH 7.5 – 0 mM Mn(II)$_{aq}$						
0	0.025(1)	66.9(5)	0.0065(1)	0.01183(4)	0.9784(1)	0
1	0.6(5)	0.7(5)	0.034(2)	0.024(1)	0.938(4)	6.9(6)
7	0.45(7)	0.62(8)	0.041(1)	0.027(1)	0.929(1)	8.8(2)
51	3(3)	0.5(1)	0.060(2)	0.0355(3)	0.901(2)	14.1(4)
pH 7.5 – 0.2 mM Mn(II)$_{aq}$						
0	236(3)	68.3(9)	0.00654(4)	0.0118(1)	0.9784(1)	0
1	3.4(2)	1.4(1)	0.034(2)	0.024(1)	0.938(3)	7.1(6)
7	2.4(7)	1.0(2)	0.045(2)	0.029(1)	0.922(3)	10.3(5)
51	10(3)	1.0(2)	0.08(2)	0.04(1)	0.87(3)	21(8)
pH 7.5 – 1 mM Mn(II)$_{aq}$						
0	1189(31)	71(2)	0.0056(2)	0.01168(5)	0.9795(3)	0
1	355(55)	2.1(4)	0.0480(4)	0.030(1)	0.918(1)	11.7(2)
7	350(11)	1.62(7)	0.0649(9)	0.038(1)	0.893(2)	16.9(3)
51	398(31)	1.35(7)	0.1024(2)	0.0538(2)	0.839(1)	29.5(1)

[a] Ni exchange calculated from eq 2 (main manuscript) using measured f^{62}Ni values for Ni(II)$_{aq}$.
[b] Numbers in parentheses represent the uncertainty in the last digit at the 95% confidence level. NA = not applicable.

Table S3. Summary of Mn and Ni concentrations, and Ni isotope fractions, for the controls of the Ni isotope tracer experiments. Reported are the $Mn(II)_{aq}$ and $Ni(II)_{aq}$ concentrations for Ni-substituted MnOOH-free reactions at pH 7.5 and the concentrations for $Mn(II)_{aq}$- and $Ni(II)_{aq}$-free controls at pH 7.5 and pH 5.5, respectively.

Time (d)	$[Mn(II)]_{aq}$ (μM)	$[Ni(II)]_{aq}$ (μM)	f ^{58}Ni	f ^{60}Ni	f ^{62}Ni	% ^{62}Ni Exchange
pH 7.5 – Mn(II)$_{aq}$ + Ni(II)$_{aq}$						
0	1189(31)[a]	71(2)	0.0056(2)	0.01168(5)	0.9795(3)	NA
1	804(135)	45.2(7)	0.00663(6)	0.01161(3)	0.9787(1)	NA
7	914(19)	47.7(6)	0.00662(6)	0.01166(4)	0.9786(1)	NA
51	950(6)	49.5(1)	0.00660(2)	0.01158(9)	0.9788(1)	NA
pH 7.5 – Ni-substituted MnOOH alone						
0	0	0	NA	NA	NA	NA
1	0.91(3)	0.085(2)	0.62(5)	0.27(1)	0.09(7)	NA
7	0.328(8)	0.054(4)	0.64(1)	0.289(6)	0.05(2)	NA
51	2.6(2)	0.11(3)	0.61(2)	0.27(1)	0.09(4)	NA
pH 5.5 – Ni-substituted MnOOH alone						
0	0	0	NA	NA	NA	NA
1	245(5)	2.76(1)	0.642(9)	0.290(1)	0.05(1)	NA
7	281.5(2)	3.079(7)	0.646(2)	0.290(2)	0.049(3)	NA
51	397(30)	4.14(3)	0.646(1)	0.290(1)	0.0510(2)	NA

[a] Numbers in parentheses represent the uncertainty in the last digit at the 95% confidence level. NA = not applicable.

REFERENCES

1.   Murray, J. W.; Balistrieri, L. S.; Paul, B., The oxidation state of manganese in marine sediments and ferromanganese nodules. *Geochimica et Cosmochimica Acta* **1984,** *48*, (6), 1237-1247.

2.   Birkner, N.; Nayeri, S.; Pashaei, B.; Najafpour, M. M.; Casey, W. H.; Navrotsky, A., Energetic basis of catalytic activity of layered nanophase calcium manganese oxides for water oxidation. *Proceedings of the National Academy of Sciences* **2013,** *110*, (22), 8801-8806.

3.   Kohler, T.; Armbruster, T.; Libowitzky, E., Hydrogen Bonding and Jahn-Teller Distortion in Groutite, α-MnOOH, and Manganite, γ-MnOOH, and Their Relations to the Manganese Dioxides Ramsdellite and Pyrolusite. *J. Solid State Chem.* **1997,** *133*, (2), 486-500.

S10

Chapter 3

Nickel Exchange Between Aqueous Ni(II) and Synthetic Phyllomanganates

54

1. Abstract
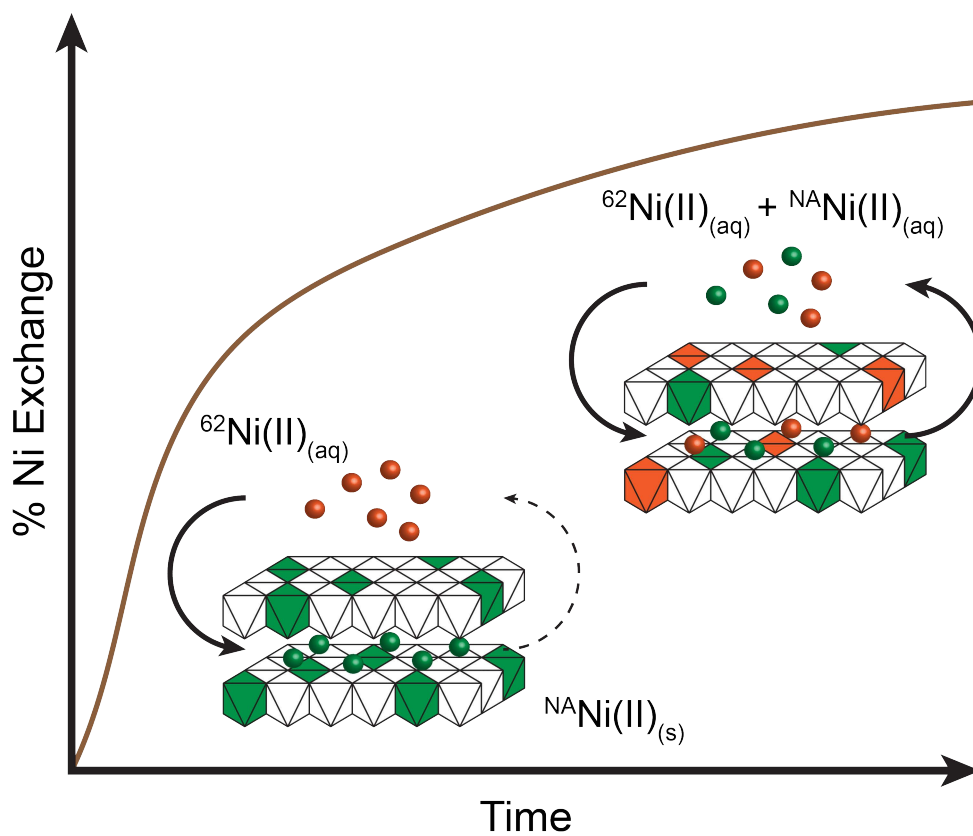
Manganese oxide minerals, such as phyllomanganates, are important host phases for metals (e.g., Ni) in deep-sea ferromanganese nodules and crusts, soils, and sediments. During (bio)geochemical Mn redox cycling, Mn(III,IV) oxides can undergo recrystallization which is catalyzed by aqueous Mn(II) ($Mn(II)_{aq}$). The induced cycling of structurally incorporated metals in these Mn oxides remains poorly constrained. Here, we investigate Ni exchangeability between $^{62}Ni(II)$-enriched $Ni(II)_{aq}$ and three Ni-substituted phyllomanganates (vernadite, c-disordered H^+-birnessite, and triclinic birnessite). The effects of different mineralogical properties are examined during reactions in 1 mM $Mn(II)_{aq}$ and in Mn(II)-free solutions under variable pH conditions (pH 5.5 and 7.5) over time. Our results demonstrate that up to 29% of incorporated Ni is exchangeable with the fluid in some samples after 14 days. While variable Mn(III) content and layer vacancies of phyllomanganates appear to be an impacting factor for Ni exchange, prevalent mechanisms of Ni cycling are likely a combination of bulk reductive transformation and $Mn(II)_{aq}$-catalyzed recrystallization. The fact that structurally incorporated Ni is cycled between solid and fluid phases indicates a labile behavior of Ni, which has implications for Ni speciation and mobility in terrestrial and marine environments.

2. Introduction

Layer-type manganese oxides (phyllomanganates) occur as nanoparticulate, poorly crystalline, and highly reactive mineral phases in aquatic environments, where they exert strong control on trace metal concentrations and speciation, bioavailability of contaminants, and micronutrients in seawater (Clement et al., 2009; Dick et al., 2009; Grangeon et al., 2010; Post, 1999; Saratovsky et al., 2006; Tan et al., 2010; Villalobos et al., 2005a; Villalobos et al., 2003). These minerals consist of layered Mn(III,IV) octahedral sheets of variable sheet stacking order, symmetry, vacancy density, and Mn(III) content, and are among the strongest naturally occurring metal scavengers. For instance, they constitute the predominant Mn oxide phases in deep-sea ferromanganese nodules and crusts (Bargar et al., 2009; Burns and Burns, 1977; Gadde and Laitinen, 1974; Goldberg, 1954; Hein and Koschinsky, 2014; Post, 1999; Usui and Terashima, 1997). Their strong scavenging capacity for dissolved metals result from the presence of vacancy sites, which induce negative layer charges that require compensation (Hinkle et al., 2017; Manceau et al., 1997; Peacock, 2009; Peacock and Sherman, 2007a; Peacock and Sherman, 2007b; Silvester et al., 1997; Toner et al., 2006). Dissolved cations (e.g., Ni(II)$_{aq}$) can provide charge neutralization along basal planes by adsorption to vacancy sites as well as complexation to octahedral edge sites and structural incorporation into sheets, as the accessible interlayer region between stacked sheets allows for interaction between aqueous metal species and phyllomanganates (Manceau et al., 2007; Post, 1999; Tebo et al., 2004; Villalobos et al., 2005b).

In natural systems, phyllomanganates are formed by precipitation following biologically-mediated oxidation of Mn(II) and Mn(III) to Mn(IV) as part of biogeochemical redox cycling (Santelli et al., 2011; Spiro et al., 2009; Tebo et al., 2004; Tebo et al., 2005), due to abiotic Mn(II) oxidation being kinetically slow (e.g., Bargar et al., 2000; Morgan, 2005; Nealson et al., 1988). Similarly, phyllomanganates can serve as final electron acceptors during microbial respiration (Lovely, 2000; Myers and Nealson, 1988), which can lead to reductive dissolution of Mn(IV) oxides and subsequent release of dissolved Mn(II) (Mn(II)$_{aq}$) into seawater and pore water. Consequently, phyllomanganates are in contact with Mn(II)$_{aq}$-bearing solution at redox interfaces and other regions of active Mn cycling, such as oxic regions, hydrothermal vents, and stratified soils (e.g., Graybeal and Heath, 1984; Tebo et al., 2004; Tebo et al., 2005; Van Cappellen et al., 1998), where abiotic back-reactions between Mn(III,IV) oxides and Mn(II)$_{aq}$ are common (Mandernack et al., 1995; Santelli et al., 2011; Tebo et al., 2004; Villalobos et al., 2003).

At low Mn(II)$_{aq}$ concentrations, adsorption of Mn(II) on the mineral surface and subsequent incorporation can be a major pathway for Mn(III)-enrichment, as layer- and interlayer Mn(III) contents increase through Mn(II)-Mn(IV) comproportionation reactions, which in turn decreases the average oxidation state (Bargar et al., 2009; Bargar et al., 2005; Frierdich et al., 2011; Learman et al., 2011; Mandernack et al., 1995; Mann et al., 1988; Pecher et al., 2003; Toner et al., 2005). Filling or blocking of sheet vacancies by Mn(III) can, however, limit the uptake capacity of trace elements (e.g., Ni) by these phases (Droz et al., 2015; Hinkle et al., 2017; Lefkowitz and Elzinga, 2017). While Mn(II) may induce modifications to the phyllomanganate sheet structure and layer stacking, depending on pH, reaction time, and initial mineral composition (Bargar et al., 2005; Hinkle et al., 2016; Zhao et al., 2016; Zhu et al., 2010a), mineral phase transformations do not occur at lower Mn(II):Mn(IV) ratios (Elzinga, 2011; Hinkle et al., 2017; Hinkle et al., 2016; Lefkowitz et al., 2013; Zhao et al., 2016).

Phyllomanganates may, however, exhibit reductive phase transformation when subjected to high concentrations of Mn(II)$_{aq}$, as a result of net Mn(II) oxidation and Mn(IV) reduction (Elzinga, 2011; Elzinga and Kustka, 2015; Lefkowitz et al., 2013; Perez-Benito, 2002). During these phase transformations near-complete exchange between dissolved and solid-phase Mn, driven by substrate recrystallization, has been observed (Elzinga and Kustka, 2015). Elzinga (2016) has, furthermore, shown that even in the absence of observable phase transformations, Mn(II)$_{aq}$ actively catalyzes phyllomanganate recrystallization through coupled comproportionation (Mn(II) + Mn(IV) $\rightarrow$ 2Mn(III)) and disproportionation (2Mn(III) $\rightarrow$ Mn(II) + Mn(IV)) of Mn species.

Similarly, results of our recent investigation on the effects of Mn(II)$_{aq}$-catalyzed recrystallization of Ni-substituted manganite (γ-Mn(III)OOH) indicate that Ni cycling between solid and solution occurs through coupled disproportionation-comproportionation (DP-CP) and electron transfer-atom exchange (ET-AE) reactions mediated by Mn(II)$_{aq}$ (Hens et al., 2018). The prevailing mechanism was shown to be pH-dependent, with DP-CP likely being the dominant process at lower pH (5.5) and ET-AE at higher pH (7.5), while no significant manganite phase transformations were observed. Thus, we hypothesize that interactions between phyllomanganates and Mn(II)-bearing fluids may lead to similar mineral-fluid repartitioning of structurally compatible trace metals and contaminants associated with these Mn oxide mineral phases. This may have implications for contaminant mobility in natural environments.

In this study, the effects of Mn(II)$_{aq}$ on Ni(II) cycling between aqueous solutions and Ni-substituted birnessite-type phyllomanganates with varying degrees of sheet vacancies and Mn(III) content are investigated. The following three phyllomanganates were prepared: (i) the synthetic analogue (δ-MnO$_2$) of vernadite [(Ca,Na,K)(Mn^{4+},□)O$_2$·nH$_2$O] (Villalobos et al., 2006) with turbostratic stacking and high vacancy content (denoted by □), (ii) c-disordered H$^+$-birnessite [(Ca,Na,K)(Mn^{4+}, Mn^{3+},□)O$_2$·nH$_2$O]) with turbostratic stacking, Mn(III) substitutions, and vacancies (Lanson et al., 2000; Silvester et al., 1997), (iii) triclinic birnessite [(Ca,Na,K)(Mn$^{4+}_x$, Mn$^{3+}_{1-x}$)O$_2$·nH$_2$O]) with ordered layer-stacking, a high degree of Mn(III) substitutions, and few vacancies (Drits et al., 1997; Lopano et al., 2007; Post et al., 2002; Post and Veblen, 1990).

Mineral phase characterization was achieved by wet-chemistry analytical techniques (inductively coupled plasma – mass spectrometry (ICP-MS), iodine titrations to determine the average Mn oxidation state) and X-ray diffraction. Following a similar experimental approach as described in our other study (Hens et al., 2018) and Chapter 4, the amount of Ni associated with the solid phase that exchanges with solution was subsequently quantified as a function of Mn(II)$_{aq}$ concentration, pH, and reaction time, after phyllomanganates were subjected to ^{62}Ni-enriched Ni(II)$_{aq}$ solutions and variable concentrations of Mn(II)$_{aq}$.

3. Materials and Methods

3.1. Syntheses of Ni-substituted Phyllomanganates

Variants of vernadite (δ-MnO$_2$), c-disordered H$^+$-birnessite, and triclinic birnessite, coprecipitated with Ni(II) (hereon vernadite, HexB, and TriB, respectively), were synthesized following previously published methods. Vernadite was prepared employing a modified approach of the redox method described by Villalobos et al. (2003). Briefly, a solution of 4.00 g KMnO$_4$ in 128 mL deionized $\geq$18.2MΩ·cm water (hereon water) was added to a solution of 2.50 g NaOH in 144 mL water over approximately five minutes while stirring vigorously. This was followed by the addition of a solution containing 7.51 g MnCl$_2$·4H$_2$O in 128 mL water mixed with 1.28 mL of 1 M NiCl$_2$·6H$_2$O over approximately 35 min to yield partial Ni substitution. After the resulting suspension settled for four hours, pH was checked and found to be around pH 7.0. The suspension was centrifuged (~10,000 g) to remove the initial supernatant and then subjected to six 1 M NaCl washes, followed by six water washes with the last one shaken overnight.

HexB was synthesized following the c-disordered H^+-birnessite synthesis method detailed in the work of Villalobos et al. (2003). This procedure is similar to the vernadite synthesis described above including the number of NaCl- and water washes. In this case, however, 5.00 g of $KMnO_4$ in 160 mL water, 3.67 g NaOH in 180 mL water, and a solution consisting of 11.63 g $MnCl_2 \cdot 4H_2O$ in 160 mL water mixed with 1.80 mL of 1 M $NiCl_2 \cdot 6H_2O$, were used. The pH of the resulting suspension was found to be pH 3.0 after synthesis and readjusted to pH 8.0 following the final water wash.

Similar to what has been described by Hinkle et al. (2016), TriB was prepared following the procedures for Na-birnessite synthesis procedure outlined in Lopano et al. (2007), based on the methods described by Post and Veblen (1990) and (Golden et al., 1987; 1986). Briefly, solutions of 55.0 g of NaOH in 250 mL water and 200 mL of a 0.5 M $MnCl_2 \cdot 4H_2O$ mixed with 2.0 mL of 1 M $NiCl_2 \cdot 6H_2O$ were chilled separately to 5 °C in an ice bath while air was vigorously bubbled through the Mn(II)-Ni(II) solution. The NaOH solution was then added slowly to the Mn(II)-Ni(II) solution over approximately 3 minutes. The resulting suspension was kept around 5 °C in the ice bath and bubbled with air for 22 hours in a fume hood. Centrifugation to remove the basic supernatant was followed by several washes with water until the pH of the suspension was below 10.0.

3.2. Mineral Phase Characterization

After synthesis, aliquots of the suspensions were taken for mineral phase characterization. Firstly, iodine titrations were conducted for all synthesis products to determine the Mn average oxidation state (AOS) (Birkner et al., 2013; Murray et al., 1984). Briefly, 50 mL of chilled water, 10 mL of a NaI excess solution containing 70 g NaI in 100 mL water, and 5 mL of 2 M H_2SO_4 were added to an Erlenmeyer flask. The equivalent of 30 mg of Mn oxide sample was added to the flask and dissolved while stirring. The resulting solution was titrated with a standardized $Na_2S_2O_3$ solution. Titrations were repeated four times for each synthesis product to calculate the Mn AOS. Secondly, aliquots of vernadite, HexB, and TriB were dissolved in 5 mL of 5 M HCl at 70 °C until complete dissolution and analyzed by inductively coupled plasma – mass spectrometry (ICP-MS) to yield Mn concentrations and mole percent of Ni substitution (Ni mol % = [moles Ni/(moles Ni + moles Mn)] x 100), respectively. Thirdly, substrate mineralogy was confirmed by X-ray powder diffraction as discussed in our previous work (Hens et al., 2018). Suspensions were oven-dried at 70 °C for 24 hours. The resulting powders were deposited on a zero background sample holder (SiO_2) following homogenization

with an agate mortar and pestle. XRD patterns were collected over a range of 5 to 75° 2θ with a dwell time of 1.5 s (vernadite, HexB) to 2 s (TriB), step size of 0.02° 2θ, and sample stage rotation set to 15 rpm. Measurements were conducted using Ni filtered Cu Kα radiation, a LynxEye XE strip detector, 0.5° anti-scatter slit, and 2.5° incident Soller slit with the X-ray tube voltage and current set to 40 kV and 40mA, respectively.

3.3. Ni Exchange Experiments

Ni isotope exchange experiments were conducted in an anaerobic chamber (≥97% $N_{2(g)}$ and 1.5-3.0% $H_{2(g)}$ atmosphere) with O_2 levels maintained at less than 1 ppm by continuous circulation of the atmosphere over Pd catalysts (Hens et al., 2018). Suspensions were purged with N_2 for 30 min prior to introduction into the chamber to remove residual O_2, followed by sparging with chamber atmosphere for 4 h. Labware, solutions, and samples were allowed to equilibrate with the anaerobic chamber atmosphere several days before use. Suspensions were stored in polypropylene bottles and used for experiments within the month.

Duplicate reactors were prepared for all experiments by pipetting aliquots of continuously stirred (300 rpm) phyllomanganate stock suspensions into 15 mL tubes. To yield a final vernadite-, HexB-, and TriB suspension concentration of 0.5 g L^{-1}, variable amounts of water were added to suspensions. This was followed by the addition of 1 mL of 0.1 M MOPS (3-(1-morpholino)propanesulfonic acid)/NaCl buffer solution or 1 mL of 0.1 M MES (2-(4-morpholino)ethanesulfonic acid)/NaCl solution to maintain solution pH of 7.5 or 5.5, respectively. Reactions were subsequently initiated by addition of 0.1 mL of 10 mM [62]Ni-enriched Ni(II) solution (prepared by dissolution of Ni^0, 98% [62]Ni, Isoflex, USA in 1 M HCl), and 0.1 mL of 100 mM $MnCl_2$ solution to yield a final Mn(II) concentration of 1 mM where appropriate. Small volumes (<0.1 mL) of 1 M NaOH were used for pH adjustments. Reactors were then wrapped in Al foil to avoid photochemical reactions and mixed by gyration until sampling. Between the time of reactor preparation and sampling solution pH was found to vary by less than 0.2 pH units. Filtration of samples aged 1-7 days was carried out with disposable filters (Thermo Scientific Choice 25 mm syringe filter, 0.22 μm PES), whereas the solid fraction of 14-day samples was recovered for XRD analysis with reusable syringe filter assemblies (Merck Millipore Swinnex with a 0.22 μm Durapore membrane). Filter membranes were dried inside the anaerobic chamber for ≥72 hours at room temperature and filtrates were acidified to 0.1 M HCl for ICP-MS analysis.

Monitoring of potential changes in dissolved metal concentrations and sample mineralogy unrelated to sample-Mn(II)$_{aq}$ interactions was achieved by preparation of buffered blanks and controls similar to what has been noted above. Sample-free blanks contained Ni(II)$_{aq}$ and Mn(II)$_{aq}$ solutions with concentrations identical to the Ni exchange experiments. To constrain observed buffer effects on phyllomanganates (i.e. reductive dissolution of Mn(IV) (e.g., Elzinga and Kustka, 2015; Hinkle et al., 2016), which may affect the interpretation of Ni exchange results, Mn(II)$_{aq}$- and Ni(II)$_{aq}$-free experiments with buffer concentrations identical to the Ni exchange experiments and unbuffered controls were prepared. One set consisted of sample suspensions in 10 mM buffer solution, whereas a second set of reactors contained unbuffered sample suspensions. While buffered controls were found to be within ±0.2 pH units of the set pH values following initial pH adjustment during reactor preparation, several unbuffered samples required daily adjustment of pH with aliquots of 0.01 M NaOH or HCl to keep drift within ±0.2 pH units.

3.4. Isotopic Measurements and Exchange Calculations

Ni isotope composition in filtrates, which changed over time as a result of ^{62}Ni exchange with natural abundance Ni in samples, were analyzed utilizing counts on the mass-58, mass-60, mass-61, mass-62, and mass-64 ICP-MS channels. Individual Ni isotope mole fractions (f^nNi) were calculated by dividing the counts per second (cps) of isotope n by the sum of the total Ni isotope cps as given in equation 1. The ^{64}Ni counts were excluded from the calculation of the Ni isotope fractions due to detection of an interference on the mass-64 counts at low Ni concentrations. For spiked samples ^{64}Ni counts amount to less than 0.3% (average) of the summated Ni counts and thus exert minor influence on the calculated Ni isotope fractions.

$$f^n Ni = \frac{^n cps}{^{58}cps + {}^{60}cps + {}^{61}cps + {}^{62}cps} \tag{1}$$

Calculation of percent Ni exchange in all experiments is achieved by using a homogeneous recrystallization model derived and discussed in Handler et al. (2014) as previously reported by (Hens et al., 2018):

$$\% \, Ni \, Exchange = \frac{N_{aq} \times (f_{aq}^i - f_{aq}^t)}{N_{mineral}^{Tot} \times (f_{aq}^t - f_{mineral}^i)} \times 100 \tag{2}$$

where N_{aq} represents the total moles of Ni(II)$_{aq}$, $N_{mineral}^{Tot}$ are the total moles of Ni(II) initially associated with each phyllomanganate sample, f_{aq}^i is the initial isotope composition of Ni(II)$_{aq}$, $f_{mineral}^i$ is the initial isotope composition of Ni in the phyllomanganate sample, and f_{aq}^t is the isotopic composition of Ni(II)$_{aq}$ at time t>0. As a result of the large isotopic enrichment of the ^{62}Ni tracer solution no correction for mass-dependent isotope fractionation is applied to f_{aq}^t since equilibrium and kinetic isotope fractionations exert a negligible influence. System mass balance values for all Ni isotopes were calculated as follows:

$$Mass\ balance = \frac{(f_{aq}^i \times N_{aq}) + (f_{mineral}^i \times N_{mineral}^{Tot})}{(N_{aq} + N_{mineral}^{Tot})} \tag{3}$$

4. Results

Three synthetic phyllomanganates – vernadite, HexB, and TriB– with a portion of Ni substituted for Mn, were characterized following preparation to evaluate Mn average oxidation states, amount of Ni substitution, and crystallographic structure, respectively. The samples were suspended in ^{62}Ni-enriched Ni(II)$_{aq}$ solutions in the absence or presence of Mn(II)$_{aq}$ to measure the amount of Ni bound within the mineral lattice that is exchanged with the fluid. This allows for an approximation of the degree by which the phyllomanganates undergo recrystallization in the presence of Mn(II)$_{aq}$.

4.1. Sample Characterization

Iodine titrations to determine Mn AOS revealed that vernadite is exclusively made up of Mn(IV) (Mn AOS of 4.07 ± 0.04). HexB has increased structural Mn(III) (Mn AOS 3.63 ± 0.03), whereas TriB has the lowest Mn AOS of 3.37 ± 0.02, indicating a large proportion of Mn to be Mn(III). The addition of variable volumes of Ni(II)$_{aq}$ during the syntheses procedures of vernadite, HexB, and TriB yielded partial Ni substitution for Mn of 1.74 mol% Ni, 1.11 mol% Ni , and 1.64 mol% Ni , respectively.

XRD patterns confirm that the synthesized products are indeed vernadite, hexagonal birnessite, and triclinic birnessite in accordance with previously published studies (Hinkle et al., 2017; Hinkle et al., 2016; Lopano et al., 2007; Villalobos et al., 2003). Vernadite and HexB patterns (Fig. 1) are defined by broad, low-angle reflections [(basal peaks; (001) and (002)] at ~12.6

(d ~ 7.0 Å) and ~25.1 degrees 2θ (d ~ 3.5 Å), indicating that few sheets are stacked (Grangeon et al., 2010; Lanson et al., 2000). High angle reflections [(20,11) and (02,31)] at ~37.2 (d ~ 2.4 Å) and ~66.5 degrees 2θ (d ~ 1.4 Å) with slightly asymmetric appearance are indicative of the turbostratic character of these phyllomanganates (Drits et al., 2007; Lanson et al., 2000; Villalobos et al., 2003; Webb et al., 2005). Furthermore, decreased intensity of the (20,11) reflection is visible in the HexB pattern, which serves as indicator for vacancy capping by Mn or other cations in the layered sheets (Grangeon et al., 2010; Grangeon et al., 2012; Villalobos et al., 2006). Similar to the vernadite and HexB patterns, the TriB pattern displays peaks at ~12.6 and ~25.1 degrees 2θ [(low-angle reflections; (001) and (002)] and at ~37.2 degrees 2θ (20,11), which are well-defined and interpreted as rotationally ordered sheet-stacking with a large coherent scattering domain along the c-axis (Brindley and Brown, 1980). Minor hausmannite impurities, which are remnants of incomplete aeration of the TriB precursor, are visible in this pattern at ~36.3, ~50.2, and ~65.6 degrees 2θ, respectively.
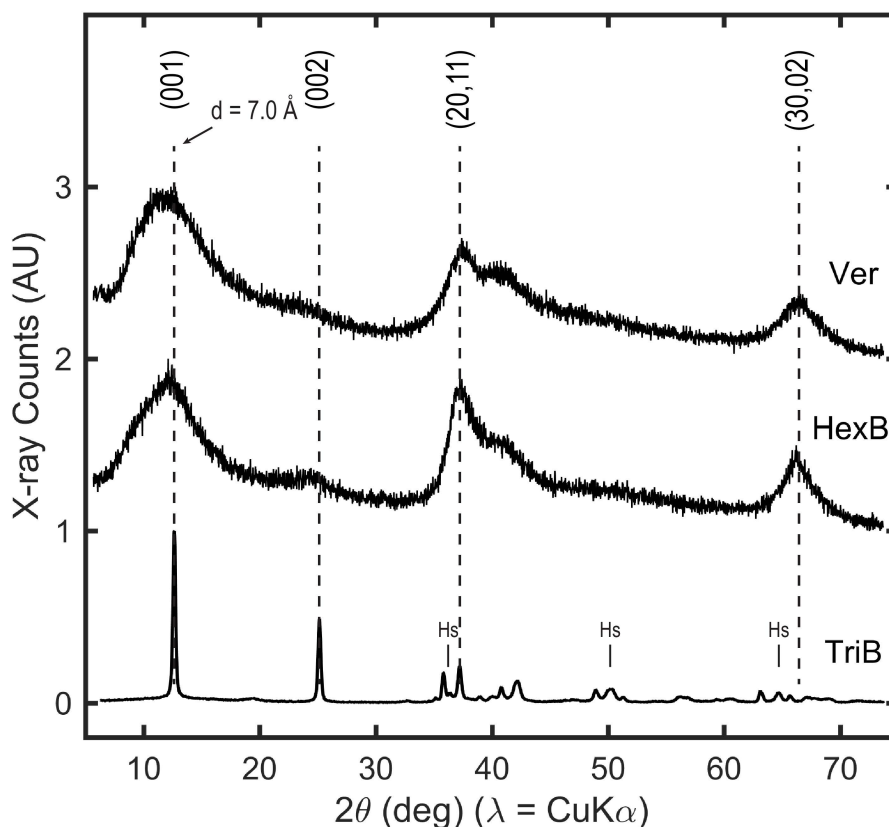
Fig. 1. XRD patterns depicting peak positions and relative intensities for synthesized Ni-substituted vernadite (Ver), hexagonal birnessite (HexB), and triclinic birnessite (TriB). Broad, low-angle reflections [(basal peaks; (001) and (002)] at ~12.6 (d ~ 7.0 Å) and ~25.1 degrees 2θ (d ~ 3.5 Å) and high angle reflections [(20,11) and (02,31)] at ~37.2 (d ~ 2.4 Å) and ~66.5 degrees 2θ (d ~ 1.4 Å) with slightly asymmetric appearance are indicative of the turbostratic character of phyllomanganates. Minor hausmannite impurities (denoted by Hs) are found in the triclinic birnessite synthesis product due to incomplete aeration during synthesis.

4.2. Ni Isotope Exchange Between Aqueous Ni(II) and Phyllomanganates

The exchange of structurally incorporated Ni with aqueous Ni(II) was examined during reactions between vernadite, HexB, and TriB. Mn and Ni concentrations as well as Ni fractions, which underwent compositional changes during reactions in the presence and absence of $Mn(II)_{aq}$, were analyzed at variable pH (pH 5.5 and pH 7.5) over time. Concentration changes of $Mn(II)_{aq}$ and $Ni(II)_{aq}$ for vernadite, HexB, and TriB are listed in Tables A1-3.

At pH 7.5, $Mn(II)_{aq}$ concentrations are small (<0.5µM) when no exogenous $Mn(II)_{aq}$ is added and $Ni(II)_{aq}$ concentrations decrease to around 1.5 µM (vernadite), 0.2 µM (HexB), and 15 µM (TriB) from the initial level of ~123 µM, respectively. When an initial $Mn(II)_{aq}$ concentration of ~1000 µM is added to the reactions, a decrease of Mn concentrations to around 356 µM (vernadite), 6 µM (HexB), and 599 µM (TriB), is observed. Here, $Ni(II)_{aq}$ concentrations similarly decrease to 43 µM (vernadite), 1.3 µM (HexB), and 33 µM (TriB), respectively.

At pH 5.5, $Mn(II)_{aq}$ concentrations increase over time to around 89 µM (vernadite), 168 µM (HexB), and 55 µM (TriB) when no exogenous $Mn(II)_{aq}$ is added, possibly due to disproportionation of Mn(III). $Ni(II)_{aq}$ concentrations decrease more subtly compared to pH 7.5 reactions to around 94 µM (vernadite), 72 µM (HexB), and 94 µM (TriB), from the initial level of ~126 µM, respectively. When a $Mn(II)_{aq}$ concentration of ~1000 µM is added to the reactions, a slight decrease of concentration to around 946 µM (vernadite), 921 µM (HexB), and 996 µM (TriB), is observed. Here, $Ni(II)_{aq}$ concentrations decrease slightly from the initial value to 121 µM (vernadite), 108 µM (HexB), and 73 µM (TriB), respectively (Tables A1-3).

The Ni isotope fractions similarly exhibit changes over the duration of the experiments since Ni exchange occurs between pools of different isotopic composition. Ni-substituted phyllomanganates are characterized by 'natural' ^{62}Ni isotope composition (f^{62}Ni = 0.047 (vernadite), f^{62}Ni =0.046 (HexB), and f^{62}Ni = 0.047 (TriB)), whereas the Ni(II) solution was initially enriched in ^{62}Ni (f^{62}Ni = 0.978) and hence depleted in other Ni isotope fractions (f^{58}Ni = 0.008, f^{60}Ni = 0.010, and f^{61}Ni = 0.003).

While sample-free blank reactions show that the isotopic fraction of ^{62}Ni ($f^{62}Ni_{aq}^{t}$) remains constant over time (Table A4, Fig. 2A-F), reactions with sample suspensions at pH 7.5 experience a decrease of $f^{62}Ni_{aq}^{t}$ in the absence of $Mn(II)_{aq}$ from the initial value of ~0.98 to about 0.89 (vernadite), 0.82 (HexB), and 0.94 (TriB), respectively (Tables A1-3).

In the presence of Mn(II)$_{aq}$, $f^{62}Ni_{aq}^t$ values decrease to about 0.88 (vernadite), 0.78 (HexB), and 0.93 (TriB) from the initial value of ~0.98 (Tables A1-3). Similar trends are observed at pH 5.5, where $f^{62}Ni_{aq}^t$ decreases in the absence of Mn(II)$_{aq}$ from the initial value of ~0.98 to about 0.89 (vernadite), 0.83 (HexB), and 0.90 (TriB), respectively (Tables A1-3). In the presence of Mn(II)$_{aq}$, $f^{62}Ni_{aq}^t$ values decrease to about 0.89 (vernadite), 0.84 (HexB), and 0.90 (TriB) from the initial value of ~0.98 (Tables A1-3). Decreasing values of $f^{62}Ni_{aq}^t$ are indicative for isotopic mixing as the dissolved Ni pool, which is initially highly enriched in ^{62}Ni, is being diluted by Ni isotopes of natural abundance composition over time. Mn(II)$_{aq}$ does not seem to exert a significant influence on Ni exchange as evidenced by the consistency within error of the decreasing $f^{62}Ni_{aq}^t$ values, except in the case of HexB at pH 7.5 where significant differences of decreasing $f^{62}Ni_{aq}^t$ are observable (Table A2; Fig. 2B).

Opposite and increasing trends are observed for other Ni(II)$_{aq}$ fractions, such as f^{58}Ni and f^{60}Ni (Tables A1-3, Fig. 3A-F). This, furthermore, indicates movement of Ni atoms from the samples with natural abundance Ni composition into the initially ^{62}Ni-enriched aqueous phase. Isotopic compositions equal to the system mass balance are, however, not attained despite Ni fractions decreasing (f^{62}Ni) or increasing (f^{58}Ni and f^{60}Ni). Resultantly, this is interpreted as significant, but incomplete, exchange of solid and aqueous Ni.

Percent Ni exchange in the absence and presence of 1 mM Mn(II)$_{aq}$ at pH 7.5 and pH 5.5 over a 14-day experiment duration was calculated by insertion of $f^{62}Ni_{aq}^t$ values into equation 2 (Tables A1-3, Fig. 4A-F). At pH 7.5, vernadite exhibits ~22.2% Ni exchange in the absence of Mn(II)$_{aq}$, whereas in the presence of Mn(II)$_{aq}$ this value increases to ~23.7% (Table A1, Fig. 4A). HexB experiences the largest difference in Ni exchange of all samples with ~21.5% in the absence of Mn(II)$_{aq}$ and ~29.1% in the presence of Mn(II)$_{aq}$ (Table A2, Fig. 4B). The lowest percentages of Ni exchange are observed for TriB. In the absence of Mn(II)$_{aq}$ TriB exhibits ~7.5% Ni exchange and ~8.8% in the presence of Mn(II)$_{aq}$ (Table A3, Fig. 4C). At pH 5.5, vernadite exhibits ~21.5% Ni exchange in the absence of Mn(II)$_{aq}$ and ~21.9% when Mn(II)$_{aq}$ is added (Table A1, Fig. 4D). Calculation of Ni exchange for HexB yields similar values for both Mn(II)$_{aq}$ concentrations (~21.4% in the absence of Mn(II)$_{aq}$ and ~19.7% in the presence of Mn(II)$_{aq}$) as shown in Fig. 4E (Table A2). The same trend is seen for TriB with Ni exchange values of ~15.0% in the absence of Mn(II)$_{aq}$ and ~15.4% in the presence of Mn(II)$_{aq}$ (Table A3, Fig. 4F).
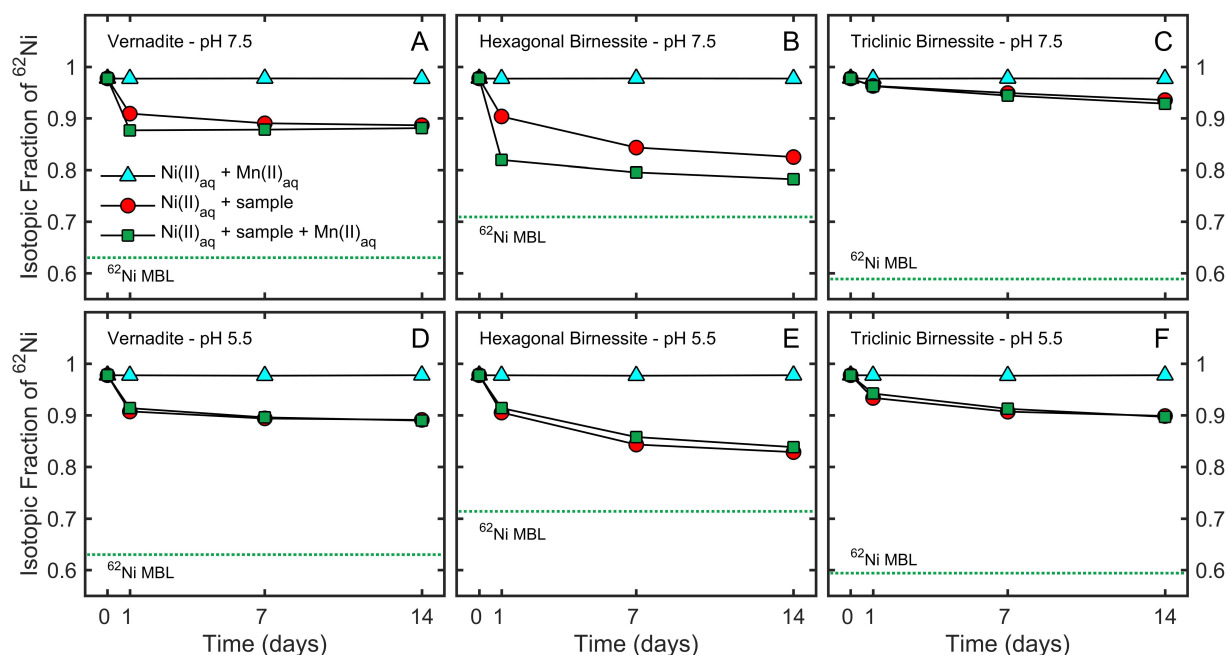
Fig. 2. Evolution of the ^{62}Ni isotope fractions of Ni(II)$_{aq}$ in a sample-free 1 mM Mn(II)$_{aq}$ solution and in suspensions of vernadite (A,D), HexB (B,E), and TriB (C,F) in the absence and presence of 1 mM Mn(II)$_{aq}$ at pH 7.5 and pH 5.5. Values for data points represent the mean of duplicate reactions; error bars not visible are smaller than symbols. ^{62}Ni MBL = mass balance line of $f^{62}Ni$.
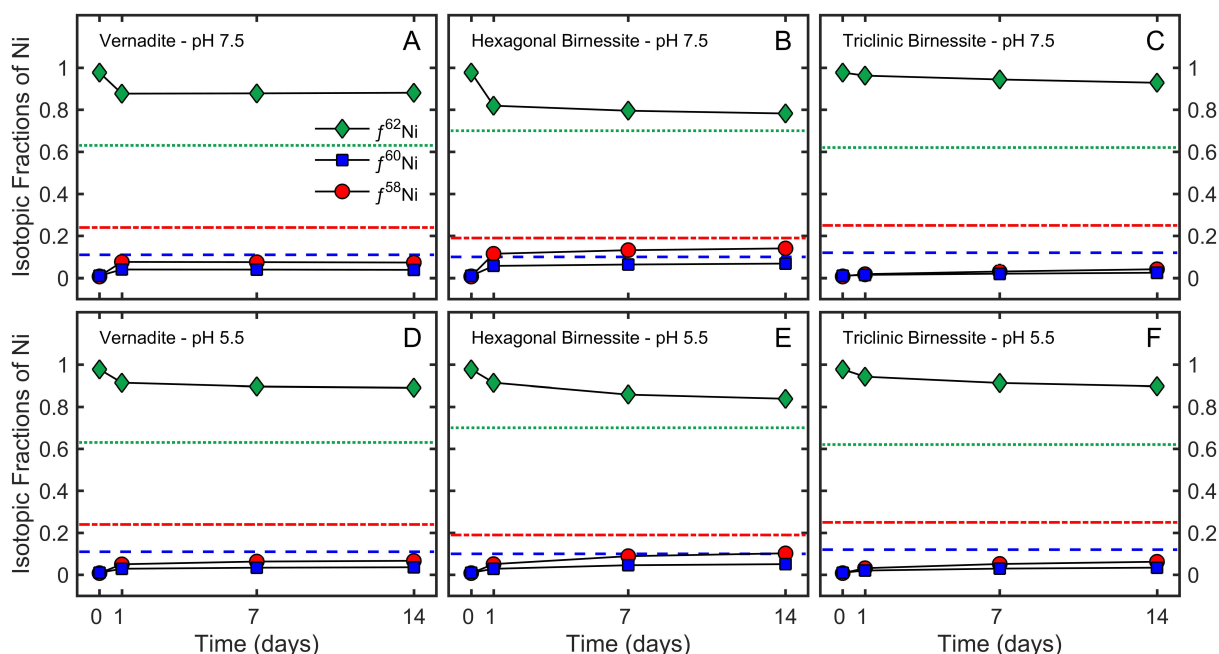
Fig. 3. Evolution of the ^{n}Ni isotope fraction of Ni(II)$_{aq}$ during its reaction with vernadite (A,D), HexB (B,E), and TriB (C,F) and 1 mM Mn(II)$_{aq}$ over 14 days at pH 7.5. Aqueous Ni(II) was initially enriched in ^{62}Ni ($f^{62}Ni = 0.977$), and hence depleted in the remaining Ni isotopes ($f^{58}Ni = 0.008$, $f^{60}Ni = 0.010$, and $f^{61}Ni = 0.003$), whereas vernadite, HexB, and TriB have a natural abundance Ni isotope composition. Values for data points represent the mean of duplicate reactions; error bars not visible are smaller than symbols. Mass balance lines: $f^{58}Ni$ = red dashed-dotted line, $f^{60}Ni$ = blue dashed line, $f^{62}Ni$ = green dotted line.
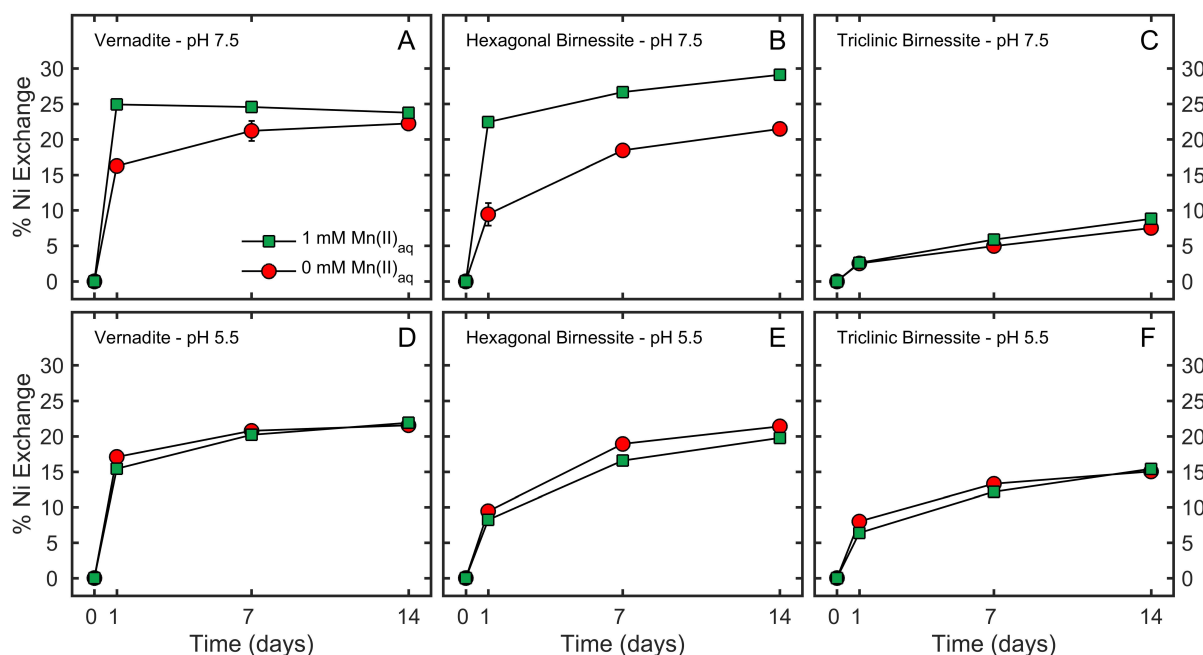
Fig. 4. Percent Ni exchange between vernadite (A,D), HexB (B,E), and TriB (C,F) in ^{62}Ni-enriched Ni(II)$_{aq}$ solutions over time at pH 7.5 and pH 5.5 in the absence and presence of 1 mM Mn(II)$_{aq}$. Percent Ni exchange was calculated by inserting f^{62}Ni values of Ni(II)$_{aq}$ into eq 2. Values for data points represent the mean of duplicate reactions; error bars not visible are smaller than symbols.

Overall, it can be seen that while vernadite experiences slightly more Ni exchange in the presence of Mn(II)$_{aq}$ than in the absence of dissolved Mn at pH 7.5, Ni exchange under both reaction conditions at pH 5.5 is nearly identical to the pH 7.5 reaction in the absence of Mn(II)$_{aq}$. Similar behavior of Ni exchange is observed for HexB. This is consistent with what has been reported in our previous study (Hens et al., 2018), where Ni exchange between manganite (γ-Mn(III)OOH) and Mn(II)$_{aq}$-bearing solutions at pH 5.5 appeared to be almost identical to Ni exchange at pH 7.5 when no Mn(II)$_{aq}$ was added to solution. Moreover, Ni exchange of HexB in the absence of Mn(II)$_{aq}$ at pH 5.5 is minimally higher than in the presence of Mn(II)$_{aq}$, which is interpreted as competition for vacancy sites in favor of Mn(II) instead of Ni(II). In contrast, TriB shows higher Ni exchange at pH 5.5 than at pH 7.5 (>6% difference), however, with values being almost identical in the presence and absence of Mn(II)$_{aq}$ at each pH level. Since equal amounts within error, of solid-phase Ni are exchangeable with Ni(II)$_{aq}$ for all samples in the absence or presence of Mn(II)$_{aq}$ after 1,7, and 14 days at pH 5.5, Ni exchange appears to be independent of Mn(II)$_{aq}$ concentrations at pH 5.5 reaction conditions.

Graphical representation of Ni exchange, furthermore, illustrates that vernadite exhibits a rapid increase of Ni exchange in the first day of reaction at both pH levels (Fig. 4A,D). A less pronounced trend is seen for HexB (Fig. 4B,E) and TriB (Fig. 4C,F). In the latter cases, the initial increases during the 1-day reactions are followed by a more steady increase to the final Ni exchange value after 14 days of reaction.

4.3. Structural Modification Following Reaction with Mn(II)$_{aq}$

Of the samples reacted in the absence and presence of Mn(II)$_{aq}$ for 14 days, HexB was chosen for post-reaction XRD analysis. Overall, significant changes to the HexB XRD patterns can be observed for samples reacted under variable reaction conditions, with new peaks in the 5-70º 2θ range clearly visible (Fig. 5). A decreasing intensity of the (001) reflection is observed in all reacted samples compared to the starting material, independent of the Mn(II)$_{aq}$ concentration. Samples reacted in the absence of Mn(II)$_{aq}$ show the formation of peaks in the 20-30º 2θ range (e.g., HexB reacted at pH 7.5, 0 mM Mn(II)$_{aq}$), as well as splitting of the (20,11) reflection. Reactions in the presence of 1 mM Mn(II)$_{aq}$ exhibit an amplification of the (20,11) peak splitting. Most notably, the occurrence of a newly formed well-defined peak at ~19.4º 2θ, indicative of meta-stable feitknechtite (β-Mn(III)OOH), is observed, as well as the formation of several peaks in the 30-70º 2θ range. While this is a more subtle characteristic of the pH 5.5 sample, HexB reacted at pH 7.5 in the presence of 1 mM Mn(II)$_{aq}$, shows significant structural modification to feitknechtite.

4.4. Effects of MOPS and MES Buffers on Ni Exchange

To evaluate potential influences of Good's buffers on Ni exchange results, the release of Mn(II) into solution was measured in Mn(II)$_{aq}$- and Ni(II)$_{aq}$-free controls over time. All Mn(II) concentrations can be found in Table A5, whereas Fig. 6 shows concentration values expressed in percent dissolved Mn(II) (%Mn(II) Dissolved) of total Mn available in each reactor. At pH 7.5, the buffer-free controls for vernadite exhibit increasing release of Mn(II) into solution over time with a maximum of ~18 µM Mn(II), or ~2.3% of total Mn available, detected in solution after 14 days. HexB experiences up to ~0.27% (~6.1 µM) of Mn(II) release during the first day. This value then decreases to ~5.1 µM (~0.22%) after 14 days. The buffer-free controls containing TriB show relatively constant Mn(II) release of ~2.0-2.9 µM (~0.20-0.27%) over the entire experiment duration. In the presence of 10 mM MOPS, considerably smaller amounts of Mn(II) are released into solution at pH 7.5. Maximum values

of ~0.02 and ~0.25 µM Mn(II), equivalent to ~0.003 and ~0.001% of total Mn available, are measured on the first day of reaction in the cases of vernadite and HexB, respectively. TriB exhibits ~0.21µM (~0.02%) of Mn(II) release after 14 days.

While at pH 7.5 the buffered samples show minimal Mn(II) release and the unbuffered samples exhibit increased Mn(II) in solution, trends at a lower pH level are opposite. At pH 5.5, the buffer-free vernadite controls experience ~3.5 µM Mn(II) (~0.45%) release after 14 days. HexB shows ~6.4 µM Mn(II) (~0.28%) release during the first day with values decreasing to ~3.9 µM Mn(II) (~0.17%) after 14 days. TriB exhibits ~1.8 µM (~0.17%) Mn(II) release after 14 days. When sample suspensions are buffered in 10 mM MES considerable amounts of Mn(II) are almost linearly released into solution. For vernadite up to ~56 µM Mn(II) (~7.3%) are released after 14 days, whereas HexB exhibits release of ~81 µM Mn(II) in the same period of time, which is equivalent to ~3.5% of total Mn available in the HexB reactor, respectively. Of the three samples, TriB experiences the lowest amount of Mn(II) release with up to ~26 µM Mn(II) (~2.5%) detected in solution after 14 days.
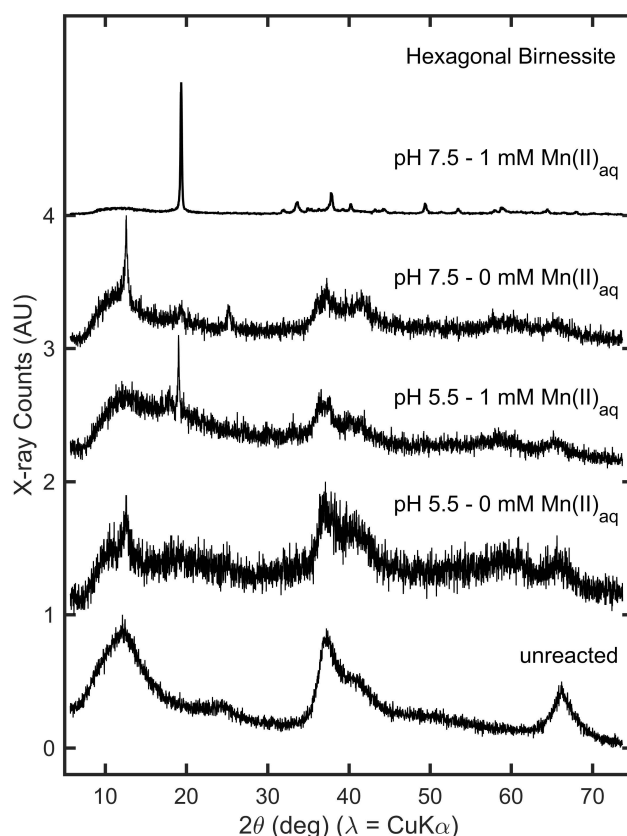
Fig. 5. XRD patterns for the HexB starting material (unreacted) and HexB reacted in the presence and absence of Mn(II)$_{aq}$-bearing solutions at pH 7.5 and pH 5.5. Reacted samples exhibit changes of peak shapes and the formation of new peaks in the 30-70° 2θ range, which are indicative of mineral phase transformations as well as changes in sheet symmetry and structural ordering of phyllomanganate sheets.
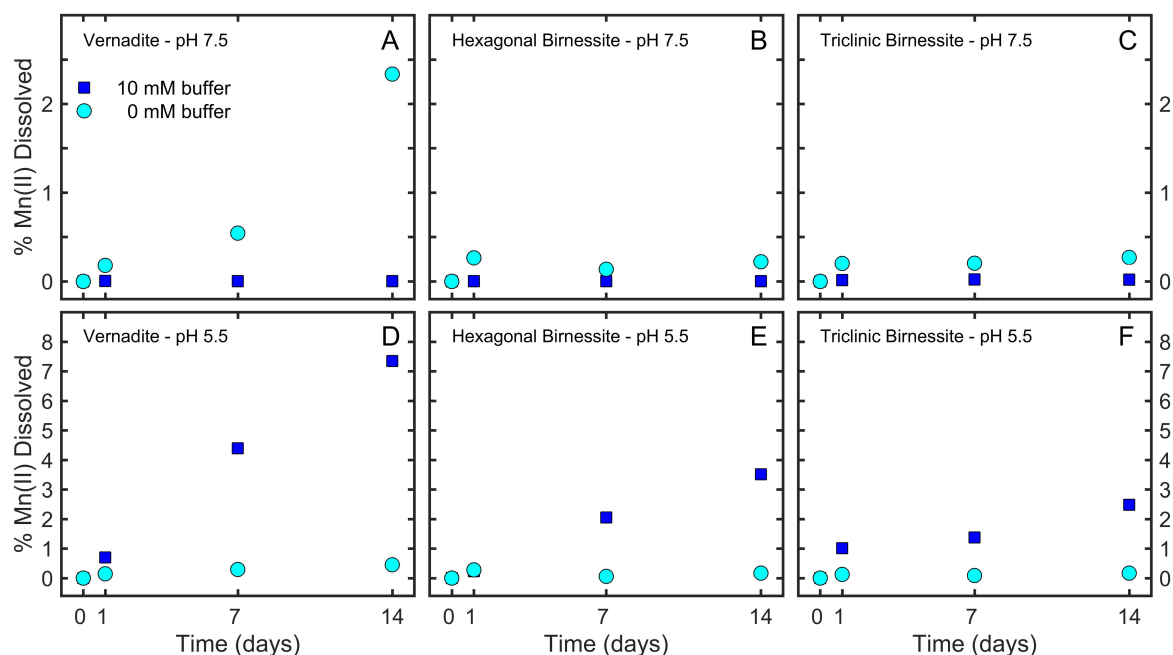
Fig. 6. Release of Mn(II) into solution during reaction of phyllomanganate controls with variable buffer concentrations. The first set of controls was buffered in 10 mM MOPS (pH 7.5) and MES (pH 5.5), respectively. The second set of controls was unbuffered, but pH-adjusted daily with small amounts of 0.01 M NaOH or HCl. Values are reported as percent Mn(II)$_{aq}$ dissolved of total Mn available in each reactor and represent single data points.

5. Discussion

5.1. Mechanistic Considerations

Our results show that Ni exchanges between Ni-substituted phyllomanganates and fluids containing ^{62}Ni(II)-enriched Ni(II)$_{aq}$. The extent of Ni exchange is largely independent of the Mn(II)$_{aq}$ concentrations employed in this study. Furthermore, we observe effects of Mn(II)$_{aq}$ and buffers on the substrates as well as pH-dependent behavior of Ni exchange, similar to what has previously been reported (Hinkle et al., 2016; Lefkowitz and Elzinga, 2017; Lefkowitz et al., 2013). Based on these Mn(II)$_{aq}$-induced effects and results presented in this study it is thus proposed that Ni exchange between synthetic Ni-substituted phyllomanganates and Ni(II)-bearing fluids is likely driven by a combination of pH-dependent bulk reductive structural alterations and Mn(II)$_{aq}$-accelerated recrystallization as discussed below.

Previous studies have shown that Mn(II) likely affects birnessite-type Mn(IV) oxides through multi-step, coupled comproportionation-disproportionation (CP-DP) reactions (Elzinga and Kustka, 2015). Initial Mn(II) sorption to the mineral surface is followed by interfacial electron transfer from Mn(II) to lattice-bound Mn(IV). This produces a transient Mn(III) species, which

either nucleates metastable feitknechtite (β-Mn(III)OOH) that may further convert to stable manganite (γ-Mn(III)OOH), or disproportionates into Mn(II) and Mn(IV) in the absence of stabilizing ligands (Klewicki and Morgan, 1998; Wang and Stone, 2008) to drive atom-exchange. The nucleation and subsequent transformation of feitknechtite as well as two pathways of Mn(III) disproportionation can be summarized as derived and discussed by Elzinga (2011) and Elzinga and Kustka (2015):

Nucleation of metastable feitknechtite and transformation into manganite:

$$Mn(II)_{(aq)} + Mn(IV)O_{2(s)} + H_2O \rightarrow 2\beta\text{-Mn(III)OOH}_{(s)} + 2H^+ \tag{4}$$

$$\beta\text{-Mn(III)OOH}_{(s)} \rightarrow \gamma\text{-Mn(III)OOH}_{(s)} \tag{5}$$

to yield the total reaction:

$$Mn(II)_{(aq)} + Mn(IV)O_{2(s)} + H_2O \rightarrow 2\gamma\text{-Mn(III)OOH}_{(s)} + 2H^+ \tag{6}$$
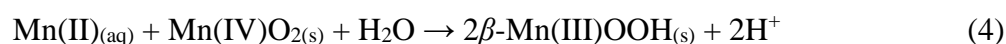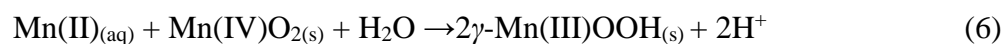
Pathway 1 of Mn(III) disproportionation:

$$Mn(II)_{(aq)} + {}^*Mn(IV)_{(s)} \rightarrow >Mn(III) + >{}^*Mn(III) \tag{7}$$

$$>{}^*Mn(III) + >Mn(III) \rightarrow Mn(IV)_{(s)} + {}^*Mn(II)_{(aq)} \tag{8}$$
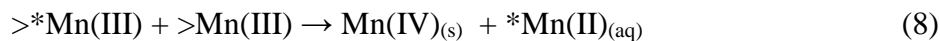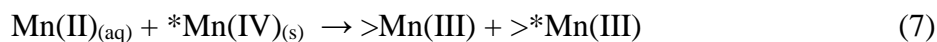
where * indicates the exchanging atom and >Mn(III)/>*Mn(III) represent labile Mn(III).

Pathway 2 of Mn(III) disproportionation:

$$2Mn(II)_{(aq)} + {}^*Mn(IV)_{(s)} \rightarrow 2>Mn(III) + {}^*Mn(II)_{(aq)} \tag{9}$$

$$2Mn(II)_{(aq)} + {}^*Mn(IV)_{(s)} \rightarrow Mn(II)_{(aq)} + {}^*Mn(II)_{(aq)} + Mn(IV)_{(s)} \tag{10}$$

which yield the total reaction:

$$Mn(II)_{(aq)} + {}^*Mn(IV)_{(s)} \rightarrow {}^*Mn(II)_{(aq)} + Mn(IV)_{(s)} \tag{11}$$
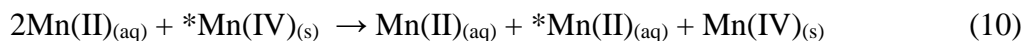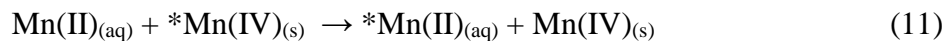
It has been observed that these pathways are similar for vernadite and HexB, with the impact of Mn(II)-induced reductive transformation on vernadite being faster (Elzinga, 2011; Lefkowitz et al., 2013) due to its lower crystallinity and higher specific surface area (Villalobos et al., 2003). As a result of differences in structural Mn(III) content, which may lead to modified properties of Mn(IV) oxides, initially prevalent reaction pathways are expected to undergo changes over

time (Elzinga and Kustka, 2015). Furthermore, differences in structural composition between HexB and TriB may also affect metal uptake and reactivity (Peacock and Sherman, 2007a; Peacock and Sherman, 2007b). HexB may sorb cations above/below Mn(III)-vacancy sites of the octahedral Mn sheets to balance negative layer charge. TriB cannot sorb metals via this pathway since vacancy sites are already filled with Mn(III,IV) and negative charge balancing occurs through hydrated interlayer cations (Drits et al., 1997; Peacock and Sherman, 2007a). Overall, the prevalent reaction mechanism is dependent on several variables such as pH (Lefkowitz et al., 2013), the $Mn(II)_{aq}$ concentration and thus ratio of $Mn(II)_{aq}$ to $Mn(IV)_{(s)}$ (Elzinga, 2011), and the presence of trace metals such as Ni (Zhu et al., 2010a; Zhu et al., 2010b).

The influence of pH and $Mn(II)_{aq}$ can be exemplified with the XRD results of HexB. At pH 7.5 in the absence of $Mn(II)_{aq}$ (Mn(II):Mn(IV) <0.5), no phase transformations of the initial substrate into feitknechtite or manganite occur. However, the sharp peak within the (001) reflection is interpreted as the formation of interstratified defective layers (Fig. 5) (Drits et al., 2007; Hinkle et al., 2016; Lanson et al., 2000). This structural modification, with interspersed hexagonal and orthogonal sheets, minimizes electrostatic repulsion and maximizes Mn atom distances in adjacent sheets and distances between Mn sites and Mn atom capping vacancies (Hinkle et al., 2016). Conversely, at the same pH level and in the presence of 1 mM $Mn(II)_{aq}$ (Mn(II):Mn(IV) $\geq$0.5) almost complete transformation of HexB into feitknechtite occurs as evident from the appearance of new XRD reflections (Fig. 5). Such bulk structural conversions into a lower-valence Mn phase through precipitation of Mn(III) oxides have been described previously (Bargar et al., 2005; Elzinga, 2011; Lefkowitz et al., 2013).

Analogous to the reaction at pH 7.5, at pH 5.5 and in the absence of $Mn(II)_{aq}$ no HexB bulk transformation into feitknechtite is observed, despite significant $Mn(II)_{aq}$ sorption onto the substrate (Table A2). Mn(III)OOH nucleation is limited at acidic pH by unfavorable thermodynamics for Mn(III) precipitation rather than the absence of Mn(III) (Lefkowitz and Elzinga, 2015; Lefkowitz and Elzinga, 2017). In the presence of 1 mM $Mn(II)_{aq}$ (Mn(II):Mn(IV) $\geq$0.5) early stages of bulk transformation are, however, observable with the appearance of the most prominent feitknechtite peak (Fig. 5).

Differences in Ni exchange between the samples may partially be explained by the initial properties of phyllomanganates, any structural modifications due to their variable susceptibility to $Mn(II)_{aq}$ as well as changing reaction pathways. Additionally, Ni exchange results may be

affected by Ni coordination. EXAFS studies have shown that during Ni adsorption experiments Ni(II) is predominantly adsorbed as triple-corner sharing complexes at layer vacancies in the absence of Mn(II)$_{aq}$ (Lefkowitz and Elzinga, 2017). The presence of Mn(II), however, causes partial desorption of adsorbed Ni from layer vacancy sites, enhancing Ni(II) coordination of edge-sharing complexes (Lefkowitz and Elzinga, 2017) and structural incorporation of Ni through Mn(II)$_{aq}$-catalyzed recrystallization. However, when Ni is coprecipitated during phyllomanganate synthesis, as in this study, a large fraction of Ni is incorporated into the phyllomanagante sheets, while structural properties of the synthesis products do not systematically affect the fraction of incorporated Ni (Hinkle et al., 2017).

Lastly, calculated Ni exchange results and observed structural modifications of phyllo-manganates may result from competitive displacement of Ni(II) from layer vacancies by Mn(II), or Mn(III) which can be formed by interfacial Mn(II)-Mn(IV) comproportionation. Competition for surface-site adsorption has also been attributed to an overall lower structural Mn(III) content in birnessites grown in Ni(II)-bearing solutions, as Ni(II) inhibits Mn(III) formation via comproportionation (Zhu et al., 2010b). Facile substitution of Ni(II) into Mn(III) sites through incorporation and the ability of Ni(II) to substitute into the birnessite layer vacancies that are occupied by Mn(III) have been observed (Peacock, 2009; Peacock and Sherman, 2007a; Peacock and Sherman, 2007b; Zhu et al., 2010a; Zhu et al., 2010b). This may explain the variable Mn AOS of our Ni-coprecipitated phyllomanganate products and apparent stability of feitknechtite, as competition between Ni(II) and Mn(II) may cause interference with Mn(II)$_{aq}$-catalyzed transformation of feitknechtite into manganite (Elzinga, 2011).

5.2. Effects of Buffers on Ni Exchange

In addition to the aforementioned factors impacting phyllomanganates in contact with Mn(II)$_{aq}$, the influence of buffers has to be critically examined. In the past, MOPS and MES (Good's) buffers have been considered: (i) non-complexing tertiary amine buffer compounds (Kandegedara and Rorabacher, 1999; Kaushal and Barnes, 1986; Lleu and Rebel, 1991; Yu et al., 1997) or (ii) less reactive than HEPES due to the presence of morpholine compounds instead of the piperazine compound characteristic for HEPES (Lleu and Rebel, 1991; Wang and Sayre, 1989). These buffers, including HEPES, have commonly been employed in studies utilizing Mn(IV) oxides (e.g., Bargar et al., 2005; Droz et al., 2015; Elzinga, 2011; Elzinga and Kustka, 2015; Hinkle et al., 2016; Learman et al., 2011; Lefkowitz and Elzinga, 2015; Peña et al., 2011; Peña et al., 2015; Peña et al., 2010; Zhu et al., 2010a).

However, these buffers can induce structural modification by partial reductive dissolution of Mn(IV) and the generation of structural or interlayer Mn(II,III) (Elzinga and Kustka, 2015; Hinkle et al., 2016; Simanova and Peña, 2015). Initial release and subsequent adsorption of Mn(II), which led to structural changes of phyllomanganate substrates as a result of hydration with MES have, for instance, been observed and attributed to the redox reactivity of organic MES compounds (Hinkle et al., 2016). Furthermore, MES was found to promote the formation of edge-sharing Ni(II) sorption complexes through partial reduction of Mn(IV) (Lefkowitz and Elzinga, 2017). Although MES may not necessarily induce changes in bulk mineralogy of the phyllomanganate substrate (Lefkowitz and Elzinga, 2017), changes in XRD patterns such as decreased intensity of high angle reflections indicate capping of vacancy sites by heavy cations such as Mn (III) (Drits et al., 2007; Grangeon et al., 2010; Villalobos et al., 2006) and Ni(II) (Grangeon et al., 2008). This has been attributed to the stabilization of Mn(II,III) at vacancy sites (Elzinga, 2011). Consequently, it is possible that partial reduction of Mn(IV) by buffers could affect the observed amount of Ni exchange in our experiments.

The results of our Mn(II)$_{aq}$- and Ni(II)$_{aq}$-free control experiments clearly support the evidence that MES has an effect on phyllomanganate substrates. While less than 1% of Mn(II) release was observed for all samples in unbuffered controls at pH 5.5, in the presence of 10 mM MES linear release of Mn(II) up to 7.35, 3.51, and 2.49% were measured for vernadite, HexB, and TriB, respectively (Table A5). In contrast, at pH 7.5 both MOPS-buffered and unbuffered controls show similar patterns of Mn(II) release with values below 0.5%. The unbuffered vernadite control is an exception with up to 2.33% Mn(II) release detected. This either indicates that MES acts as a stronger reductant than MOPS, or increased release of Mn(II) at pH 5.5 in comparison to pH 7.5 is instead a result of Mn disproportionation.

Since release of Mn(II) occurs at both pH levels, it cannot be fully ruled out that buffers may induce partial reduction of the phyllomanganates in our experiments. Ultimately, any endogenous Mn(II) can act as a positive feedback mechanism influencing Ni exchange, suggesting that Mn(II) and MOPS/MES may affect Ni(II) in a similar fashion. However, at pH 7.5 the influence of small amounts of Mn(II) on the Ni exchange results are considered negligible, as they are almost three orders of magnitude lower than Mn(II) concentrations present during the Ni exchange experiments. Moreover, despite increased buffer redox reactivity at pH 5.5 the extent of Ni exchange catalyzed through rapid interfacial redox chemistry is unlikely to be significantly affected by buffer redox reactivity.

5.3. Environmental Implications

Phyllomanganates are ubiquitous in a wide variety of environments, such as soils, sediments and aquatic systems, where dissolved Mn(II) can be present in concentrations ranging from µM to mM levels (i.e., in suboxic pore waters, redoxclines, mineral seeps, and areas affected by acid mine drainage). Mn(II) may induce structural changes and affect redox reactivity of Mn oxides across a broad pH range (Lefkowitz and Elzinga, 2017; Lefkowitz et al., 2013; McKenzie, 1980; Posselt et al., 1968) through abiotic back-reactions. Moreover, pH-dependent sorption behavior of Ni(II) has been observed, which affects Ni retention by either promoting or inhibiting Ni(II) sorption (Lefkowitz and Elzinga, 2017). Interactions between $Mn(II)_{aq}$ and phyllomanganates may thus initiate substantial changes in Ni partitioning and speciation. Our study demonstrates that structurally incorporated Ni in synthetic layer-type Mn(III,IV) oxides is susceptible to mineral-fluid cycling in both the presence and absence of $Mn(II)_{aq}$.

These phyllomanganates represent close analogues to the poorly crystalline Mn oxides host phases that are considered effective and irreversible sinks for metals and metalloids in deep-sea ferromanganese nodules and crusts (e.g., Peacock, 2009; Peacock and Sherman, 2007a; Peacock and Sherman, 2007b). The extent of Ni exchange observed in our experiments implies that Mn(II)-induced reaction pathways may affect trace element uptake and release in these polymetallic concretions, which, in turn, may alter the availability of Ni during Fe-Mn nodule and crust formation and subsequent alteration. It may thus have to be reconsidered if Fe-Mn concretions, under certain environmental conditions, are (at least partially) open system that have the potential to equilibrate with seawater over long time scales.

6. References

Bargar, J.R., Fuller, C.C., Marcus, M.A., Brearley, A.J., De la Rosa, M.P., Webb, S.M., Caldwell, W.A., 2009. Structural characterization of terrestrial microbial Mn oxides from Pinal Creek, AZ. Geochimica et Cosmochimica Acta, 73: 889-910.

Bargar, J.R., Tebo, B.M., Bergmann, U., Webb, S.M., Glatzel, P., Chiu, V.Q., Villalobos, M., 2005. Biotic and abiotic products of Mn(II) oxidation by spores of the marine *Bacillus* sp. strain SG-1. American Mineralogist, 90(1): 143-154.

Bargar, J.R., Tebo, B.M., Villinski, J.E., 2000. In situ characterization of Mn (II) oxidation by spores of the marine *Bacillus sp.* strain SG-1. Geochimica et Cosmochimica Acta, 64: 2775-2778.

Birkner, N., Nayeri, S., Pashaei, B., Najafpour, M.M., Casey, W.H., Navrotsky, A., 2013. Energetic basis of catalytic activity of layered nanophase calcium manganese oxides for water oxidation. Proceedings of the National Academy of Sciences, 110(22): 8801-8806.

Brindley, G.W., Brown, G., 1980. Crystal structures of clay minerals and their X-ray identification. Mineralogical Society London: 361-410.

Burns, R.G., Burns, V.M., 1977. The mineralogy and crystal chemistry of deep-sea manganese nodules, a polymetallic resource of the twenty-first century. Philosophical Transactions of the Royal Society London, A286: 283-301.

Clement, B.G., Luther III, G.W., Tebo, B.M., 2009. Rapid, oxygen-dependent microbial Mn(II) oxidation kinetics at submicromolar oxygen concentrations in the Black Sea suboxic zone. Geochimica et Cosmochimica Acta, 73: 1878-1889.

Dick, G.J., Clement, B.G., Webb, S.M., Fodrie, F.J., Bargar, J.R., Tebo, B.M., 2009. Enzymatic microbial Mn(II) oxidation and Mn biooxide production in the Guaymas Basin deep-sea hydrothermal plume. Geochimica et Cosmochimica Acta, 73: 6517-6530.

Drits, V.A., Lanson, B., Gaillot, A.-C., 2007. Birnessite polytype systematics and identification by powder X-ray diffraction. American Mineralogist, 92: 771-788.

Drits, V.A., Silvester, E., Gorshkov, A.I., Manceau, A., 1997. Structure of synthetic monoclinic Na-rich birnessite and hexagonal birnessite: I. Results from X-ray diffraction and selected-area electron diffraction. American Mineralogist, 82(9-10): 946-961.

Droz, B., Dumas, N., Duckworth, O.W., Peña, J., 2015. A Comparison of the Sorption Reactivity of Bacteriogenic and Mycogenic Mn Oxide Nanoparticles. Environmental Science & Technology, 49(7): 4200-4208.

Elzinga, E.J., 2011. Reductive Transformation of Birnessite by Aqueous Mn(II). Environmental Science & Technology, 45(15): 6366-6372.

Elzinga, E.J., 2016. [54]Mn Radiotracers Demonstrate Continuous Dissolution and Reprecipitation of Vernadite (δ-MnO$_2$) during Interaction with Aqueous Mn(II). Environmental Science & Technology, 50(16): 8670-8677.

Elzinga, E.J., Kustka, A.B., 2015. A Mn-54 Radiotracer Study of Mn Isotope Solid-Liquid Exchange during Reductive Transformation of Vernadite (δ-MnO$_2$) by Aqueous Mn(II). Environmental Science & Technology, 49(7): 4310-4316.

Frierdich, A.J., Luo, Y., Catalano, J.G., 2011. Trace element cycling through iron oxide minerals during redox-driven dynamic recrystallization. Geology, 39(11): 1083-1086.

Gadde, R.R., Laitinen, H.A., 1974. Heavy metal adsorption by hydrous iron and manganese oxides. Analytical Chemistry, 46(13): 2022-2026.

Goldberg, E.D., 1954. Marine Geochemistry 1. Chemical scavengers of the sea. The Journal of Geology, 62: 249-265.

Golden, D.C., Chen, C.C., Dixon, J.B., 1987. Transformation of birnessite to buserite, todorokite, and manganite under mild hydrothermal treatment. Clays and Clay Minerals, 35: 271-280.

Golden, D.C., Dixon, J.B., Chen, C.C., 1986. Ion exchange, thermal transformations, and oxidizing properties of birnessite. Clays and Clay Minerals, 34: 511-520.

Grangeon, S., Lanson, B., Lanson, M., Manceau, A., 2008. Crystal structure of Ni-sorbed synthetic vernadite: a powder X-ray diffraction study. Mineralogical Magazine, 72(1279-1291).

Grangeon, S., Lanson, B., Miyata, N., Tani, Y., Manceau, A., 2010. Structure of nanocrystalline phyllomanganates produced by freshwater fungi. American Mineralogist, 95(11-12): 1608–1616.

Grangeon, S., Manceau, A., Guilhermet, J., Gaillot, A.-C., Lanson, M., Lanson, B., 2012. Zn sorption modifies dynamically the layer and interlayer structure of vernadite. Geochimica et Cosmochimica Acta, 85: 302-313.

Graybeal, A.L., Heath, G.R., 1984. Remobilization of transition metals in surficial pelagic sediments from the eastern Pacific. Geochimica et Cosmochimica Acta, 48: 965-975.

Hein, J.R., Koschinsky, A., 2014. 13.11 - Deep-Ocean Ferromanganese Crusts and Nodules. In: Holland, H., Turekian, K. (Eds.), Treatise on Geochemistry. Elsevier, Oxford, pp. 273-291.

Hens, T., Brugger, J., Cumberland, S.A., Etschmann, B., Frierdich, A.J., 2018. Recrystallization of Manganite (γ-MnOOH) and Implications for Trace Element Cycling. Environmental Science & Technology, 52(3): 1311-1319.

Hinkle, M.A.G., Dye, K.G., Catalano, J.G., 2017. Impact of Mn(II)-Manganese Oxide Reactions on Ni and Zn Speciation. Environmental Science & Technology, 51: 3187-3196.

Hinkle, M.A.G., Flynn, E.D., Catalano, J.G., 2016. Structural response of phyllomanganates to wet aging and aqueous Mn(II). Geochimica et Cosmochimica Acta, 192: 220-234.

Kandegedara, A., Rorabacher, D.B., 1999. Noncomplexing Tertiary Amines as "Better" Buffers Covering the Range of pH 3-11. Temperature Dependence of Their Acid Dissociation Constants. Analytical Chemistry, 71(15): 3140-3144.

Kaushal, V., Barnes, L.D., 1986. Effect of zwitterionic buffers on measurement of small masses of protein with bicinchoninic acid. Analytical Biochemistry, 157(2): 291-294.

Klewicki, J.K., Morgan, J.J., 1998. Kinetic behavior of Mn(III) complexes of pyrophosphate, EDTA, and citrate. Environmental Science & Technology, 32: 2916.

Lanson, B., Drits, V.A., Silvester, E., Manceau, A., 2000. Structure of H-exchanged hexagonal birnessite and its mechanism of formation from Na-rich monoclinic buserite at low pH. American Mineralogist, 85: 826-838.

Learman, D.R., Wankel, S.D., Webb, S.M., Martinez, N., Madden, A.S., Hansel, C.M., 2011. Coupled biotic-abiotic Mn(II) oxidation pathway mediates the formation and structural evolution of biogenic Mn oxides. Geochimica et Cosmochimica Acta, 75(20): 6048-6063.

Lefkowitz, J.P., Elzinga, E.J., 2015. Impacts of aqueous Mn(II) on the sorption of Zn(II) by hexagonal birnessite. Environmental Science & Technology, 49: 4886-4893.

Lefkowitz, J.P., Elzinga, E.J., 2017. Structural alteration of hexagonal birnessite by aqueous Mn(II): Impacts on Ni(II) sorption. Chemical Geology, 466: 524-532.

Lefkowitz, J.P., Rouff, A.A., Elzinga, E.J., 2013. Influence of pH on the reductive transformation of birnessite by aqueous Mn(II). Environmental Science & Technology, 47(18): 10364−10371.

Lleu, P.L., Rebel, G., 1991. Interference of Good's buffers and other biological buffers with protein determination. Analytical Biochemistry, 192(1): 215-218.

Lopano, C.L., Heaney, P.J., Post, J.E., Hanson, J., Komarneni, S., 2007. Time-resolved structural analysis of K- and Ba-exchange reactions with synthetic Na-birnessite using synchrotron X-ray diffraction. American Mineralogist, 92(2-3): 380-387.

Lovely, D.R., 2000. Fe(III) and Mn(IV) reduction. In: Lovely, D.R. (Ed.), Environmental metal-microbe interactions. ASM Press, Washington, D.C., pp. 3-30.

Manceau, A., Drits, V.A., Silvester, E., Bartoli, C., Lanson, B., 1997. Structural mechanism of Co^{2+} oxidation by the phyllomanganate buserite. American Mineralogist, 88(11-12): 1150-1175.

Manceau, A., Lanson, M., Geoffroy, N., 2007. Natural speciation of Ni, Zn, Ba, and As in ferromanganese coatings on quartz using X-ray fluorescence, absorption and diffraction. Geochimica et Cosmochimica Acta, 71: 95-128.

Manceau, A., Marcus, M.A., Grangeon, S., 2012. Determination of Mn valence states in mixed-valent manganates by XANES spectroscopy. American Mineralogist, 97(5-6): 816-827.

Mandernack, K.W., Post, J., Tebo, B.M., 1995. Manganese mineral formation by bacterial spores of the marine *Bacillus*, strain SG-1: Evidence for the direct oxidation of Mn(II) to Mn(IV). Geochimica et Cosmochimica Acta, 59(21): 4393-4408.

Mann, S., Sparks, N.H.C., Scott, G.H.E., De Vrind-de Jong, E.W., 1988. Oxidation of manganese and formation of Mn_3O_4 (hausmannite) by spore coats of a marine *Bacillus sp*. Applied and Environmental Microbiology, 54(8): 2140-2143.

McKenzie, R.M., 1980. The adsorption of lead and other heavy metals on oxides of manganese and iron. Australian Journal of Soil Research, 18: 61-73.

Morgan, J.J., 2005. Kinetics of reaction between O_2 and Mn(II) species in aqueous solutions. Geochimica et Cosmochimica Acta, 69: 35-48.

Murray, J.W., Balistrieri, L.S., Paul, B., 1984. The oxidation state of manganese in marine sediments and ferromanganese nodules. Geochimica et Cosmochimica Acta, 48(6): 1237-1247.

Myers, C.R., Nealson, K.H., 1988. Bacterial manganese reduction and growth with manganese oxide as the sole electron acceptor. Science, 240: 1319-1321.

Nealson, K.H., Tebo, B.M., Rosson, R.A., 1988. Occurrence and mechanisms of microbial oxidation of manganese. Advances in Applied Microbiology, 33: 2027-2035.

Peacock, C.L., 2009. Physiochemical controls on the crystal-chemistry of Ni in birnessite: Genetic implications for ferromanganese precipitates. Geochimica et Cosmochimica Acta, 73: 3568-3578.

Peacock, C.L., Sherman, D.M., 2007a. Crystal-chemistry of Ni in marine ferromanganese crusts and nodules. American Mineralogist, 92(7): 1087-1092.

Peacock, C.L., Sherman, D.M., 2007b. Sorption of Ni by birnessite: Equilibrium controls on Ni in seawater. Chemical Geology, 238(1-2): 94-106.

Pecher, K., McCubbery, D., Kneedler, E., Rothe, J., Bargar, J., Meigs, G., Cox, L., Nealson, K., Tonner, B., 2003. Quantitative charge state analysis of manganese biominerals in aqueous suspension using scanning transmission X-ray microscopy (STXM). Geochimica et Cosmochimica Acta, 67(6): 1089-1098.

Peña, J., Bargar, J.R., Sposito, G., 2011. Role of bacterial biomass in the sorption of Ni by biomass-birnessite assemblages. Environmental Science & Technology, 45: 7338-7344.

Peña, J., Bargar, J.R., Sposito, G., 2015. Copper sorption by the edge surfaces of synthetic birnessite nanoparticles. Chemical Geology, 396: 196-207.

Peña, J., Kwon, K.D., Refson, K., Bargar, J.R., Sposito, G., 2010. Mechanisms of nickel sorption by a bacteriogenic birnessite. Geochimica et Cosmochimica Acta, 74: 3076-3089.

Perez-Benito, J.F., 2002. Reduction of Colloidal Manganese Dioxide by Manganese(II). Journal of Colloid and Interface Science, 248(1): 130-135.

Posselt, H.S., Anderson, F.J., Weber, W.J., 1968. Cation sorption on colloidal hydrous manganese dioxide. Environmental Science & Technology, 2: 1087-1093.

Post, J.E., 1999. Manganese oxide minerals: Crystal structures and economic and environmental significance. Proceedings of the National Academy of Sciences of the United States of America, 96(7): 3447-3454.

Post, J.E., Heaney, P.J., Hanson, J., 2002. Rietveld refinement of a triclinic structure for synthetic Na-birnessite using synchrotron powder diffraction data. Powder Diffraction, 17: 218-221.

Post, J.E., Veblen, D.R., 1990. Crystal structure determinations of synthetic sodium, magnesium, and potassium birnessite using TEM and the Rietveld method. American Mineralogist, 75: 477-489.

Santelli, C.M., Webb, S.M., Dohnalkova, A.C., Hansel, C.M., 2011. Diversity of Mn oxides produced by Mn(II)-oxidizing fungi. Geochimica et Cosmochimica Acta, 75: 2762-2776.

Saratovsky, I., Wightman, P.G., Pasten, P.A., Gaillard, J.F., Poeppelmeier, K.R., 2006. Manganese oxides: parallels between abiotic and biotic structures. Journal of the American Chemical Society, 128: 11188-11198.

Silvester, E., Manceau, A., Drits, V.A., 1997. Structure of synthetic monoclinic Na-rich birnessite and hexagonal birnessite; II, Results from chemical studies and EXAFS spectroscopy. American Mineralogist, 82(9-10): 962-978.

Simanova, A.A., Peña, J., 2015. Time-Resolved Investigation of Cobalt Oxidation by Mn(III)-Rich δ-MnO$_2$ Using Quick X-ray Absorption Spectroscopy. Environmental Science & Technology, 49(18): 10867-10876.

Spiro, T.G., Bargar, J.R., Sposito, G., Tebo, B.M., 2009. Bacteriogenic manganese oxides. Accounts of Chemical Research, 43(1): 2-9.

Tan, H., Zhang, G., Heaney, P.J., Webb, S.M., Burgos, W.D., 2010. Characterization of manganese oxide precipitates from Appalachian coal mine drainage treatment systems. Applied Geochemistry, 25: 389-399.

Tebo, B.M., Bargar, J.M., Clement, B.G., Dick, G.J., Murray, K.J., Parker, D., Verity, R., Webb, S.M., 2004. Biogenic manganese oxides: Properties and Mechanisms of Formation. Annual Review of Earth and Planetary Sciences, 32: 287-328.

Tebo, B.M., Johnson, H.A., McCarthy, J.K., Templeton, A.S., 2005. Geomicrobiology of manganese(II) oxidation. Trends in Microbiology, 13(9): 421-428.

Toner, B., Fakra, S., Villalobos, M., Warwick, T., Sposito, G., 2005. Spatially Resolved Characterization of Biogenic Manganese Oxide Production within a Bacterial Biofilm. Applied and Environmental Microbiology, 71(3): 1300-1310.

Toner, B., Manceau, A., Webb, S.M., Sposito, G., 2006. Zinc sorption by biogenic hexagonal birnessite particles within a hydrated bacterial biofilm. Geochimica et Cosmochimica Acta, 70: 27-43.

Usui, A., Terashima, S., 1997. Deposition of hydrogenetic and hydrothermal manganese minerals in the Ogasawara (Bonin) Arc Area, Northwest Pacific. Marine Georesources & Geotechnology, 15(2): 127-154.

Van Cappellen, P., Viollier, E., Roychoudhury, A., Clark, L., Ingall, E., Lowe, K., Dichristina, T., 1998. Biogeochemical cycles of manganese and iron at the oxic-anoxic transition of a stratified marine basin (Orca Basin, Gulf of Mexico). Environmental Science & Technology, 32: 2931-2939.

Villalobos, M., Bargar, J., Sposito, G., 2005a. Trace metal retention on biogenic manganese oxide nanoparticles. Elements, 1(4): 223-226.

Villalobos, M., Bargar, J.R., Sposito, G., 2005b. Mechanisms of Pb(II) sorption on a biogenic manganese oxide. Environmental Science & Technology, 39: 569-576.

Villalobos, M., Lanson, B., Manceau, A., Toner, B., Sposito, G., 2006. Structural model for the biogenic Mn oxide produced by *Pseudomonas putida*. American Mineralogist, 91(4): 489-502.

Villalobos, M., Toner, B., Bargar, J., Sposito, G., 2003. Characterization of the manganese oxide produced by *Pseudomonas putida* strain MnB1. Geochimica et Cosmochimica Acta, 67(14): 2649-2662.

Wang, F., Sayre, L.M., 1989. Oxidation of Tertiary Amine Buffers by Copper(II). Inorganic Chemistry, 28(2): 169-170.

Wang, Y., Stone, A.T., 2008. Phosphonate- and carboxylate-based chelating agents that solubilize (hydr)oxide-bound Mn(III). Environmental Science & Technology, 42: 4397-4403.

Webb, S.M., Tebo, B.M., Bargar, J.R., 2005. Structural characterization of biogenic Mn oxides produced in seawater by the marine *bacillus sp.* strain SG-1. American Mineralogist, 90(8-9): 1342-1357.

Yu, Q., Kandegedara, A., Xu, Y., Rorabacher, D.B., 1997. Avoiding interferences from Good's buffers: A contiguous series of noncomplexing tertiary amine buffers covering the entire range of pH 3-11. Analytical Biochemistry, 253(1): 50-56.

Zhao, H., Zhu, M., Li, W., Elzinga, E.J., Villalobos, M., Liu, F., Zhang, J., Feng, X., Sparks, D.L., 2016. Redox Reactions between Mn(II) and Hexagonal Birnessite Change Its Layer Symmetry. Environmental Science & Technology, 50(4): 1750-1758.

Zhu, M., Ginder-Vogel, M., Parikh, S.J., Feng, X.H., Sparks, D.L., 2010a. Cation effects on the layer structure of biogenic Mn-oxides. Environmental Science & Technology, 44: 4465-4471.

Zhu, M., Ginder-Vogel, M., Sparks, D.L., 2010b. Ni(II) Sorption on Biogenic Mn-Oxides with Varying Mn Octahedral Layer Structure. Environmental Science & Technology, 44(12): 4472-4478.

7. Appendix

Table A1. Summary of Mn and Ni concentrations, and Ni isotope fractions, for reactions between vernadite and ^{62}Ni-enriched aqueous Ni(II) in the presence and absence of Mn(II)$_{aq}$ in pH 7.5 and 5.5 fluid.

	[Mn] (µM)	[Ni] (µM)	f ^{58}Ni	f ^{60}Ni	f ^{62}Ni	
Initial solid	4196	73	0.641	0.298	0.047	
Time (d)	[Mn(II)]$_{aq}$ (µM)	[Ni(II)]$_{aq}$ (µM)	f ^{58}Ni	f ^{60}Ni	f ^{62}Ni	% Ni Exchange[a]
pH 7.5 – 0 mM Mn(II)$_{aq}$						
0	0	123.3(3)[b]	0.0079(4)	0.0101(2)	0.9773(5)	0
1	0.11(2)	0.62(7)	0.054(2)	0.033(1)	0.909(2)	16.2(5)
7	0.074(9)	1.04(2)	0.067(8)	0.039(1)	0.890(5)	21(1)
14	0.101(8)	1.50(3)	0.071(2)	0.039(1)	0.887(2)	22.2(4)
pH 7.5 – 1 mM Mn(II)$_{aq}$						
0	1033.7(9)	123.3(3)	0.0079(4)	0.0101(2)	0.9773(5)	0
1	386.4(6)	46.4(5)	0.076(1)	0.0401(3)	0.877(1)	24.9(2)
7	395(53)	45(4)	0.069(8)	0.037(4)	0.88(1)	24.55
14	356(4)	43.0(8)	0.0732(2)	0.038(1)	0.881(1)	23.7(2)
pH 5.5 – 0 mM Mn(II)$_{aq}$						
0	0	126.4(5)	0.00786(3)	0.0100(2)	0.9775(2)	0
1	13.0(3)	60.2(7)	0.05545(2)	0.0307(2)	0.9077(4)	17.0(1)
7	54(3)	82(1)	0.0644(3)	0.0350(4)	0.894(1)	20.7(2)
14	89(2)	94(1)	0.066(1)	0.0356(1)	0.8912(4)	21.5(1)
pH 5.5 – 1 mM Mn(II)$_{aq}$						
0	1065(10)	126.4(5)	0.00786(3)	0.0100(2)	0.9775(2)	0
1	886(14)	118(1)	0.0504(3)	0.0290(1)	0.9140(2)	15.42(6)
7	887(1)	117.42(6)	0.0633(4)	0.03394(2)	0.8961(2)	20.21(6)
14	946(3)	121.2(6)	0.0669(3)	0.0361(1)	0.890(1)	21.9(2)

[a] Ni exchange calculated from eq 2 using measured f^{62}Ni values for Ni(II)$_{aq}$.
[b] Numbers in parentheses represent the uncertainty in the last digit at the 95% confidence level.

Table A2. Summary of Mn and Ni concentrations, and Ni isotope fractions, for reactions between HexB and ^{62}Ni-enriched aqueous Ni(II) in the presence and absence of Mn(II)$_{aq}$ in pH 7.5 and 5.5 fluid.

	[Mn] (μM)	[Ni] (μM)	f ^{58}Ni	f ^{60}Ni	f ^{62}Ni	
Initial solid	4693	52	0.643	0.296	0.046	
Time (d)	[Mn(II)]$_{aq}$ (μM)	[Ni(II)]$_{aq}$ (μM)	f ^{58}Ni	f ^{60}Ni	f ^{62}Ni	% Ni Exchange[a]
pH 7.5 – 0 mM Mn(II)$_{aq}$						
0	0	123.3(3)[b]	0.0079(4)	0.0101(2)	0.9773(5)	0
1	0.022(2)	0.150(4)	0.060(2)	0.033(1)	0.90(1)	9(1)
7	0.038(1)	0.14(1)	0.102(9)	0.054(5)	0.843(4)	18.4(6)
14	0.142	0.240	0.108	0.058	0.825	21.46
pH 7.5 – 1 mM Mn(II)$_{aq}$						
0	1033.7(9)	123.3(3)	0.0079(4)	0.0101(2)	0.9773(5)	0
1	20.9(2)	6.12(5)	0.1151(2)	0.057(1)	0.8193(4)	22.43(7)
7	6.3(5)	1.7(1)	0.132(1)	0.064(1)	0.795(2)	26.6(3)
14	6.0(3)	1.32(2)	0.141(1)	0.068(1)	0.782(1)	29.1(1)
pH 5.5 – 0 mM Mn(II)$_{aq}$						
0	0	126.4(5)	0.00786(3)	0.0100(2)	0.9775(2)	0
1	25.68(3)	36.2(6)	0.0564(1)	0.032(1)	0.905(1)	9.4(1)
7	103(2)	58.8(8)	0.098(1)	0.050(1)	0.8434(1)	18.93(2)
14	168(3)	72(1)	0.109(1)	0.0543(0)	0.829(1)	21.4(1)
pH 5.5 – 1 mM Mn(II)$_{aq}$						
0	1065(10)	126.4(5)	0.00786(3)	0.0100(2)	0.9775(2)	0
1	838.5(4)	100.1(4)	0.0512(2)	0.0287(1)	0.9141(3)	8.22(4)
7	846(1)	102.7(9)	0.089(2)	0.046(1)	0.858(4)	16.5(5)
14	921(17)	108.7(3)	0.103(1)	0.051(1)	0.838(2)	19.7(3)

[a] Ni exchange calculated from eq 2 using measured f^{62}Ni values for Ni(II)$_{aq}$.

[b] Numbers in parentheses represent the uncertainty in the last digit at the 95% confidence level.

Table A3. Summary of Mn and Ni concentrations, and Ni isotope fractions, for reactions between TriB and ^{62}Ni-enriched aqueous Ni(II) in the presence and absence of Mn(II)$_{aq}$ in pH 7.5 and 5.5 fluid.

	[Mn] (µM)	[Ni] (µM)	f ^{58}Ni	f ^{60}Ni	f ^{62}Ni	
Initial solid	4628	76	0.642	0.297	0.047	
Time (d)	[Mn(II)]$_{aq}$ (µM)	[Ni(II)]$_{aq}$ (µM)	f ^{58}Ni	f ^{60}Ni	f ^{62}Ni	% Ni Exchange[a]
pH 7.5 – 0 mM Mn(II)$_{aq}$						
0	0	123.3(3)[b]	0.0079(4)	0.0101(2)	0.9773(5)	0
1	0.47(2)	24(1)	0.0184(2)	0.0142(3)	0.963(1)	2.5(1)
7	0.496(6)	25(3)	0.027(2)	0.018(1)	0.949(4)	4.9(7)
14	0.44(8)	15(2)	0.037(2)	0.023(1)	0.935(3)	7.5(5)
pH 7.5 – 1 mM Mn(II)$_{aq}$						
0	1033.7(9)	123.3(3)	0.0079(4)	0.0101(2)	0.9773(5)	0
1	743(8)	73.7(9)	0.018(2)	0.014(1)	0.962(3)	2.5(5)
7	616(8)	39(1)	0.031(2)	0.020(1)	0.944(2)	5.8(4)
14	599(20)	33(2)	0.041(1)	0.0247(3)	0.9285(3)	8.80(5)
pH 5.5 – 0 mM Mn(II)$_{aq}$						
0	0	126.4(5)	0.00786(3)	0.0100(2)	0.9775(2)	0
1	38.0(6)	102.3(4)	0.0372(4)	0.0232(3)	0.934(1)	8.0(1)
7	43.96(6)	102(1)	0.0553(5)	0.0314(1)	0.9072(3)	13.31(5)
14	55(3)	94(10)	0.062(2)	0.0333(1)	0.899(2)	15.0(4)
pH 5.5 – 1 mM Mn(II)$_{aq}$						
0	1065(10)	126.4(5)	0.00786(3)	0.0100(2)	0.9775(2)	0
1	972(12)	73.7(7)	0.032(2)	0.0205(1)	0.942(2)	6.3(3)
7	984(27)	77(7)	0.0517(1)	0.0297(1)	0.9128(3)	12.18(6)
14	996(32)	73(9)	0.062(1)	0.034(1)	0.897(2)	15.4(4)

[a] Ni exchange calculated from eq 2 using measured f^{62}Ni values for Ni(II)$_{aq}$.

[b] Numbers in parentheses represent the uncertainty in the last digit at the 95% confidence level.

Table A4. Summary of Mn and Ni concentrations, and Ni isotope fractions, for sample-free controls in pH 7.5 and 5.5 fluid.

Time (d)	[Mn(II)]$_{aq}$ (μM)	[Ni(II)]$_{aq}$ (μM)	f ^{58}Ni	f ^{60}Ni	f ^{62}Ni	% ^{62}Ni Exchange
pH 7.5 – Mn(II)$_{aq}$ + Ni(II)$_{aq}$						
0	1033.7(9)[a]	123.3(3)	0.0079(4)	0.0101(2)	0.9773(5)	NA
1	1043(14)	123(1)	0.00807(2)	0.0101(1)	0.9771(1)	NA
7	1017(21)	120(2)	0.008(1)	0.0100(1)	0.9775(1)	NA
14	1039(35)	121(6)	0.0079(3)	0.0101(2)	0.9772(4)	NA
pH 5.5 – Mn(II)$_{aq}$ + Ni(II)$_{aq}$						
0	1065(10)	126.4(5)	0.00786(3)	0.0100(2)	0.9775(2)	NA
1	1028(6)	122.6(6)	0.00792(4)	0.01013(1)	0.9774(2)	NA
7	1049(4)	124.2(7)	0.00830(1)	0.01037(5)	0.9766(1)	NA
14	1074(18)	128(2)	0.0078(1)	0.01003(3)	0.9775(7)	NA

[a] Numbers in parentheses represent the uncertainty in the last digit at the 95% confidence level. NA = not applicable.

Table A5. Summary of Mn concentrations for buffered (10 mM MOPS or MES) and pH-adjusted $Mn(II)_{aq}$- and $Ni(II)_{aq}$-free controls in pH 7.5 and 5.5 fluid. Reported are the Mn concentrations and the equivalent percent Mn dissolved of total Mn available in each reactor.

Time (d)	$[Mn(II)]_{aq}$ (µM)	%Mn(II) Dissolved	$[Mn(II)]_{aq}$ (µM)	%Mn(II) Dissolved
	pH 7.5 – Vernadite, 10 mM MES		**pH 5.5 – Vernadite, 10 mM MES**	
0	0	0	0	0
1	0.02[a]	0.003	5.38	0.70
7	0.01	0.001	33.78	4.39
14	0.01	0.001	56.49	7.35
	pH 7.5 – HexB, 10 mM MES		**pH 5.5 – HexB, 10 mM MES**	
0	0	0	0	0
1	0.03	0.001	5.50	0.24
7	0.02	0.001	47.72	2.06
14	0.02	0.001	81.54	3.51
	pH 7.5 – TriB, 10 mM MES		**pH 5.5 – TriB, 10 mM MES**	
0	0	0	0	0
1	0.14	0.01	10.86	1.01
7	0.22	0.02	14.78	1.38
14	0.21	0.02	26.63	2.49
	pH 7.5 – Vernadite, buffer-free		**pH 5.5 – Vernadite, buffer-free**	
0	0	0	0	0
1	1.37	0.18	1.15	0.15
7	4.16	0.54	2.25	0.29
14	17.95	2.33	3.46	0.45
	pH 7.5 –HexB, buffer-free		**pH 5.5 –HexB, buffer-free**	
0	0	0	0	0
1	6.10	0.26	6.44	0.28
7	3.15	0.14	1.36	0.06
14	5.10	0.22	3.91	0.17
	pH 7.5 – TriB, buffer-free		**pH 5.5 – TriB, buffer-free**	
0	0	0	0	0
1	2.14	0.20	1.35	0.13
7	2.17	0.20	0.95	0.09
14	2.88	0.27	1.83	0.17

[a] Single reactors only

Chapter 4

Nickel Exchange Between Aqueous Ni(II) and Deep-Sea Ferromanganese Nodules and Crusts

Tobias Hens[1], Joël Brugger[1], Barbara Etschmann[1], David Paterson[2], Helen E. A. Brand[1,2], Anne Whitworth[1], Andrew J. Frierdich[1]

[1]School of Earth, Atmosphere & Environment, Monash University, Clayton, VIC 3800, Australia
[2]Australian Synchrotron, ANSTO, Clayton, VIC 3168, Australia

88

1. Abstract

Deep-sea ferromanganese (Fe-Mn) nodules and crusts are rich in traditional and non-traditional metals with both current and emerging economic value. Mn(III,IV) oxides (e.g., phyllomanganates) are important host phases for these metals (e.g., Ni), which are structurally incorporated during nodule and Fe-Mn crust formation. Recrystallization of phyllomanganates can be catalyzed by aqueous Mn(II) ($Mn(II)_{aq}$) during (bio)geochemical Mn redox cycling. The fate of structurally incorporated metals during such recrystallization of Mn(III,IV) oxides remains, however, poorly constrained. Here, we use a ^{62}Ni isotope tracer to determine the exchangeability of dissolved Ni with structurally incorporated Ni in two deep-sea Fe-Mn nodules and one crust. Ni exchange between solid and solution was investigated during reactions in 1 mM $Mn(II)_{aq}$ and in Mn(II)-free solutions under variable pH conditions (pH 5.5 and 7.5) over time. Sample characterization shows that all samples are of hydrogenetic or mixed hydrogenetic-diagenetic origin and Ni is preferentially associated with the phyllomanganates. Our Ni exchange experiments reveal that in some samples up to 25% of incorporated Ni is exchangeable with the fluid after 14 days. The prevalent reaction pathways exhibit pH-dependent behavior during phyllomanganate recrystallization and differ between sample types, with $Mn(II)_{aq}$ enhancing Ni exchange in the Fe-Mn crust-fluid system and Ni exchange being independent of $Mn(II)_{aq}$ concentrations in the Fe-Mn nodule-fluid systems. The exchangeability of structurally-incorporated Ni in ferromanganese nodules and crusts indicates a labile behavior that potentially makes it available for biogeochemical processes in the marine environment.

2. Introduction

Deep-sea ferromanganese (Fe-Mn) nodules and crusts are considered future potential resources due to their strong enrichment in base and high-tech metals, such as Co, Ni, Cu, Zn, Li, Ti, Zr, Nb, Mo, Te, W, Pt, Bi, Th, as well as rare earth elements and yttrium (REY) (Hein and Koschinsky, 2014; Hein et al., 2013). The most commonly occurring Fe-Mn deposits with resource potential are mixed-type hydrogenetic-diagenetic nodules and hydrogenetic crusts, which form through precipitation of dissolved metals from oxic seawater (hydrogenetic formation) or remobilization of elements by pore fluids under oxic/suboxic conditions within the sediment (diagenetic formation) (Hein and Koschinsky, 2014; Hein et al., 2003; Koschinsky and Halbach, 1995; Koschinsky and Hein, 2003; Kuhn et al., 2017). The predominant mineral phases of Fe-Mn nodules and crusts are poorly crystalline Mn and Fe (oxyhydr)oxides (e.g., vernadite, feroxyhyte, and ferrihydrite), which are intimately intergrown (Baturin, 1988; Hein and Koschinsky, 2014). More recently, deep-sea Fe-Mn concretions have also become recognized as valuable archives for ocean and climatic evolution over the past 70 Ma due to the stratigraphic layer-by-layer growth of their Fe and Mn (oxyhydr)oxide mineral phases (Conrad et al., 2017; Frank et al., 1999; Glasby, 2006; Goto et al., 2017; Klemm et al., 2005; Koschinsky and Hein, 2017; Levasseur et al., 2004; Lusty and Murton, 2018).

Mn (oxyhydr)oxides, such as negatively charged phyllo- and tectomanganates prevalent in Fe-Mn nodules and crusts, are among the strongest known metal scavengers in the environment (Goldberg, 1954; Hein and Koschinsky, 2014; Miyata et al., 2007; Tebo et al., 2004). Negative charge balancing, and consequently metal enrichment, occurs through adsorption of mono- or divalent cations below/above Mn octahedra layer vacancies, into the interlayer(s) of phyllomanganates (Drits et al., 1997; Manceau et al., 1992; Manceau et al., 2014; Peacock and Sherman, 2007a; Peacock and Sherman, 2007b; Villalobos et al., 2003), and by incorporation of cations into the phyllomanganate sheets or tectomanganate tunnel structure (Bodeï et al., 2007; Post, 1999; Post et al., 2003). Nickel has been shown to adsorb above vacancy sites and incorporate within the structure of synthetic birnessite, although with continued reaction the proportion of incorporated Ni increases (Peacock, 2009). Natural Fe-Mn deposits, on the other hand, consist exclusively of incorporated Ni (Peacock and Sherman, 2007a).

Fe-Mn nodules and crusts, moreover, harbor diverse microbial communities, which among others consist of Mn^{2+}-oxidizing and Mn^{4+}-reducing bacteria (Blöthe et al., 2015; Ehrlich, 1963; Ehrlich et al., 1972). During microbial respiration of organic matter, Mn oxides can

serve as terminal electron acceptors (Lovely, 2000; Myers and Nealson, 1988) as part of the biogeochemical manganese cycle, resulting in reductive dissolution of Mn(IV) oxides and corresponding release of dissolved Mn(II) ($Mn(II)_{aq}$) into seawater and pore water. Biogenic processes can also oxidize $Mn(II)_{aq}$ (Emerson, 2000; Tebo et al., 2005) to form δ-MnO_2-like phyllomanganates (Lovely, 2000; Myers and Nealson, 1988; Skinner and Fitzpatrick, 1992; Villalobos et al., 2006; Webb et al., 2005). At redox interfaces this interplay of processes leads to coexistence and abiotic back-reactions between $Mn(II)_{aq}$ and Mn(IV) oxides.

Phyllomanganates subjected to high concentrations of $Mn(II)_{aq}$ may exhibit reductive phase transformation to Mn(III)-bearing minerals due to net Mn(II) oxidation and Mn(IV) reduction (Elzinga, 2011; Elzinga and Kustka, 2015; Lefkowitz et al., 2013; Perez-Benito, 2002). Near-complete exchange between dissolved and solid-phase Mn has been observed during these phase transformations (Elzinga and Kustka, 2015). Furthermore, it has been shown that phyllomanganate recrystallization is actively catalyzed by $Mn(II)_{aq}$ through coupled comproportionation (Mn(II) + Mn(IV) → 2Mn(III)) and disproportionation (2Mn(III) → Mn(II) + Mn(IV)) of Mn species, even in the absence of observable phase transformation (Elzinga, 2016).

Reactions between newly formed phyllomanganates and low concentrations of $Mn(II)_{aq}$ (e.g., $Mn(II)_{aq}/Mn(IV)_s$ < 1) result in mineral phase products with high degrees of crystallinity and low Mn average oxidation states (Bargar et al., 2009; Bargar et al., 2005; Frierdich et al., 2011b; Learman et al., 2011; Mandernack et al., 1995; Mann et al., 1988; Pecher et al., 2003; Toner et al., 2005). This is attributed to abiotic comproportionation between Mn(II) and Mn(IV), resulting in the formation of Mn(III) within and above/below octahedral sheet vacancies (Hinkle et al., 2016; Zhao et al., 2016). This, in turn, can limit trace element uptake by these phases (Droz et al., 2015; Hinkle et al., 2017; Lefkowitz and Elzinga, 2017) as a result of the filling or blocking of phyllomanganate sheet vacancies by Mn(III).

We have recently investigated the effects of $Mn(II)_{aq}$ on Ni speciation during the recrystallization of manganite (γ-Mn(III)OOH) (Hens et al., 2018). Our results indicate that Ni is cycled between solid and solution by coupled disproportionation-comproportionation (DP-CP) and electron transfer-atom exchange (ET-AE) reactions mediated by $Mn(II)_{aq}$. In the absence of manganite phase transformations, a pH dependency of the prevailing mechanism was observed with DP-CP likely being the dominant process at lower pH (5.5) and

ET-AE at higher pH (7.5). Based on these findings we hypothesize that reactions between Mn(II)-bearing fluids and Mn oxides of deep-sea ferromanganese concretions may lead to similar mineral-fluid repartitioning of structurally compatible trace metals and contaminants associated with the Mn oxide mineral phases, which may have implications for contaminant mobility or trace element availability in natural environments.

Here, we evaluate the role of $Mn(II)_{aq}$ on Ni(II) cycling between aqueous solutions and two Fe-Mn nodules and one Fe-Mn crust. The elemental and structural composition of the samples was investigated with inductively coupled plasma optical emission spectrometry and mass spectrometry (ICP-OES and ICP-MS), synchrotron X-ray diffraction (SXRD), and synchrotron X-ray fluorescence microscopy (SXFM) to elucidate how Ni is associated with these materials. Subsequently, the samples were reacted with a ^{62}Ni-enriched $Ni(II)_{aq}$ solution and variable concentrations of $Mn(II)_{aq}$ to quantify the available solid-phase Ni that exchanges with the solution. The effects of $Mn(II)_{aq}$, pH, and reaction time were examined.

3. Materials and Methods

3.1. Sample Recovery and Processing

Two Fe-Mn nodules (TS-5, 8FFG-007-2) and one crust (SP-8) from locations (south)east of Australia and the Southern Central Pacific Basin were utilized in this study (Table 1).

Table 1. List of ferromanganese samples utilized in this study.

Sample ID	Type	Location	Coordinates	Depth (m)
TS-5[a]	Nodule	W. slope of South Tasman Rise	47°24'06"S 145°09'60"E	3670-3968 (dredge)
8FFG-007-2[b]	Nodule	Southern Central Pacific Basin	1°26'39"S 170°00'55"W	5525 (free-fall grab)
SP-8[c]	Crust	Northern flank of South Rennell Trough	13°49'07"S 160°34'06"E	3400 (free-fall grab)

[a]See Bolton et al. (1988), [b]Bolton et al. (1992), and [c]Bolton et al. (1986) for further details.

A comprehensive discussion of the sampling locations, geological settings, and macroscopic Fe-Mn nodule and crust features, such as surface textures and internal structures, are reported elsewhere (Bolton et al., 1992; Bolton et al., 1988; Bolton et al., 1986). First, petrographic thin sections were prepared for SXFM analysis. A portion of each sample was mounted on quartz slides (SiO_2) and polished to 100 µm thickness. Next, ~8 g of ferromanganese material was

dislodged from the remaining parts of the samples and processed in bulk using a Rocklabs Standard Ring Mill with mounted agate mill head for 5 minutes. The powder was sieved (90 µm), transferred to, and stored in glass vials until further analysis. Special care was taken not to introduce nucleus or substrate components in the milling process. The mill head was cleaned with 8 M HCl and rinsed with water between the milling of each sample.

3.2. Elemental Mapping with X-ray Fluorescence Microscopy (SXFM)

The spatial distribution of selected major and trace elements was examined by using the Maia detector system on the X-ray fluorescence microscopy beamline at the Australian Synchrotron (Paterson 2011). This system allows for the fast collection of high-definition elemental maps of complex natural materials by focusing a monochromatic X-ray beam (18.5 keV) to ~2x2 µm with the help of Kirkpatrick-Baez mirrors (Paterson et al., 2011; Ryan et al., 2010; Ryan et al., 2014). Petrographic thin sections were mounted on a Perspex sample holder with Kapton tape and moved through the beam focus on a translation stage.

Overview maps of the entire thin section and regions of interest were raster-scanned to accumulate X-ray fluorescence spectra of each scan pixel. Data collection was performed in continuous mode at scanning speeds varying between 2 and 20 mm s^{-1}, resulting in dwell times of 0.20 to 2.0 ms and effective pixel sizes between 2x2 µm to 40x40 µm. Full spectra information was collected at each pixel; for the scope of this study quantitative elemental maps for Mn, Fe, Ni were produced from the raw data set with the GeoPIXE® software (CSIRO, 2011). Standard foils (Pt, Mn, and Fe) were used as external standards to constrain the quantification parameters, including the detector geometry as well as the efficiency and calibration of the ion chamber to measure photon flux.

3.3. Determination of Mn Oxidation State with XANES Imaging

The oxidation state of Mn in the starting materials was investigated using XANES imaging (Etschmann et al., 2010; Etschmann et al., 2014) for regions of interest, which were selected from the overview maps. The XANES images were constructed from stacks of SXFM maps collected for each region at 116 irregularly spaced monochromator energies that spanned the Mn-K edge, with 0.5 eV steps across the edge. The Mn Kα peak intensities for each map and at each pixel were recovered using GeoPIXE® (i.e., peak intensities are corrected for baseline including the changing energy of the scatter peak, matrix composition, and X-ray flux), and used to construct XANES spectra at each pixel (4x4 µm pixels; 58 k to 105 k pixels per

XANES map). Because of the short dwell times per pixel (2 ms), spectra from individual pixels are noisy. We extracted XANES from regions by (i) selecting pixels based on the ratio of Mn Kα peak intensity at 6.559 and 6.549 keV, highlighting potential edge shifts that are correlated primarily to the average oxidation state of Mn (Manceau et al., 2012); and (ii) selecting pixels based on the Mn concentrations.

3.4. Sample Digestion and Bulk Geochemical Analyses

To analyze bulk major, minor, and trace element concentrations, 50 ± 1 mg of each sample was dissolved by HF-HNO$_3$ digestion. Prior to digestion, aliquots of powdered samples were dried at $110 \pm 2°$ C in uncapped 10 mL glass vials for 24 hours. Samples were subsequently dissolved with a 2 % HF – 16 M HNO$_3$ solution (ratio 2:1) in sealed Teflon PFA screw-cap beakers and placed on a hot plate at $160°$ C for 5 days. 1 mL of 10 M HCl was then added to the beakers and heated for 3 days at $130°$C. The decomposed samples were evaporated for ~8 hours until dryness following the addition of 1 mL doubly distilled 16 M HNO$_3$. The residue was re-dissolved with 2% HNO$_3$ and diluted to 1:1000 by mass.

Major elements (Na, Mg, Al, P, K, Ca, Ti, Mn, Fe) were analyzed by ICP-OES (Thermo Scientific iCAP 7000 Duo operated in radial mode) whereas ICP-MS (Thermo Scientific iCAP-Q quadrupole operated in standard mode) was utilized to measure minor and trace element concentrations, including rare earth elements plus yttrium (REY). Blanks and certified calibration standards (Sigma-Aldrich Choice) were run with each sample set. Accuracy of elemental determinations was assessed by analysis of United States Geological Survey certified reference materials NOD-A-1 and NOD-P-1 (Flanagan and Gottfried, 1980), which were processed and analyzed in the same manner as Fe-Mn samples. Measured values for Mn, Fe, and Ni were within 5% of the certified values.

3.5. Mineral Phase Identification

Mineral phase identities were determined by SXRD on the powder diffraction beamline (Wallwork et al., 2007) at the Australian Synchrotron. Sample powders were ground with a mortar and pestle before transfer to a 0.3 mm diameter borosilicate glass capillary. During data collection, the capillaries were rotated at ~1 Hz to increase powder averaging. Diffraction patterns were collected with the MYTHEN-II microstrip detector (Schmitt et al., 2003), at a wavelength of 0.7745(1) Å, determined from refinement of NIST SRM LaB$_6$ 660b. To cover the gaps between detector modules, two datasets, each of collection time 300 s, were collected

94

with the detector set 5° apart. Paired 300 s datasets were subsequently merged using the in-house PDViPeR software. Bruker DIFFRAC.EVA was used to identify the minerals present in the samples using the Crystallography Open Database.

3.6. Ni Exchange Experiments

Ni isotope exchange experiments were conducted in an anaerobic chamber (1.5-3.0% H_2 atmosphere, balance N_2) with O_2 levels maintained at less than 1 ppm by continuous circulation of the atmosphere over Pd catalysts. Solutions were purged with N_2 for 30 min prior to introduction into the chamber. Labware and samples were allowed to equilibrate with the anaerobic chamber atmosphere several days before use. Anoxic conditions were maintained to prevent the external oxidation of $Mn(II)_{aq}$ by O_2 which may nucleate new mineral phases. A detailed description of the protocols can be found in (Hens et al., 2018).

Experiments were carried out in duplicate with 20 mg of Fe-Mn nodules or crust suspended in 8.7 mL $\geq$18.2 MΩ·cm water (hereon water). Solution pH was then adjusted to 7.5 or 5.5 by addition of 1 mL of a 0.1 M MOPS (3-(1-morpholino)propanesulfonic acid)/NaCl buffer solution or 1 mL of a 0.1 M MES (2-(4-morpholino)ethanesulfonic acid)/NaCl buffer solution. Subsequently, 0.1 mL of 10 mM ^{62}Ni-enriched Ni(II) solution (prepared by dissolution of Ni^0, 98% ^{62}Ni, Isoflex, USA in 1 M HCl), and no or 0.1 mL of 100 mM $MnCl_2$ solution, to yield a final nominal Mn(II) concentration of 0 or 1 mM, were added to initiate the reactions. Adjustment of pH was achieved by addition of small volumes (<0.1 mL) of 1 M NaOH. Final reactor volumes were 10 mL. Reactors were then wrapped in Al foil to avoid photochemical reactions and mixed by gyration until sampling. Solution pH of 7.5 and 5.5 varied by less than 0.2 pH units between the time of reactor preparation and sampling.

Samples aged for 1-7 days were filtered with disposable filters (Thermo Scientific Choice 25 mm syringe filter, 0.22 µm PES). 14-day samples were filtered with a reusable syringe filter assembly (Merck Millipore Swinnex with a 0.22 µm Durapore membrane) to recover the solid fraction which was then dried on filter membranes inside the anaerobic chamber for $\geq$72 hours at room temperature and subsequently characterized by SXRD. All filtrates were acidified to 0.1 M HCl and analyzed by ICP-MS.

Buffered blank and control reactors were prepared in a similar fashion to what has been noted above to monitor potential changes in dissolved metal concentrations and sample mineralogy

(e.g., phase transformations) unrelated to Mn(II)$_{aq}$-sample interactions. The blanks contained Ni(II)$_{aq}$ and Mn(II)$_{aq}$ solutions with concentrations identical to the Ni exchange experiments but no Fe-Mn sample. The control reactors consisted of Fe-Mn sample powders in buffered Ni(II)$_{aq}$- and Mn(II)$_{aq}$-free suspensions.

3.7. Isotopic Measurements and Exchange Calculations

Similar to what has been reported in our previous work (Hens et al., 2018), quantification of Ni exchange was achieved by analyzing the Ni isotope composition in filtrates utilizing the counts on the mass-58, mass-60, mass-61, mass-62, and mass-64 ICP-MS channels. Ni counts were summed for concentration calibration of the ^{62}Ni tracer experiments, which had a changing isotope composition as a result of exchange with natural abundance Ni in samples. Individual Ni isotope mole fractions (f^{n}Ni) were calculated by dividing the counts per second (cps) of isotope n by the sum of the total Ni isotope cps as given in equation 1. An interference on the mass-58 counts was observed due to the high Fe content of the digested Fe-Mn samples. Consequently, an interference correction was applied to the ^{58}Ni counts. Aqueous samples collected during exchange experiments had negligible dissolved Fe and thus this correction had no effect on those data. At low Ni concentrations an interference on the mass-64 counts was detected. Since ^{64}Ni counts amounted to less than 0.8% (average) of the Ni counts for spiked samples, and thus exert minor influence on the calculated Ni isotope fractions, ^{64}Ni counts were excluded from the calculation of the Ni isotope fractions.

$$\mathcal{f}^{\,n}Ni = \frac{^{n}cps}{^{58}cps + \,^{60}cps + \,^{61}cps + \,^{62}cps} \tag{1}$$

The percentage of Ni in Fe-Mn samples that exchanges with Ni(II)$_{aq}$ was calculated as reported previously (Hens et al., 2018) using a homogeneous recrystallization model:

$$\% \, Ni \, Exchange = \frac{N_{aq} \times (f_{aq}^{i} - f_{aq}^{t})}{N_{solid}^{tot} \times (f_{aq}^{t} - f_{solid}^{i})} \times 100 \tag{2}$$

where N_{aq} represents the total moles of Ni(II)$_{aq}$, N_{solid}^{tot} are the total moles of Ni(II) initially associated with each Fe-Mn sample, f_{aq}^{i} is the initial isotope composition of Ni(II)$_{aq}$, f_{solid}^{i} is the initial isotope composition of Ni in the Fe-Mn sample, and f_{aq}^{t} is the isotopic composition of Ni(II)$_{aq}$ at time t>0. Furthermore, since equilibrium and kinetic isotope fractionations are insignificant relative to the large isotopic enrichment of the ^{62}Ni tracer solution, no correction

for mass-dependent isotope fractionation is applied to f_{aq}^t. The isotopic fractions of isotope n for a completely mixed system (f_{sys}^n) were calculated as follows based on mass balance:

$$f_{sys}^n = \frac{(f_{aq}^i \times N_{aq}) + (f_{solid}^i \times N_{solid}^{tot})}{(N_{aq} + N_{solid}^{tot})} \tag{3}$$

4. Results

Two deep-sea Fe-Mn nodules and one Fe-Mn crust from locations (south)east of Australia and the southern part of the Central Pacific Basin were analyzed with ICP-OES, ICP-MS, SXRD, and SXFM to characterize their geochemical and mineralogical composition. This information is important for understanding how Ni is associated with these deposits. The samples were then reacted with a ^{62}Ni-enriched Ni(II)$_{aq}$ solution in the presence or absence of Mn(II)$_{aq}$ to measure the amount of Ni associated with the samples that is exchangeable with the fluid as a function of time, Mn(II)$_{aq}$ concentration, and solution pH. As a result, the degree by which the Mn oxide phases undergo dynamic recrystallization in Mn(II)$_{aq}$-bearing solutions can be approximated.

4.1. Major and Trace Element Concentration

Fe-Mn nodules TS-5 and 8FFG-007-2 have Mn concentrations of 23.7 wt% and 21.6 wt%, Ni concentrations of 1.23 wt% and 0.76 wt%, and Fe concentrations of 9.6 wt% and 11.2 wt%, respectively. The Fe-Mn crust has lower Mn and Ni concentrations and a higher Fe concentration compared to the nodules (c.f. 12.8 wt% Mn, 0.18 wt% Ni, and 20.8 wt% Fe) (Table S1). Analyzed concentrations of P (<0.4 wt%), Ca (<2.3 wt%), and Al (<3.7 wt%) in all samples indicate a negligible degree of phosphatization and only minor contribution of detrital material to the chemical composition of the samples (Hein et al., 1997). Other major and trace elements, such as K, Mg, Na, Co, Ni, Cu, Zn, and REY have measured concentrations similar to typical Fe-Mn nodules and crusts found in the global oceans (Table S1) (Hein and Koschinsky, 2014; Kuhn et al., 2017).

An elegant approach to visualize the authigenic enrichment of major, minor, and trace elements of the samples is the comparison of normalized element concentrations to average Upper Continental Crust (UCC) values as shown in Figure 1 (Hein et al., 2003; Peucker-Ehrenbrink and Jahn, 2001; Rudnick and Gao, 2003). The following metals exhibit strong enrichment compared to UCC values: Mn, Co, Ni, Cu, Mo, Cd, and Tl (>100-fold), Te (>10000-fold), and Zn, Sb, W, Pb, and Bi (>10-fold).Considering the negligible influence of detrital minerals and

phosphatization on the observed enrichment it is likely that these elements are associated with Mn and Fe oxide phases, which is consistent with reports from previous studies (Hein and Koschinsky, 2014; Mohwinkel et al., 2014).
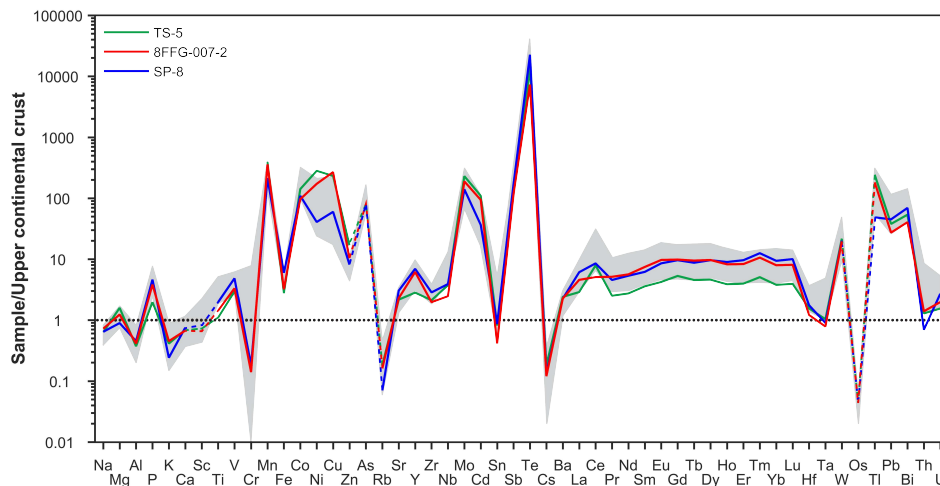
Fig. 1. Element enrichment patterns of Fe-Mn nodules TS-5, 8FFG-007-2, and crust SP-8 relative to their mean abundances in the upper continental crust (UCC) (Hein et al., 2003; Rudnick and Gao, 2003). The grey area represents UCC-normalized minimum and maximum element enrichment values of Mn nodules from the Cook Islands EEZ (Hein et al., 2015) whereas colored dashed lines represent elements that have not been analyzed or were below detection limit (Table S1). Figure modified after Goto et al. (2017).
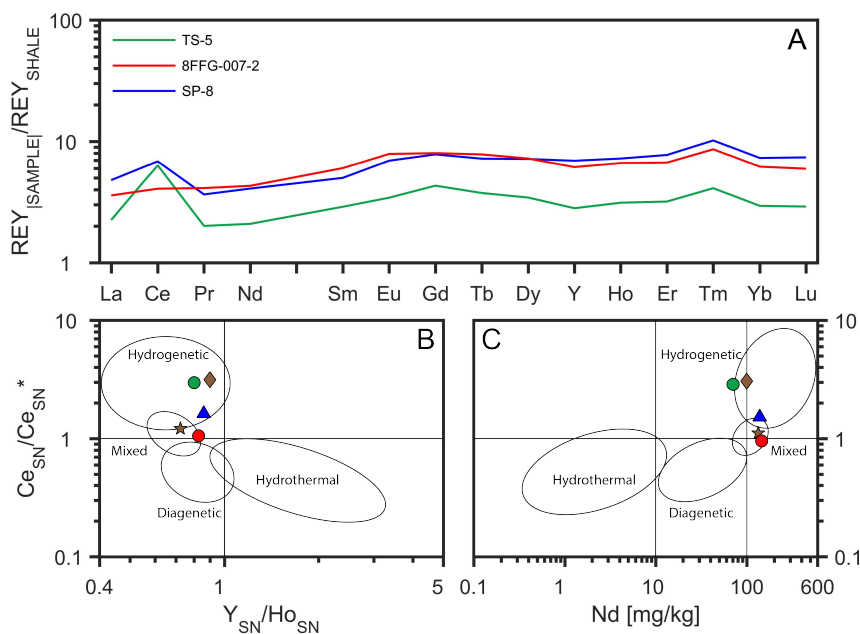
Fig. 2. (A) Post-Archean Australian Shale-normalized (McLennan, 2001; Taylor and McLennan, 1985) REY_{SN} patterns for TS-5, 8FFG-007-2, and SP-8. Samples show patterns characteristic of hydrogenetic (TS-5, SP-8) and mixed-type hydrogenetic-diagenetic deposits (8FFG-007-2), respectively. (B) Genetic classification of samples using the Ce_{SN}/Ce_{SN}^* ratio vs Y_{SN}/Ho_{SN} ratio and (C) Ce_{SN}/Ce_{SN*} ratio vs Nd. TS-5 (green circle), SP-8 (blue triangle), and USGS reference material NOD-A1 (brown diamond; measured in this study) plot in the hydrogenetic field. 8FFG-007-2 (red circle) and USGS reference material NOD-P1 (brown star, measured in this study) plot in the mixed-type field. Discrimination plots and fields modified after Bau et al. (2014).

4.2. Sample Classification

Major, minor, and REY concentrations were used to discriminate genetic sample types (e.g., hydrogenetic vs. diagenetic formation) (Bau et al., 2014; Bonatti et al., 1972). Hydrogenetic deposits generally have high Fe and Mn concentrations (>10%), whereas diagenetic and hydrothermal deposits are characterized by a strong fractionation of Fe or Mn (Bonatti et al., 1972; Glasby, 2006). Consequently these deposit types plot in distinct regions of the conventionally used ternary discrimination diagram first proposed by Bonatti et al. (1972), which utilizes Fe – Mn – 10x(Cu + Ni + Co) as axes (Fig. S1).

Nodules TS-5 and 8FFG-007-2 have Mn/Fe ratios of 2.47 and 1.93, respectively, and elevated concentrations of Cu, Ni, and Co (Table S1). SP-8 is characterized by a Mn/Fe ratio of 0.62 and low Cu, Ni, Co concentrations (Table S1). Halbach et al. (1988) note that Mn/Fe ratios ≤5 are typical for hydrogenetic nodules, whereas Glasby (2006) found Mn/Fe ratios of 1 to 2.5 to be indicative of interactions between hydrogenetic processes and oxic diagenesis. It has, however, been argued by other authors that the bulk element concentrations may be an insufficient tool to clearly infer genesis, since element concentrations of individual growth layers of Fe-Mn nodules and crusts may distinctly differ from bulk composition as a result of changing environmental conditions (Josso et al., 2016; Kuhn et al., 2017).

Discrimination diagrams that utilize Post-Archean Australian Shale-normalized REY (REY_{SN}) concentrations to discriminate the genetic type of non-phosphatized ferromanganese deposits were proposed by Bau et al. (2014). This approach exploits the coherent behavior of REY during fractionation in natural environments. The REY_{SN} patterns of TS-5, 8FFG-007-2, and SP-8 show a pronounced Ce anomaly, and slightly negative Y anomaly, characteristics which are indicative of hydrogenetic to mixed hydrogenetic-diagenetic deposits (Fig. 2A). The REY_{SN} values can be plotted in bivariate diagrams (Fig. 2B,C) of Ce_{SN}/Ce_{SN*} vs. Nd and Ce_{SN}/Ce_{SN*} vs. Y_{SN}/Ho_{SN}, where Ce_{SN*} was calculated as $Ce_{SN*} = 0.5La_{SN} + 0.5Pr_{SN}$. TS-5 and SP-8 plot in the hydrogenetic field whereas 8FFG-007-2 plots in the mixed-type hydrogenetic-diagenetic field. The reference materials NOD-A-1 and NOD-P-1 plot in positions similar to what has been reported previously by Bau et al. (2014). The bivariate diagrams thus support the results from the ternary diagram (Fig. S1) in that the dominant formation process of the samples is indeed hydrogenetic, despite a recognizable diagenetic influence for sample 8FFG-007-2. Moreover, the diagrams clearly show that hydrothermal influence on the formation process of all samples is negligible.

4.3. Bulk Mineralogical Composition, Element Distribution, and Mn Oxidation State

SXRD and SXFM were employed to examine the mineralogical composition and element distribution within the ferromanganese samples. SXRD patterns show the samples to be dominantly composed of disordered phyllomanganates (e.g., vernadite, birnessite) and accessory minerals, such as phillipsite, feldspar, apatite, muscovite, and crystalline Fe oxide in the form of goethite (Fig. 3). The majority of single well-defined peaks present in all patterns are characteristic of crystalline quartz. The occurrence of todorokite (tectomanganate), which also exhibits a phyllomanganate-like 10 Å reflection but has structural stability until 175 ℃, is suspected as heating the samples to 110 °C for 72 hours did not conclusively collapse the layer spacing to 7 Å (Post et al., 2003).

Despite the similar mineralogical composition of all samples, striking differences in the prevailing Mn oxide phases exist between nodules and the Fe-Mn crust. Patterns of TS-5 and 8FFG-007-2 clearly depict the presence of c-layer ordering in form of (001) reflections, which is indicative of birnessite (Fig. 3). This is in clear contrast to SP-8 where these layer reflections are absent, thus indicating a predominantly vernadite-based Mn oxide composition. Additional phyllomanganate high angle reflections [(20,11) and (30,02)] also show these slight variations with changing peak intensities (Fig. 3).
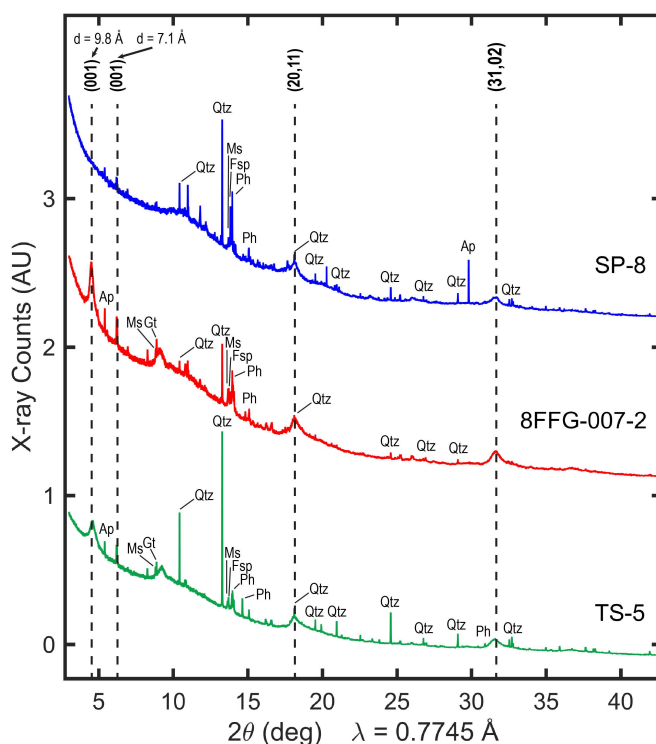
Fig. 3. SXRD patterns of Fe-Mn samples TS-5, 8FFG-007-2, and SP-8. The vertical dashed lines indicate the position of characteristic Mn oxide reflections. Identifiable accessory mineral phases include apatite (Ap), feldspar (Fsp), goethite (Gt), muscovite (Ms), phillipsite (Ph), and quartz (Qtz).

The SXFM-mapped spatial element distribution of Mn, Ni, and Fe, provides further insight into the differences between the samples. Nodule TS-5 is composed of a Fe-rich nucleus, which is covered by dark-brown and dark-grey layers comprised mostly of intergrown Fe-Mn layers (Fig. 4A-B). A positive correlation between Mn and Ni exists (Fig. S2) with the highest concentrations Ni found in a distinctly recognizable outer rim that mainly consists of Mn-rich phases and components of detrital material (Fig. 4A, C-F). Prevalent growth structures of TS-5 are columnar (core) and dendritic (outer rim). The existence of an abrupt contact between inner core and outer rim layers indicates different phases of Fe-Mn oxide precipitation presumably due to changes in environmental conditions, which may have led to partial dissolution of older layers prior to the formation of the dendritic layers, similar to what has been described by Benites et al. (2018). The three-color SXFM map of 8FFG-007-2 shows similar features and, moreover, highlights the intricate filling of fractures by Fe-Mn oxides phases (Fig. S3). SP-8, in contrast, is characterized by massive laminae of intermixed phases that indicate stable environmental conditions during Fe-Mn crust formation (Fig. 4G-H). While bulk Ni concentrations of SP-8 are significantly lower in comparison to the nodules (Table S1), Ni distribution is strongly associated with regions of high Mn concentrations as depicted in Figure 4I-L.

XANES imaging on each of the three Fe-Mn samples appear to reveal two different components (Fig. 5), which is best illustrated by the fact that the spectra and their derivatives show a number a well-defined isosbestic points (arrows in Fig. 5F-G). The edge position clearly indicates that the average oxidation state of Mn in these samples is mostly tetravalent (average >3.8). However, the apparent edge shift towards lower wavelengths may suggest the presence of varying amounts of Mn in a lower oxidation state. This interpretation, however, is incorrect, since the high Mn concentrations in these samples induce self-absorption in the X-ray signal. As illustrated in Figure S4, the nature of the XANES spectra depends on the Mn concentration. Using the self-absorption correction in the ATHENA package (Ravel and Newville, 2005), it was further verified that the differences in XANES spectra reflect self-absorption rather than changes in Mn speciation. Zhu et al. (2017) confirmed by colorimetric methods that Mn in birnessite and vernadite is tetravalent with an oxidation state of 4.00 ± 0.02. These authors, furthermore, show that the method of Manceau et al. (2012), based on XANES spectroscopy, underestimates the oxidation states of Mn in the measured vernadite and birnessite, with values of 3.80 ± 0.04 and 3.85 ± 0.04, respectively.

In conclusion, results of µXANES need to be interpreted carefully, because variation in spectra among pixels can be induced by effects such as self-absorption. However, in the case of the Fe-Mn samples studied here, the XANES data clearly indicate a highly homogeneous material with respect to Mn coordination and average oxidation state. In particular, no localized area with contrasting speciation was found in any of the XANES maps (e.g., Etschmann et al., 2017; Etschmann et al., 2014).
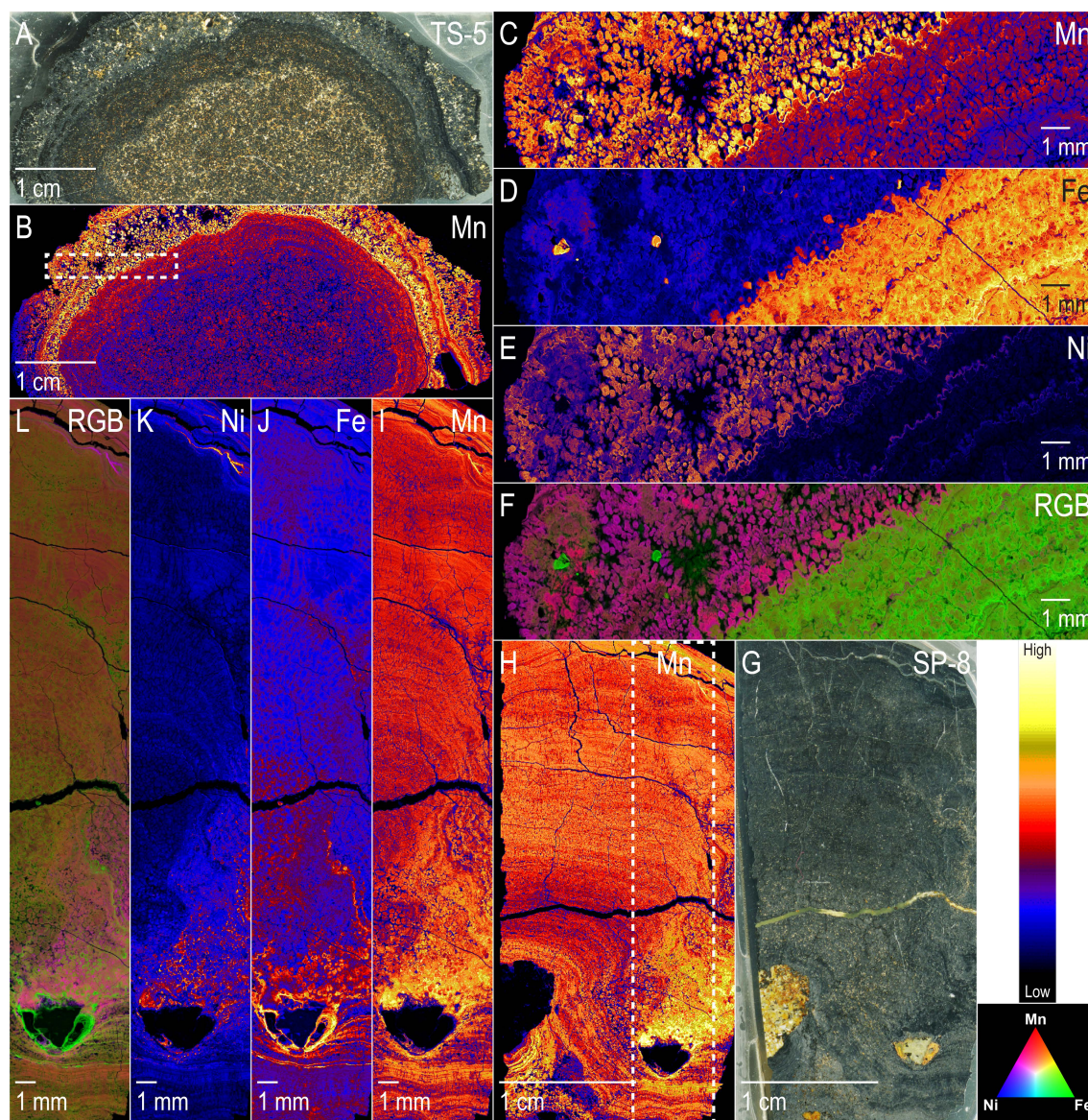
Fig. 4. High-resolution SXFM single-element and multi-element (RGB) maps of Fe-Mn nodule TS-5 (A-F) and crust SP-8 (G-L). (A-B) Photograph and SXFM single-element (Mn) overview map of the petrographic thin section of TS-5. (C-E) Single-element detail maps of the core-rim boundary of TS-5 depicting distinct Mn-Ni association and distribution of high Mn/Ni concentrations in the outer rim (C,E) and Fe in the core (D). (F) Multi-element detail map of the TS-5 core-rim boundary. (G-H) Photograph and SXFM single-element (Mn) overview map of the petrographic thin section of SP-8. (I-K) Single-element detail maps of SP-8 showing dense layering of intermixed Mn-Fe phases and spatial distribution of Ni. (L) Multi-element detail map of SP-8 highlighting strong Mn-Ni correlation. SXFM scan conditions: Overview maps – pixel size 40x40 µm, dwell time 2.0 ms; Detail maps – pixel size 2x2 µm, dwell time 0.2 ms.
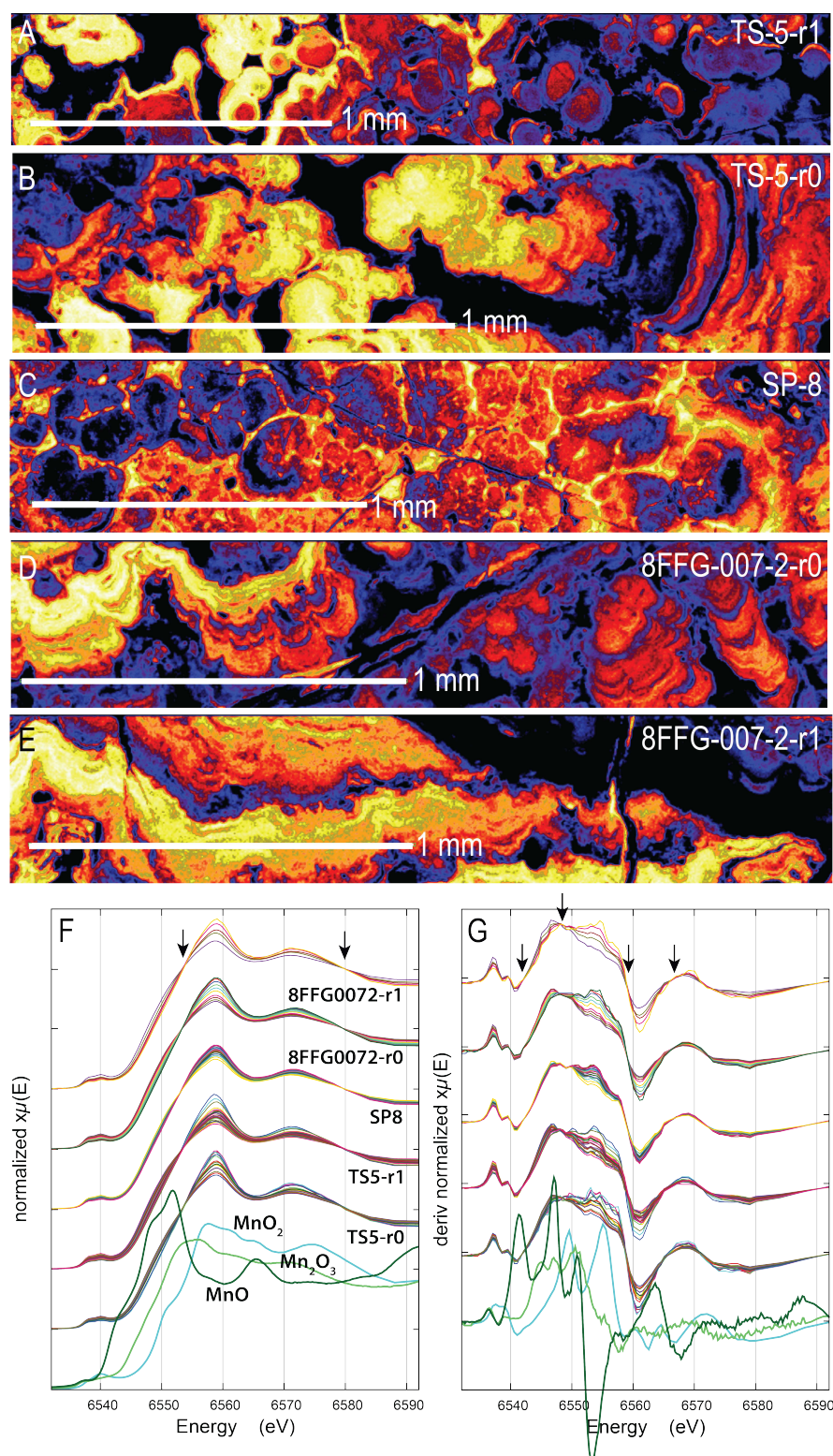
Fig. 5. XANES stack images for regions of interest of samples TS-5 (A-B), SP-8 (C), and 8FFG-007-2 (D-E). Extracted XANES spectra (F) and derivatives (G) of these regions suggest two different components as illustrated by well-defined isosbestic points (arrows) though these changes in spectral intensity are likely due to self-absorption (see Fig. S4). Map legend identical to Fig. 4 (light colors indicate high intensity, dark colors correspond to low intensity).

4.4. Ni Isotope Exchange Between Ni(II)$_{aq}$ and Ferromanganese Samples

All reactions with Fe-Mn samples exhibit similar Mn(II)$_{aq}$ and Ni(II)$_{aq}$ concentration changes over the course of the experiments. At pH 7.5, when no exogenous Mn(II)$_{aq}$ is added, Mn(II)$_{aq}$ concentrations are low (<1 µM). When Mn(II)$_{aq}$ is added to Fe-Mn sample suspensions, initial Mn(II)$_{aq}$ concentrations of ~1000 µM decrease rapidly to around 66 µM (TS-5), 42 µM (8FFG-007-2), and 171 µM (SP-8) after 14 days, with the most pronounced decrease occurring after 1 day (Tables S2-S4). Ni(II)$_{aq}$ concentrations decrease in a similar rapid fashion from their initial value of ~106 µM to <1.0-2.5 µM for all pH 7.5 reactions (Tables S2-S4).

When Fe-Mn samples are suspended in pH 5.5 Mn(II)$_{aq}$-free solutions, the Mn(II)$_{aq}$ concentrations slightly increase to ≤17 µM. Reactions with an initial Mn(II)$_{aq}$ concentration of ~1000 µM show a decreasing trend similar to pH 7.5 reactions. However, this trend is far less pronounced as less Mn(II)$_{aq}$ sorption occurs and values decrease from ~1000 µM to 570 µM (TS-5), 477 µM (8FFG-007-2), and 697 µM (SP-8), respectively. Ni(II)$_{aq}$ concentrations also decline but to a lesser extent than at pH 7.5 (Tables S2-S4).

The initial ^{62}Ni isotope composition of the samples reflects 'natural abundance' composition (measured f^{62}Ni = 0.046 (TS-5), 0.045 (8FFG-007-2), and 0.040 (SP-8)), whereas the Ni(II) solution was initially enriched in ^{62}Ni (f^{62}Ni = 0.978) and hence depleted in other Ni isotopes (f^{58}Ni = 0.006, f^{60}Ni = 0.011, and f^{61}Ni = 0.003). The ^{62}Ni isotopic fraction of Ni(II)$_{aq}$ ($f^{62}Ni_{aq}^{t}$) in pure solutions remains constant over time when no Fe-Mn sample is present (Tables S5-S6, Fig. 6A), since changes in isotopic composition are only expected to occur during Ni exchange between pools of different isotopic composition. A decrease of $f^{62}Ni_{aq}^{t}$ from the initial value of ~0.98 to about 0.71 (TS-5), 0.78 (8FFG-007-2), and 0.87 (SP-8) is observed in the presence of Fe-Mn samples and Mn(II)$_{aq}$ at pH 7.5 (Tables S2-S4). This indicates that dissolved Ni is being diluted and replaced by Ni atoms of a different isotope. This decrease is significantly larger in comparison to changes in the Ni isotope composition of Ni(II)$_{aq}$ in the absence of Mn(II)$_{aq}$ (Fig. 6A).

Other Ni(II)$_{aq}$ fractions (e.g., f^{58}Ni and f^{60}Ni) display similar, but opposite trends (Fig. 6B) which implies movement of Ni atoms from the samples with natural abundance Ni composition into the initially ^{62}Ni-enriched aqueous phase. While a decrease (f^{62}Ni) or increase (f^{58}Ni and f^{60}Ni) from their initial values towards the respective Ni isotope mass balance values is observed for all Ni isotope fractions, system mass balance values are not attained. Nevertheless, significant, yet incomplete, exchange of solid-phase Ni with Ni(II)$_{aq}$ is observed.

104
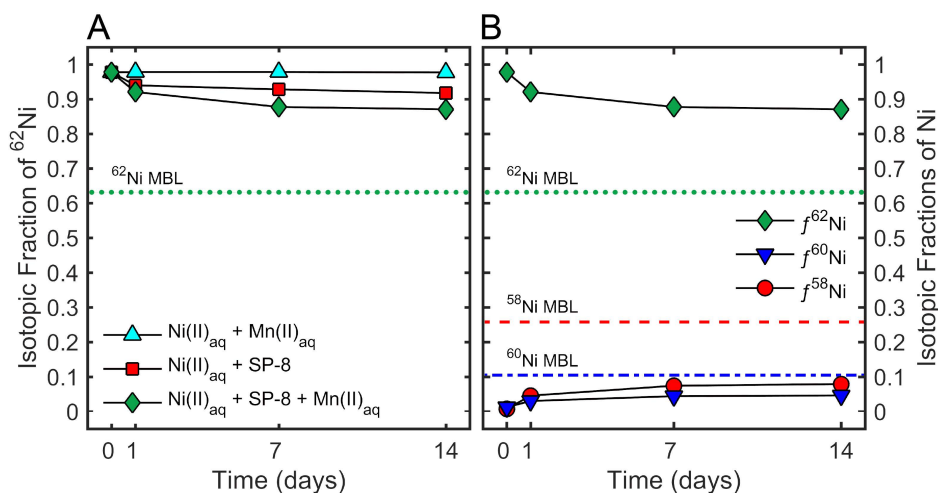
Fig. 6. (A) Evolution of the ^{62}Ni isotope fractions of 0.1 mM Ni(II)$_{aq}$ in a 1 mM Mn(II)$_{aq}$ solution, and in suspension of SP-8 in the absence and presence of 1 mM Mn(II)$_{aq}$ at pH 7.5. (B) Evolution of the Ni isotope fractions of Ni(II)$_{aq}$ during its reaction with SP-8 and 1 mM Mn(II)$_{aq}$ over 14 days at pH 7.5. Aqueous Ni(II) was initially enriched in ^{62}Ni (f^{62}Ni = 0.977), and hence depleted in the remaining Ni isotopes (f^{58}Ni = 0.007, f^{60}Ni = 0.012, and f^{61}Ni = 0.003), whereas SP-8 has a natural abundance Ni isotope composition and measured f^{n}Ni values of 0.686, 0.263, 0.012, and 0.040 for ^{58}Ni, ^{60}Ni, ^{61}Ni, and ^{62}Ni, respectively. Fe-Mn nodules (TS-5, 8FFG-007-2) show similar trends. Values for data points represent the mean of duplicate reactions; error bars not visible are smaller than symbols. MBL = mass balance line (see eq 3).

Insertion of $f^{62}Ni_{aq}^{t}$ values into equation 2 yields values of percent Ni exchange over 14 days at pH 7.5 and pH 5.5 in the absence and presence of 1 mM Mn(II)$_{aq}$ (Fig. 7A-F). Fe-Mn nodules TS-5 and 8FFG-007-2 exhibit ~8% and ~9.2% Ni exchange at pH 7.5 in the absence of Mn(II)$_{aq}$, respectively (Tables S2-S3, Fig. 7A,B). A Mn(II)$_{aq}$ concentration of 1 mM results in an increase of Ni exchange to ~9.7% and ~10.3%, respectively (Tables 2-3, Fig. 7A,B). SP-8 experiences a significantly larger extent of Ni exchange. In Mn(II)$_{aq}$-free suspensions ~11.6% are observed in comparison to ~21.9% in the presence of Mn(II)$_{aq}$ after 14 days at pH 7.5 (Table S4, Fig. 7C).

At pH 5.5, however, Ni exchange for TS-5 and 8FFG-007-2 appears to be independent of Mn(II)$_{aq}$ concentrations, since almost equal amounts within error, of solid-phase Ni are exchangeable with Ni(II)$_{aq}$ in the absence or presence of Mn(II)$_{aq}$ after 1,7, and 14 days (Fig. 7D,E). Furthermore, Ni exchange values in the absence and presence of Mn(II)$_{aq}$ for TS-5 and 8FFG-007-2 are slightly larger compared to pH 7.5 reactions. TS-5 exhibits ~10.8-11.1% Ni exchange depending on the Mn(II)$_{aq}$ concentrations whereas 8FFG-007-2 experiences ~12.4-13.7% exchange after 14 days of reaction, respectively (Tables S2-3). SP-8 experiences a discernible extent of Ni exchange depending on the Mn(II)$_{aq}$ concentrations at pH 5.5 compared to pH 7.5 although the percentage of Ni exchange is larger at lower pH (Fig. 7F). Here, about 23.1-24.8% exchange is observed in the absence and presence of Mn(II)$_{aq}$ after

14 days reaction time, respectively (Table S4). Interestingly, the calculated percentages of exchangeable Ni in the solid-phase for pH 5.5 reactions are slightly higher compared to the Ni exchange values at pH 7.5 when $Mn(II)_{aq}$ is added to solution. This contrasts the results of our previous work (Hens et al., 2018) where pH 5.5 reactions appeared to be almost identical to Ni exchange at pH 7.5 when no $Mn(II)_{aq}$ was added to solution.
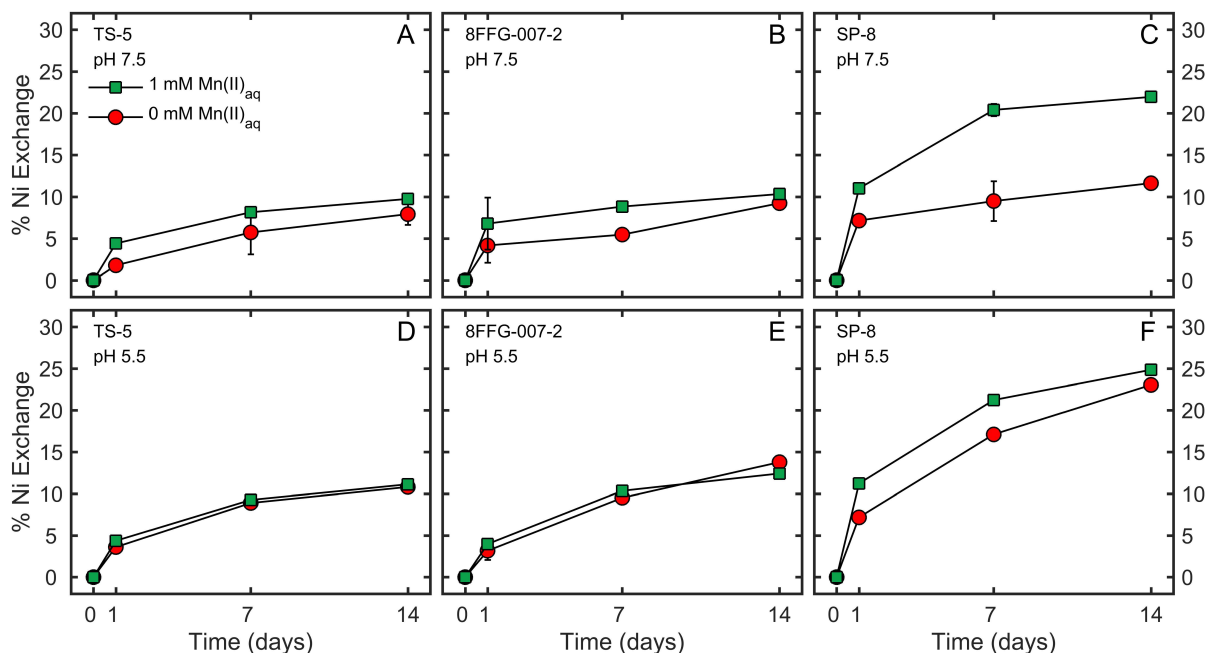
Fig. 7. Percent Ni exchange in Fe-Mn nodules TS-5 (A,D), 8FFG-007-2 (B,E), and Fe-Mn crust SP-8 (C,F) over time at pH 7.5 and pH 5.5 in the absence and presence of 1 mM $Mn(II)_{aq}$. Percent Ni exchange was calculated by inserting $f^{62}Ni$ values of $Ni(II)_{aq}$ into eq 2. Values for data points represent the mean of duplicate reactions; error bars not visible are smaller than symbols.

4.5. Structural Modifications Following Reaction with $Mn(II)_{aq}$ and $Ni(II)_{aq}$

SXRD patterns for solids that have been reacted in $Ni(II)_{aq}$-bearing fluids in the absence and presence of $Mn(II)_{aq}$ over 14 days reveal no significant bulk mineral phase transformations. A comparison of starting materials and reacted patterns for SP-8 and 8FFG-007-2 (Fig. S5A-I) shows that the reacted and unreacted Fe-Mn crust patterns (SP-8) are mostly identical with the exception of minor peak intensity variations in the region of higher angle Mn oxide reflections [(20,11) and (30,02)] (Fig. S5D-E). These intensity changes may be due to a number of factors including the packing density of sample in the borosilicate glass capillaries, variation in the thickness of the capillary wall, or slight preferred orientation. A shift in the (001) peak position towards higher 2 θ values, and thus smaller d-spacing, is seen for 8FFG-007-2 (Fig. S5F). This likely indicates replacement of larger cations (e.g., K^+ and Ba^{2+}) in the phyllomanganate structure by smaller Na^+, which is introduced by buffers during the Ni exchange experiments.

5. Discussion

This study combined synchrotron-based techniques with stable Ni isotope tracer experiments to characterize (i) the extent and dynamics of Ni exchange between $Ni(II)_{aq}$ and deep-sea Fe-Mn nodules and crusts and (ii) assess the impact of $Mn(II)_{aq}$ on Ni exchange. The main finding of our work is that Ni associated with phyllomanganates in deep-sea Fe-Mn nodules and crusts exchanges with dissolved Ni(II) in the presence as well as the absence of $Mn(II)_{aq}$. This contrasts previous research proposing that Ni sorption may be irreversible, when sorbed Ni(II) in Fe-Mn nodules and crusts is structurally incorporated into the phyllomanganate layer through replacement of Mn(III,IV) (Peacock and Sherman, 2007a; Peacock and Sherman, 2007b). Furthermore, we find that reaction mechanisms and extent of Ni exchange differ between these types of Fe-Mn concretions. While Fe-Mn crust SP-8 experiences increased Ni exchange promoted by $Mn(II)_{aq}$, Ni exchange between nodules and fluid phases is largely independent of the $Mn(II)_{aq}$ concentrations employed in this study.

5.1. Mechanistic Considerations

Previous Mn(II)-catalyzed recrystallization experiments between Ni-substituted manganite and $Mn(II)_{aq}$- and $^{62}Ni(II)_{aq}$-bearing solutions inferred two pH-dependent mechanisms controlling Ni exchange. At low pH (5.5), coupled disproportionation-comproportionation (DP-CP) drives manganite recrystallization, whereas interfacial Mn(II)-Mn(III) electron transfer-atom exchange (ET-AE) was attributed to reactions at pH 7.5 (Hens et al., 2018). Similar mechanisms have been proposed for Mn(II)-catalyzed recrystallization of synthetic vernadite (δ-Mn(IV)O_2), resulting in complete Mn exchange between $Mn(II)_{aq}$ and vernadite at pH 5.0 through extensive amounts of recrystallization (Elzinga, 2016). Here, $Mn(II)_{aq}$-Mn(IV) interactions were attributed to interfacial Mn(II)-Mn(IV) comproportionation coupled to subsequent disproportionation of transient Mn(III) species on the MnO_2 surface as derived and discussed by Elzinga (2016):

$$Mn(II)_{aq} + *Mn(IV)_s \leftrightarrow >Mn(III) + >*Mn(III) \leftrightarrow Mn(IV)_s + *Mn(II)_{aq} \qquad (4)$$
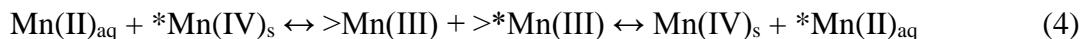
where * denotes the exchanging Mn atom and >Mn(III) and >*Mn(III) represent transient Mn(III) species.

Interfacial Mn(II)-Mn(III) ET-AE (eqs. 5-6), may also occur as alternate reaction pathways, considering that phyllomanganates may have substantial amounts of structural Mn(III)

(Elzinga, 2016; Elzinga and Kustka, 2015). In this case, Mn(II) sorption to the mineral surface takes place under favorable conditions through coupled oxidative growth (eq. 5) and reductive dissolution (eq. 6) as discussed by Frierdich et al. (2016) and Hens et al. (2018):

$$Mn(II)_{aq} \rightarrow Mn(III) + e^- \tag{5}$$

$$*Mn(III)_s + e^- \rightarrow *Mn(II)_{aq} \tag{6}$$

We observe less pronounced Mn(II) sorption in our experiments at pH 5.5 than at pH 7.5 and significant removal of Mn(II) from solution at pH 7.5, as increased sorption of Mn(II) is dependent on increasing pH (Lefkowitz et al., 2013; Zhu et al., 2010a). Resultantly, DP-CP reactions are more plausible than ET-AE under low pH conditions, whereas ET-AE becomes a prevalent reaction pathway at circum-neutral pH.

Ni exchange promoted by Mn(II)-accelerated mineral recrystallization is only observed for sample SP-8. The Fe-Mn nodules exhibit similar Ni exchange within error regardless of the initial Mn(II)$_{aq}$ concentration. This contrasts the findings of our previous study (Mn(II)$_{aq}$-manganite system), where significant Mn(II) sorption at higher pH was connected to larger extents of Ni exchange (Hens et al., 2018). The prevalence of Mn(III) in the form of Mn(III)OOH presumably enabled more Ni exchange through ET-AE at pH 7.5 where DP-CP is unfavorable. In the present study, negligible Mn(III) is associated with the initial Fe-Mn samples (Fig. 5, Fig. S4) and increased Mn(III) may only occur by reaction of added Mn(II).

Moreover, the extent of Ni exchange observed during our experiments may be influenced by the initial crystallinity of the phyllomanganates and the tendency of these phases to undergo pH-dependent structural modification towards higher crystallinity and stability (Bargar et al., 2005; Lefkowitz and Elzinga, 2017; Santelli et al., 2011). Although all samples mainly consists of poorly crystalline phyllomanganate phases, differences in crystallinity of the unreacted starting materials exist as a result of mineralogical variations between the two Fe-Mn nodules and Fe-Mn crust SP-8. XRD results show that the nodules are primarily comprised of a birnessite-based mineralogy as indicated by prominent 7 and 10 Å peaks (Fig. 3). The mineralogical composition of SP-8 appears to be dominated by vernadite and is less crystalline due to the absence of the 10 Å and decreased intensity of the 7 Å peak (Fig. 3). Highly disordered phyllomanganate sheets and higher specific surface area of vernadite compared to birnessite (Villalobos et al., 2003) accordingly contribute to the lower crystallinity of SP-8 and may explain the overall increased extent of Ni exchange observed for this sample at pH 5.5 and the enhanced exchange in the presence of Mn(II)$_{aq}$ at pH 7.5.

These observations are comparable to a recent study of goethite recrystallization in an aqueous Fe(II) system, which has shown that the initial crystallite size of goethite has a significant effect on reactivity during dynamic mineral recrystallization (Southall et al., 2018). Repeated cycles of recrystallization increased goethite crystallite sizes, which initially have greater surface area to volume ratio and thus more reactive surface sites that are able to interact with the fluid. Decreasing reactivity over time was attributed to particle coarsening by Ostwald ripening, as has been observed for other types of mineral recrystallization (Heberling et al., 2018; Heberling et al., 2016; Li et al., 2011), and the annealing of crystal defects (Notini et al., 2018; Southall et al., 2018). However, despite initial differences in crystallinity and possible occurrence of structural modifications, no complete bulk structural conversions into a lower-valence Mn phase due to precipitation of Mn(III) oxides (Bargar et al., 2005; Elzinga, 2011; Lefkowitz et al., 2013) were observed. This may be due to the mineralogical complexity (i.e., epitaxial intergrowth, multiple sorbed/incorporated trace metals) of the Fe- and Mn oxide phases.

5.2. Effects of Good's Buffers on Ni Exchange

Good's buffers are commonly employed in studies utilizing Mn(IV) oxides (Bargar et al., 2005; Droz et al., 2015; Elzinga, 2011; Elzinga and Kustka, 2015; Hinkle et al., 2016; Learman et al., 2011; Lefkowitz and Elzinga, 2015; Lefkowitz et al., 2013; Peña et al., 2011; Peña et al., 2015; Peña et al., 2007; Peña et al., 2010; Zhu et al., 2010a; Zhu et al., 2010b). These buffers have been shown to cause metal ion interference as a result of complexation (Hegetschweiler and Saltman, 1986; Kandegedara and Rorabacher, 1999) and may act as reductants for Mn(IV) by producing structural or interlayer Mn(II,III) (Elzinga and Kustka, 2015; Hinkle et al., 2016; Simanova and Peña, 2015). Hence, their use as supposedly inert compounds in redox studies has to be carefully considered.

Structural modification and partial reduction of Mn oxide substrates has been observed following hydration with HEPES during atom exchange experiments between vernadite and Mn(II)$_{aq}$, which has been attributed to piperazine moieties on the HEPES buffer molecules (Elzinga and Kustka, 2015). In contrast, MOPS and MES buffers used in this study have long been considered either non-complexing tertiary amine buffer compounds (Kandegedara and Rorabacher, 1999; Kaushal and Barnes, 1986; Lleu and Rebel, 1991; Yu et al., 1997) or weaker reductants than HEPES due to the presence of a morpholine rather than a piperazine ring (Lleu and Rebel, 1991; Wang and Sayre, 1989). MES, however, has been found to induce partial

reduction of synthetic Mn(IV) oxides (Hinkle et al., 2016). The authors observed initial release and subsequent adsorption of Mn(II), which led to structural changes of the phyllomanganate materials, and attributed these changes to the oxidation of MES (Hinkle et al., 2016). Partial reduction of Mn(IV) oxide phases by buffers, which could release $Mn(II)_{aq}$ into solution or generate structural Mn(III), could thus potentially affect the amount of Ni exchange in our experiments, although control reactions (see below) suggest these processes are minimal.

The results of our MOPS- and MES-buffered, $Mn(II)_{aq}$- and $Ni(II)_{aq}$-free controls show a negligible increase of $Mn(II)_{aq}$ in solution over the 14-day duration of the experiments at pH 7.5 (Tables S5) but slightly higher $Mn(II)_{aq}$ release is detected at pH 5.5 (Table S6), with the highest amounts of Mn(II) release occurring for SP-8. At pH 5.5 a maximum of ~17.6 µM (0.38%) of total Mn available is released, whereas pH 7.5 the highest Mn(II) concentration measured is ~0.07 µM, which equals 0.001% of total Mn available (Tables S5-6). This could be interpreted as MES acting as a stronger reductant than MOPS. However, it is more likely that increased $Mn(II)_{aq}$ release is a result of Mn disproportionation as this reaction is favored at lower pH (Hens et al., 2018).

Following the line of argument discussed by Frierdich et al. (2016), we cannot rule out that MOPS and MES may induce partial reduction of the Mn oxides associated with the Fe-Mn nodule and crust samples, as any released $Mn(II)_{aq}$ may act as a positive feedback mechanism influencing Ni exchange. However, the influence of authigenic $Mn(II)_{aq}$ on the overall Ni exchange results are likely negligible, as they are almost three orders of magnitude lower than $Mn(II)_{aq}$ concentrations present during the Ni exchange experiments. This suggests that MOPS and MES do not induce significant reduction of our samples during the Ni exchange experiments.

5.3. Environmental Implications and Conclusions

Phyllomanganates in deep-sea Fe-Mn nodules and crusts have long been recognized as effective sinks for a large array of metals and metalloids. Our work suggests that structurally-incorporated Ni in Fe-Mn nodules and crusts will continue to interact with dissolved Ni in seawater after deposition. Although $Mn(II)_{aq}$ may promote Ni exchange between phyllomanganates and solution, considerable Ni exchange also occurs in the absence of $Mn(II)_{aq}$, without observable mineral phase transformations. This highlights that Ni sorption and incorporation in the phyllomanganate layers may at least be partially reversible, which

implies that other divalent cations (e.g., Zn(II)) may similarly be susceptible to mineral-fluid repartitioning. Since pore space of consolidated Fe-Mn concretions can be largely interconnected (Blöthe et al., 2015), these mineral-fluid interactions may thus lead to significant implications for trace metal speciation and contaminant mobility, and may affect trace element uptake and release in deep-sea ferromanganese concretions (Hein and Koschinsky, 2014; Peacock and Sherman, 2007b). Hence, these interactions could alter the capacity of phyllomanganates to act as sources or sinks for important metals, which implies that Ni contents of marine Fe-Mn deposits may not be reliable proxies, for instance, of changing seawater Ni concentrations due to redox state changes in the global oceans in the past. In light of the emerging interest in deep-sea Fe-Mn nodules and crusts as paleoarchives (Koschinsky and Hein, 2017; Lusty and Murton, 2018), the reliability of such proxies thus requires careful evaluation as Ni uptake may be partially reversible.

In addition to marine settings, phyllomanganates are ubiquitous in a wide variety of terrestrial environments, such as soils and sediments, where dissolved Mn(II) can be present. Here, $Mn(II)_{aq}$ concentrations can range from µM to mM levels (i.e., in suboxic pore waters, redoxclines, mineral seeps, and areas affected by acid mine drainage (e.g., Bargar et al., 2009; Frierdich et al., 2011a)) depending on the prevalent pH conditions. Abiotic reactions between $Mn(II)_{aq}$ and phyllomanganates have been shown to induce structural changes and affect redox reactivity of Mn oxides in circum-neutral pH as well as across a broad pH range (Lefkowitz and Elzinga, 2017; Lefkowitz et al., 2013; McKenzie, 1980; Posselt et al., 1968). In the case of Ni(II), pH-dependent sorption behavior has been found (Peacock and Sherman, 2007b), which affects Ni retention by either promoting or inhibiting Ni(II) sorption (Lefkowitz and Elzinga, 2017). Consequently, interactions between phyllomanganates and $Mn(II)_{aq}$ – and under suitable environmental conditions $Mn(II)_{aq}$-accelerated recrystallization – may initiate substantial changes in Ni partitioning and speciation of terrestrial settings.

From an economic point of view, the spontaneous initiation of Ni exchange in the presence and absence of $Mn(II)_{aq}$ at ambient temperatures and near-neutral pH conditions may represent an advantage for the development of sustainable (e.g., low-energy, low toxicity, minimum-waste) hydrometallurgical methods. Utilizing established metallurgical treatment and conventional beneficiation methods for Fe-Mn nodules and crusts have been considered challenging due to the complex composition and nm-µm scale intergrowth of Fe-Mn minerals (Burns and Burns, 1977; Haynes et al., 1985; Von Heimendahl et al., 1976; Wegorzewski et al., 2018). Thus, new and potentially more sustainable metal extraction pathways warrant further investigation.

6. References

Bargar, J.R., Fuller, C.C., Marcus, M.A., Brearley, A.J., De la Rosa, M.P., Webb, S.M., Caldwell, W.A., 2009. Structural characterization of terrestrial microbial Mn oxides from Pinal Creek, AZ. Geochimica et Cosmochimica Acta, 73: 889-910.

Bargar, J.R., Tebo, B.M., Bergmann, U., Webb, S.M., Glatzel, P., Chiu, V.Q., Villalobos, M., 2005. Biotic and abiotic products of Mn(II) oxidation by spores of the marine *Bacillus* sp. strain SG-1. American Mineralogist, 90(1): 143-154.

Baturin, G.N., 1988. The Geochemistry of Manganese and Manganese Nodules in the Ocean. Sedimentology and Petroleum Geology. Springer Netherlands, Dordrecht, 356 pp.

Bau, M., Schmidt, K., Koschinsky, A., Hein, J., Kuhn, T., Usui, A., 2014. Discriminating between different genetic types of marine ferro-manganese crusts and nodules based on rare earth elements and yttrium. Chemical Geology, 381: 1-9.

Benites, M., Millo, C., Hein, J.R., Nagender Nath, B., Murton, B.J., Galante, D., Jovane, L., 2018. Integrated Geochemical and Morphological Data Provide Insights into the Genesis of Ferromanganese Nodules. Minerals, 8(488): 16.

Blöthe, M., Wegorzewski, A.V., Müller, C., Simon, F., Kuhn, T., Schippers, A., 2015. Manganese-Cycling Microbial Communities Inside Deep-Sea Manganese Nodules. Environmental Science & Technology, 49(13): 7692-7700.

Bodeï, S., Manceau, A., Geoffroy, N., Baronnet, A., Buatier, M., 2007. Formation of todorokite from vernadite in Ni-rich hemipelagic sediment. Geochimica et Cosmochimica Acta, 71(23): 5698-5716.

Bolton, B.R., Bogi, J., Cronan, D.S., 1992. Geochemistry and mineralogy of ferromanganese nodules from the Kiribati region of the eastern Central Pacific Basin. In: Keating, B.H., Bolton, B.R. (Eds.), Geology and offshore mineral resources of the central Pacific basin, Circum-Pacific Council for Energy and Mineral Resources Earth Science Series Springer, New-York, pp. 247-260.

Bolton, B.R., Exon, N.F., Ostwald, J., Kudrass, H.R., 1988. Geochemistry of ferromanganese crusts and nodules from the South Tasman Rise, southeast of Australia. Marine Geology, 84: 53-80.

Bolton, B.R., Ostwald, J., Monzier, M., 1986. Precious metals in ferromanganese crusts from the south-west Pacific. Nature, 320: 318-320.

Bonatti, E., Kraemer, T., Rydell, H., 1972. Classification and genesis of submarine iron-manganese deposits. In: Horn, D.R. (Editor), Papers from a Conference on Ferromanganese Deposits on the Ocean Floor. National Science Foundation, pp. 149-166.

Burns, R.G., Burns, V.M., 1977. The mineralogy and crystal chemistry of deep-sea manganese nodules, a polymetallic resource of the twenty-first century. Philosophical Transactions of the Royal Society London, A286: 283-301.

Conrad, T.A., Nielsen, S.G., Peucker-Ehrenbrink, B., Blusztajn, J., Winslow, D., Hein, J.R., Paytan, A., 2017. Reconstructing the evolution of the submarine Monterey Canyon System from Os, Nd, and Pb isotopes in hydrogenetic Fe-Mn crusts. Geochemistry, Geophysics, Geosystems: 18.

CSIRO, 2011. GeoPIXE Software for PIXE and SXRF Imaging. http://nmp.csiro.au/GeoPIXE.html, 26/10/2018.

Drits, V.A., Silvester, E., Gorshkov, A.I., Manceau, A., 1997. Structure of synthetic monoclinic Na-rich birnessite and hexagonal birnessite: I. Results from X-ray diffraction and selected-area electron diffraction. American Mineralogist, 82(9-10): 946-961.

Droz, B., Dumas, N., Duckworth, O.W., Peña, J., 2015. A Comparison of the Sorption Reactivity of Bacteriogenic and Mycogenic Mn Oxide Nanoparticles. Environmental Science & Technology, 49(7): 4200-4208.

Ehrlich, H.L., 1963. Bacteriology of manganese nodules: I. Bacterial action on manganese in nodules enrichments. Applied Microbiology, 11: 15-19.

Ehrlich, H.L., Yang, S.H., Mainwaring Jr., J.D., 1972. Bacteriology of manganese nodules. Zeitschrift für Allgemeine Mikrobiologie, 13(1): 39-48.

Elzinga, E.J., 2011. Reductive Transformation of Birnessite by Aqueous Mn(II). Environmental Science & Technology, 45(15): 6366-6372.

Elzinga, E.J., 2016. ^{54}Mn Radiotracers Demonstrate Continuous Dissolution and Reprecipitation of Vernadite (δ-MnO$_2$) during Interaction with Aqueous Mn(II). Environmental Science & Technology, 50(16): 8670-8677.

Elzinga, E.J., Kustka, A.B., 2015. A Mn-54 Radiotracer Study of Mn Isotope Solid-Liquid Exchange during Reductive Transformation of Vernadite (δ-MnO$_2$) by Aqueous Mn(II). Environmental Science & Technology, 49(7): 4310-4316.

Emerson, D., 2000. Microbial oxidation of Fe(II) and Mn(II) at circumneutral pH. In: Lovley, D.R. (Ed.), Environmental metal-microbe interactions. ASM Press, Washington, D.C., pp. 31-52.

Etschmann, B., Liu, W.H., Li, K., Dai, S.F., Reith, F., Falconer, D. et al., 2017. Enrichment of germanium and associated arsenic and tungsten in coal and roll-front uranium deposits. Chemical Geology, 463: 29-49.

Etschmann, B., Ryan, C., Brugger, J., Kirkham, R., Hough, R., Moorhead, G. et al., 2010. Reduced As components in highly oxidized environments: Evidence from full spectral XANES imaging using the Maia massively parallel detector. American Mineralogist, 95: 884-887.

Etschmann, B.E., Donner, E., Brugger, J., Howard, D.L., de Jonge, M.D., Paterson, D. et al., 2014. Speciation mapping of environmental samples using XANES imaging. Environmental Chemistry, 11: 341-350.

Flanagan, F.J., Gottfried, D., 1980. Manganese-nodule reference samples USGS-NOD-A-1 and USGS-NOD-P-1. U.S. Geol. Surv. Prof. Pap. 1155: 39.

Frank, M., O'Nions, R.K., Hein, J.R., Banakar, V.K., 1999. 60 Myr records of major elements and Pb-Nd isotopes from hydrogenous ferromanganese crusts: reconstruction of seawater paleochemistry. Geochimica et Cosmochimica Acta, 63: 1689–1708.

Frierdich, A.J., Hasenmueller, E.A., Catalano, J.G., 2011a. Composition and structure of nanocrystalline Fe and Mn oxide cave deposits: Implications for trace element mobility in karst systems. Chemical Geology, 284(1-2): 82-96.

Frierdich, A.J., Luo, Y., Catalano, J.G., 2011b. Trace element cycling through iron oxide minerals during redox-driven dynamic recrystallization. Geology, 39(11): 1083-1086.

Frierdich, A.J., Spicuzza, M.J., Scherer, M.M., 2016. Oxygen Isotope Evidence for Mn(II)-Catalyzed Recrystallization of Manganite (γ-MnOOH). Environmental Science & Technology, 50(12): 6374-6380.

Glasby, G.P., 2006. Manganese: predominant role of nodules and crusts. In: Schulz, H.D., Zabel, M. (Eds.), Marine Geochemistry. Springer-Verlag, Berlin, Heidelberg, pp. 371–427.

Goldberg, E.D., 1954. Marine Geochemistry 1. Chemical scavengers of the sea. The Journal of Geology, 62: 249-265.

Goto, K.T., Nozaki, T., Toyofuku, T., Augustin, A.H., Shimoda, G., Chang, Q. et al., 2017. Paleoceanographic conditions on the São Paulo Ridge, SW Atlantic Ocean, for the past 30 million years inferred from Os and Pb isotopes of a hydrogenous ferromanganese crust. Deep Sea Research Part II: Topical Studies in Oceanography, 146: 82-92.

Halbach, P., Friedrich, G., Von Stackelberg, U., 1988. The manganese nodule belt of the Pacific Ocean. Enke, Stuttgart, 254 pp.

Haynes, B.W., Law, S.L., Barron, D.C., Kramer, G.W., Maeda, R., 1985. Pacific Manganese Nodules: Characterization and Processing Bulletin (United States Bureau of Mines), pp. 43.

Heberling, F., Metz, V., Böttle, M., Curti, E., Geckeis, H., 2018. Barite recrystallization in the presence of ^{226}Ra and ^{133}Ba. Geochimica et Cosmochimica Acta 232: 124−139.

Heberling, F., Paulig, L., Nie, Z., Schild, D., Finck, N., 2016. Morphology Controls on Calcite Recrystallization. Environmental Science & Technology, 50: 11735−11741.

Hegetschweiler, K., Saltman, P., 1986. Interaction of Copper(II) with *N*-(2-Hydroxyethyl)piperazine-*N'*-ethanesulfonic Acid (HEPES). Inorganic Chemistry, 25(1): 107-109.

Hein, J.R., Koschinsky, A., 2014. 13.11 - Deep-Ocean Ferromanganese Crusts and Nodules. In: Holland, H.D., Turekian, K.K. (Eds.), Treatise on Geochemistry (Second Edition). Elsevier, Oxford, pp. 273-291.

Hein, J.R., Koschinsky, A., Halbach, P., Manheim, F.T., Bau, M., Kang, J.-K., Lubick, N., 1997. Iron and manganese oxide mineralization in the Pacific. In: Nicholson, K., Hein, J.R., Bühn, B., Dasgupta, S. (Eds.), Manganese Mineralization: Geochemistry and Mineralogy of Terrestrial and Marine Deposits Geological Society Special Publication. Geological Society of London, London, pp. 123-138.

Hein, J.R., Koschinsky, A., Halliday, A.N., 2003. Global occurrence of tellurium-rich ferromanganese crusts and a model for the enrichment of tellurium. Geochimica et Cosmochimica Acta, 67(6): 1117-1127.

Hein, J.R., Mizell, K., Koschinsky, A., Conrad, T.A., 2013. Deep-ocean mineral deposits as a source of critical metals for high- and green-technology applications: Comparison with land-based resources. Ore Geology Reviews, 51: 1-14.

Hein, J.R., Spinardi, F., Okamoto, N., Mizell, K., Thorburn, D., Tawake, A., 2015. Critical metals in manganese nodules from the Cook Islands EEZ, abundances and distributions. Ore Geology Reviews, 68: 97-116.

Hens, T., Brugger, J., Cumberland, S.A., Etschmann, B., Frierdich, A.J., 2018. Recrystallization of Manganite (γ-MnOOH) and Implications for Trace Element Cycling. Environmental Science & Technology, 52(3): 1311-1319.

Hinkle, M.A.G., Dye, K.G., Catalano, J.G., 2017. Impact of Mn(II)-Manganese Oxide Reactions on Ni and Zn Speciation. Environmental Science & Technology, 51: 3187-3196.

Hinkle, M.A.G., Flynn, E.D., Catalano, J.G., 2016. Structural response of phyllomanganates to wet aging and aqueous Mn(II). Geochimica et Cosmochimica Acta, 192: 220-234.

Josso, P., Pelleter, E., Pourret, O., Fouquet, Y., Etoubleau, J., Cheron, S., Bollinger, C., 2016. A new discrimination scheme for oceanic ferromanganese deposits using high field strength and rare earth elements. Ore Geology Reviews, 87: 3-15.

Kandegedara, A., Rorabacher, D.B., 1999. Noncomplexing Tertiary Amines as "Better" Buffers Covering the Range of pH 3-11. Temperature Dependence of Their Acid Dissociation Constants. Analytical Chemistry, 71(15): 3140-3144.

Kaushal, V., Barnes, L.D., 1986. Effect of zwitterionic buffers on measurement of small masses of protein with bicinchoninic acid. Analytical Biochemistry, 157(2): 291-294.

Klemm, V., Levasseur, S., Frank, M., Hein, J.R., Halliday, A.N., 2005. Osmium isotope stratigraphy of a marine ferromanganese crust. Earth and Planetary Science Letters, 238: 42-48.

Koschinsky, A., Halbach, P., 1995. Sequential leaching of marine ferromanganese precipitates: Genetic implications. Geochimica et Cosmochimica Acta, 59(24): 5113-5132.

Koschinsky, A., Hein, J.R., 2003. Uptake of elements from seawater by ferromanganese crusts: solid-phase associations and seawater speciation. Marine Geology, 198(3-4): 331-351.

Koschinsky, A., Hein, J.R., 2017. Marine ferromanganese encrustations: archives of changing oceans. Elements, 13: 177-182.

Kuhn, T., Wegorzewski, A., Rühlemann, C., Vink, A., 2017. Composition, Formation, and Occurence of Polymetallic Nodules. In: Sharma, R. (Ed.), Deep-Sea Mining. Springer International Publishing AG, Cham, pp. 23-63.

Learman, D.R., Wankel, S.D., Webb, S.M., Martinez, N., Madden, A.S., Hansel, C.M., 2011. Coupled biotic-abiotic Mn(II) oxidation pathway mediates the formation and structural evolution of biogenic Mn oxides. Geochimica et Cosmochimica Acta, 75(20): 6048-6063.

Lefkowitz, J.P., Elzinga, E.J., 2015. Impacts of aqueous Mn(II) on the sorption of Zn(II) by hexagonal birnessite. Environmental Science & Technology, 49: 4886-4893.

Lefkowitz, J.P., Elzinga, E.J., 2017. Structural alteration of hexagonal birnessite by aqueous Mn(II): Impacts on Ni(II) sorption. Chemical Geology, 466: 524-532.

Lefkowitz, J.P., Rouff, A.A., Elzinga, E.J., 2013. Influence of pH on the reductive transformation of birnessite by aqueous Mn(II). Environmental Science & Technology, 47(18): 10364−10371.

Levasseur, S., Frank, M., Hein, J.R., Halliday, A.N., 2004. The global variation in the iron isotope composition of marine hydrogenetic ferromanganese deposits: implications for seawater chemistry. Earth and Planetary Science Letters, 224(1-2): 91-105.

Li, W., Beard, B.L., Johnson, C.M., 2011. Exchange and fractionation of Mg isotopes between epsomite and saturated $MgSO_4$ solution. Geochimica et Cosmochimica Acta, 75: 1814−1828.

Lleu, P.L., Rebel, G., 1991. Interference of Good's buffers and other biological buffers with protein determination. Analytical Biochemistry, 192(1): 215-218.

Lovely, D.R., 2000. Fe(III) and Mn(IV) reduction. In: Lovely, D.R. (Ed.), Environmental metal-microbe interactions. ASM Press, Washington, D.C., pp. 3-30.

Lusty, P.A.J., Murton, B.J., 2018. Deep-ocean mineral deposits: metal resources and windows into Earth processes. Elements, 14: 301-306.

Manceau, A., Gorshkov, A.I., Drits, V.A., 1992. Structural chemistry of Mn, Fe, Co, and Ni in manganese hydrous oxides: Part II. Information from EXAFS spectroscopy and electron and X-ray diffraction. American Mineralogist, 77(11): 1144-1157.

Manceau, A., Lanson, M., Takahashi, Y., 2014. Mineralogy and crystal chemistry of Mn, Fe, Co, Ni, and Cu in a deep-sea Pacific polymetallic nodule. American Mineralogist, 99(10): 2068-2083.

Manceau, A., Marcus, M.A., Grangeon, S., 2012. Determination of Mn valence states in mixed-valent manganates by XANES spectroscopy. American Mineralogist, 97(5-6): 816-827.

Mandernack, K.W., Post, J., Tebo, B.M., 1995. Manganese mineral formation by bacterial spores of the marine *Bacillus*, strain SG-1: Evidence for the direct oxidation of Mn(II) to Mn(IV). Geochimica et Cosmochimica Acta, 59(21): 4393-4408.

Mann, S., Sparks, N.H., Scott, G.H., de Vrind-de Jong, E.W., 1988. Oxidation of Manganese and Formation of Mn_3O_4 (Hausmannite) by Spore Coats of a Marine *Bacillus* sp. Applied and Environmental Microbiology, 54(8): 2140-2143.

McKenzie, R.M., 1980. The adsorption of lead and other heavy metals on oxides of manganese and iron. Australian Journal of Soil Research, 18: 61-73.

McLennan, S.M., 2001. Relationships between the trace element composition of sedimentary rocks and upper continental crust. Geochemistry Geophysics Geosystems, 2(4): 2000GC000109.

Miyata, N., Tani, Y., Sakata, M., Iwahori, K., 2007. Microbial manganese oxide formation and interaction with toxic metal ions. Journal of Bioscience and Bioengineering, 104(1): 1-8.

Mohwinkel, D., Kleint, C., Koschinsky, A., 2014. Phase associations and potential selective extraction methods for selected high-tech metals from ferromanganese nodules and crusts with siderophores. Applied Geochemistry, 43: 13-21.

Myers, C.R., Nealson, K.H., 1988. Bacterial manganese reduction and growth with manganese oxide as the sole electron acceptor. Science, 240: 1319-1321.

Notini, L., Latta, D.E., Neumann, A., Pearce, C.I., Sassi, M., N'Diaye, A.T., Rosso, K.M., Scherer, M.M., 2018. The Role of Defects in Fe(II)-Goethite Electron Transfer. Environmental Science & Technology, 52: 2751−2759.

Paterson, D., de Jonge, M.D., Howard, D.L., Lewis, W., McKinlay, J., Starritt, R. et al., 2011. The X‑ray Fluorescence Microscopy Beamline at the Australian Synchrotron. AIP Conference Proceedings, 1365: 219-222.

Peacock, C.L., 2009. Physiochemical controls on the crystal-chemistry of Ni in birnessite: Genetic implications for ferromanganese precipitates. Geochimica et Cosmochimica Acta, 73: 3568-3578.

Peacock, C.L., Sherman, D.M., 2007a. Crystal-chemistry of Ni in marine ferromanganese crusts and nodules. American Mineralogist, 92(7): 1087-1092.

Peacock, C.L., Sherman, D.M., 2007b. Sorption of Ni by birnessite: Equilibrium controls on Ni in seawater. Chemical Geology, 238(1-2): 94-106.

Pecher, K., McCubbery, D., Kneedler, E., Rothe, J., Bargar, J., Meigs, G., Cox, L., Nealson, K., Tonner, B., 2003. Quantitative charge state analysis of manganese biominerals in aqueous suspension using scanning transmission X-ray microscopy (STXM). Geochimica et Cosmochimica Acta, 67(6): 1089-1098.

Peña, J., Bargar, J.R., Sposito, G., 2011. Role of bacterial biomass in the sorption of Ni by biomass-birnessite assemblages. Environmental Science & Technology, 45: 7338-7344.

Peña, J., Bargar, J.R., Sposito, G., 2015. Copper sorption by the edge surfaces of synthetic birnessite nanoparticles. Chemical Geology, 396: 196-207.

Peña, J., Duckworth, O.W., Bargar, J.R., Sposito, G., 2007. Dissolution of hausmannite (Mn_3O_4) in the presence of the trihydroxamate siderophore desferrioxamine B. Geochimica et Cosmochimica Acta, 71: 5661-5671.

Peña, J., Kwon, K.D., Refson, K., Bargar, J.R., Sposito, G., 2010. Mechanisms of nickel sorption by a bacteriogenic birnessite. Geochimica et Cosmochimica Acta, 74: 3076-3089.

Perez-Benito, J.F., 2002. Reduction of Colloidal Manganese Dioxide by Manganese(II). Journal of Colloid and Interface Science, 248(1): 130-135.

Peucker-Ehrenbrink, B., Jahn, B.M., 2001. Rhenium–osmium isotope systematics and platinum group element concentrations: loess and the upper continental crust. Geochemistry, Geophysics, Geosystems, 2(10): 2001GC000172.

Posselt, H.S., Anderson, F.J., Weber, W.J., 1968. Cation sorption on colloidal hydrous manganese dioxide. Environmental Science & Technology, 2: 1087-1093.

Post, J.E., 1999. Manganese oxide minerals: Crystal structures and economic and environmental significance. Proceedings of the National Academy of Sciences of the United States of America, 96(7): 3447-3454.

Post, J.E., Heaney, P.J., Hanson, J., 2003. Synchrotron X-ray diffraction of the structure and dehydration behavior of todorokite. American Mineralogist, 88: 142-150.

Ravel, B., Newville, M., 2005. ATHENA, ARTEMIS, HEPHAESTUS: data analysis for X-ray absorption spectroscopy using IFEFFIT. Journal of Synchrotron Radiation, 12: 537-541.

Rudnick, R.L., Gao, S., 2003. Composition of the continental crust. In: Rudnick, R.L. (Ed.), Treatise on Geochemistry. Elsevier, Amsterdam, pp. 1-64.

Ryan, C.G., Siddons, D.P., Kirkham, R., Dunn, P.A., Kuczewski, A., Moorhead, G. et al., 2010. The new Maia detector system: methods for high definition trace element imaging of natural materia. AIP Conference Proceedings, 1221(1): 9-17.

Ryan, C.G., Siddons, D.P., Kirkham, R., Li, Z.Y., de Jonge, M.D., Paterson, D.J. et al., 2014. Maia X-ray fluorescence imaging: capturing detail in complex natural samples. Journal of Physics: Conference Series, 499(1): 012002.

Santelli, C.M., Webb, S.M., Dohnalkova, A.C., Hansel, C.M., 2011. Diversity of Mn oxides produced by Mn(II)-oxidizing fungi. Geochimica et Cosmochimica Acta, 75: 2762-2776.

Schmitt, B., Brönnimann, C., Eikenberry, E.F., Gozzo, F., Hörmann, C., Horisberger, R., Patterson, B., 2003. Mythen detector system. Nuclear Instruments and Methods in Physics Research Section A: Accelerators, Spectrometers, Detectors and Associated Equipment, 501(1): 267-272.

Simanova, A.A., Peña, J., 2015. Time-Resolved Investigation of Cobalt Oxidation by Mn(III)-Rich δ-MnO$_2$ Using Quick X-ray Absorption Spectroscopy. Environmental Science & Technology, 49(18): 10867-10876.

Skinner, H.C.W., Fitzpatrick, R.W., 1992. Biomineralization Processes of Iron and Manganese: Modern and Ancient Environments. Catena-Verlag, Cremlingen-Destedt, pp. 432.

Southall, S.C., Micklethwaite, S., Wilson, S.A., Frierdich, A.J., 2018. Changes in Crystallinity and Tracer-Isotope Distribution of Goethite during Fe(II)-Accelerated Recrystallization. ACS Earth and Space Chemistry, 2(12): 1271-1282.

Taylor, S.R., McLennan, S.M., 1985. The Continental Crust: Its Composition and Evolution. Blackwell Scientific Publications, Oxford, pp. 312.

Tebo, B.M., Bargar, J.M., Clement, B.G., Dick, G.J., Murray, K.J., Parker, D., Verity, R., Webb, S.M., 2004. Biogenic manganese oxides: Properties and Mechanisms of Formation. Annual Review of Earth and Planetary Sciences, 32: 287-328.

Tebo, B.M., Johnson, H.A., McCarthy, J.K., Templeton, A.S., 2005. Geomicrobiology of manganese(II) oxidation. Trends in Microbiology, 13(9): 421-428.

Toner, B., Fakra, S., Villalobos, M., Warwick, T., Sposito, G., 2005. Spatially Resolved Characterization of Biogenic Manganese Oxide Production within a Bacterial Biofilm. Applied and Environmental Microbiology, 71(3): 1300-1310.

Villalobos, M., Lanson, B., Manceau, A., Toner, B., Sposito, G., 2006. Structural model for the biogenic Mn oxide produced by *Pseudomonas putida*. American Mineralogist, 91(4): 489-502.

Villalobos, M., Toner, B., Bargar, J., Sposito, G., 2003. Characterization of the manganese oxide produced by *Pseudomonas putida* strain MnB1. Geochimica et Cosmochimica Acta, 67(14): 2649-2662.

Von Heimendahl, M., Hubred, G.L., Fuerstenau, D.W., Thomas, G., 1976. A transmission electron microscope study of deep-sea manganese nodules. Deep Sea Research Oceanography Abstracts 23: 69-79.

Wallwork, K.S., Kennedy, B.J., Wang, D., 2007. The High Resolution Powder Diffraction Beamline for the Australian Synchrotron. AIP Conference Proceedings, 879(1): 879-882.

Wang, F., Sayre, L.M., 1989. Oxidation of Tertiary Amine Buffers by Copper(II). Inorganic Chemistry, 28(2): 169-170.

Webb, S.M., Tebo, B.M., Bargar, J.R., 2005. Structural characterization of biogenic Mn oxides produced in seawater by the marine *bacillus sp.* strain SG-1. American Mineralogist, 90(8-9): 1342-1357.

Wegorzewski, A., Köpcke, M., Kuhn, T., Sitnikova, M., Wotruba, H., 2018. Thermal Pre-Treatment of Polymetallic Nodules to Create Metal (Ni, Cu, Co)-Rich Individual Particles for Further Processing. Minerals, 8(11): 523.

Yu, Q., Kandegedara, A., Xu, Y., Rorabacher, D.B., 1997. Avoiding interferences from Good's buffers: A contiguous series of noncomplexing tertiary amine buffers covering the entire range of pH 3-11. Analytical Biochemistry, 253(1): 50-56.

Zhao, H., Zhu, M., Li, W., Elzinga, E.J., Villalobos, M., Liu, F., Zhang, J., Feng, X., Sparks, D.L., 2016. Redox Reactions between Mn(II) and Hexagonal Birnessite Change Its Layer Symmetry. Environmental Science & Technology, 50(4): 1750-1758.

Zhu, M., Ginder-Vogel, M., Parikh, S.J., Feng, X.H., Sparks, D.L., 2010a. Cation effects on the layer structure of biogenic Mn-oxides. Environmental Science & Technology, 44: 4465-4471.

Zhu, M., Ginder-Vogel, M., Sparks, D.L., 2010b. Ni(II) Sorption on Biogenic Mn-Oxides with Varying Mn Octahedral Layer Structure. Environmental Science & Technology, 44(12): 4472-4478.

Zhu, Y.H., Liang, X.R., Zhao, H.Y., Yin, H., Liu, M.M., Liu, F., Feng, X.H., 2017. Rapid determination of the Mn average oxidation state of Mn oxides with a novel two-step colorimetric method. Analytical Methods, 9: 103-109.

SUPPORTING INFORMATION FOR:

Nickel Exchange Between Aqueous Ni(II) and Deep-Sea Ferromanganese Nodules and Crusts

Tobias Hens[1], Joël Brugger[1], Barbara Etschmann[1], David Paterson[2], Helen E. A. Brand[1,2], Anne Whitworth[1], Andrew J. Frierdich[1,*]

[1]School of Earth, Atmosphere & Environment, Monash University, Clayton, VIC 3800, Australia
[2]Australian Synchrotron, ANSTO, Clayton, VIC 3168, Australia

*Corresponding author: Tel.: (+61) 03 9905 4899; Fax: (+61) 03 9905 4903; E-mail: andrew.frierdich@monash.edu

S1

FIGURES
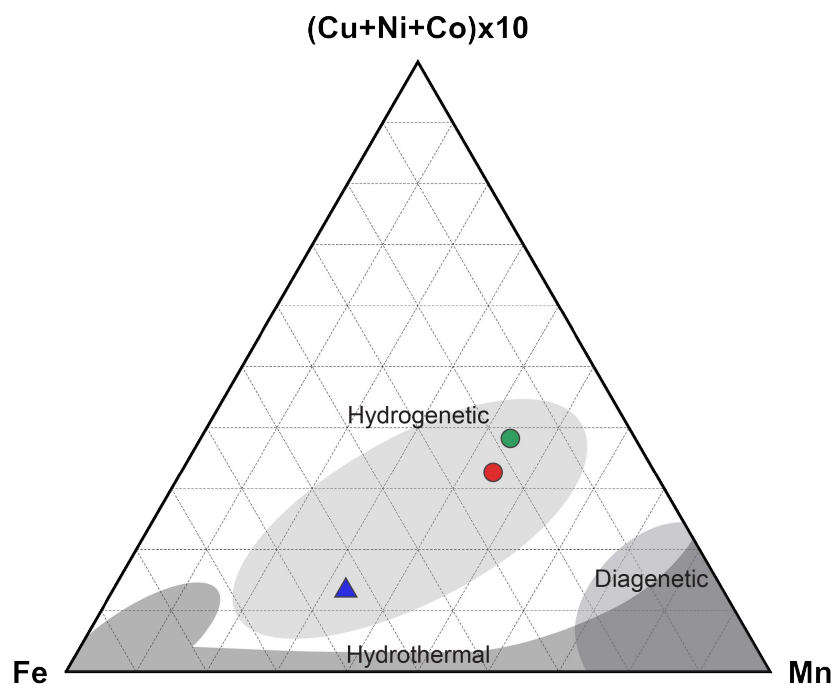
Fig. S1. Data for Fe-Mn nodules TS-5 (green circle), 8FFG-007-2 (red circle), and crust SP-8 (blue triangle) plot in the hydrogenetic field of the ternary discrimination diagram; modified after (Bonatti et al., 1972).
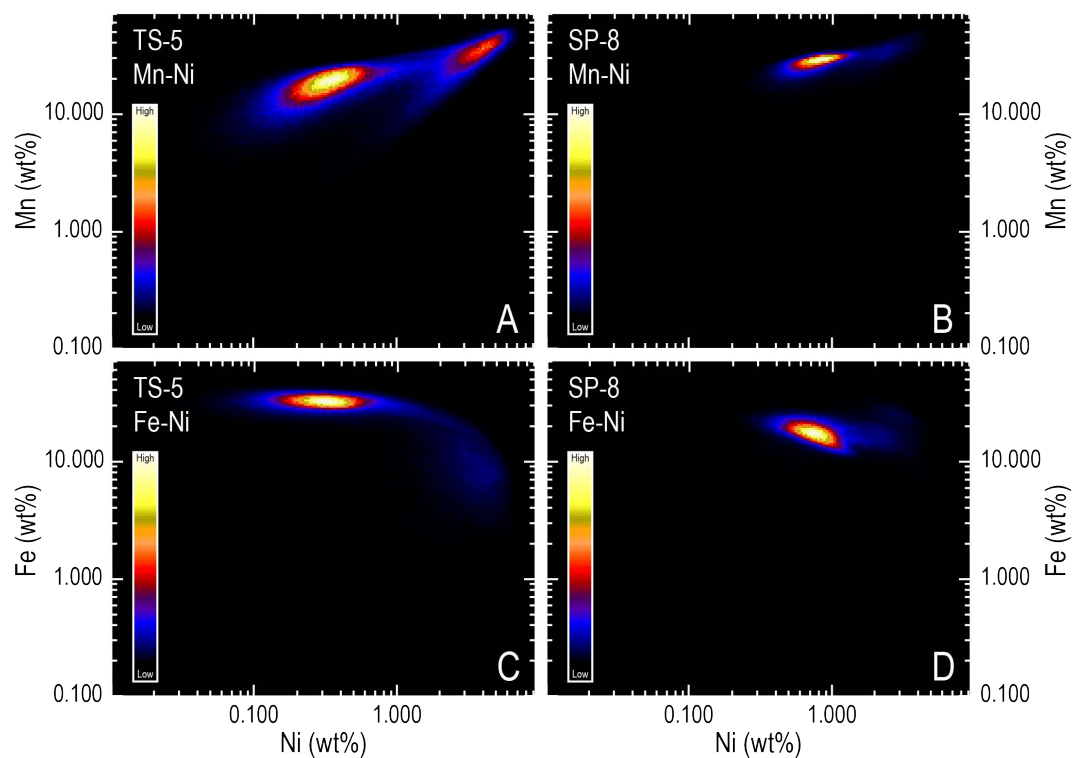
Fig. S2. Element-element correlation plots depicting Mn-Ni and Fe-Ni correlations for TS-5 (A,C) and SP-8 (B,D), respectively.
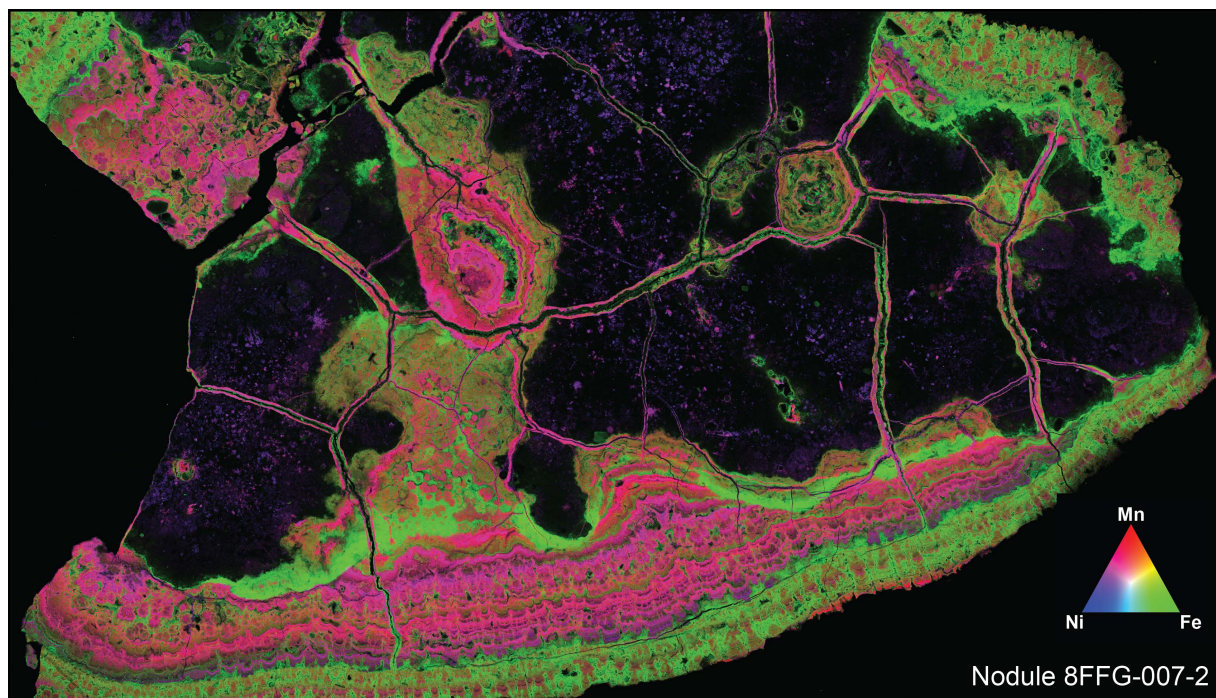
Fig. S3. Three-color (RGB) image of 8FFG-007-2 highlighting intricate growth structures and fine intergrowth of Fe-Mn oxides as well as the spatial distribution of Ni. Filling of fractures by Fe-Mn oxides can be observed.
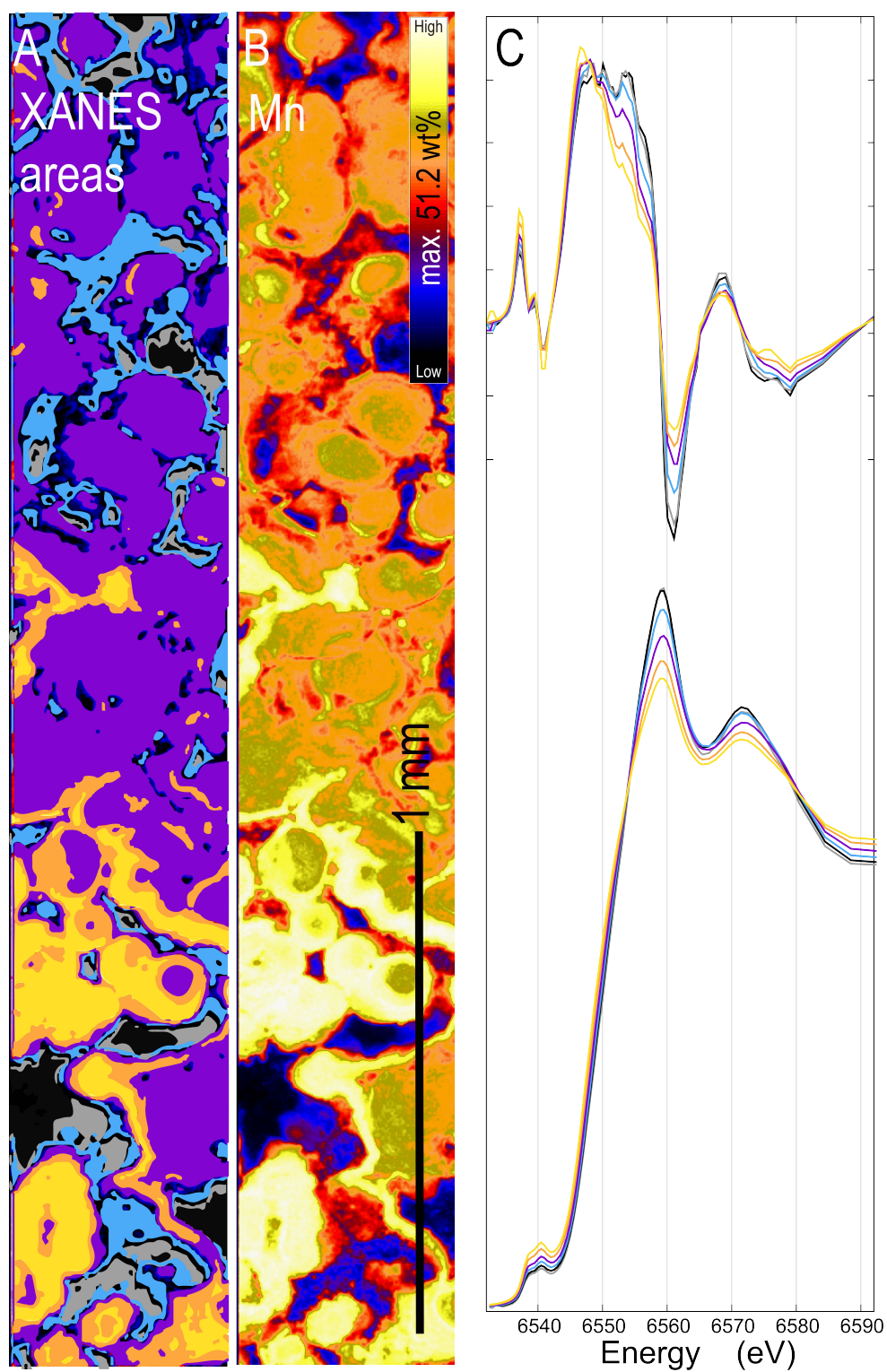
Fig. S4. Variability of XANES spectra dependent on Mn concentration and Mn self-absorption correction features illustrated for Fe-Mn nodule TS-5 region of interest TS-5-r1 (see Fig. 5 in main manuscript for full description).
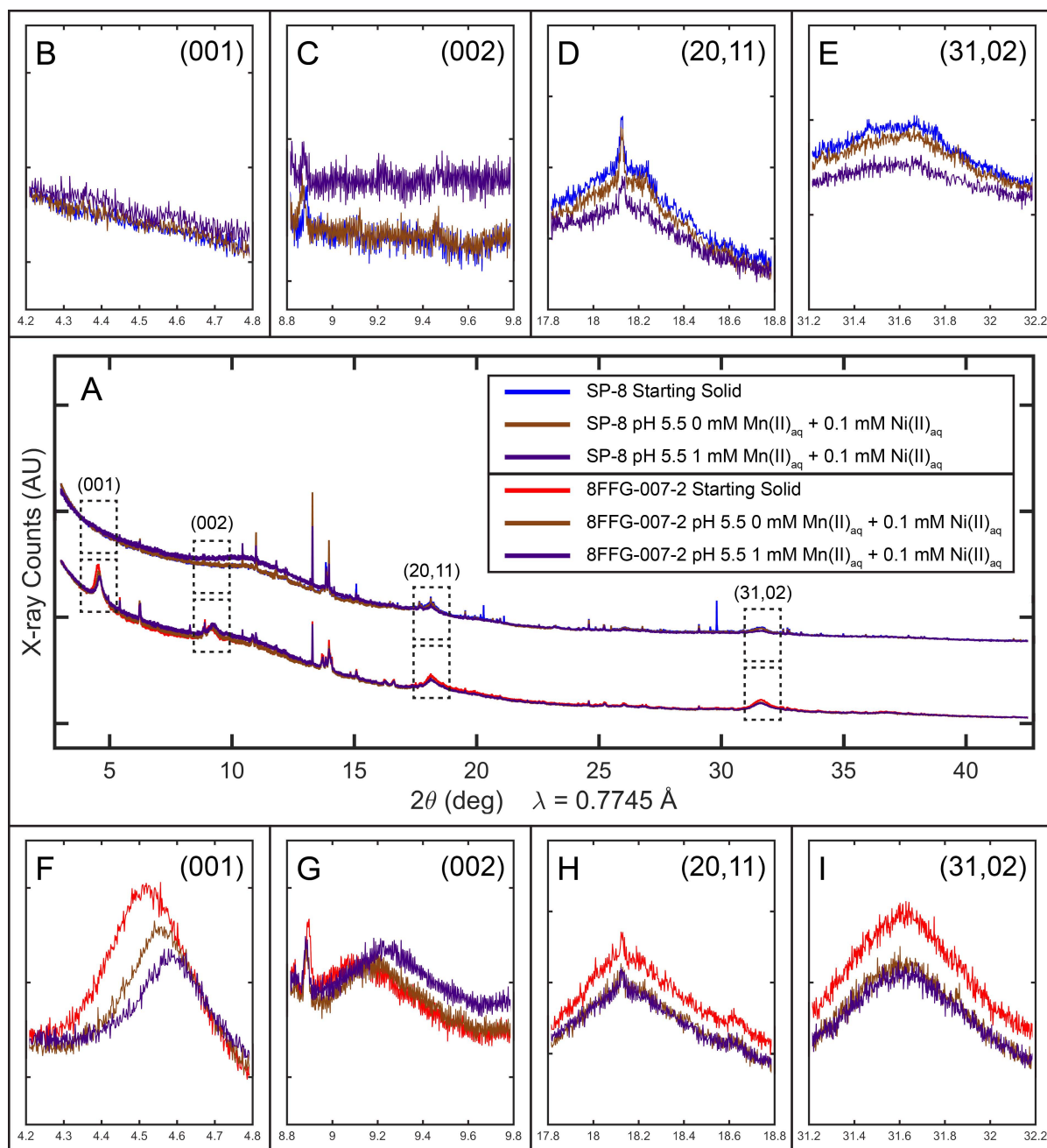
Fig. S5. (A) PD patterns of Fe-Mn crust SP-8 (top) and nodule 8FFG-007-2 (bottom) starting materials (unreacted) and solids after 14 days of reaction with Ni(II)$_{aq}$ in the presence and absence of Mn(II)$_{aq}$ at pH 5.5 displayed from 3 to 45° 2θ. (B-E) Regions of the (001), (002), (20,11), and (31,02) phyllomanganate reflections of SP-8 displaying the absence of bulk mineral transformations of reacted solids in comparison to the starting material. (F-I) Regions of the same phyllomanganate reflections for 8FFG-007-2 highlighting minor structural modifications (i.e. decrease of peak width and peak shift towards higher 2 θ in (001)) of reacted solids in comparison to the starting material (F,I), indicating a possible increase of crystallinity.

TABLES

Table S1. Element concentrations of ferromanganese nodule and crust samples TS-5, 8FFG-007-2, SP-8, and reference materials NOD-A-1 and NOD-P-1 measured by ICP-OES/MS.

Element	TS-5	8FFG-007-2	SP-8	NOD-A-1	NOD-P-1	Element (cont.)	TS-5	8FFG-007-2	SP-8	NOD-A-1	NOD-P-1
Fe[a]	9.60	11.22	20.82	11.10	5.90	Te	14	7	23	38	7
Mn	23.68	21.62	12.83	20.33	32.50	Cs (ppb)	812	535	580	632	1658
Mn/Fe	2.47	1.93	0.62	1.83	5.51	Ba	1320	1238	1232	1512	2450
Ni	1.24	0.76	0.18	0.64	1.38	La	86	137	183	119	112
Na	1.83	2.08	1.84	0.84	1.69	Ce	505	324	545	753	316
Mg	2.10	1.64	1.19	3.04	2.10	Pr	18	36	32	26	32
Al	2.95	3.26	3.66	2.01	2.37	Nd	71	146	138	100	133
P	0.14	0.27	0.32	0.51	0.15	Sm	16	33	28	23	33
K	1.16	1.26	0.66	0.50	1.00	Eu	4	9	7	6	8
Ca	2.06	2.02	2.24	11.29	2.32	Gd	20	37	36	30	32
Sc	bDL[b]	bDL	bDL	bDL	bDL	Tb	3	6	6	4	5
Ti	0.45	0.60	0.83	0.30	0.28	Dy	16	34	34	24	26
V	314	354	516	567	438	Ho	3	7	7	5	5
Cr	bDL	12	15	11	5	Er	9	19	22	16	14
Co	2401	1640	1861	3041	2148	Tm	2	3	4	3	3
Cu	5811	6738	1494	1107	11609	Yb	8	17	21	14	14
Zn	1193	733	574	605	1657	Lu	1	3	3	2	2
As	-[c]	-	-	-	-	Hf	9	7	10	6	4
Rb	20	18	8	10	24	Ta (ppb)	1026	782	891	1775	1178
Sr	756	798	1061	1597	680	W	44	39	40	89	60
Y	62	135	153	109	89	Os	-	-	-	-	-
Zr	402	372	539	300	270	Tl	183	137	36	120	210
Nb	45	30	47	44	22	Pb	643	463	764	795	434
Mo	345	283	210	376	635	Bi	7	5	9	10	4
Cd	11	9	4	8	24	Th	14	15	7	24	16
Sn	4	2	5	4	3	U	4	6	8	7	4
Sb	27	23	34	35	50						

[a] Major elements (Fe, Mn, Na, Mg, Al, P, K, Ca, Ti) and Ni reported in weight percent (wt%); all other elements in (ppm) except when explicitly stated.

[b] below detection limit (bDL).

[c] not analysed.

Table S2. Summary of Mn and Ni concentrations, and Ni isotope fractions, for reactions between ferromanganese nodule TS-5 and ^{62}Ni-enriched aqueous Ni(II) in the presence and absence of Mn(II)$_{aq}$ in pH 7.5 and 5.5 fluid.

	[Mn] (μM)	[Ni] (μM)	$f\ ^{58}Ni$	$f\ ^{60}Ni$	$f\ ^{62}Ni$	
Initial solid	8620	422	0.648	0.293	0.046	
Time (d)	**[Mn(II)]$_{aq}$ (μM)**	**[Ni(II)]$_{aq}$ (μM)**	$f\ ^{58}Ni$	$f\ ^{60}Ni$	$f\ ^{62}Ni$	**% Ni Exchange[a]**
pH 7.5 – 0 mM Mn(II)$_{aq}$						
0	0.03	100(2)[b]	0.0077(5)	0.0133(2)	0.9755(6)	0
1	0.026(6)	0.37(6)	0.0489(2)	0.0328(1)	0.9142(6)	1.79(2)
7	0.023(1)	0.16(1)	0.12(4)	0.06(2)	0.80(6)	5(2)
14	0.40(1)	0.17(4)	0.16(1)	0.081(9)	0.75(2)	8(1)
pH 7.5 – 1 mM Mn(II)$_{aq}$						
0	950(4)	106.6(3)	0.0074(1)	0.01221(1)	0.9773(2)	0
1	115.7(8)	2.47(8)	0.1024(3)	0.05661(8)	0.8362(1)	4.412(4)
7	87(6)	1.4(1)	0.162(3)	0.085(1)	0.746(4)	8.1(2)
14	66(1)	1.069(1)	0.1846(4)	0.095(1)	0.713(1)	9.7(1)
pH 5.5 – 0 mM Mn(II)$_{aq}$						
0	0.27	112(1)	0.0073(1)	0.0131(1)	0.9760(2)	0
1	5.1(4)	13(1)	0.078(1)	0.0458(3)	0.870(2)	3.61(9)
7	20.2(1)	13.6(5)	0.157(5)	0.083(2)	0.752(7)	8.9(4)
14	16.69	9.12	0.1811	0.0949	0.7174	10.81
pH 5.5 – 1 mM Mn(II)$_{aq}$						
0	986(15)	120(1)	0.0072(5)	0.0124(3)	0.9773(8)	0
1	554(24)	53.7(5)	0.0918(1)	0.05240(4)	0.85143(3)	4.367(1)
7	509(25)	47(1)	0.163(2)	0.0857(6)	0.745(3)	9.2(2)
14	570(45)	50(4)	0.185(5)	0.096(2)	0.712(8)	11.1(4)

[a] Ni exchange calculated from eq 2 (main manuscript) using measured $f^{62}Ni$ values for Ni(II)$_{aq}$.
[b] Numbers in parentheses represent the uncertainty in the last digit at the 95% confidence level. NA = not applicable.

Table S3. Summary of Mn and Ni concentrations, and Ni isotope fractions, for reactions between ferromanganese nodule 8FFG-007-2 and ^{62}Ni-enriched aqueous Ni(II) in the presence and absence of Mn(II)$_{aq}$ in pH 7.5 and 5.5 fluid.

	[Mn] (µM)	[Ni] (µM)	f ^{58}Ni	f ^{60}Ni	f ^{62}Ni	
Initial solid	7870	258	0.636	0.305	0.045	
Time (d)	**[Mn(II)]$_{aq}$ (µM)**	**[Ni(II)]$_{aq}$ (µM)**	f ^{58}Ni	f ^{60}Ni	f ^{62}Ni	**% Ni Exchange**[a]
pH 7.5 – 0 mM Mn(II)$_{aq}$						
0	0.03	100(2)[b]	0.0077(5)	0.0133(2)	0.9755(6)	0
1	0.0050(3)	0.19(1)	0.06(2)	0.03(1)	0.89(3)	4(2)
7	0.0109(9)	0.111(3)	0.081(2)	0.047(1)	0.866(2)	5.4(1)
14	0.03(4)	0.06(1)	0.123(6)	0.066(2)	0.804(8)	9.2(5)
pH 7.5 – 1 mM Mn(II)$_{aq}$						
0	950(4)	106.6(3)	0.0074(1)	0.01221(1)	0.9773(2)	0
1	51(4)	1.46(3)	0.09(3)	0.05(1)	0.84(5)	6(3)
7	49.1	1.468	0.1191	0.0653	0.8102	8.84
14	42(1)	1.26(3)	0.1351(2)	0.0718(7)	0.7875(5)	10.34(3)
pH 5.5 – 0 mM Mn(II)$_{aq}$						
0	0.27	112(1)	0.0073(1)	0.0131(1)	0.9760(2)	0
1	1.50(2)	10(2)	0.04(1)	0.031(6)	0.91(1)	3(1)
7	8.1(8)	9.5(1)	0.114(5)	0.063(2)	0.816(8)	9.5(6)
14	14.8(3)	10.2(3)	0.152(1)	0.0810(4)	0.761(2)	13.7(2)
pH 5.5 – 1 mM Mn(II)$_{aq}$						
0	986(15)	120(1)	0.0072(5)	0.0124(3)	0.9773(8)	0
1	489(1)	48.9(1)	0.0568(6)	0.03640(3)	0.9026(5)	3.98(3)
7	458(8)	47(1)	0.122(2)	0.067(1)	0.805(4)	10.3(3)
14	477(83)	46(4)	0.140(3)	0.075(1)	0.778(4)	12.4(3)

[a] Ni exchange calculated from eq 2 (main manuscript) using measured f^{62}Ni values for Ni(II)$_{aq}$.
[b] Numbers in parentheses represent the uncertainty in the last digit at the 95% confidence level. NA = not applicable.

Table S4. Summary of Mn and Ni concentrations, and Ni isotope fractions, for reactions between ferromanganese crust SP-8 and ^{62}Ni-enriched aqueous Ni(II) in the presence and absence of Mn(II)$_{aq}$ in pH 7.5 and 5.5 fluid.

	[Mn] (μM)	[Ni] (μM)	f ^{58}Ni	f ^{60}Ni	f ^{62}Ni	
Initial solid	4670	61	0.686	0.263	0.040	
Time (d)	**[Mn(II)]$_{aq}$ (μM)**	**[Ni(II)]$_{aq}$ (μM)**	f ^{58}Ni	f ^{60}Ni	f ^{62}Ni	**% Ni Exchange**[a]
pH 7.5 – 0 mM Mn(II)$_{aq}$						
0	0.03	100(2)[b]	0.0077(5)	0.0133(2)	0.9755(6)	0
1	0.040(6)	0.68(5)	0.032(2)	0.024(1)	0.939(3)	7.1(6)
7	0.0588(2)	0.55(2)	0.040(7)	0.027(4)	0.92(1)	9(2)
14	0.0606(8)	0.515(8)	0.047(1)	0.0310(4)	0.917(2)	11.6(5)
pH 7.5 – 1 mM Mn(II)$_{aq}$						
0	950(4)	106.6(3)	0.0074(1)	0.01221(1)	0.9773(2)	0
1	228(6)	4.3(1)	0.04557(9)	0.0301(2)	0.9205(4)	11.02(9)
7	186(7)	2.7(1)	0.074(2)	0.0440(9)	0.877(3)	20.4(7)
14	171(26)	2.5(4)	0.0789(6)	0.04616(5)	0.8705(6)	21.9(1)
pH 5.5 – 0 mM Mn(II)$_{aq}$						
0	0.27	112(1)	0.0073(1)	0.0131(1)	0.9760(2)	0
1	6.11(3)	24.2(3)	0.029(1)	0.0229(7)	0.943(2)	7.1(4)
7	16.3(6)	23.3(1)	0.058(1)	0.0365(7)	0.901(1)	17.1(4)
14	15.0(3)	15.1(4)	0.07384(3)	0.0442(1)	0.8774(2)	23.05(7)
pH 5.5 – 1 mM Mn(II)$_{aq}$						
0	986(15)	120(1)	0.0072(5)	0.0124(3)	0.9773(8)	0
1	662(8)	58(1)	0.0421(9)	0.0283(6)	0.925(1)	11.2(3)
7	651.70(6)	58.0(1)	0.0699(1)	0.04122(9)	0.88452(4)	21.24(1)
14	697(1)	62(1)	0.0793(3)	0.0458(6)	0.8705(8)	24.8(2)

[a] Ni exchange calculated from eq 2 (main manuscript) using measured f^{62}Ni values for Ni(II)$_{aq}$.
[b] Numbers in parentheses represent the uncertainty in the last digit at the 95% confidence level. NA = not applicable.

Table S5. Summary of Mn and Ni concentrations, and Ni isotope fractions, for the controls of the Ni isotope tracer experiments at pH 7.5. Reported are the $Mn(II)_{aq}$ and $Ni(II)_{aq}$ concentrations for sample-free blanks and the concentrations for $Mn(II)_{aq}$- and $Ni(II)_{aq}$-free controls at pH 7.5, respectively.

Time (d)	[Mn(II)]$_{aq}$ (μM)	[Ni(II)]$_{aq}$ (μM)	f ^{58}Ni	f ^{60}Ni	f ^{62}Ni	% ^{62}Ni Exchange
pH 7.5 – Mn(II)$_{aq}$ + Ni(II)$_{aq}$						
0	950(4)^a	106.6(3)	0.0074(1)	0.01221(1)	0.9773(2)	NA
1	912(14)	112(1)	0.0070(2)	0.0117(2)	0.9782(4)	NA
7	920(1)	108(1)	0.006860(2)	0.01183(8)	0.9783(1)	NA
14	923(12)	104(1)	0.0075(3)	0.01244(8)	0.9769(5)	NA
pH 7.5 – TS-5 only						
0	0	0	NA	NA	NA	NA
1	0.022(4)	0.026(1)	0.59(5)	0.28(2)	0.11(7)	NA
7	0.0193(6)	0.022(2)	0.640(2)	0.29213(7)	0.051(3)	NA
14	0.015(1)	0.014(3)	0.632(2)	0.292(1)	0.06(3)	NA
pH 7.5 – 8FFG-007-2 only						
0	0	0	NA	NA	NA	NA
1	0.008(6)	0.013(8)	0.634(1)	0.300(4)	0.053(1)	NA
7	0.009(1)	0.009(2)	0.629(8)	0.31(1)	0.0520(1)	NA
14	0.05(6)	0.017(4)	0.626(1)	0.309(1)	0.049(2)	NA
pH 7.5 – SP-8 only						
0	0	0	NA	NA	NA	NA
1	0.022(3)	0.025(7)	0.64(1)	0.291(2)	0.05(1)	NA
7	0.05(3)	0.0251(4)	0.6334(5)	0.3027(5)	0.0518(8)	NA
14	0.07(5)	0.025(9)	0.64(1)	0.290(1)	0.05(1)	NA

^{a} Numbers in parentheses represent the uncertainty in the last digit at the 95% confidence level. NA = not applicable.

Table S6. Summary of Mn and Ni concentrations, and Ni isotope fractions, for the controls of the Ni isotope tracer experiments at pH 5.5. Reported are the $Mn(II)_{aq}$ and $Ni(II)_{aq}$ concentrations for sample-free blanks and the concentrations for $Mn(II)_{aq}$- and $Ni(II)_{aq}$-free controls at pH 5.5, respectively.

Time (d)	[Mn(II)]$_{aq}$ (µM)	[Ni(II)]$_{aq}$ (µM)	f ^{58}Ni	f ^{60}Ni	f ^{62}Ni	% ^{62}Ni Exchange
pH 5.5 – Mn(II)$_{aq}$ + Ni(II)$_{aq}$						
0	986(15) [a]	120(1)	0.0072(5)	0.0124(3)	0.9773(8)	NA
1	981(22)	121(1)	0.0068(2)	0.01210(3)	0.9780(3)	NA
7	975(6)	119.7(7)	0.00709(5)	0.01224(9)	0.9776(1)	NA
14	924(20)	117(2)	0.0067(2)	0.01211(4)	0.9781(2)	NA
pH 5.5 – TS-5 only						
0	0	0	NA	NA	NA	NA
1	1.764(1)	0.400(6)	0.62(1)	0.301(1)	0.05(1)	NA
7	8.97(4)	1.073(4)	0.626(2)	0.3049(5)	0.053(1)	NA
14	16.3(2)	1.52(2)	0.0625(2)	0.3065(2)	0.053(1)	NA
pH 5.5 – 8FFG-007-2 only						
0	0	0	NA	NA	NA	NA
1	0.28(1)	0.12(1)	0.634(2)	0.300(4)	0.052(6)	NA
7	4.1(2)	0.57(2)	0.626(1)	0.3112(6)	0.0493(2)	NA
14	9.8(5)	1.00(1)	0.629(1)	0.306(2)	0.0503(8)	NA
pH 5.5 – SP-8 only						
0	0	0	NA	NA	NA	NA
1	2.24(9)	0.225(6)	0.625(8)	0.301(4)	0.05(1)	NA
7	9.6(4)	0.70(4)	0.630(1)	0.302(2)	0.051(1)	NA
14	17.6(6)	1.03(4)	0.6272(6)	0.3063(5)	0.051(1)	NA

[a] Numbers in parentheses represent the uncertainty in the last digit at the 95% confidence level. NA = not applicable.

References

Bonatti, E., Kraemer, T., Rydell, H., 1972. Classification and genesis of submarine iron-manganese deposits. In: Horn, D.R. (Editor), Papers from a Conference on Ferro-manganese Deposits on the Ocean Floor. National Science Foundation, pp. 149-166.

Chapter 5

Conclusions
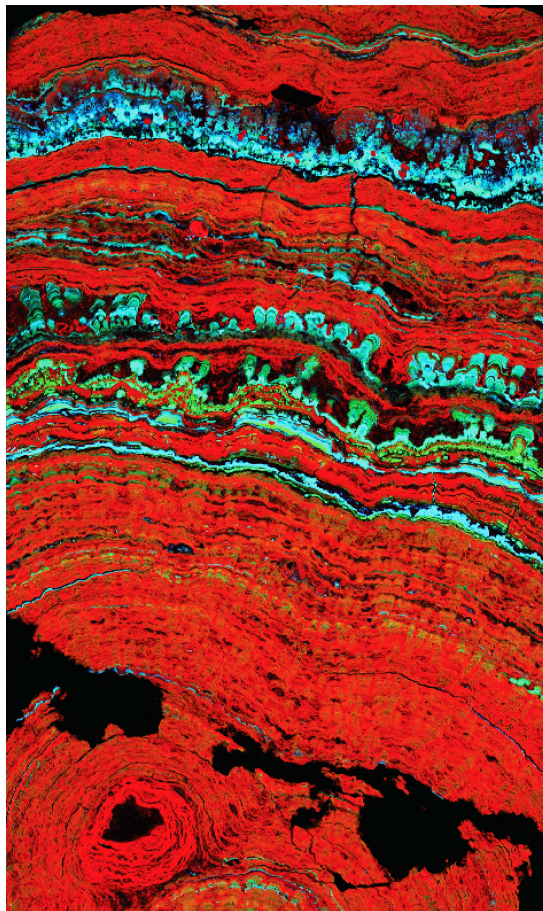
1. General Conclusions

The overarching research aim of this thesis was to investigate the effects of $Mn(II)_{aq}$-catalyzed mineral recrystallization on Ni cycling between Mn oxides and aqueous solutions, in order to infer influences on deep-sea ferromanganese nodule and crust genesis, alteration, and trace element mobility. Recent studies have shown that $Mn(II)_{aq}$-driven mineral-fluid interactions affect Mn oxides and associated trace metals through multiple reaction pathways with far-reaching implications for trace metal mobility in a broad range of natural settings (e.g., Elzinga, 2011; Elzinga, 2016; Elzinga and Kustka, 2015; Hinkle et al., 2017; Hinkle et al., 2016; Lefkowitz and Elzinga, 2015; Lefkowitz and Elzinga, 2017; Lefkowitz et al., 2013; Peacock, 2009; Peacock and Sherman, 2007a). Fe-Mn nodules and crusts can be in direct contact with variable $Mn(II)_{aq}$ concentrations over long timescales (ka to Ma) as a result of their slow growth rates, yet our understanding of their interactions with $Mn(II)_{aq}$-bearing fluids and the implications for trace metals remains limited. Hence, it was imperative to address the reaction mechanisms and the fate of trace metals (e.g., Ni) associated with the Mn oxide phases in these deposits.

The three key objectives of this thesis, which have been consolidated into a published article (Chapter 2), a self-contained chapter (3), and a submitted manuscript (Chapter 4), were to:

- Examine the role of $Mn(II)_{aq}$-$Mn(III)_s$ interactions during Ni(II) sorption and incorporation into synthetic manganite (γ-Mn(III)OOH).

- Determine likely controls of Ni exchange on synthetic phyllomanganates (vernadite, hexagonal birnessite, triclinic birnessite), which represent suitable analogues for Mn oxides in deep-sea Fe-Mn concretions.

- Elucidate on the fate of Ni during interactions between $Mn(II)_{aq}$-bearing fluids and hydrogenetic Fe-Mn nodules and crusts.

These key objectives examined Mn oxide systems of increasing mineralogical complexity by transitioning from synthetic Ni-substituted manganite (Chapter 2) and Ni-substituted phyllomanganates (Chapter 3) to natural Fe-Mn samples (Chapter 4). In this conclusion chapter, significant implications of $Mn(II)_{aq}$-$Mn(III,IV)_s$ interactions for Ni exchange in these systems as well as environmental settings are discussed. Furthermore, potential applicability of this research for tailored hydrometallurgical processing of deep-sea Fe-Mn concretions are considered.

2. Research Implications

2.1. Effects of Mn(II) on Ni Exchange Between Mn Oxides and Aqueous Solutions

The findings of Chapters 2 and 3 demonstrated the complexity of $Mn(II)_{aq}$-$Mn(III,IV)_s$ interactions during recrystallization of synthetic Mn oxides and the effects on Ni exchange. These strictly controlled binary systems, which utilized a single sorbate (Ni) and synthesized substrates to reduce interferences of other metals (e.g. Fe), are characterized by changing reaction pathways. Differences in Ni uptake behavior and extent of Ni exchange were observed between pH 7.5 and pH 5.5 in the Mn(II)-manganite system examined in Chapter 2. This led to the identification of two pH-dependent reaction pathways, interfacial electron transfer-atom exchange (ET-AE) and disproportionation-comproportionation (DP-CP), affecting Ni exchange. The overall observed Ni exchange (~30% of total Ni) exceeded the number of Ni atoms sorbed on the manganite surface at pH 7.5, indicating that structurally incorporated Ni was exchanged with the fluid phase in the absence of observable structural modifications. Hence, aqueous Mn(II) enabled accessibility of the bulk mineral structure of manganite without inducing mineral phase transformations.

Initial crystallinity and Mn average oxidation state of layer-type Mn oxides, which are directly related to their structural Mn(III) content, were shown to affect the extent of Ni exchange between phyllomanganates and solution (Chapter 3). Higher structural Mn(III) content led to decreased Ni exchange, as competitive displacement between $Mn(II)_{aq}$ and $Ni(II)_{aq}$ occurs on vacancy sites. This competition may generally depend on metal properties (i.e. Jahn-Teller distortion, ionic radius, and electronegativity), indicating contaminant uptake may be dictated by greater metal affinity for the Mn oxide surface (Holguera et al., 2018).

For Ni, Lefkowitz and Elzinga (2017) have shown that surface-sorbed Ni may inhibit feitknechtite transformation into manganite during multi-step $Mn(II)_{aq}$-driven phase transformations of hexagonal birnessite. Similarly, the incorporation of Co into birnessite precursors may disrupt birnessite transformation into todorokite, as structurally incorporated Co(III) reduces the number of Jahn-Teller distorted Mn(III) octahedral, which act as structural weak points for the initiation of the birnessite-todorokite phase transformation. (Atkins et al., 2014; Bodeï et al., 2007; Grangeon et al., 2014; Wu et al., 2019; Zhao et al., 2015). The absence of bulk phase transformations in Chapter 2, yet observed $Mn(II)_{aq}$-induced structural modifications in Chapter 3, reinforce that changing reaction pathways and competitive displacement create complex systems even under supposedly simplified experimental settings.

The use of deep-sea ferromanganese nodules and crusts in Ni exchange experiments of Chapter 4, moreover, hinted at the complexity that can be expected to occur during $Mn(II)_{aq}$-$Mn(III,IV)_s$ interactions in natural settings (see Section 2.2 below). As Fe-Mn nodules and crusts have long been recognized as (irreversible) sinks for metals and metalloids (Holguera et al., 2018; Kwon et al., 2013; Miyata et al., 2007; Peacock, 2009; Simanova and Peña, 2015), it is a significant finding that Ni exchanges between these concretions and solutions. This implies that these Fe-Mn deposits are susceptible to solid-fluid interactions and sorption of Ni through structural incorporation may at least be partially reversible.

2.2. Significance of Research in the Context of Natural Settings

Marine and terrestrial environments can exhibit broad variability of $Mn(II)_{aq}$ concentrations and thus impact $Mn(II)_{aq}$-$Mn(III,IV)_s$ interactions. For instance, $Mn(II)_{aq}$ concentrations of 1 nM have been reported for surface and subsurface waters of the Southern Ocean, whereas the suboxic zone in Black Sea sediments may have $Mn(II)_{aq}$ concentrations of up to 500 µM (Konovalov et al., 2007; Middag et al., 2011). In localized environments contaminated by acid mine drainage up to 1.5 mM $Mn(II)_{aq}$ have been measured (Fuller and Harvey, 2000). Similarly, biofilms that may facilitate biogenic MnO_2 growth have been found to exhibit concentration gradients (Flemming and Wingender, 2010; Haack and Warren, 2003; Holguera et al., 2018). Although the influence of microbially-mediated activity (biofilms) on Fe-Mn nodule and crust growth remains unclear, this may suggest that the concentration of $Mn(II)_{aq}$ in direct contact with Mn oxide surfaces may be elevated in comparison to pore waters or seawater.

In environments with high Mn(II)aq concentrations, Mn oxide vacancies may become preferentially occupied by Mn(II,III) through competitive displacement of trace metals. In addition, the relative amount of vacancies and initial structural Mn(III) content also affect the ability of phyllomanganates to incorporate trace metals. Particularly in Mn oxides of Fe-Mn nodules and crusts, metals (e.g., Co, Ni, and Zn) occupy vacancies, which results in structural incorporation above, below, or within the layer vacant site (Manceau et al., 1997; Manceau et al., 2007; Peacock and Sherman, 2007a; Peacock and Sherman, 2007b). As competitive displacement decreases vacancy content and increases structural Mn(III) in phyllomanganates, their trace metal uptake capacity decreases. Hence, in settings where low Mn(II)aq concentrations are prevalent, Mn oxides with large vacancy content may form, allowing for greater uptake of dissolved metals from seawater (Burns, 1976; Lanson et al., 2002; Peacock and Sherman, 2007b; Zhao et al., 2009).

Moreover, as the pore space of Fe-Mn nodules has been found to be largely connected (Blöthe et al., 2015), it may allow fluids to induce Mn oxide recrystallization and/or trace metal cycling on a significantly larger surface area even in the absence of elevated Mn(II)aq concentrations. This may occur over long timescales since growth rates of deep-sea Fe-Mn deposits are slow (mm/Ma). Lastly, since reaction mechanisms exhibit pH dependence, as discussed in Chapters 2-4, the effects on trace metal cycling are likely to be dynamic when alterations in environmental conditions (i.e. changes in oxygenation levels of sediments) occur.

2.3.   Significance of Research in the Context of Hydrometallurgical Processing

Advancements of green technologies, such as the rise of electric vehicles and renewable power production, are going to accelerate the demand for raw materials (e.g., Månberger and Stenqvist, 2018). Since deep-sea ferromanganese nodules and crusts are enriched in a wide variety of traditional and non-traditional metals, interest in these deposits has re-emerged in recent years after unsuccessful attempts of deep-sea mining in the 1970-80s (Hein, 2016). To make seabed mining of Fe-Mn concretions a reality within the next decade(s), mining companies, engineers, policy makers, and geoscientists must ensure the efficacy of multidisciplinary solutions for deep-sea mining challenges.

At present, geoscientific research strongly focuses on exploration, which entails resource estimates, environmental impact assessments as well as biodiversity studies. Aspects that are positioned at the 'back-end' of the marine mining value chain, such as the development of innovative processing solutions going beyond mere modification of established methods, still receive little attention. Estimates assign about 50% of the overall investment costs of deep-sea mining ventures to processing technology of Fe-Mn deposits (Yamazaki, 2008). Yet, established metallurgical treatment and conventional beneficiation methods are considered challenging due to the complex mineralogical composition and nm-µm scale intergrowth of Fe-Mn minerals (Burns and Burns, 1977; Haynes et al., 1985; Von Heimendahl et al., 1976; Wegorzewski et al., 2018), as mentioned in Chapter 4. Hence, innovative processing solutions are required to positively affect the deep-sea mining value chain and balance any operational footprint in an environmentally responsible way (i.e., low energy input requirements, zero-waste approach).

The exchangeability of Ni between Fe-Mn concretions and fluids may represent a key step for the development of hydrometallurgical treatments. Accessibility of bulk-incorporated Ni by fluid phases and subsequent mineral-fluid repartitioning indicates that trace metals associated with

Fe-Mn nodules and crusts may be available for selective extraction as part of tailored metal processing techniques. Further research, going beyond the scope of this thesis, is required to fully assess the applicability of $Mn(II)_{aq}$-$Mn(III,IV)_s$ interactions for hydrometallurgical treatments.

3. Summary and Future Research Priorities

The key objectives of this thesis set out to advance our fundamental understanding of Ni cycling during interactions between dissolved Mn(II) and Mn(III,IV) oxides under variable reaction conditions (pH, $Mn(II)_{aq}$ concentrations, and time) in systems of increasing mineralogical complexity. The findings presented in Chapters 2-4 have led to an improved understanding of Ni cycling during mineral-fluid interactions between synthetic and natural Mn oxides and $Mn(II)_{aq}$-bearing fluids. Where Chapters 2 and 3 investigated binary systems (i.e., $Mn(II)_{aq}$-manganite and $Mn(II)_{aq}$-phyllomanganates), Chapter 4 transitioned from synthetic samples towards a highly complex mineralogical system by utilizing deep-sea ferromanganese nodules and crusts.

A key finding is that structurally incorporated Ni may freely exchange between solids and solutions regardless of the initial $Mn(II)_{aq}$ concentration. This highlights that Fe-Mn concretions may not necessarily be finite sinks for metals as previously thought, but instead act as (partially) open systems, notwithstanding that potential study limitations exist (e.g., assumption of homogenous Ni exchange – see Gorski and Fantle (2017) for a detailed review on recrystallization models). The findings reinforce that $Mn(II)_{aq}$ is an important factor in controlling structural properties of Mn oxides and subsequently exerts significant influence on the fate of trace elements. As natural environments are characterized by greater complexity than examined in this work, and layer-type Mn oxides are considered for remediation attempts of polluted environments (e.g., Han et al., 2006), future research efforts should be directed towards the following priorities:

- Conduct multi-sorbate experiments with synthetic Mn oxides as well as natural samples to constrain trace metal interferences on $Mn(II)_{aq}$-induced recrystallization.

- Examine the impact of $Fe(II)_{aq}$-catalyzed mineral recrystallization on Fe-Mn nodules and crusts since Fe (oxyhydr)oxides are similarly important host phases for trace metals.

- Constrain interactions between $Fe(II)_{aq}$ and $Mn(II)_{aq}$ when in contact with Fe-Mn concretions in both experimental and natural settings.

4. References

Atkins, A.L., Shaw, S., Peacock, C.L., 2014. Nucleation and growth of todorokite from birnessite: Implications for trace-metal cycling in marine sediments. Geochimica et Cosmochimica Acta, 144: 109-125.

Blöthe, M., Wegorzewski, A.V., Müller, C., Simon, F., Kuhn, T., Schippers, A., 2015. Manganese-Cycling Microbial Communities Inside Deep-Sea Manganese Nodules. Environmental Science & Technology, 49(13): 7692-7700.

Bodeï, S., Manceau, A., Geoffroy, N., Baronnet, A., Buatier, M., 2007. Formation of todorokite from vernadite in Ni-rich hemipelagic sediment. Geochimica et Cosmochimica Acta, 71(23): 5698-5716.

Burns, R.G., 1976. The uptake of cobalt into ferromanganese nodules, soils, and synthetic manganese (IV) oxides. Geochimica et Cosmochimica Acta, 40(1): 95-102.

Burns, R.G., Burns, V.M., 1977. The mineralogy and crystal chemistry of deep-sea manganese nodules, a polymetallic resource of the twenty-first century. Philosophical Transactions of the Royal Society London, A286: 283-301.

Elzinga, E.J., 2011. Reductive Transformation of Birnessite by Aqueous Mn(II). Environmental Science & Technology, 45(15): 6366-6372.

Elzinga, E.J., 2016. ^{54}Mn Radiotracers Demonstrate Continuous Dissolution and Reprecipitation of Vernadite (δ-MnO$_2$) during Interaction with Aqueous Mn(II). Environmental Science & Technology, 50(16): 8670-8677.

Elzinga, E.J., Kustka, A.B., 2015. A Mn-54 Radiotracer Study of Mn Isotope Solid-Liquid Exchange during Reductive Transformation of Vernadite (δ-MnO$_2$) by Aqueous Mn(II). Environmental Science & Technology, 49(7): 4310-4316.

Flemming, H.-C., Wingender, J., 2010. The biofilm matrix. Nature Reviews Microbiology, 8(9): 623-633.

Fuller, C.C., Harvey, J.W., 2000. Reactive Uptake of Trace Metals in the Hyporheic Zone of a Mining-Contaminated Stream, Pinal Creek, Arizona. Environmental Science & Technology, 34: 1150-1155.

Gorski, C.A., Fantle, M.S., 2017. Stable mineral recrystallization in low temperature aqueous systems: A critical review. Geochim. Cosmochim. Acta, 198: 439-465.

Grangeon, S., Lanson, B., Lanson, M., 2014. Solid-state transformation of nanocrystalline phyllomanganate into tectomanganate: influence of initial layer and interlayer structure. Acta Crystallographica Section B, 70: 828-838.

Haack, E.A., Warren, L.A., 2003. Biofilm hydrous manganese oxyhydroxides and metal dynamics in acid rock drainage. Environmental Science & Technology, 37(18): 4138-4147.

Han, R., Zou, W., Zhang, Z., Shi, J., Yang, J., 2006. Removal of copper (II) and lead (II) from aqueous solution by manganese oxide coated sand: I. Characterization and kinetic study. Journal of Hazardous Materials, 137(1): 384-395.

Haynes, B.W., Law, S.L., Barron, D.C., Kramer, G.W., Maeda, R., 1985. Pacific Manganese Nodules: Characterization and Processing Bulletin (United States Bureau of Mines), pp. 43.

Hein, J.R., 2016. Manganese Nodules. In: Harff, J., Meschede, M., Petersen, S., Thiede, J. (Eds.), Encyclopedia of Marine Geosciences. Encyclopedia of Earth Sciences Series. Springer, Dordrecht, pp. 408-412.

Hinkle, M.A.G., Dye, K.G., Catalano, J.G., 2017. Impact of Mn(II)-Manganese Oxide Reactions on Ni and Zn Speciation. Environmental Science & Technology, 51: 3187-3196.

Hinkle, M.A.G., Flynn, E.D., Catalano, J.G., 2016. Structural response of phyllomanganates to wet aging and aqueous Mn(II). Geochimica et Cosmochimica Acta, 192: 220-234.

Holguera, J.G., Etui, I.D., Jensen, L.H.S., Peña, J., 2018. Contaminant loading and competitive access of Pb, Zn and Mn(III) to vacancy sites in biogenic MnO_2. Chemical Geology, 502: 76-87.

Konovalov, S.K., Luther, G.W., Yücel, M., 2007. Porewater redox species and processes in the Black Sea sediments. Chemical Geology, 245: 254-274.

Kwon, K.D., Refson, K., Sposito, G., 2013. Understanding the trends in transition metal sorption by vacancy sites in birnessite. Geochimica et Cosmochimica Acta, 101: 222-232.

Lanson, B., Drits, V.A., Gaillot, A.-C., Silvester, E., Plançon, A., Manceau, A., 2002. Structure of heavy-metal sorbed birnessite: part 1. Results from X-ray diffraction. American Mineralogist, 87: 1631-1645.

Lefkowitz, J.P., Elzinga, E.J., 2015. Impacts of aqueous Mn(II) on the sorption of Zn(II) by hexagonal birnessite. Environmental Science & Technology, 49: 4886-4893.

Lefkowitz, J.P., Elzinga, E.J., 2017. Structural alteration of hexagonal birnessite by aqueous Mn(II): Impacts on Ni(II) sorption. Chemical Geology, 466: 524-532.

Lefkowitz, J.P., Rouff, A.A., Elzinga, E.J., 2013. Influence of pH on the reductive transformation of birnessite by aqueous Mn(II). Environmental Science & Technology, 47(18): 10364−10371.

Månberger, A., Stenqvist, B., 2018. Global metal flows in the renewable energy transition: Exploring the effects of substitutes, technological mix and development. Energy Policy, 119: 226-241.

Manceau, A., Drits, V.A., Silvester, E., Bartoli, C., Lanson, B., 1997. Structural mechanism of Co^{2+} oxidation by the phyllomanganate buserite. American Mineralogist, 88(11-12): 1150-1175.

Manceau, A., Lanson, M., Geoffroy, N., 2007. Natural speciation of Ni, Zn, Ba, and As in ferromanganese coatings on quartz using X-ray fluorescence, absorption and diffraction. Geochimica et Cosmochimica Acta, 71: 95-128.

Middag, R., de Baar, H.J.W., Laan, P., Cai, P.H., van Ooijen, J.C., 2011. Dissolved manganese in the Atlantic sector of the Southern Ocean. Deep Sea Research Part II: Topical Studies in Oceanography 58: 2661-2677.

Miyata, N., Tani, Y., Sakata, M., Iwahori, K., 2007. Microbial manganese oxide formation and interaction with toxic metal ions. Journal of Bioscience and Bioengineering, 104(1): 1-8.

Peacock, C.L., 2009. Physiochemical controls on the crystal-chemistry of Ni in birnessite: Genetic implications for ferromanganese precipitates. Geochimica et Cosmochimica Acta, 73: 3568-3578.

Peacock, C.L., Sherman, D.M., 2007a. Crystal-chemistry of Ni in marine ferromanganese crusts and nodules. American Mineralogist, 92(7): 1087-1092.

Peacock, C.L., Sherman, D.M., 2007b. Sorption of Ni by birnessite: Equilibrium controls on Ni in seawater. Chemical Geology, 238(1-2): 94-106.

Simanova, A.A., Peña, J., 2015. Time-Resolved Investigation of Cobalt Oxidation by Mn(III)-Rich δ-MnO_2 Using Quick X-ray Absorption Spectroscopy. Environmental Science & Technology, 49(18): 10867-10876.

Von Heimendahl, M., Hubred, G.L., Fuerstenau, D.W., Thomas, G., 1976. A transmission electron microscope study of deep-sea manganese nodules. Deep Sea Research Oceanography Abstracts 23: 69-79.

Wegorzewski, A., Köpcke, M., Kuhn, T., Sitnikova, M., Wotruba, H., 2018. Thermal Pre-Treatment of Polymetallic Nodules to Create Metal (Ni, Cu, Co)-Rich Individual Particles for Further Processing. Minerals, 8(11): 523.

Wu, Z., Peacock, C.L., Lanson, B., Yin, H., Zheng, L., Chen, Z. et al., 2019. Transformation of Co-containing birnessite to todorokite: Effect of Co on the transformation and implications for Co mobility. Geochimica et Cosmochimica Acta, 246: 21-40.

Yamazaki, T., 2008. Model mining units of the 20th century and the economies. Technical paper for ISA Workshop on Polymetallic Nodule Mining Technology-Current Status and Challenges Ahead: 18-22.

Zhao, H., Liang, X., Yin, H., Liu, F., Tan, W., Qiu, G., Feng, X., 2015. Formation of todorokite from ''c-disordered'' H^+-birnessites: the roles of average manganese oxidation state and interlayer cations. Geochemical Transactions, 16: 1-11.

Zhao, W., Cui, H.J., Feng, X.H., Tan, W.F., Liu, F., 2009. Relationship between Pb^{2+} adsorption and average Mn oxidation state in synthetic birnessites. Clays and Clay Minerals, 57: 338-345.